FUNCTIONS OF THE NONSTRUCTURAL PROTEIN σNS IN REOVIRUS REPLICATION

By

Paula Francisca Zamora Vargas

Dissertation

Submitted to the Faculty of the

Graduate School of Vanderbilt University

in partial fulfillment of the requirements

for the degree of

DOCTOR OF PHILOSOPHY

in

Microbiology and Immunology

August 10, 2018

Nashville, Tennessee

Approved by:

Earl Ruley, Ph.D.

Todd R. Graham, Ph.D.

Anne K. Kenworthy, Ph.D.

Kristen M. Ogden, Ph.D.

Larry L. Swift, Ph.D.

Terence Dermody, M.D

To everyone who encouraged my passion for science

My family, who stimulated my curiosity from a young age

Beatriz Rodriguez, my high-school biology teacher, who never doubted my talents

My husband, my biggest fan

And to myself, keep dreaming big

!La que lo sigue, lo consigue!

ACKNOWLEDGEMENTS

I am grateful for the financial support provided by the Cell Biology of Reovirus Infection Grant (R01 AI032539), the Vanderbilt Program in Microbial Pathogenesis (CTRA1 3045080025), and Lamb Center for Pediatric Research at Vanderbilt University.

I am eternally grateful for the Vanderbilt International Scholar Program for their financial, logistical, and emotional support. Being accepted in this program truly changed my life. I appreciate that the Steering Committee gave me this opportunity. I am thankful for the help and camaraderie offered by Amanda Connolly and the international students. I would probably have not stayed a month in Nashville if it was not for the support of Andrea Belovich and Erica Pruett Anderson, who let me stay in their place when I was homesick. Thanks also to my neighbors Alex Fish and Arwen Frick-Cheng who helped me with every aspect of my life when I first arrived to the US, from driving me to school to taking me grocery shopping. Thanks to David and Janice Hoagey for becoming my “adults to go” when I needed them.

I would like to thank Terry Dermody for giving me the opportunity to work in his lab and for training me to become a scientist. I am grateful for his efforts to make me a better communicator and help me feel comfortable speaking and writing in another language. Terry, thanks for the life lessons. My least favorite, “choice means loss”, has helped me a lot. I will miss your sense of humor. It brightens my day to be able to joke with you.

If it was not for Bernardo Mainou and Alison Ashbrook, I would probably not be writing this dissertation. I cannot thank Bernardo enough for being my mentor and my

friend. Thanks for teaching me virology and cell biology, for always being available when I had questions, and for sticking up for me. I would like to thank Alison for her friendship, for being a great listener, and for always having a shoulder for me to lean on. You both encouraged me through tough times.

I would like to thank the Dermody lab for making work not seem like work. You all have been my extended family abroad. I appreciate the moments we spent laughing together. Special thanks are owed to the Wilson lab members for their science help and life guidance. Thanks to my bay 11 mates Pavithra Aravamudhan and Jonathan Knowlton for the fun times and encouragement. You put up with all my whining, complaining, jokes, stair and push up challenges, and videos of my dogs. You even let me take your reagents for experiments and your money for candy.

I am grateful to my collaborators who contributed to this work. I would like to acknowledge Liya Hu for the almost kilograms of purified protein sent to me and for the TEM images of σNS and RNA. Thanks to Jonathan Knowlton, Roni Lahr, and Rodolfo Moreno for contributing with experiments and data interpretation. Raquel Tenorio and Isabel Fernandez de Castro were instrumental in helping with high-resolution imaging of reovirus infection. Thanks to Bernardo Mainou for his molecular biology expertise and to John Parker for the helpful discussions. I appreciate the training and assistance I received from the Vanderbilt University Cell Imaging Shared Resource, especially from Carol Ann Bonner and Bob Matthews who taught me confocal microscopy.

I am thankful for the members of my thesis committee, Todd Graham, Anne Kenworthy, Kristen Ogden, Earl Ruley, and Larry Swift for the useful ideas and important suggestions. Special thanks to my chair Earl Ruley. I appreciate his guidance, honesty,

and mentoring style. I am better at critical thinking thanks to him. Thanks to the PMI department and everyone that contributed to my education.

I am deeply thankful to Adams Carroll for being my principal support. Thanks for directly contributing to this work by spending hours in lab with me, helping me practice oral presentations, proofreading documents, and assisting with illustrations. You moved to Pittsburgh so that I could pursue my education. Thanks for encouraging me to follow my passions and thanks for taking care of us and our dogs while I spend my time doing what I love. I promise that someday I will do the chores.

Thanks to my family and friends from the other side of the world. I am grateful to my parents for the motivation they offered, their yearly birthday visits, and the constant reminders that family comes first. Thanks to my sister Susana for her help making illustrations and for taking care of our parents while I am away pursuing my dreams. I am very grateful for my Chilean friends for understanding that I have been busy for the last seven years but one day I will be back and we will make up for lost time. Special thanks to Natacha Marini and Kelly Cautivo, who were fundamental in my decision to apply to graduate school in the US.

Last but not least, thanks to Lily, Laika, and Toqui for cheering me up after bad science days. There is no better medicine than their wagging tails and sloppy kisses.

TABLE OF CONTENTS

LIST OF FIGURES

Figure Page

LIST OF TABLES

LIST OF ABBREVIATIONS

(-) RNA	Negative-sense single-stranded RNA
(+) RNA	Positive-sense single-stranded RNA
2D	Two-dimensions
3D	Three-dimensions
ANOVA	One-way analysis of variance
ARV	Avian reovirus
ATCC	American Type Culture Collection
ATP	Adenosine triphosphate
ATPase	ATP monophosphatase
Bev	Bevacizumab
BHK	Baby hamster kidney
BioID	Proximity-dependent biotin identification
BirA	Biotin ligase
BSA	Bovine serum albumin
BTV	Bluetongue virus
Caf	Carfilzomin
Car	Carboplatin
cDNAs	Complementary DNA
CHX	Cycloheximide
CIP	Calf intestinal alkaline phosphatase

CMV	Cytomegalovirus
CPM	Counts per minute
CPV	Cypovirus
Cryo-EM	Electron cryomicroscopy
Cyc	Cyclophosphamide
DAPI	4’,6-diamidino-2-phenylindole
Dex	Dexamethasone
DMEM	Dulbecco’s modified Eagle medium
DNA	Deoxyribonucleic acid
Doc	Docetaxel
dsRNA	Double-stranded RNA
DTT	1,4-dithiothreitol
EDTA	Ethylenediaminetetraacetic acid
eIF2α	Eukaryotic Initiation Factor 2 alpha
eIF3A	Eukaryotic Translation Initiation Factor 3 Subunit A
EM	Electron microscopy
EMSA	Electrophoretic mobility shift assays
ER	Endoplasmic reticulum
FAST	Fusion-associated small transmembrane
FBS	Fetal bovine serum
FFU	Fluorescent focus unit
Fol	FOLFIRI
Fol6	FOLFOX-6

G3BP1	Rad-GAP SH3-binding protein 1
GADPH	Glyceraldehyde-3-phosphate dehydrogenase
GCRV	Grass carp reovirus
Gen	Gemcitabine
GFP	Green fluorescent protein
GPI	Glycosylphosphatidylinositol
GTP	Guanosine triphosphate
GUSB	Beta-glucuronidase
HBMEC	Human brain microvascular endothelial cell
HEK293T	Human embryonic kidney 293T cell
HEPES	4-(2-hydroxyethyl)-1-piperazineethanesulfonic acid
HIT	Histidine triad
HITS-CLIP	High-throughput sequencing of RNA purified by cross-linking immunoprecipitation
HIV	Human immunodeficiency virus
h	Hour(s)
hpi	Hours post-infection
HPRT	Hypoxanthine phosphoribosyltransferase
Hsc70	Heat shock cognate 71 kDa protein
HTS	High-throughput sequencing
IBDV	Infectious bursal disease virus
ICTV	International Committee on Taxonomy of Viruses
IFN	Interferon

IgG	Immunoglobulin G
IgSF	Immunoglobulin superfamily
IP	Intraperitoneal
IPNV	Infectious pancreatic necrosis virus
IPTG	Isopropyl β-D-1-thiogalactopyranoside
IRF	Interferon regulatory factor
ISG	Interferon-stimulated gene
ISVPs	Infectious subvirion particle
ITu	Intratumoral
IV	Intravenous
JAM-A	Junction adhesion molecule-A
JMEM	Joklik's modified Eagle's minimal essential medium
kb	Kilobase
K_D	Dissociation constant
kDa	Kilodalton
lig	Ligation
m	Meter(s)
M	Molar
MDA5	Melanoma differentiation-associated protein 5
min	Minute(s)
MOI	Multiplicity of infection
mRNA	Messenger RNA
N	Normal

NDP	Nucleoside-diphosphate
NgR1	Nogo receptor 1
NSCLC	Non-small cell lung cancer
NSP	Nonstructural protein
NTP	Nucleoside triphosphate
NPC1	Niemann-Pick disease, type C
ORF	Open reading frame
ORP1L	Oxysterol-binding protein-related protein 1L
OSBP	Oxysterol-binding protein 1
Pac	Paclitaxel
PAGE	Polyacrylamide gel electrophoresis
PBS	Phosphate-buffered saline
PCR	Polymerase chain reaction
PEI	Polyethylenimine
Pem	Pemetrexed
PDI	Protein disulfide isomerase
PFA	Paraformaldehyde
PFU	Plaque forming unit
PKR	Protein kinase RNA-activated
poly[C]	Polycytidylate
Pre	Prednisone
Prot	Protein
Prot K	Proteinase K

PRR	Pattern recognition receptor
pS6R	Phosphorylated ribosomal protein S6
qPCR	Quantitative real time PCR
Rad	Radiation
RBSDV	Rice black-streaked dwarf virus
RdRp	RNA-dependent RNA Polymerase
Reovirus	Mammalian orthoreovirus
RER	Rough ER
RiboP	Ribosomal P protein
RIG-I	Retinoic acid-inducible gene 1
RNA	Ribonucleic acid
RNAi	RNA interference
RNase A	Ribonuclease A
rpS3	Ribosomal protein S3
rpS6	Ribosomal protein S6
RT	Reverse transcription
RT	Room temperature
SARM1	Sterile alpha and TIR motif-containing protein 1
SD	Standard deviation
SDS	Sodium dodecyl sulfate
shRNA	short-hairpin RNA
siRNA	short-interfering RNA
SM	Synonymous mutation

snRNA	Small nuclear RNA
ssDNA	Single-stranded DNA
ssRNA	Single-stranded RNA
STAT	Signal transducer and activator of transcription
SV40	Simian virus 40
T1L	Type 1 Lang
T2J	Type 2 Jones
T3D	Type 3 Dearing
T4N	Type 4 Ndelle
TCA	Trichloroacetic acid
TEM	Transmission EM
TL	Translational study
TLC	Thin-layer chromatography
TLR	Toll-like receptor
TRiC	Tcp-1 containing ring complex
ts	Temperature-sensitive
UTP	Uridine-5'-triphosphate
UTR	Untranslated region
UV	Ultraviolet
V	Volts
VSVG	Vesicular stomatitis virus glycoprotein G
WGA	Wheat germ agglutinin
WT	Wild-type

CHAPTER I

INTRODUCTION

Replication Mechanisms of Double-Stranded RNA Viruses

Background

Double-stranded RNA (dsRNA) viruses are a large group of viruses classified in eight unique families according to the International Committee for the Taxonomy of Viruses (ICTV) (Table I-1) (1). DsRNA viruses infect both prokaryotic and eukaryotic hosts, and many of these viruses are considered important pathogens of agricultural, medical, and veterinary relevance (Figure I-1) (2). Most of the pathogenic dsRNA viruses are members of the *Reoviridae* family. Some examples include rotavirus, which infects and replicates in the human intestine causing gastroenteritis and is responsible for approximately 200,000 deaths annually in children younger than 5 years old (3). Bluetongue virus (BTV) is a pathogen that infects ruminants, particularly sheep, and has caused more than 800,000 animal deaths in southern Europe (4). Rice black-streaked dwarf virus (RBSDV), which causes black-streaked dwarf disease in rice, is a major agricultural problem in China, Japan, and Korea (5). In general, dsRNA viruses show striking structural and functional similarities, likely due to conserved mechanisms of dsRNA genome replication. Understanding how these viruses replicate is important, and there are several gaps in knowledge regarding dsRNA virus replication that will be discussed later in this chapter.

Table I-1. Double-stranded RNA virus families and characteristics.

Family	Host	Example	Genome segment number	Capsid size	Capsid symmetry	Envelope
Birnaviridae	Invertebrates and vertebrates	Infectious bursal disease virus	2	65 nm	Icosahedral	No
Chrysoviridae	Fungi	Penicillium chrysogenum virus	4	40 nm	Icosahedral	No
Cystoviridae	Bacteria (*Pseudomona*)	Bacteriophage phi6	3	85 nm	Icosahedral	Yes
Endornaviridae	Plants	Vicia faba endornavirus	1	No true capsid	None reported	None reported
Partitiviridae	Fungi and plants	Penicillium stoloniferum virus S	2	30-43 nm	Icosahedral	No
Picobirnaviridae	Amniotes	Human picobirnavirus	2	33–37 nm	Spherical triacontahedral	No
Reoviridae	Fungi, plants, invertebrates, and vertebrates	Orthoreovirus	9-12	60-80 nm	Icosahedral	No
Totiviridae	Fungi and protozoa	Saccharomyces cerevisiae virus L-A	1	30-40 nm	Icosahedral	No

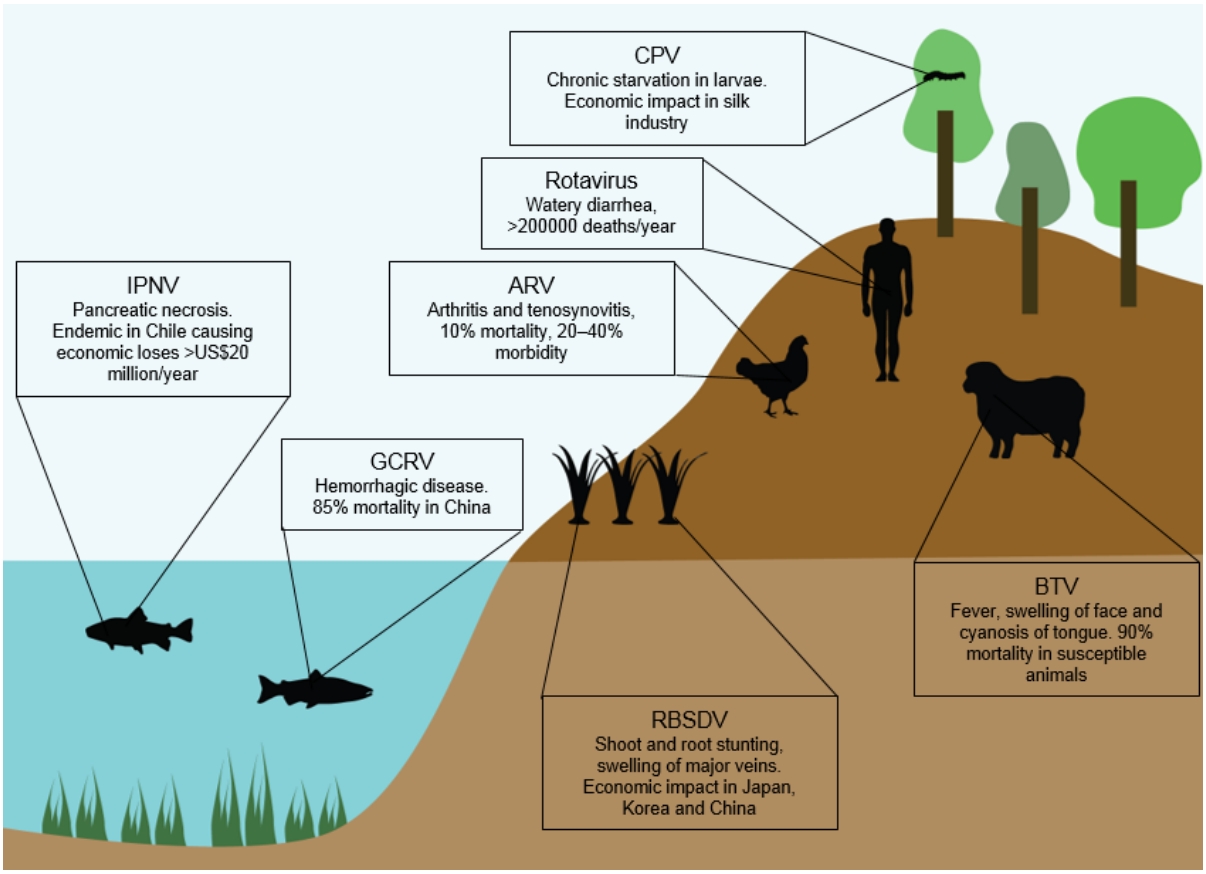

Figure I-1. Schematic of the diversity of dsRNA virus pathogens. DsRNA viruses are pathogens with a high economic impact. Rotavirus is responsible for thousands of human deaths worldwide. Bluetongue virus (BTV) and avian reovirus (ARV) are important livestock pathogens. Infectious pancreatic necrosis virus (IPNV) and grass carp reovirus (GCRV) cause economic loses in the fish industry. Rice black-streaked dwarf virus (RBSDV) is a major infection of rice in Asia. Cypoviruses (CPV) are a significant threat to the silk industry.

Mechanisms of dsRNA replication

Viruses with dsRNA genomes share mechanisms of viral replication. Common themes observed in the replication of these viruses include: (i) RNA-synthesis occurs inside a protein shell, (ii) genome replication and capsid assembly proceed in parallel, and (iii) *cis*-acting elements in the viral RNAs are important for template specificity (6).

All known dsRNA viruses confine their genomes, RNA-dependent RNA polymerases (RdRps), and auxiliary replication proteins inside a protein core (7). The dsRNA genome is used as a template for transcription, which occurs following entry into the cytoplasm during infection. In the cytoplasm, mRNAs are translated into viral proteins by host ribosomes, and newly synthesized proteins and transcribed mRNAs assemble into intermediate structures or replicase complexes. By a mechanism that is not understood, dsRNA synthesis follows (8).

The protein core and RdRps of different dsRNA viruses are similar (Figure I-2). Most cores organize in icosahedral structures that contain the RdRp either covalently linked to the core shell, as is the case of totivirus L-A (9), or positioned under the vertices, as seen for *Cystoviridae* and *Reoviridae* viruses (10, 11). Structurally, the polymerases of ϕ6 (12), infectious bursal disease virus (IBDV) (13), human picobirnavirus (14), rotavirus (15), and mammalian orthoreovirus (called reovirus in this thesis) (16) contain a core polymerase domain with a right-hand shape that includes fingers, palm, and thumb sub-domains, and an internally located active site (17). RdRps of dsRNA viruses can operate in a semi-conservative or fully-conservative manner (8). Before transcription, the positive-sense (+) RNA is separated from the negative-sense (-) RNA that form the dsRNA genome. Semi-conservative polymerases, such as those

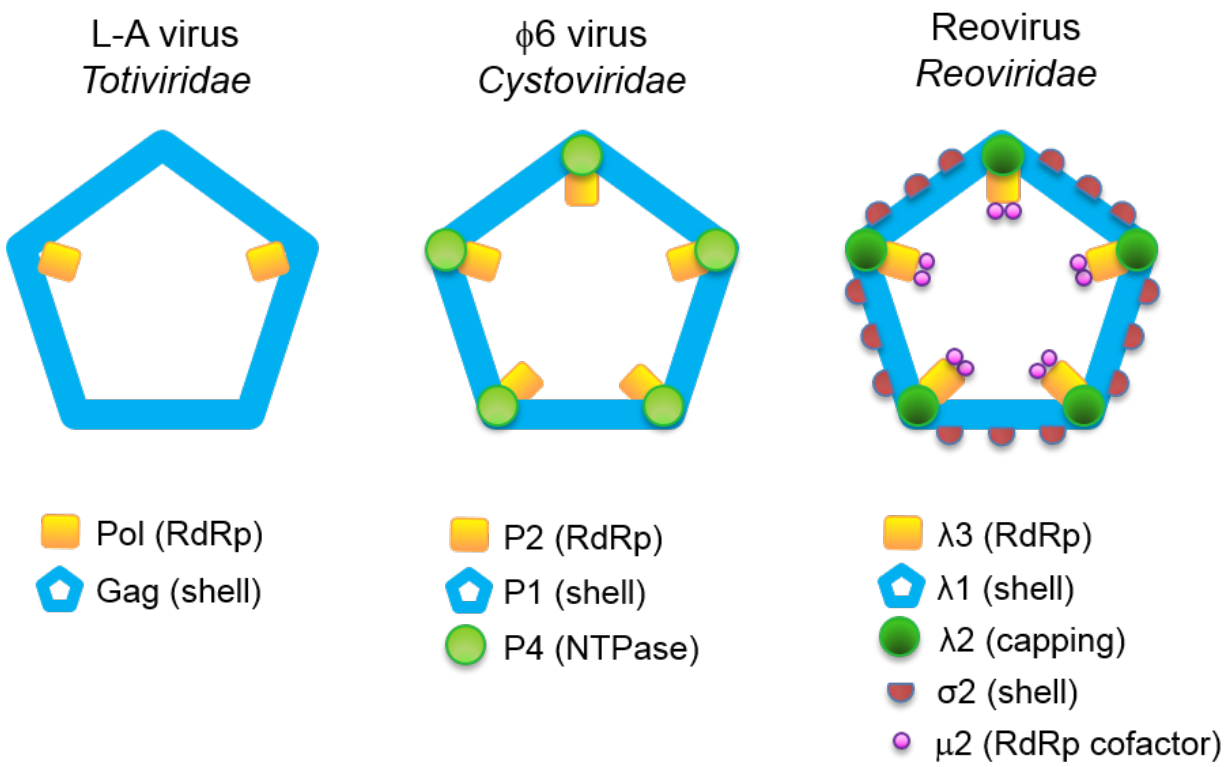

Figure I-2. Core components of three dsRNA viruses. DsRNA viruses share structural similarities. A protein shell contains the RdRp and auxiliary proteins. L-A virus, one of the simplest dsRNA viruses, has two copies of the RdRp covalently attached to the shell protein Gag. Phage ϕ6 and reovirus contain 12 RdRp copies underneath the shell vertices. The shell is composed of the P1 protein, and λ1 and σ2, for ϕ6 virus and reovirus, respectively. Auxiliary proteins also are found within the cores.

from ϕ6 and IBDV, shuttle out the (+) RNA from the core. This (+) RNA serves as a template for protein synthesis, while the (-) RNA inside the core is used as a template for a nascent (+) RNA strand. On the other hand, transcription by fully-conservative RdRps, such as those from reoviruses and rotaviruses, occurs by using the (-) RNA strand as a template for transcription of a nascent (+) RNA, which is shuttled from the core. The parental (+) RNA strand re-anneals with the (-) RNA strand to maintain the dsRNA genome. Thus, dsRNA viruses share mechanisms of dsRNA replication, although differences exist between evolutionary distant families.

Another feature of dsRNA virus replication is that genome synthesis and core assembly occur simultaneously. Considering that dsRNA is a potent inducer of the cellular antiviral response (18), protecting the dsRNA from the cellular environment is essential for viral fitness. Two models are proposed to explain the mechanism of genome replication and core assembly. A “core-filling” model suggests that a closed core without nucleic acid is assembled, followed by packaging of each gene segment inside the closed core and replication of the RNAs (Figure I-3) (19). A second model is called the “concerted model” and is based on the hypothesis that the RdRp and auxiliary proteins bind (+) RNAs before core formation, forming a replicase complex, or pre-core, that lacks polymerase activity. DsRNA synthesis occurs concomitant with the formation of a closed, mature core.

Specific RNA-protein and RNA-RNA interactions must occur to ensure that equimolar amounts of each RNA are packed within virions. For most segmented RNA viruses, the specificity of assortment and packaging – or choosing the correct gene segment – has been attributed to *cis*-acting signals in the viral RNAs (6). ϕ6 RNAs form

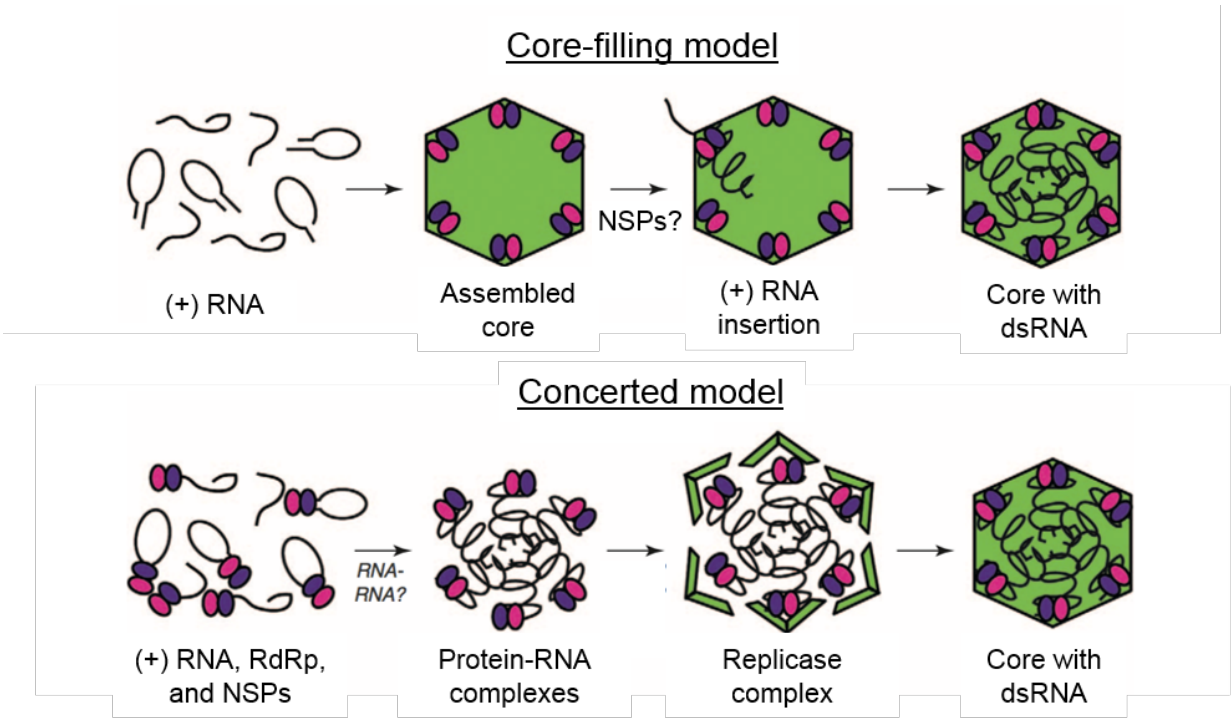

Figure I-3. Genome replication models for dsRNA viruses. There are two models to explain genome replication for dsRNA viruses. A “core-filling” model indicates that the protein shell assembles in the absence of (+) RNA. RNAs are then shuttled inside with the assistance of nonstructural proteins (NSPs), followed by RNA replication to form dsRNA. A “concerted model” suggests that viral (+) RNAs interact with NSPs that fold RNA in the proper conformation to mediate RNA-RNA interactions with the different gene segments. Protein-RNA complexes interact with the components of the core, forming a replicase complex. Concomitant with the replication of the RNA, the core closes. (Figure adapted from McDonald *et. al.* 2011 (19)).

stem-loops that fold distinctively depending on the gene segment, and these RNA structures mediate packaging. The recognition of each gene segment is based on unique *pac* sequences located at the 5'-end of each gene segment, which have affinity for the ϕ6 core proteins (20).

The specific packaging signals for *Reoviridae* viruses are less known, likely because of their complexity and larger number of gene segments. Packaging signals for reoviruses are thought to reside at the 5'- and 3'-ends of each (+) RNA (21-23). These sequences can form panhandle structures, which are hypothesized to be important for packaging (24). Rotavirus (+) RNA 5'- and 3'-untranslated regions (UTRs) have been suggested to form similar panhandle structures (25). It is thought that a stem-loop within these secondary structures acts as an assortment and packaging signal (26). Despite this knowledge, we still do not understand how between nine and twelve gene segments are specifically packed for the formation of progeny *Reoviridae* virions.

Common problems dsRNA viruses encounter during replication

Viruses with dsRNA genomes have developed various strategies to overcome common problems, including the lack of a primer for RNA synthesis, sensing of replication intermediates by the host antiviral response, gene segment assortment, and the use of the same (+) RNA as template for translation and genome replication.

RdRps initiate RNA polymerization at the 3'-end of the RNA template. This process can occur in a primer-dependent or independent manner (27). In primer-dependent initiation, a protein primer, a snatched-cap, or an oligonucleotide is used as a primer. The 3'-terminus of the template also can fold back and mimic a primer. In

primer-independent initiation, which is how dsRNA viruses initiate RNA polymerization, interactions between the RNA template and the incoming nucleotides occur to keep these nucleotides correctly positioned in the active site of the RdRp (28).

DsRNA viruses have RdRps with structural motifs that allow binding of a priming nucleotide for *de novo* initiation of RNA synthesis (6). The RdRp of ϕ6 has a four amino acid loop in a carboxyl terminal region referred to as the "initiation platform," that stabilizes the first incoming nucleotides (29). The RdRps from reovirus and rotavirus have a "priming loop," which is a flexible motif that binds the incoming nucleotides, supporting the formation of an initiation complex (15). Both the initiation platform of ϕ6 RdRp and priming loop of reovirus and rotavirus RdRps shift their location following formation of the first phosphodiester bond to accommodate the elongating RNA duplex (17). Thus, RdRps from dsRNA viruses have overcome the lack of priming during RNA polymerization by expressing specialized RdRps with additional motifs.

DsRNA is a potent stimulator of the cellular antiviral response. This response is based on the recognition of viral components by host cell pattern-recognition receptors (PRRs), which trigger signaling pathways that lead to the production and secretion of interferons (IFNs) (30). IFNs are sensed by specific receptors on host cells, culminating in the induction of IFN-stimulated genes (ISGs). The expression of ISGs results in up-regulation of PRRs and several signal-transducing molecules, reinforcing the IFN response. Additional ISGs encode proapoptotic proteins, leading to cell death and prevention of viral replication (31).

Mammalian hosts sense dsRNA using various mechanisms. Toll-like receptor 3 (TLR3) engages viral dsRNA in endosomes after viral entry, inducing expression of

IFNs. Retinoic acid-inducible gene 1 (RIG-I) and melanoma differentiation-associated protein (MDA5) are cytoplasmic viral RNA sensors that are recruited to the outer membrane of the mitochondria as part of a macromolecular signaling complex that leads to IFN expression after detection of viral dsRNA (31). DsRNA is also sensed by protein kinase R (PKR), which autophosphorylates and activates following dsRNA binding. PKR phosphorylates eIF2α, inhibiting protein synthesis in infected cells (32).

Mammalian dsRNA viruses have evolved to avoid the host antiviral response and express proteins that inhibit innate immunity. For example, reovirus prevents induction of IFN by disrupting the function of IRF9 (33) as well as by expressing dsRNA-binding proteins that prevent PKR activation (34). Rotavirus represses the IFN response by mediating the degradation of IRF3, IRF5, and IRF7 (35) and preventing nuclear translocation of STAT1 and STAT2, which are required for the induction of a cellular antiviral state (36).

Mammalian dsRNA viruses also protect their RNA intermediates by replicating within neoorganelles called viral inclusions, factories, or viroplasms. Viral inclusions are intracellular compartments where viral replication and particle assembly take place. Formation of inclusions usually involves reorganization of cellular membranes and the cytoskeleton. Inclusions facilitate viral replication by confining necessary metabolites to increase their local concentration (37). Viral inclusions are studied using optical and electron microscopy and have been observed during infection with members of the *Birnaviridae* (38) and *Reoviridae* (39-41) families.

By localizing replication intermediates in the same place, viral inclusions facilitate genome assortment of segmented dsRNA viruses. The rotavirus nonstructural protein

NSP2, which locates to rotavirus inclusions (40), binds to (+) RNAs and promotes their remodeling, which leads to the formation of stable and specific RNA-RNA interactions that might be required for assortment (42). Assortment of gene segments might follow a specific order, as *in vitro* transcribed rotavirus RNAs interact specifically with each other in a process initiated by small gene segments (43). Sequential packaging of gene segments also has been shown for BTV (44) and it is thought to be mediated by the 3'-UTRs of each gene segment, as the packaging signals reside in this region (45). Much less is known for reovirus. However, experiments using chimeric (+) RNAs, in which an open reading frame (ORF) is flanked by 5'- and 3'-UTRs from different gene segments, suggest that the 5'-UTRs are important for recognition of each gene segment (23). By introducing mutations in the S3 gene and attempting to recover viable virus using the reovirus reverse genetics system (46), it was determined that the 5'-UTR and immediate 18 nucleotides in the ORF could not be mutated to recover viable virus, suggesting that the assortment and packaging signals for reovirus might extend beyond the UTRs (47). Collectively, these data suggest that RNA-protein and RNA-RNA interactions mediate *Reoviridae* genome assortment.

Lastly, it is not clear how dsRNA viruses modulate the use of (+) RNA as templates for translation and genome replication. There are no published studies that address this issue for dsRNA viruses, but there is evidence of different mechanisms used by viruses with (+) RNA genomes. Most of the non-template functions of RNAs for these viruses are mediated through the interaction between specific motifs in the RNAs with host or viral *trans* activating factors (48). For poliovirus, the RNA polymerase is unable to replicate templates undergoing translation. A region in the 5'-UTR of

poliovirus RNA folds into a cloverleaf-like structure and acts as a bifunctional element regulating translation and genome replication. The binding of cellular proteins to this region enhances viral translation, whereas the binding of a viral protein represses translation and facilitates genome replication (49). Thus, viruses use viral and host proteins as well as RNA-RNA interactions to modulate replication cycle events.

Reoviruses

Background

The *Reoviridae* family is the largest of the dsRNA virus families. This family is divided into two subfamilies: *Sedoreovirinae* and *Spinareovirinae*, which include 15 distinct genera comprising 91 assigned species and several to-be-assigned (Figure I-4) (1). These two subfamilies differentiate according to their surface appearance. *Sedoreovirinae* (*Sedo:* Latin for smooth) viruses have a smooth or spherical appearance. In contrast, *Spinareovirinae* (*Spina:* Latin for spike) viruses possess relatively large spikes or turrets situated at the 12 icosahedral virion vertices (50).

Mammalian orthoreovirus (or reovirus) is the type species for the genus *Orthoreovirus*. These viruses infect vertebrates and are spread by respiratory or fecal-oral routes. Reoviruses were first isolated from stool samples from children during the 1950s. The name is an acronym for respiratory enteric orphan virus, as infection of humans often involves the respiratory and intestinal tracts with minimal or no associated disease (51). There are four reovirus serotypes that have been isolated from a variety of hosts, each represented by a prototype strain: type 1 Lang (T1L), type 2 Jones (T2J), type 3 Dearing (T3D), and type 4 Ndelle (T4N) (1).

Despite the fact that reovirus infection of humans rarely causes disease, reovirus infection has been associated with loss of oral tolerance to food antigens in genetically susceptible individuals (52, 53). Reovirus is an oncolytic agent and is currently being used in clinical studies to determine its efficacy against a variety of human cancers (Table I-2) (54). Thus, understanding basic mechanisms of reovirus replication could improve therapeutics against celiac disease and cancer.

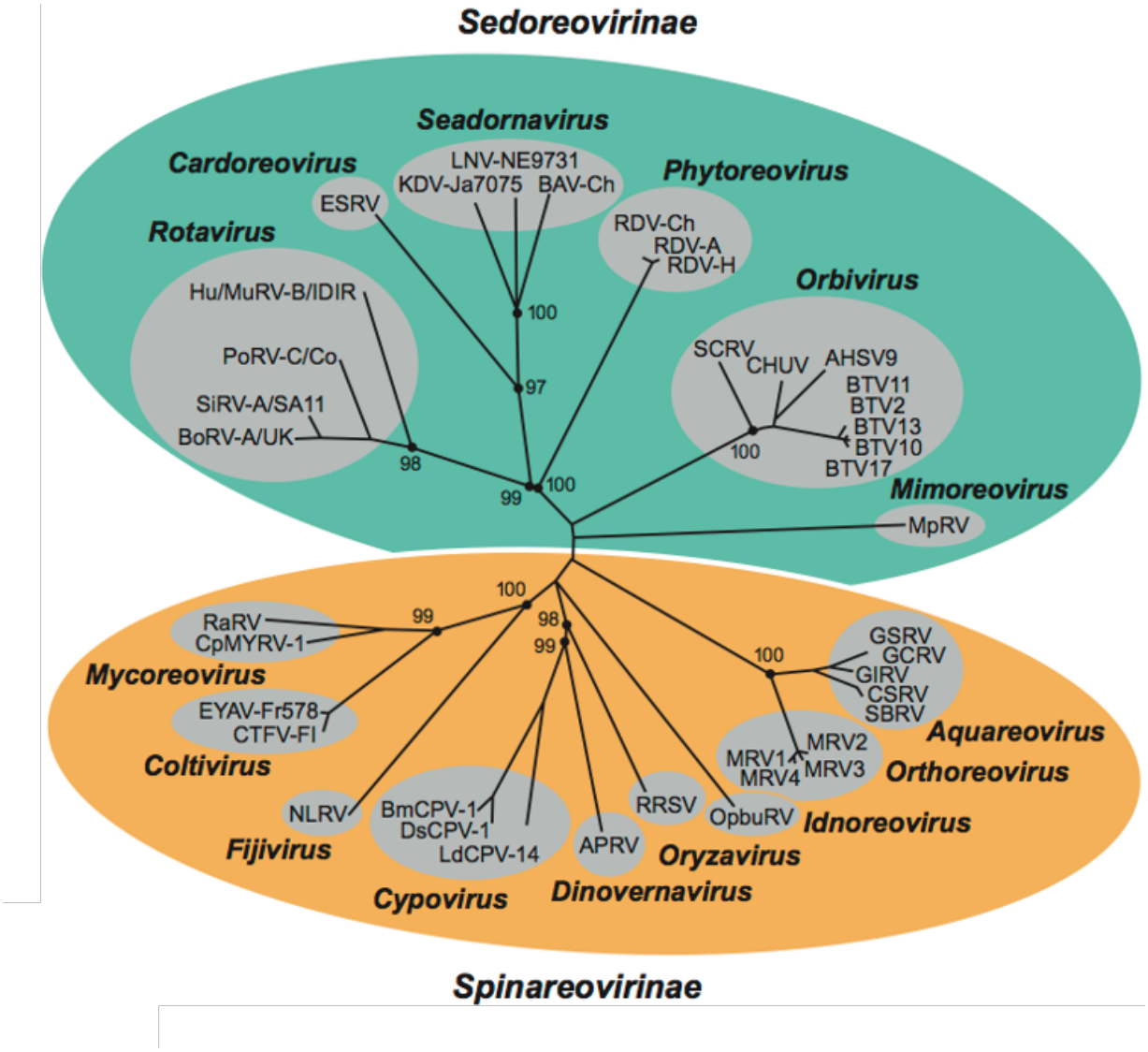

Figure I-4. Phylogenetic tree for the Reoviridae family. According to the amino acid sequences of putative RdRps for representative viruses, *Reoviridae* viruses are divided into two subfamilies: *Sedoreovirinae* and *Spinareovirinae*. Values at the nodes represent confidence levels. (Figure from ICTV 9th Report (2011) (1)).

Table I-2. Clinical trials using reovirus as an oncolytic agent.
[a] NSCLC: Non-small cell lung cancer
[b] IP: intraperitoneal, ITu: intratumoral, IV: intravenous, TL: translational study, Bev: bevacizumab, Caf: carfilzomin, Car: carboplatin, Cyc: cyclophosphamide, Dex; dexamethasone, Doc: docetaxel, Fol: FOLFIRI, Fol6: FOLFOX-6, Gen: gemcitabine, Pac: paclitaxel, Pem: pemetrexed, Pre: prednisone, Rad: radiation. (Figure adapted from Chakrabarty *et. al*. 2015 (54)).

Type of cancer	Treatment [b]	Phase
Various	ITu	I
Prostate	ITu	TL
Various gliomas	ITu	I
Various	IV	I
Various	IV	I
Various	ITu	I
Various gliomas	ITu	I/II
Various	ITu + Rad	II
Advanced malignancies	IV + Gem	I
Advanced malignancies	IV + Doc	I
Head & neck	IV + Pac, Car	I/II
Advanced malignancies	IV + Cyc	I
Colorectal	IV	TL
Brain	IV	I
Bone & soft tissue carcinoma	IV	II
Head & neck	IV + Pac, Car	II
Lung – NSCLC[a]	IV + Pac, Car	II
Pancreatic	IV + Gem	II
Head & neck	IV + Pac, Car	III
Melanoma	IV + Pac, Car	II
Lung – NSCLC[a]	IV + Pac, Car	II
KRAS mutant colorectal	IV + Fol	I
Melanoma	IV	II
Ovarian	IV and IP	I/II
Multiple myeloma	IV	I
Pancreatic	IV + Pac, Car	II
Solid tumors	IV + Cyc	I
Ovarian, fallopian tube	IV + Pad	II
Prostate	IV + Doc, Pre	II
Colorectal	IV + Fol6, Bev	II
Lung - NSCLC[a]	IV + Doc, IV + Pem	II
Breast	IV + Pac	II
Multiple myeloma	IV + Caf, Dex	TL

Genome organization and virion structure

The reovirus genome is divided into ten linear dsRNA segments with a total size of ~23.5 kb, which constitutes approximately ~11.5% of the virion mass (24). The ten gene segments are classified according to their size, and they are grouped into three classes: large (L1–L3, ~3.9–3.8 kb/each), medium (M1–M3, ~2.3–2.2 kb/each) and small (S1–S4, ~1.4–1.2 kb/each) (Figure I-5A). The three large gene segments (L1, L2, and L3) encode the λ3, λ2, and λ1 proteins, respectively. The three medium gene segments (M1, M2, and M3) encode the μ2, μ1, and μNS proteins, respectively. The four small gene segments (S1, S2, S3, and S4) encode the σ1 and σ1s, σ2, σNS, and σ3 proteins, respectively (Table I-3). Reovirus gene segments have 5'-UTRs that are shorter than the 3'-UTRs, and both regions contain conserved 5′- and 3′-terminal sequences (Figure I-5B) (24).

The reovirus virion is composed of two concentric protein shells with icosahedral symmetry that surround the dsRNA genome (Figure I-6). The inner capsid is formed by a shell of λ1 decamers that are stabilized by σ2. This shell is ~60 nm in diameter and has T=1 symmetry. Inside this inner capsid, the λ3 RdRp and μ2 polymerase co-factor reside at the base of the icosahedral vertices (Figure I-6). The outer capsid is formed by 200 μ1-σ3 heterohexamers. This shell is ~85 nm in diameter and has T=13 symmetry. The λ2 protein forms a pentameric turret at each icosahedral vertex from which the trimeric σ1 attachment protein is anchored (24). Both protein layers make reovirus remarkably stable to extreme ionic conditions, high temperature, variations in pH, and detergents (1).

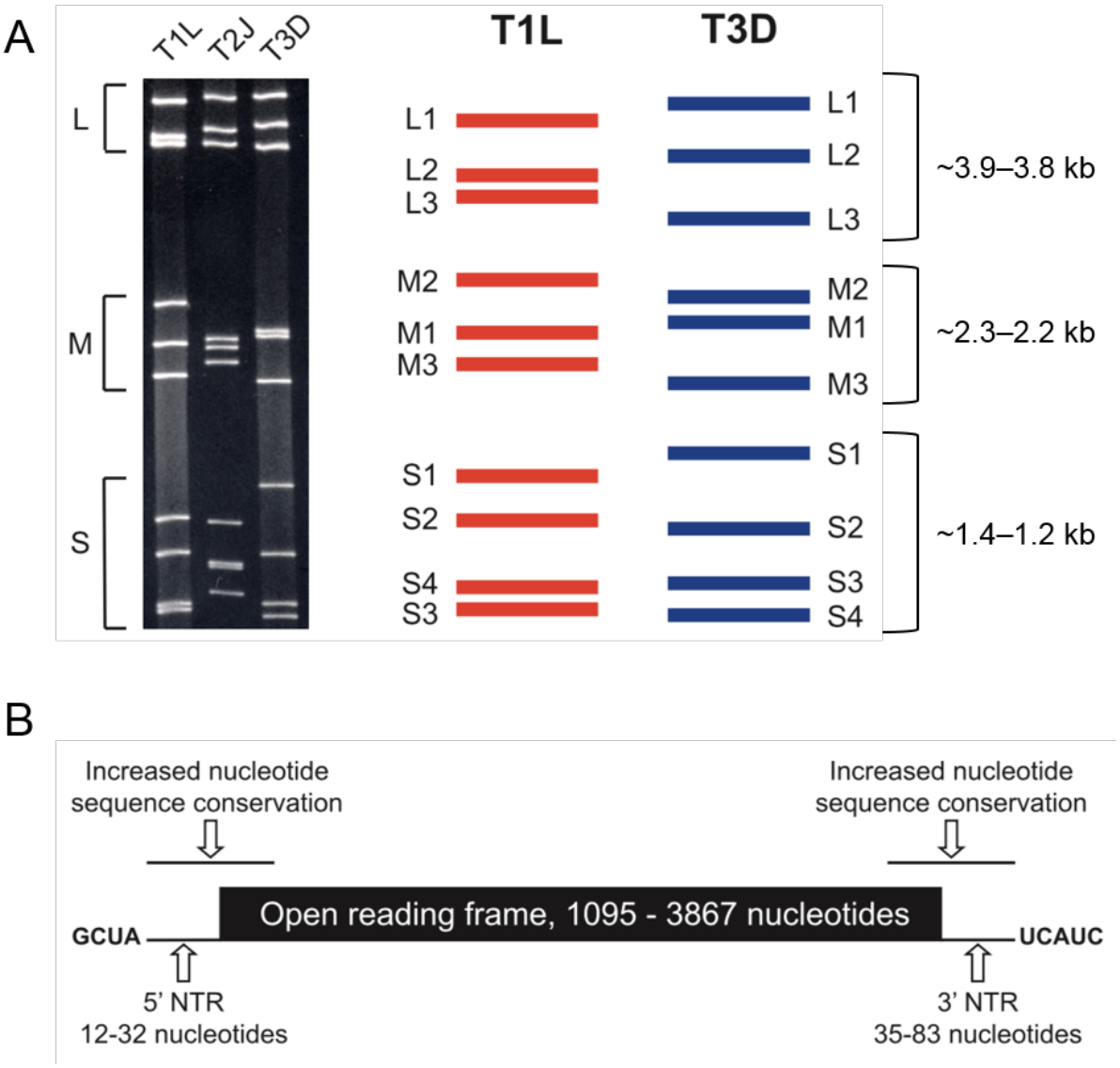

Figure I-5. The reovirus genome. (A) The reovirus genome is composed of ten gene segments, which are classified according to their size. There are three large, three medium, and four small segments, with different electrophoretic mobilities depending on the serotype. (B) Structure of reovirus gene segments. Each ORF is framed by UTRs, which are conserved among different segments and serotypes (Figure adapted from Fields Virology (24)).

Table I-3. Reovirus gene segments and their proteins.

Gene segment	Protein	Mass (kDa)	Copy number per virion
L1	λ3	142.3	12
L2	λ2	144	60
L3	λ1	142	120
M1	μ2	83.3	24
M2	μ1	76.3	600
M3	μNS	80	NSP
S1	σ1/ σ1s	51.4 (T1L), 49.2 (T3D) /14	36/NSP
S2	σ2	47.2	150
S3	σNS	41	NSP
S4	σ3	41.5	600

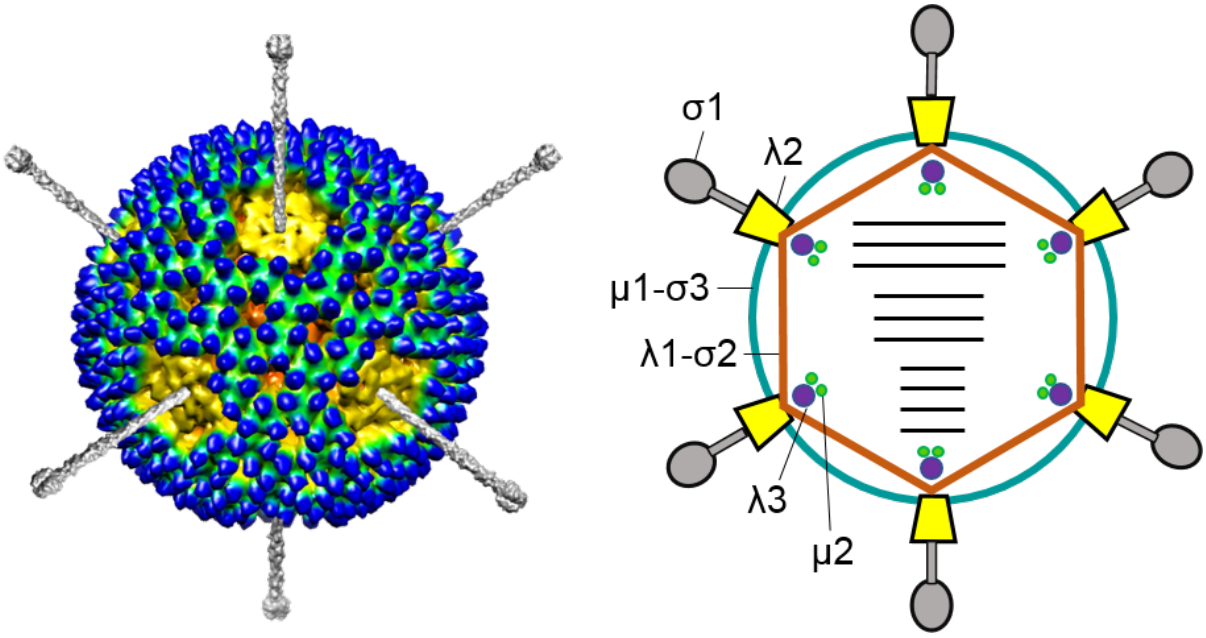

Figure I-6. The reovirus virion. Reoviruses are composed of two concentric protein shells that surround the dsRNA genome. The outer capsid is formed by 200 μ1-σ3 heterohexamers, while the inner capsid is formed by a shell of λ1 decamers that are stabilized by σ2. The λ3 RdRp and μ2 co-factor locate underneath the vertices. At each vertex, the λ2 protein forms a pentameric turret. σ1 is attached to these turrets. (Figure adapted from Nason *et. al*. 2001 and Dietrich *et. al*. 2018 (55, 56)).

Replication cycle

The reovirus life cycle begins with attachment of the virus to cell-surface receptors (Figure I-7). There are two known proteinaceous receptors that mediate reovirus attachment. Junctional adhesion molecule A (or JAM-A) is a member of the immunoglobulin superfamily (IgSF) involved in regulation of tight junction formation. This receptor is engaged by the S1-encoded reovirus σ1 protein (57-59). Nogo receptor NgR1 is a glycosylphosphatidylinositol (GPI)-anchored, leucine-rich repeat (LRR) protein expressed on the surface of neurons. It is not clear what viral components mediate engagement of this receptor (60). Reovirus also interacts with glycans on the cell surface through low-affinity, high-avidity interactions, facilitating initial attachment events (61-63).

Following attachment, reovirus is endocytosed using multiple pathways (64-67) and undergoes acid-dependent proteolytic disassembly within endosomes (68, 69). Cathepsin proteases in the lumen of these organelles are responsible for uncoating the reovirus virion, forming infectious subvirion particles (ISVPs) (70). ISVPs are characterized by cleavage of the μ1 protein to form fragments δ and Φ. They also lack σ3, and their σ1 protein undergoes a conformational change. ISVPs mediate endosomal membrane penetration through formation of pores to access the cytoplasm (71-73). This process occurs concomitantly with the total loss of the outer capsid. The particle that reaches the cytoplasm is the reovirus core.

In the cytoplasm, reovirus cores become transcriptionally active, and the λ3 RdRp and its co-factor μ2 transcribe mRNAs for the 10 gene segments (Figure I-8) (74, 75). The mRNAs exit the cores simultaneously at each of the vertices. As the mRNAs

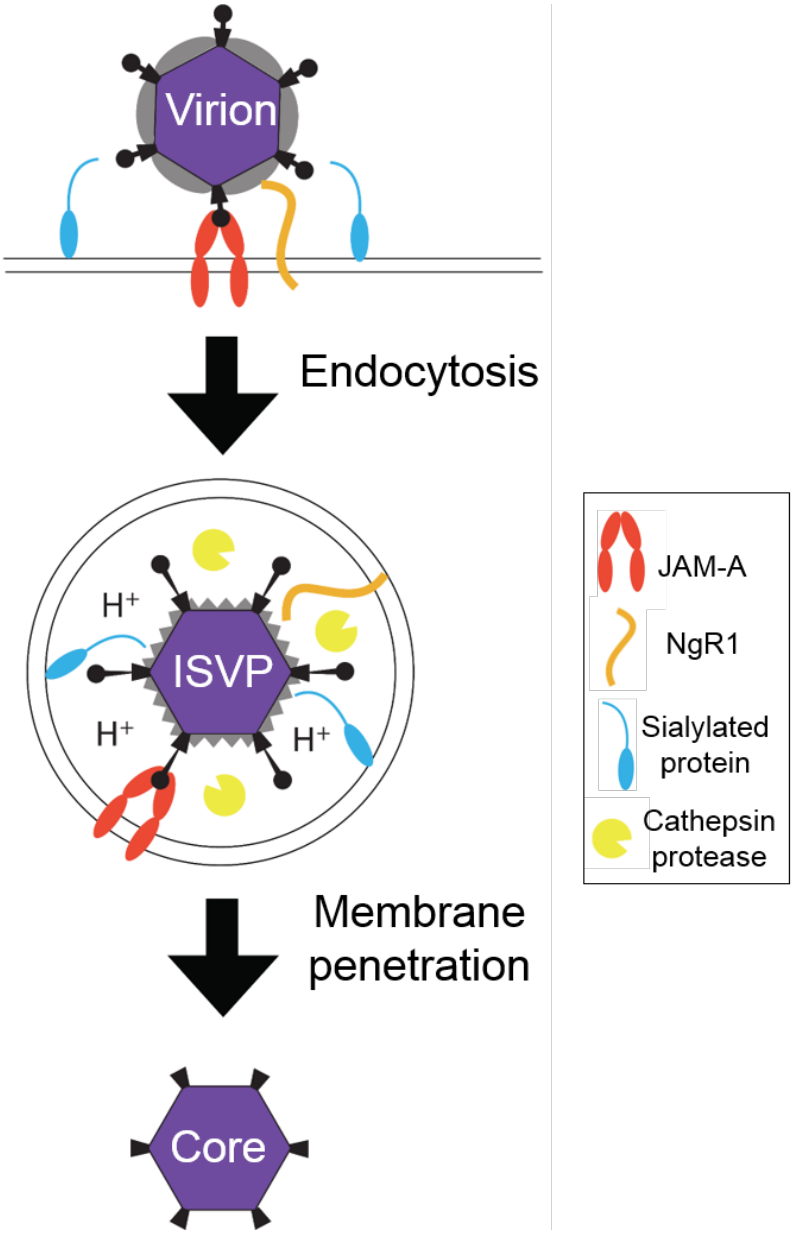

Figure I-7. Reovirus cell entry. Reovirus enters cells through receptor-mediated endocytosis. Reovirus binds high-affinity receptors, such as JAM-A and NgR1, and low-affinity ones such as sialic acid. Within endosomes, reovirus undergoes acid-dependent proteolytic disassembly, which allows it to penetrate membranes. The particle that reaches the cytoplasm is the reovirus core.

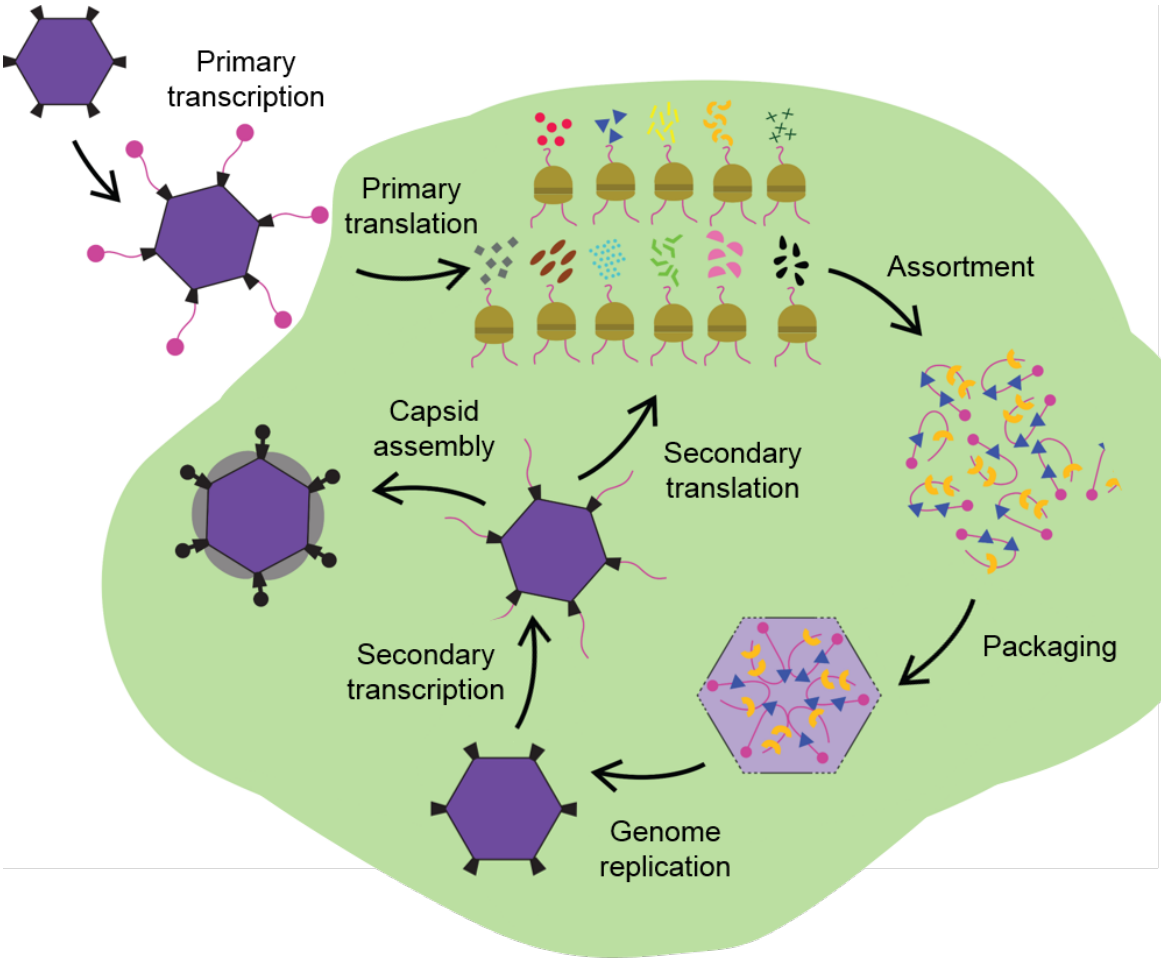

Figure I-8. Post-entry reovirus replication cycle steps. In the cytoplasm, reovirus cores undergo primary transcription. These mRNAs are capped and are translated into viral proteins. RNA-RNA and protein-RNA interactions are thought to mediate assortment. Transcripts, core proteins, and nonstructural proteins form replicase complexes prior to genome replication. Nascent cores are transcriptionally active, synthesizing uncapped mRNAs that are translated. Several rounds of transcription, translation, and genome replication take place within inclusions. Secondary transcription is terminated by assembly of the outer capsid onto cores.

pass through the λ2 channels, they are capped and 2'-O-methylated (76, 77). These mRNAs are used for translation of the eleven viral proteins. Prior to the replication of the genome, assortment of the individual gene segments must occur to obtain equimolar amounts. It has been hypothesized that replicase or pre-core complexes form, which contain λ3, core components, auxiliary proteins, and each reovirus mRNA. The replicase complex synthesizes (-) RNA for each reovirus mRNA to form dsRNA in a process that appears to occur at the same time as the core forms (24). Nascent cores are transcriptionally active and release uncapped mRNAs. These mRNAs are not capped because λ2 must be proteolytically cleaved to be active, a process that occurs during entry (78). Transcription, translation, and genome replication occur until transcription is silenced through the coalescence of the outer-capsid proteins onto nascent cores. Mature reovirus particles are released from cells through at least two mechanisms, one that disrupts cellular membrane permeability and one that does not (79, 80).

Viral inclusions

Most reovirus replication cycle steps occur within viral inclusions. Viral inclusions concentrate reovirus components to ensure proper genome replication and particle assembly. They also provide protection from the cellular antiviral response by masking replication intermediates from innate immune proteins (81). Viral inclusions form early in the replication cycle. They are highly dynamic and move and fuse with each other in a microtubule-dependent manner (39, 82-84). Ultrastructurally, reovirus inclusions organize as paracrystalline arrays of particles that arrange virions in a parallel manner along microtubules (82, 85).

Although the morphogenesis of reovirus inclusions is not clear, stress granules may be involved in their nucleation. Stress granules are aggregates of proteins and RNA that form in a reversible manner following cellular stress (86). Stress granules appear shortly after infection, but disappear before viral inclusions are formed (87). When expressed alone, the viral nonstructural protein μNS, thought to be responsible for viral inclusion nucleation (88), localizes to sodium arsenite-induced stress granules (89). In addition, stress granule proteins such as G3BP1 are found within inclusions (90), further supporting the idea that stress granules are involved in inclusion morphogenesis. The cellular protein dynein functions in the assembly and structural maintenance of reovirus inclusions (91). Other host proteins are found in inclusions, such as TRiC (92), Hsc70 (93), and clathrin (94), although it is not known whether they function in the morphogenesis of these neorganelles.

Nonstructural proteins

For productive infection of a host, viral genomes must be replicated at sites of primary infection and packaged into new virions for dissemination to susceptible cells at local or distant sites. Viruses encode proteins that are not packaged into virions to aid in these post-entry replication steps. These proteins are called nonstructural proteins. Nonstructural proteins participate in multiple viral replication steps, including translation of viral mRNAs (95), replication of viral genomes (96), construction of sites for particle assembly (97), and inhibition of innate immune responses (98). Due to constraints on viral genome size (99), most nonstructural proteins serve multiple roles during infection (100). Consequently, teasing out individual activities of viral nonstructural proteins is challenging.

Reovirus encodes three nonstructural proteins: σ1s, μNS, and σNS. σ1s is a protein encoded by the S1 gene segment. The σ1s ORF is located within the coding sequence of σ1, but in a different reading frame. σ1s is important for viral translation, as wild-type (WT) viruses produce higher protein levels than σ1s-null viruses (95). These findings correlate with other studies, which have defined σ1s as essential for reovirus bloodstream dissemination after infection of mice (101). These studies suggest that dissemination might be enhanced by high levels of viral proteins. σ1s also appears to be required for cell cycle arrest (102, 103), which occurs soon after infection (104).

The μNS protein forms the structural matrix of viral inclusions (105, 106) and can arrange in viral-like inclusions in uninfected cells when expressed alone (88). μNS is also responsible for recruiting core proteins μ2, λ1, λ2, λ3, and σ2, and the nonstructural protein σNS to viral inclusions (107). Additionally, μNS recruits Hsc70 (93) and clathrin (94) to these structures. μNS might also bind single-stranded RNA (ssRNA), as antibodies against μNS co-immunoprecipitate viral ssRNA (108). Additionally, μNS could have a function enhancing transcription, as it binds transcribing cores, preventing the coalescence of the outer capsid (109).

Another nonstructural protein relevant for reovirus inclusion formation is σNS. During infection, the σNS protein is found within reovirus inclusions and co-localizes with the μNS protein in the periphery of these structures (110). σNS-μNS interactions appear to be moderately dependent on the presence of RNA, as treatment with RNase A reduces their interaction in co-immunoprecipitation studies (111). σNS does not nucleate inclusions, but it appears to aid in their development (112). *In vitro*, σNS is a ssRNA-binding protein (113). The specific function of σNS during the viral life cycle is

not known, but due to its ssRNA-binding capacity, it has been suggested that σNS might aid in stabilizing viral transcripts within inclusions.

In summary, reovirus nonstructural proteins aid in post-entry replication steps. σ1s appears to have functions required for dissemination in the host, while μNS and σNS are important for inclusion formation.

Reovirus nonstructural protein σNS

Background

The nonstructural protein σNS is a 41 kDa protein encoded by the S3 gene. σNS was initially called essential noncapsid protein σ2A (114), and it was incorrectly defined as a polycytidylate (poly[C])-dependent RNA polymerase (115). Soon after, studies using σNS derived from reovirus-infected cells identified it as a nucleic acid-binding protein (113), and this function was corroborated using baculovirus-derived σNS (116). In terms of amino acid sequence, σNS is highly conserved among different reovirus serotypes (117). When analyzing the nucleotide sequence of the σNS-encoding S3 gene from different field isolates, the 5'- and 3'- UTRs and the first 15 nucleotides of the ORF are more conserved than the rest of the gene (118).

As a nonstructural protein, σNS is not a component of mature reovirus virions and is only translated after reovirus entry. σNS is one of the first viral proteins translated (24) and can be detected by immunofluorescence microcopy in infected cells at ~6-10 hours post-infection (hpi), depending on the infected cell type (110). σNS is recruited to reovirus inclusions through its interaction with μNS (107). When expressed alone, σNS appears diffuse in the cytoplasm (111). Residues 1 to 11 of σNS are important for localization to inclusions, as co-transfection of cells with μNS and a Δ1-11 σNS construct changes σNS localization from inclusion-like structures to being diffuse in the cytoplasm (111). The precise role of the amino terminal region of σNS during the reovirus replication cycle is not clear.

Functions of σNS

Studies using cells expressing an siRNA targeting the σNS-encoding S3 gene have determined that σNS expression is required for production of viral progeny (119). The mechanism by which σNS promotes viral replication is unknown, but it may enhance genome synthesis. A temperature-sensitive reovirus mutant, tsE320, has a lesion in the S3 gene (120) and is impaired in dsRNA synthesis when incubated at the restrictive temperature (121). A nonsynonymous mutation in the S3 gene of tsE320 encodes a σNS protein with a M260T mutation (117).

It also has been hypothesized that σNS has a function in viral protein synthesis, although a direct function for σNS in translation has not been reported. Reovirus inclusions contain actively-translating ribosomes, 40S and 60S ribosomal subunits, and translation initiation, elongation, termination, and recycling factors (122). In immunofluorescence studies of infected cells, σNS co-localizes with eIF3A, RiboP, pS6R, and rpS3 in reovirus inclusions, suggesting that σNS is responsible for recruiting the translation machinery to these neoorganelles (122). In co-immunoprecipitation studies, σNS precipitates with eIF3A and pS6R in infected cells, further suggesting that σNS has a function in viral protein synthesis (122).

σNS also might aid in translation by disassembling stress granules. Stress granule formation impairs translation, as these structures recruit the 40S ribosomal subunit, translation initiation factors, and various RNA-binding proteins, impeding their function in protein synthesis (123). Their disassembly is required for viral translation (87) and it is thought that σNS is responsible for that function, as this protein interacts with G3BP1 during infection (90). G3BP1, or Rad-GAP SH3-binding protein 1, is an ubiquitously expressed cytosolic protein required for stress granule formation (124).

σNS binding to G3BP1 occurs independently of the amino-terminal 11 amino acids of σNS (77), suggesting that different domains in σNS mediate various functions. Thus, σNS likely is important for stress granule disassembly and efficient viral protein synthesis.

The σNS protein localizes to viral inclusions in a mechanism dependent on the amino-terminal 40 amino acids of μNS (97). However, it is not clear whether σNS has a function in inclusion structural integrity or mediates other inclusion-associated replication activities. σNS localization to viral inclusions appears to be necessary for viral replication. Infection of cells with tsE320 at the restrictive temperature yields reduced viral titers, which is associated with a diffuse intracellular distribution of σNS. These results suggest that localization of σNS to inclusions is required for optimal formation of viral progeny (110).

σNS is a nucleic-acid-binding protein (113, 125) that preferentially binds single-stranded vs. double-stranded nucleic acids and shows slightly higher affinity for ssRNA than single-stranded DNA (ssDNA) (126). Interestingly, *in vitro* studies indicate that σNS shows no preference for binding viral RNA over nonviral RNA (126), although it has been suggested that σNS has specificity for certain regions of reovirus mRNAs (127). There is a preferred order of addition of RNAs to achieve maximal binding, as addition of mRNAs derived from small or medium gene segments facilitates the formation of larger σNS-RNA complexes than does the initial addition of large mRNAs (127). In nuclease protection assays using σNS and viral RNAs, the 3’-ends of each gene segment are protected from nuclease digestion (127). These results suggest that σNS has higher affinity for certain gene segments and certain regions within the viral RNAs.

In electrophoretic mobility shift assays (EMSAs), in which increasing concentrations of σNS were incubated with a 121-nucleotide fragment derived from the viral s4 RNA, it was determined that σNS-RNA binding occurs with positive cooperativity (126). Using similar assays, each σNS unit covers ~25 nucleotides of RNA at saturation (126). Although the mechanism is unknown, increasing concentrations of GTP impair σNS-RNA binding (128).

A σNS-deletion mutant lacking residues 2 to 11 does not bind poly(A)-sepharose beads (116). WT σNS forms oligomers, whereas Δ2-11 σNS is unable to oligomerize (116). These data indicate that the amino terminal region of σNS is required for optimal RNA-binding and oligomerization. The amino terminal region of σNS is conserved among different reovirus field isolates (118) and has been predicted to form an amphipathic α-helix (116, 129). Several basic amino acids exist in this region, and they could mediate RNA-binding. RNA-binding proteins that bind RNAs without apparent sequence specificity often do so using electrostatic interactions between the negatively charged RNA phosphates and positively charged side chains (130). Although untested, this region could be a target for post-translational modifications that could neutralize its overall positive charge.

In studies using increasing concentrations of σNS and DNA-RNA hybrids, σNS has strand-displacement activity (126). Importantly, this activity does not require a source of ATP or cations, suggesting that σNS is not a canonical helicase. Instead, strand displacement activity in the absence of ATP is a property of RNA chaperones. RNA chaperones are proteins that bind transiently and nonspecifically to RNA to resolve kinetically trapped misfolded structures (131). RNA chaperones are encoded by various

RNA viruses and help in different steps in their replication cycles (132). Interestingly, avian σNS acts as an RNA chaperone (133).

Possible functions of σNS

Since reovirus only encodes eleven proteins, it is likely that each serves multiple roles during infection. σNS is required for reovirus replication (119), although the specific functions during the viral life cycle are unclear. It is possible that σNS has functions that are conserved across *Reoviridae* family viruses. Thus, information derived from functional homologs could shed light on possible roles for σNS during reovirus replication (Table 1-4). As a nonstructural protein, σNS is synthesized after primary rounds of transcription. Once translated, σNS could modulate translation of viral proteins, as it interacts with the preinitiation machinery and ribosomal proteins, and possibly disrupts stress granules (90, 122).

σNS has a function in dsRNA synthesis, although is unclear whether σNS interacts directly with the RdRp or promotes dsRNA synthesis through an indirect effect. Other *Reoviridae* nonstructural proteins have also been suggested to mediate dsRNA synthesis. Rotavirus NSP2, a functional σNS homolog, has been hypothesized to be important for dsRNA synthesis, as temperature-sensitive viruses with mutations in NSP2 fail to synthesize dsRNA after infection at their restrictive temperature (134). Although the mechanism by which NSP2 mediates rotavirus genome replication is unknown, it is thought that this protein acts as a motor and uses NTP hydrolysis to package the viral genome (135). The carboxy-terminal domain of NSP2 folds similar to histidine triad (HIT) proteins, which are cellular proteins with nucleotidyl hydrolase and

Table I-4. *Reoviridae* σNS homologs.
[a] The reovirus σNS protein has functional homologs in rotavirus, bluetongue virus (BTV), and black rice streaked dwarf virus (RBSDV).
[b] Post-translational modification

Virus[a]	Protein	Inclusion-like structures	Catalytic activities	Oligomers	PTMs[b]	Functions
Reovirus	σNS	No, requires μNS	?	Yes - ?	?	Binds ssRNA, strand-displacement
Rotavirus	NSP2	No, requires NSP5	NTPase Autokinase	Yes - octamer	Phospho-rylation	Binds ssRNA and RdRp, strand-displacement
BTV	NS2	Yes	Nucleotidyl phosphatase	Yes - ?	Phospho-rylation	Binds ssRNA and core proteins
RBSDV	P9-1	Yes	ATPase	Yes – octamer	?	Binds ssRNA

transferase activities (136). Both NTP hydrolysis (137) and nucleoside diphosphate (NDP) kinase (138) are enzymatic activities demonstrated for NSP2. It is unknown whether σNS has NTPase activity. If σNS promotes genome replication through an indirect effect, it likely does so in a step immediately before dsRNA synthesis. It is possible that σNS mediates RNA-related functions as a result of RNA-binding, such as proper RNA folding during assortment or protection of RNAs from nucleases.

Viral mRNAs are templates for protein synthesis and viral replication. Considering that σNS is a ssRNA-binding protein and likely a translation regulator, it is possible that σNS has a function in the transition between translation and dsRNA synthesis. There are no known proteins in *Reoviridae* viruses that have this activity, although it must be necessary for efficient viral replication.

The role of σNS in reovirus inclusion morphogenesis is not known. Due to its function as an ssRNA-binding protein, it is possible that σNS functions by retaining viral mRNAs and facilitating assortment and packaging. σNS also might serve a function regulating μNS, as they both co-localize in the periphery of inclusions. Post-translational modifications regulate interactions between NSP2 and NSP5 (40), the latter being a rotavirus μNS homolog. Host proteins are recruited to inclusions, and some are required for replication, as such the TRiC chaperone (92). σNS might be responsible for sequestering some of these proteins, as has been observed for G3BP1 (90). σNS also could remodel membranous organelles to scaffold viral inclusions, as has been observed for viral nonstructural proteins of (+) ssRNA viruses (139, 140).

In summary, there are three main gaps in knowledge regarding σNS functions: (1) What are the functions of σNS during the replication cycle? (2) What biochemical

activities does σNS have? and (3) How does σNS interact with the host to facilitate inclusion formation?

Hypothesis

The nonstructural protein σNS promotes the replication of the reovirus genome by stabilizing viral mRNAs.

Significance

Following infection, viruses synthesize nonstructural proteins that mediate viral replication and promote dissemination. Viruses from the *Reoviridae* family encode nonstructural proteins that are required for the formation of progeny viruses. Although nonstructural proteins of different *Reoviridae* family viruses are divergent in primary sequence, these proteins are functionally homologous and appear to facilitate conserved mechanisms of dsRNA virus replication. Understanding how σNS functions will contribute new knowledge about basic mechanisms of dsRNA virus replication.

CHAPTER II

σNS PROMOTES REPLICATION OF THE REOVIRUS GENOME

Introduction

The σNS protein is a nonstructural protein encoded by the reovirus S3 gene. As a nonstructural protein, σNS is produced after virus entry. σNS is required for virus replication, as viruses incapable of expressing σNS do not produce progeny (119). In infected cells, σNS localizes to viral inclusions and is required for their development (105, 107, 141). Studies using temperature-sensitive reoviruses with mutations in σNS suggest that this protein is essential for dsRNA synthesis in infected cells (117, 120, 121, 142). However, these studies have not determined the role of σNS in individual reovirus replication steps. To enhance knowledge about the activities of σNS during reovirus replication, I assessed several post-entry replication steps in time courses of infection using an experimental system that prevents σNS expression.

Results

Developing a system to study σNS function

To study functions of σNS during reovirus replication, I used HEK293T cells engineered to stably express an siRNA targeting the reovirus σNS-encoding S3 gene. These cells were previously engineered in the Dermody laboratory by transfecting cells with a pSUPER plasmid encoding 19 nucleotides from the T3D S3 gene (119). The pSUPER RNA interference (RNAi) system is based on the expression of a small hairpin RNA (shRNA) under control of an H1-RNA promoter. The plasmid also encodes a puromycin-resistance gene, and cells stably express the shRNA when maintained in antibiotic-containing media. Although these cells can diminish σNS expression after infection with T3D reovirus (119), I observed a high-degree of biological variability in their knockdown efficiency. Therefore, I sorted these cells using flow cytometry to obtain a homogenous population and propagated them for two weeks, after which time, cells were divided into two plates: one was maintained in cell culture, and the other was infected with reovirus T3D. After 18 h, infection was scored by fluorescent focus assay (Figure II-1). Clones that showed the highest knockdown efficiency were selected and passaged. These cells were termed σNS-siRNA cells.

I also engineered T3D reovirus strains containing synonymous mutations within the S3 gene siRNA target site, one of them containing two mutations, and the other one containing four (Figure II-2A). These viruses were used to infect σNS-siRNA cells, and expression of the σNS protein was assessed by immunoblotting (Figure II-2B). σNS expression in cells infected with the virus expressing four mutations was greater than

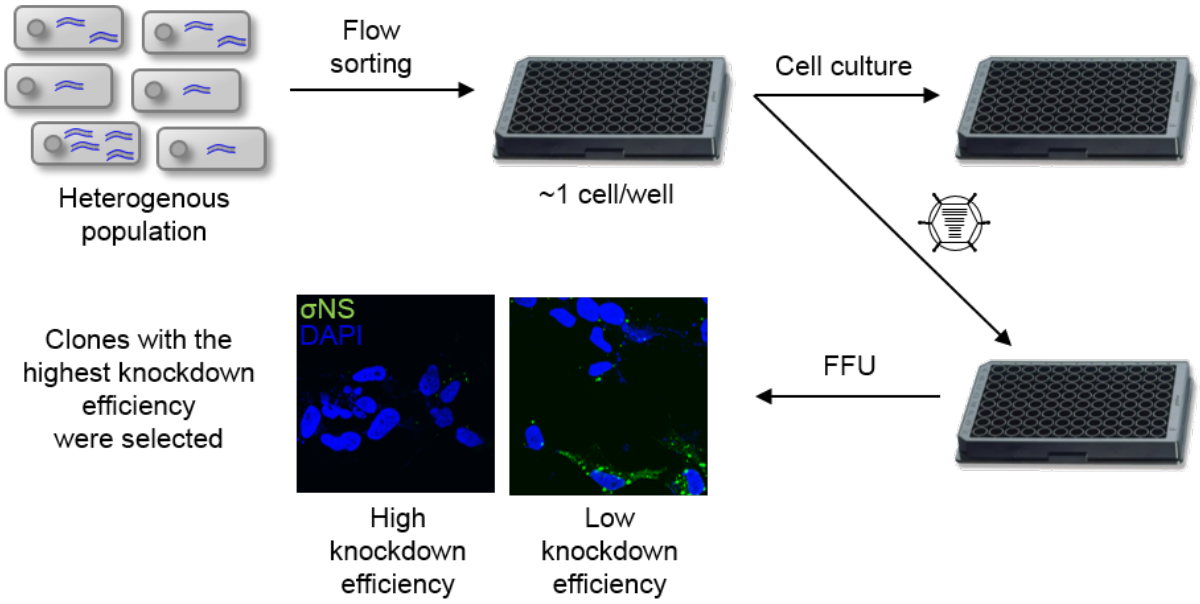

Figure II-1. Selecting σNS-siRNA cells. Cells expressing an siRNA targeting the σNS-encoding S3 gene (119) were sorted using flow cytometry. After two weeks in culture, cell clones were divided into two plates, one was maintained in cell culture, and the other was infected with reovirus T3D at an MOI of 100 plaque forming units per cell (PFU/cell). After 18 hours (h), cells were fixed and stained for fluorescent focus assay using polyclonal serum specific for σNS. Clones that showed the greatest knockdown efficiency, as determined by percentage of infected cells and mean fluorescence intensity, were selected and passaged.

A

T3D	C GAC GGA CUC AAA GGA UUA
2 SM	C GAC GGC CUC AAG GGA UUA
4 SM	C GAT GGC CUC AAG GGA UUG

B

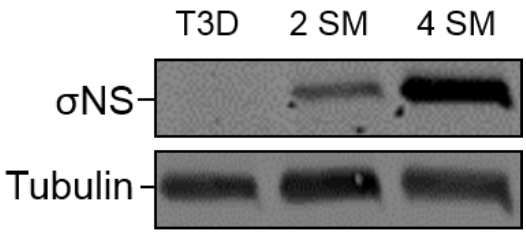

Figure II-2. Engineering of T3D-R virus. (A) Reverse genetics was used to engineer viruses containing two or four synonymous S3 gene mutations (2 SM and 4 SM, respectively) in a T3D background. Synonymous mutations are shown in red. (B) σNS-siRNA cells were adsorbed with either T3D or T3D-R virus at an MOI of 10 PFU/cell and incubated for 24 h. Cell lysates were resolved by SDS-PAGE and immunoblotted using antibodies specific for σNS and α-tubulin.

that in cells infected with the virus encoding two mutations, suggesting that the virus containing four synonymous mutations more efficiently escapes the RNAi machinery in σNS-siRNA cells. I termed this virus T3D-Resistant (R).

To confirm that T3D-R escapes RNAi in σNS-siRNA cells, I adsorbed these cells with either T3D or T3D-R and quantified σNS protein abundance by immunoblotting (Figure II-3A and 3B). Infection of σNS-siRNA cells with T3D resulted in 96% reduction of σNS protein levels relative to infection with T3D-R, indicating that σNS-siRNA cells effectively knockdown T3D σNS and confirming that T3D-R is not targeted by the siRNA expressed in σNS-siRNA cells. To check whether σNS knockdown in T3D-infected σNS-siRNA cells is specific, I adsorbed HEK293T cells expressing a nontargeting siRNA (GFP-siRNA cells) with either T3D or T3D-R and quantified levels of σNS by immunoblotting (Figure II-3A and 3B). T3D- and T3D-R-infected GFP-siRNA cells expressed comparable amounts of σNS, indicating that the σNS protein of T3D is produced in 293T cells expressing a nontargeting siRNA.

To test whether the synonymous mutations introduced in the S3 gene of T3D-R alter the production of viral progeny, I adsorbed GFP-siRNA and σNS-siRNA cells with either T3D or T3D-R and quantified viral yields at 24 h post-adsorption by plaque assay (Figure II-3C). T3D and T3D-R viruses produced comparable yields at 24 h post-adsorption in GFP-siRNA cells, suggesting that the mutations introduced in T3D-R do not alter its replication capacity. In contrast, T3D replication was impaired in σNS-siRNA cells. Thus, σNS-siRNA cells effectively and specifically diminish σNS expression when infected with T3D but not T3D-R.

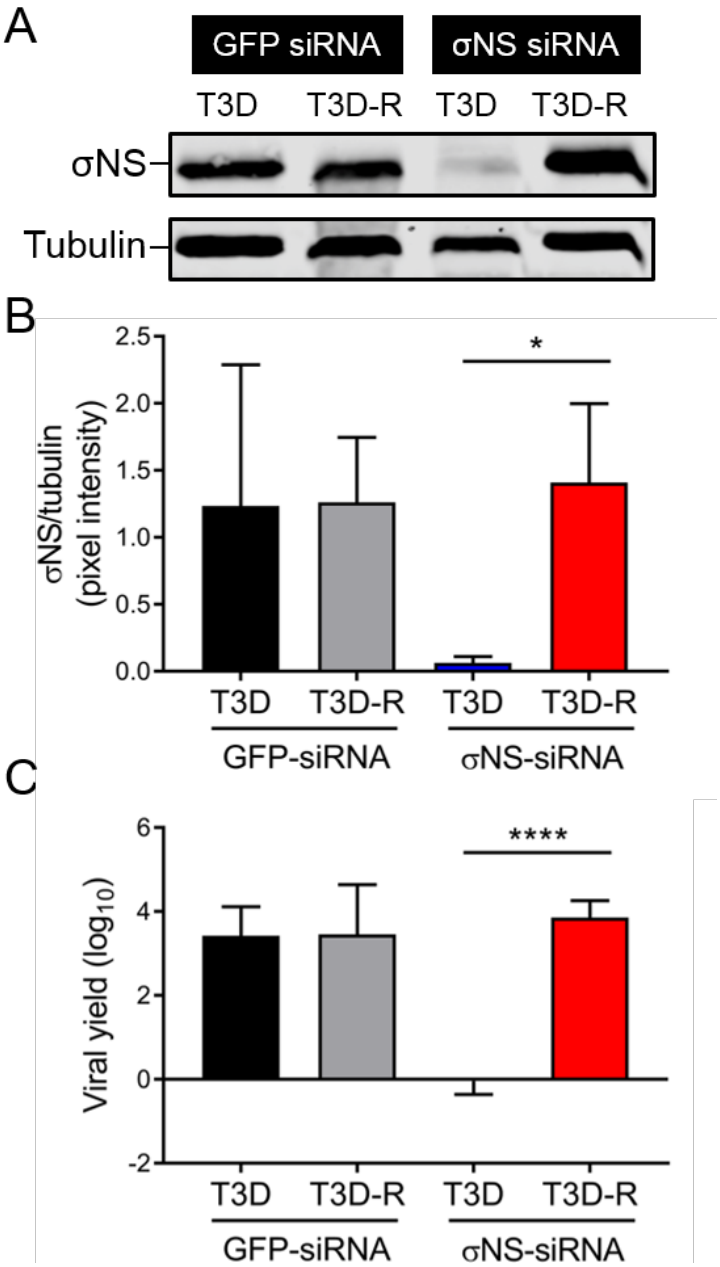

Figure II-3. T3D virus is specifically knocked down in σNS-siRNA cells. (A) σNS-siRNA cells or control cells expressing a non-targeting siRNA (GFP-siRNA cells) were adsorbed with either T3D or T3D-R virus at an MOI of 10 PFU/cell and incubated for 24 hours (h). Cell lysates were resolved by SDS-PAGE and immunoblotted using antibodies specific for σNS and α-tubulin. (B) Pixel intensity analysis of the ratio of σNS to α -tubulin in T3D- and T3D-R-infected σNS-siRNA and GFP-siRNA cells for triplicate experiments. (C) σNS-siRNA and GFP-siRNA cells were adsorbed with either T3D or T3D-R virus at an MOI of 1 PFU/cell. Viral yields at 24 h post-adsorption were determined by plaque assay. Results are presented as mean ± standard deviation (SD). *, $P < 0.05$; ****, $P < 0.0001$ as determined by Student's t test.

Reovirus T3D does not replicate in σNS-siRNA cells

To assess whether σNS is required for formation of progeny virions over a longer interval, I adsorbed σNS-siRNA cells with either T3D or T3D-R and quantified progeny virus at various times post-adsorption by plaque assay (Figure II-4A). T3D was incapable of forming new progeny when infecting σNS-siRNA cells at all intervals tested. In contrast, T3D-R yields increased throughout the time course of infection, reaching ~70-fold by 16 h and ~220-fold by 48 h, indicating that σNS is required for progeny particle production. T3D and T3D-R replicated with similar kinetics and reached comparable titers in cells lacking any siRNAs (Figure II-4B), confirming that the synonymous mutations introduced in T3D-R do not provide a replication advantage.

To determine whether σNS is required for inclusion formation, I adsorbed σNS-siRNA cells with either T3D or T3D-R, stained cells at 24 h with polyclonal serum specific for the reovirus nonstructural protein μNS to visualize inclusions, and imaged cells by confocal microscopy (Figure II-5). T3D-infected σNS-siRNA cells contained few small inclusions (< 1 μm), similar to those detected early in infection (110). In contrast, T3D-R-infected σNS-siRNA cells were filled with globular inclusions, some of which were larger than 10 μm in diameter. These results suggest that σNS is required for replication steps leading to the maturation of reovirus inclusions.

Viral RNA levels are diminished in T3D-infected σNS-siRNA cells

To estimate the timing at which primary and secondary rounds of transcription occur in HEK293T cells, I adsorbed σNS-siRNA cells with either T3D or T3D-R and quantified s4 RNA by RT-qPCR (Figure II-6). Levels of s4 RNA in T3D- and T3D-R-

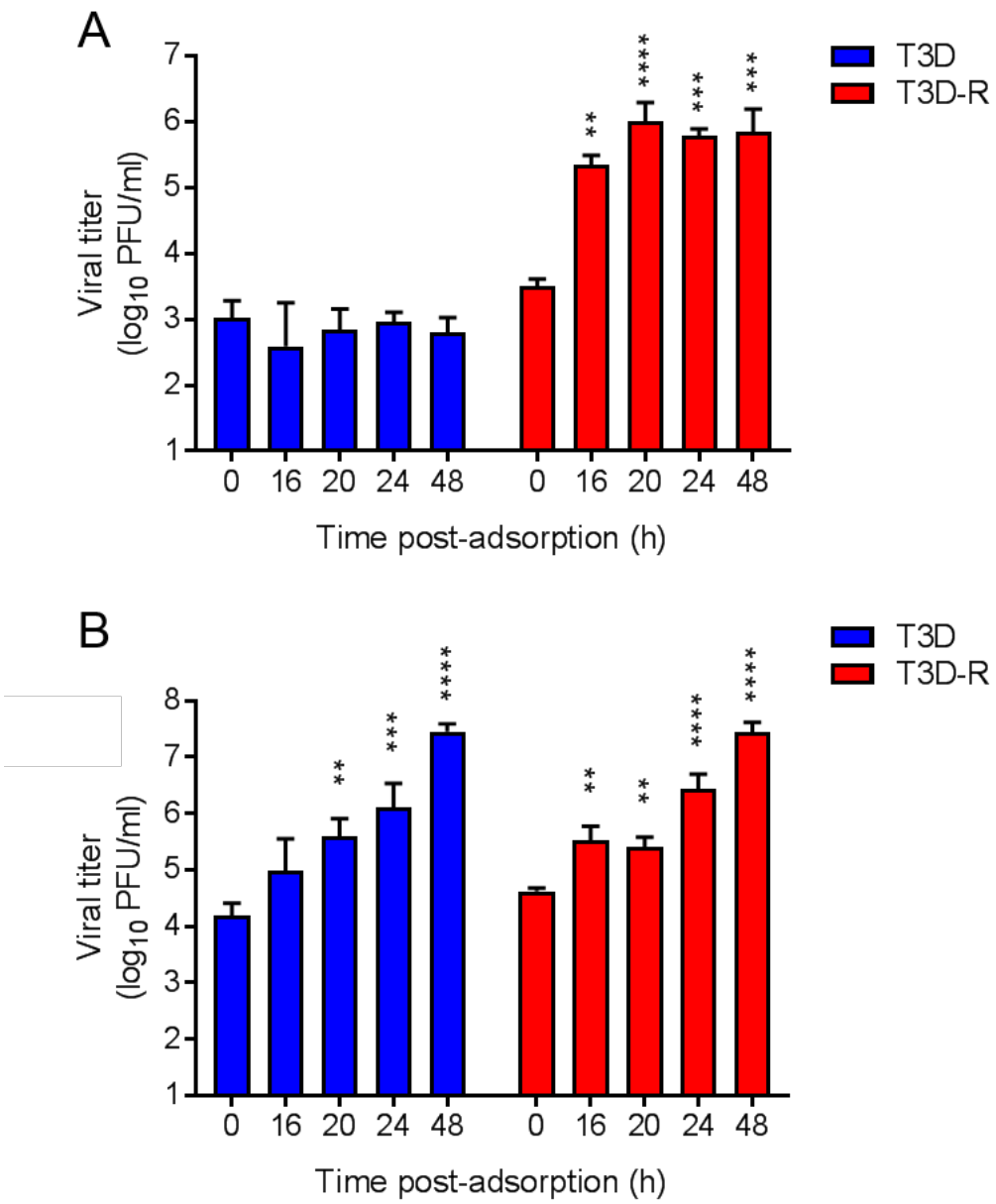

Figure II-4. Reovirus T3D does not replicate in σNS-siRNA cells. σNS-siRNA cells (A) or human brain microvascular endothelial cells (B) were adsorbed with either T3D or T3D-R virus at an MOI of 1 PFU/cell. Viral titers at 0, 16, 20, 24, and 48 h post-adsorption were determined by plaque assay. Results are presented as mean viral titers ± SD for three independent experiments. Values that differ significantly from the value at 0 h by one-way ANOVA with Tukey's multiple comparisons test are indicated (**, $P < 0.01$; ***, $P < 0.001$; ****, $P < 0.0001$).

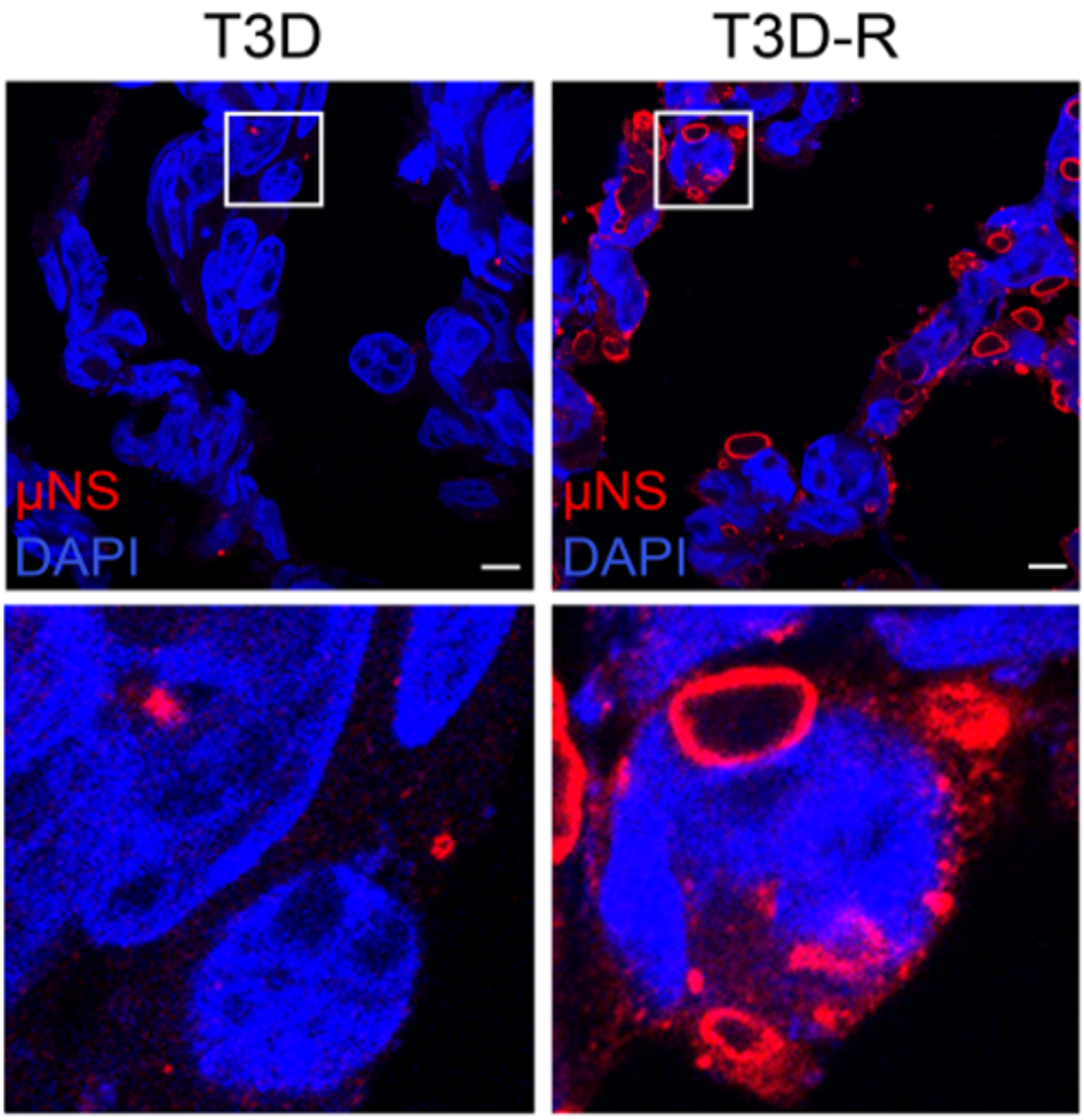

Figure II-5. Inclusion formation is impaired in T3D-infected σNS-siRNA cells. σNS-siRNA cells were adsorbed with either T3D or T3D-R virus at an MOI of 100 PFU/cell. Cells were fixed at 24 hpi, stained using μNS-specific antiserum (red) and DAPI (blue) to visualize nuclei, and imaged using confocal microscopy. Insets depict enlarged areas from boxed regions. Scale bars, 10 μm.

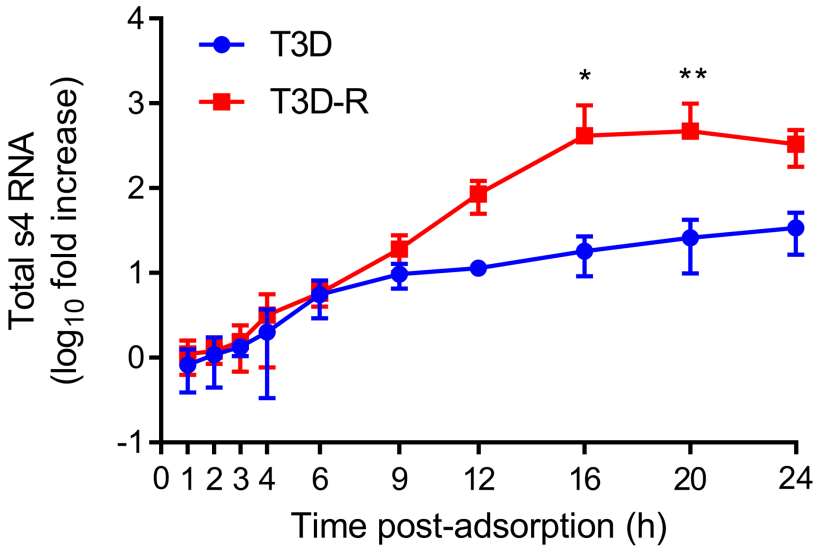

Figure II-6. Total s4 RNA levels are diminished in T3D-infected σNS-siRNA cells. σNS-siRNA cells were adsorbed with either T3D or T3D-R virus at an MOI of 1 PFU/cell. Cells were lysed at the intervals shown, and s4 RNA was quantified by RT-qPCR. Results are presented as mean RNA levels normalized to the RNA levels at 0 h for at least three independent experiments. Error bars indicate SD. Values that differ significantly between T3D- and T3D-R-infected σNS-siRNA cells at each time point by two-way ANOVA followed by Sidak's multiple comparisons test are indicated (*, $P < 0.05$; **, $P < 0.01$).

infected σNS-siRNA cells increased at a similar rate until 6 h post-adsorption. At later times, s4 RNA levels increased at higher rates in T3D-R-infected σNS-siRNA cells relative to T3D-infected cells. These results suggest that secondary rounds of transcription do not begin until after 6 h post-adsorption as previously observed (143) and that late rounds of gene expression are impaired in T3D-infected σNS-siRNA cells.

To test whether steady-state levels of viral RNAs are altered by σNS disruption, I quantified RNA levels for the L (large), M (medium), and S (small) gene segments by NanoString analysis during a time course of infection in T3D- and T3D-R-infected σNS-siRNA cells. NanoString technology is based on fluorescent probes that, following hybridization with their target RNA, allow direct quantification of RNAs in a sample without the requirement of reverse transcription or amplification (Figure II-7) (144). I adsorbed σNS-siRNA cells with either T3D or T3D-R and quantified RNA levels corresponding to the ten reovirus gene segments at various intervals post-adsorption using unique probes targeting each reovirus positive-sense RNA (Table II-1 and Figure II-8). Levels of all viral RNAs increased comparably in cells infected with T3D or T3D-R until 4-6 h post-adsorption, after which time RNA levels in T3D-infected cells increased modestly. In contrast, levels of viral RNAs in cells infected with T3D-R increased exponentially, with levels at 12 h post-adsorption elevated ~250-fold for the L-class RNAs, ~340-fold for the M-class RNAs, and ~550-fold for the S-class RNAs relative to the respective levels of these RNAs at the 0 h time point. Because secondary transcription does not occur until after 6 h post-adsorption (Figure II-6) (143), these results indicate that σNS is dispensable for primary but not secondary rounds of transcription.

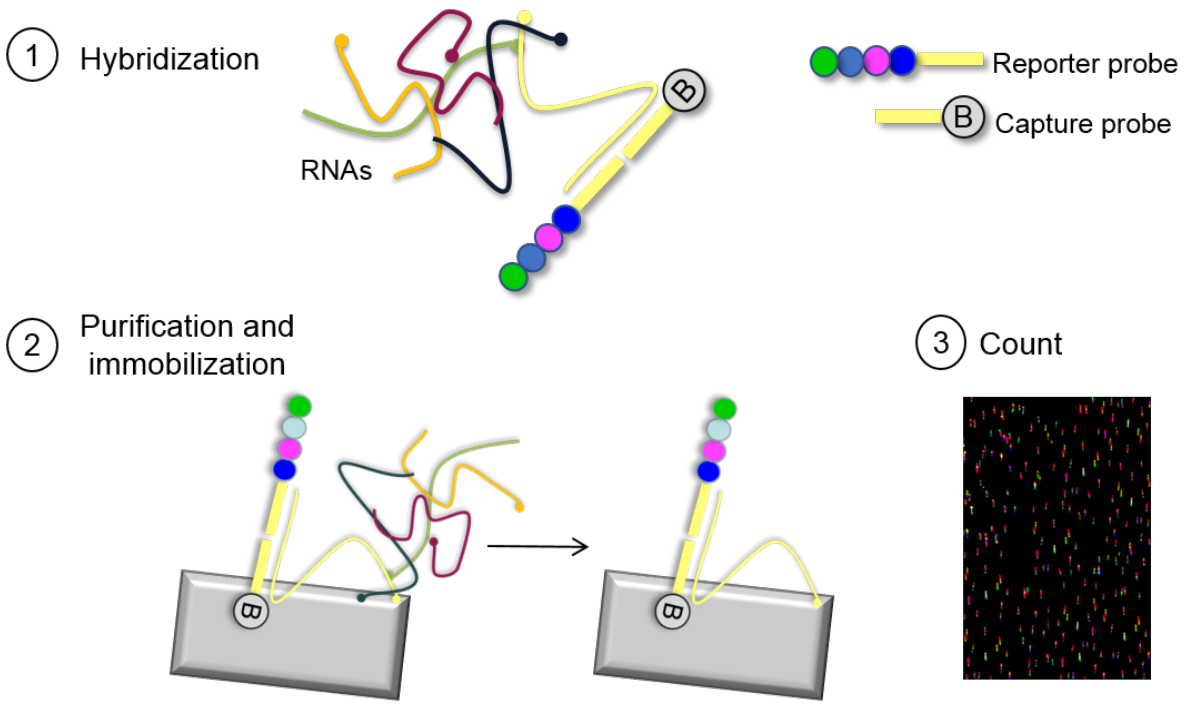

Figure II-7. NanoString technology overview. NanoString technology is based on (1) hybridization of target RNAs with two probes: a reporter probe containing a unique combination of fluorophores (barcode) and a capture probe containing a biotin moiety that mediates immobilization. (2) After hybridization, samples are transferred to an nCounter instrument to remove excess probe. Purified RNA-probe complexes are immobilized to the surface of an nCounter cartridge. (3) An automated fluorescence microscope scans the cartridge and each barcode is counted (144).

Table II-1. Custom designed probes used for NanoString.
[a] Protein

Gene	Prot[a]	Target sequence (5' → 3')
L1	λ3	GAGCTCAGTCGTCGGTGAGCTTCGTAAACGGACAAAGACGTATGTTAAACATGACTTTGCTTCAG TGAGGTACATTCGTGACGCTATGGCATGTACTAGC
L2	λ2	TGGACGAAGGCGATCTGATGGTTAGTCGGCTTACGCAACTCCCGTTACGTCCTGATTATGGTAAT ATCTGGGTCGGCGATGCGCTATCCTATTATGTGGA
L3	λ1	CCAACGCGCATGGGAACGCCGAATGTATCCAAAATATGTAATTTCGTCGCCTCTTGTGTGCGAAA TCGGGTTGGACGGTTTGATCGAGCACAGATGATGA
M1	μ2	ACGTTTGAGCAGGCGGTTATGGAGATATACAAAGGGATTGCTGGCGTTGACTCGCTGGATGATCT CATCAAGTGGGTGCTGAACTCGGATCTCATTCCGC
M2	μ1	GCTGGGATCCAAACGGCAAGAAGGTCGGATTCATCGTTTTTCAATCGAAGATACCATTCGAACTT TGGACTGCTGCTTCACAGATCGGTCAAGCCACGGT
M3	μNS	GTGTCGTATGACGTTACGCTCACTCATGAAGACCGGACGCGACGTTGATGCACACAGAGCTTTTC AGCGAGTCCTCTCTCAAGGATACACATCGCTAATG
S1	σ1	ACTTGCAGAGCTACGCGTTGATCACGACAATCTCGTTGCGAGAGTGGATACTGCAGAACGTAACA TTGGATCATTGACCACCGAGCTATCAACTCTGACG
S2	σ2	GCTTTGCAAGCACAGGCAGATCGAGTGTACGACTGCGATGATTATCCATTTCTAGCGCGTGATCC AAGATTCAAACATCGGGTGTATCAGCAATTGAGTG
S3	σNS	TGGCCACGTCATCTTTAAGTATTTCCCTGGACCGGGGTCGATGGGTGGCGGCTGACGCCAGTGA TGCTAGACTGCTGGTTTTTCCGATTCGCGTGTAATG
S4	σ3	CTGCTCACTGGAAGCGGGGTATGCTGTCCTTCGTTGCGCAGATGCACGAGATGATGAATGACGT GTCGCCAGATGACCTGGATCGTGTGCGTACTGAGGG

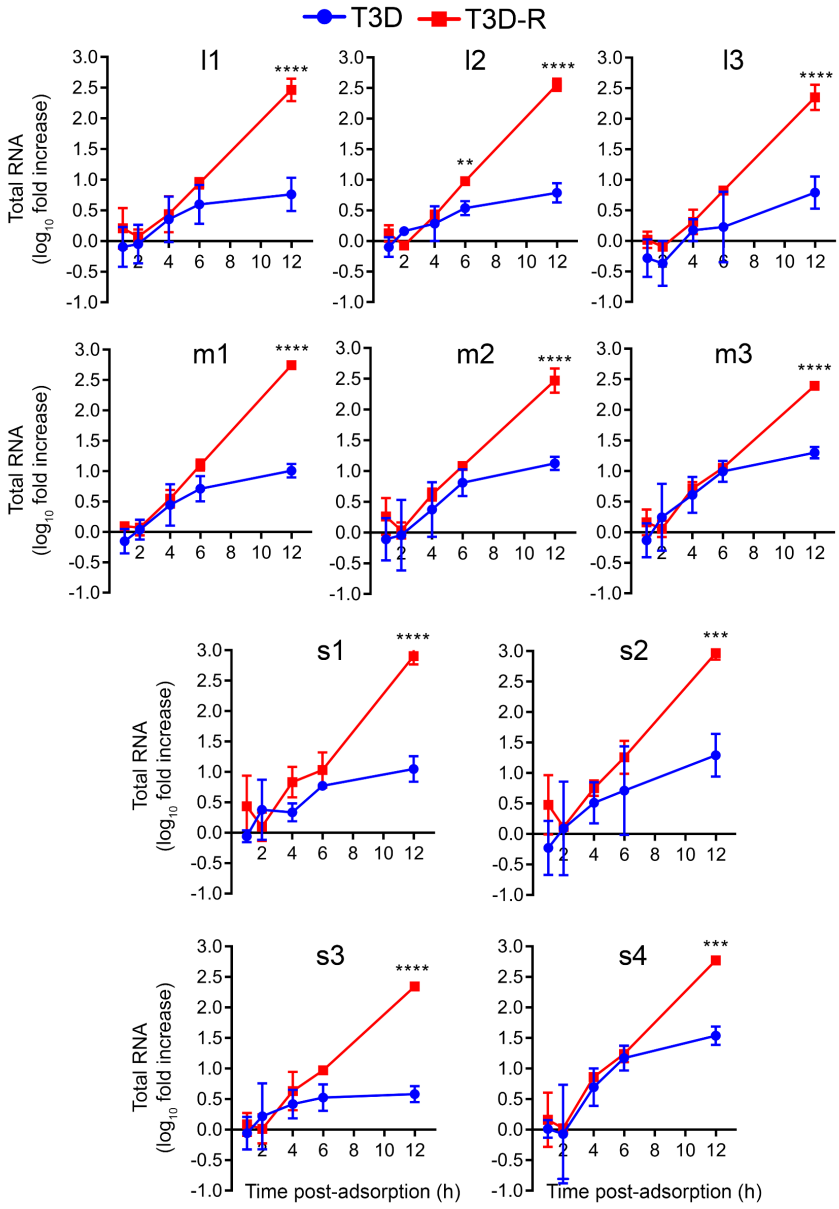

Figure II-8. Levels of all reovirus transcripts are reduced in T3D-infected σNS-siRNA cells. σNS-siRNA cells were adsorbed with either T3D or T3D-R virus at an MOI of 1 PFU/cell. Cells were lysed at the intervals shown, and RNAs were quantified by NanoString technology using custom designed probes (Table II-1) specific for each reovirus gene segment. Results are presented as mean RNA levels normalized to the RNA levels at 0 h for three independent experiments. Error bars indicate SD. Values that differ significantly between T3D- and T3D-R-infected σNS-siRNA cells at each time point by two-way ANOVA followed by Sidak's multiple comparisons test are indicated (**, $P < 0.01$; ***, $P < 0.001$; ****, $P < 0.0001$).

Reovirus T3D protein synthesis is diminished in infected σNS-siRNA cells

I hypothesized that the reduction in abundance of viral RNAs observed in T3D-infected σNS-siRNA cells would diminish viral protein levels. To test this hypothesis, σNS-siRNA cells were adsorbed with either T3D or T3D-R, and expression of the RNA-dependent RNA polymerase λ3 and nonstructural proteins μNS and σNS was quantified by SDS-PAGE followed by immunoblotting at various intervals post-adsorption (Figure II-9A and 9B). Newly synthesized viral proteins were detected at 12 h post-adsorption in T3D-R-infected σNS-siRNA cells, and levels of the three immunoblotted viral proteins increased over time. In contrast, viral protein synthesis was impaired in T3D-infected σNS-siRNA cells. These results suggest that σNS is required for replication steps leading to viral protein synthesis.

Reovirus σNS is required for genome replication

To elucidate whether σNS is required for replication of the reovirus genome, I used a modified qPCR assay to quantify s4 negative-sense ssRNA (143). In this assay, s4 RNA is reverse transcribed using a primer that binds to the negative-sense strand of the S4 dsRNA gene segment. Once the S4 negative-sense cDNA is synthesized, a complementary primer is added, and quantification by qPCR proceeds. As the genome is the only source of negative-sense viral RNA, this assay allows genome copies to be quantified. I adsorbed σNS-siRNA cells with either T3D or T3D-R and quantified s4 negative-sense RNA at various intervals post-adsorption (Figure II-10). By this analysis, genome replication appeared to initiate at 9 h post-adsorption in T3D-R-infected σNS-siRNA cells, and by 12 h, T3D-R S4 dsRNA levels were ~10-fold higher than those at the initiation of infection. T3D-R S4 dsRNA levels continued to increase over time, and

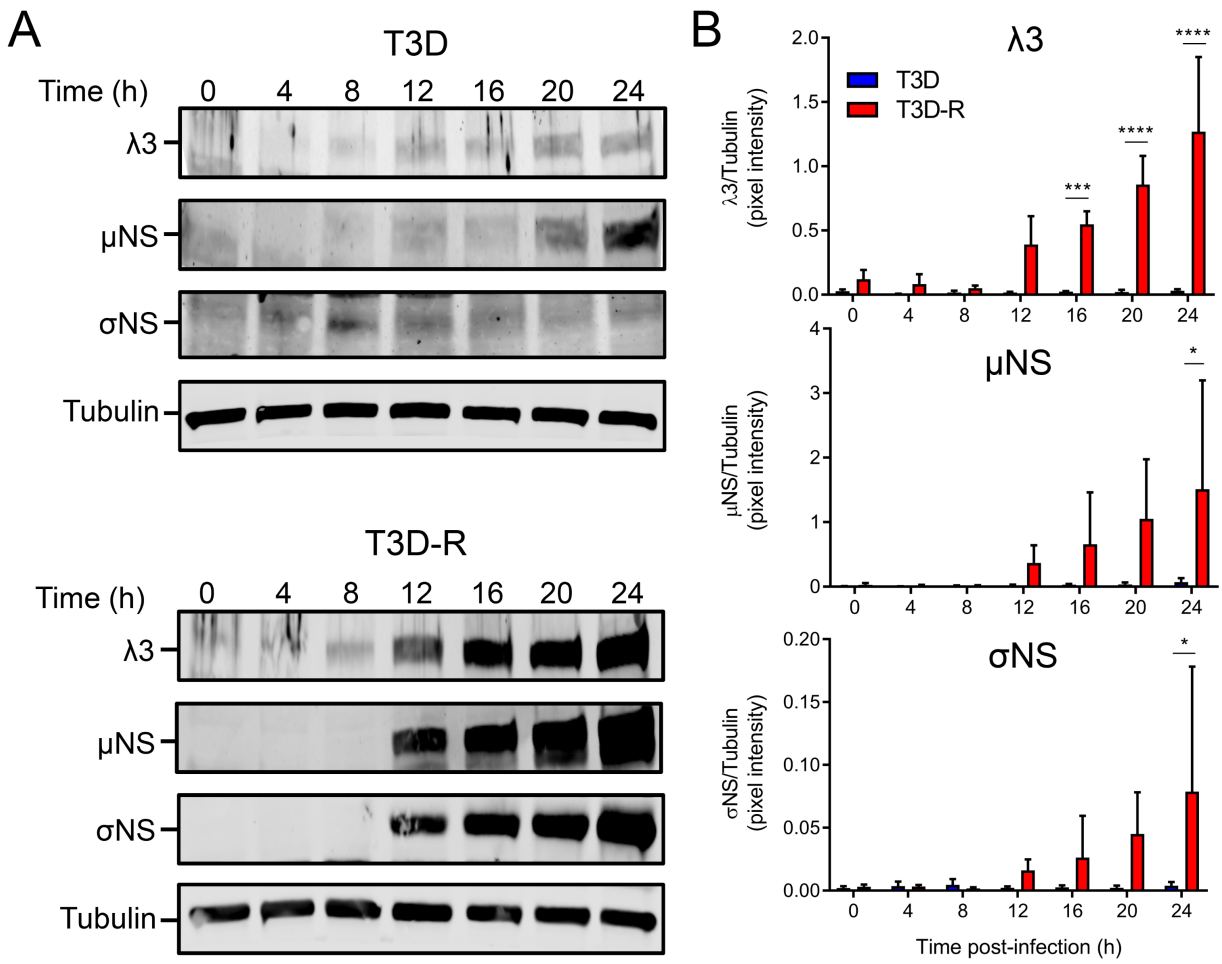

Figure II-9. T3D protein synthesis is diminished in T3D-infected σNS-siRNA cells. σNS-siRNA cells were adsorbed with either T3D or T3D-R virus at an MOI of 1 PFU/cell. (A) Cell lysates were collected at the intervals shown and analyzed by immunoblotting using antibodies specific for the λ3, μNS, and σNS proteins. (B) Pixel intensity analysis of the ratio of λ3, μNS, and σNS proteins to α-tubulin. Results are presented as mean pixel intensity ± SD for three independent experiments. Values that differ significantly between T3D- and T3D-R-infected σNS-siRNA cells at each time point by two-way ANOVA followed by Sidak's multiple comparisons test are indicated (*, $P < 0.05$; ***, $P < 0.001$; ****, $P < 0.0001$).

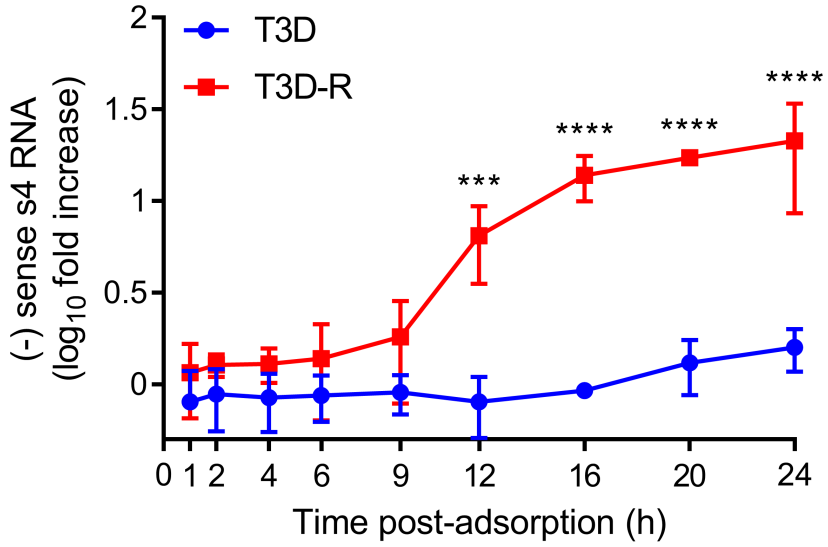

Figure II-10. Reovirus T3D does not synthesize dsRNA in σNS-siRNA cells. σNS-siRNA cells were adsorbed with either T3D or T3D-R virus at an MOI of 1 PFU/cell. Cells were lysed at the intervals shown, and negative (-) sense s4 RNA was quantified by single-strand RT-qPCR. Results are presented as mean RNA levels at each timepoint normalized to the RNA levels at 0 h for at least three independent experiments. Error bars indicate SD. Values that differ significantly between T3D- and T3D-R-infected σNS-siRNA cells at each time point by two-way ANOVA followed by Sidak's multiple comparisons test are indicated (***, $P < 0.001$; ****, $P < 0.0001$).

by 24 h, these levels were ~20-fold higher than those at 0 h. In contrast, T3D S4 dsRNA was undetectable throughout most of the time course of infection and, by 24 h, T3D S4 dsRNA levels had only increased ~1.5-fold in σNS-siRNA cells compared with the initiation of infection. These results indicate that σNS functions at a step leading to the replication of the reovirus genome. Thus, by examining the kinetics of individual replication steps, I conclude that σNS mediates a process immediately prior to reovirus genome replication, following primary but before secondary rounds of transcription.

Discussion

In this study, I found that the mammalian reovirus σNS protein, a nonstructural protein expressed early in reovirus infection (24, 110), is required for a process leading to viral genome replication (Figure II-11). In the absence of σNS, reovirus infection progressed through primary transcription. However, subsequent replication steps including protein synthesis, genome replication, secondary transcription, formation of reovirus inclusions, and generation of progeny were impaired. Considering the kinetics of the individual replication steps, I found that the first function of σNS must occur between 6 and 9 h post-adsorption.

During reovirus infection, σNS could function in several processes that are thought to occur after primary translation and before dsRNA synthesis, including promotion of the translation process itself, stabilization of viral RNAs, facilitation of RNA-RNA interactions throughout genome assortment, or direct interaction with the RdRp to enhance its polymerization capacity (Figure II-11). In addition, these processes could be aided by the formation of viral inclusions, which also could be augmented by σNS.

σNS recruits the host translational apparatus to viral inclusions likely to enhance viral translation (122). σNS also could augment translation by disrupting stress granules (90). Stabilization of viral RNAs is a process that has not been reported for σNS, but considering that multiple copies of σNS bind ssRNA (126), it is possible that σNS protects viral transcripts by hindering nuclease-target sites. Promotion of RNA-RNA interactions has been shown for avian σNS and rotavirus NSP2. Avian σNS facilitates RNA annealing between different RNAs upon helix unwinding (133), whereas rotavirus

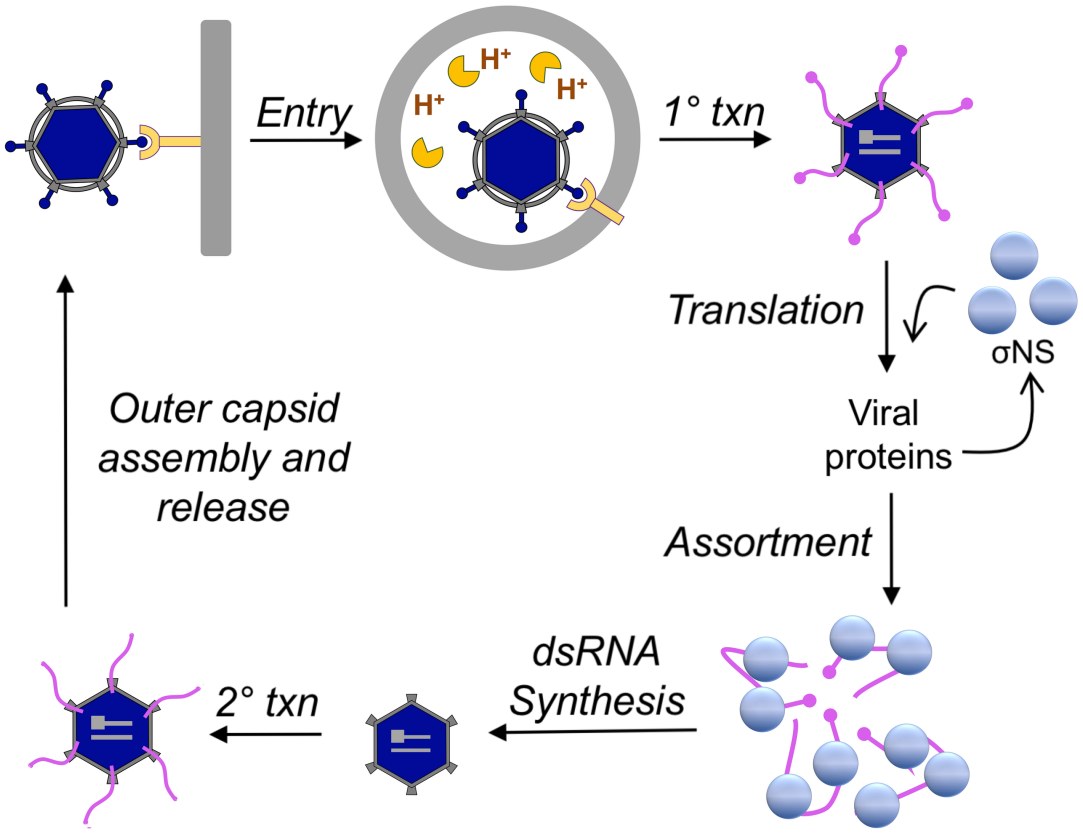

Figure II-11. Model of σNS function during reovirus replication. Reovirus enters cells by receptor-mediated endocytosis, and following acid-dependent proteolytic disassembly, the inner-capsid or core is released into the cytoplasm. Cores transcribe viral mRNAs corresponding to each gene segment, which are subsequently translated to yield each viral protein. I hypothesize that σNS mediates genome replication through multiple possible mechanisms, including promotion of translation, stabilization of viral RNAs, facilitation of RNA-RNA interactions throughout genome assortment, or interaction with the RdRp to enhance RNA polymerization. After synthesis of the negative-sense strand and formation of new cores, secondary rounds of transcription occur. The outer capsid assembles, silencing secondary transcription, and particles are released from infected cells by an unknown mechanism

NSP2 remodels RNA after binding and facilitates specific RNA-RNA contacts between different gene segments (42).

The mechanisms mentioned above imply an indirect effect of σNS in genome replication, but it is possible that σNS directly interacts with λ3 to promote dsRNA synthesis. During packaging, λ3 must bind the 3'-ends of each viral mRNA to initiate RNA polymerization. RNA folding predictions suggest that the ends of the viral mRNAs form panhandle structures (145), suggesting that the 3'-ends might be inaccessible to the polymerase. σNS could unwind these structures to allow polymerase binding. Other *Reoviridae* nonstructural proteins interact with their respective polymerases. NSP2 interacts with the rotavirus RdRp, VP1. The importance of this interaction is not known, but it has been suggested that NSP2 acts as a motor to recruit ssRNAs to VP1 for dsRNA synthesis (146).

Collectively, data gathered in this chapter provide evidence for a function of σNS in promoting the replication of the reovirus genome and establish a foundation for future studies to determine the mechanism by which σNS acts prior to dsRNA synthesis.

CHAPTER III

THE σNS PROTEIN ACTS AS AN RNA-STABILITY FACTOR

Introduction

The nonstructural protein σNS is a ssRNA-binding protein (113, 116, 127) required for the replication of the reovirus genome. σNS binds RNA in multiple copies, and each binding unit covers a length of 25-27 nucleotides at saturation (126). Binding to RNA appears to occur without sequence specificity and with positive cooperativity (126).

During reovirus replication, it has been hypothesized that viral RNAs are protected from cytoplasmic nucleases and RNA-modifying enzymes by sequestration within inclusions. However, reovirus inclusions are only detectable after 6 to 10 h post-adsorption (110). In addition, viral inclusions are dynamic structures that allow diffusion of proteins and metabolites (122). Thus, if reovirus inclusions were the only source of RNA-protection, viral transcripts would be unprotected at early times. Viral mRNAs are nonpolyadenylated and uncapped through most of the replication cycle, which should make them unstable (147-149). Therefore, I hypothesized that reovirus has additional mechanisms to protects its transcripts to ensure successful replication.

RNA-stability factors are RNA-binding proteins that increase RNA half-life, resulting in a net increase in gene expression (150). These proteins regulate RNA stability through binding to different regions in their target RNAs, forming ribonucleoprotein complexes, and delaying RNA decay (151).

To better understand σNS RNA-binding properties, I used *in vitro* and cell-culture approaches to investigate the biochemistry of σNS-RNA complexes. Some of the experiments described in this chapter include purified, recombinant WT and mutant σNS, and rotavirus NSP2, which were engineered by Liya Hu and Anish Thachangattuthodi in BVV Prasad's laboratory at Baylor College of Medicine. Liya Hu and Rodolfo Moreno, also from BVV Prasad's laboratory, conducted the cryo-EM experiments. EMSAs were performed with the help of Roni Lahr from Andrea Berman's laboratory at the University of Pittsburgh. Jonathan Knowlton from our laboratory conducted the *in vitro* translation experiments using rabbit reticulocyte lysates.

Results

Expression of the reovirus σNS protein increases mRNA levels during infection

To examine the effect of σNS overexpression on mRNA levels during infection, I developed an experimental system in which baby hamster kidney (BHK) cells were engineered to stably express σNS using lentiviruses. I chose BHK cells because of their ease of transduction (152) and susceptibility to reovirus infection (153). To obtain a homogeneous population, I conducted a cell-sorting protocol similar to that described in Figure II-1. We selected and passaged clones with the highest σNS expression. These cells were termed BHK-σNS cells.

To test whether σNS overexpression affects reovirus replication, I adsorbed BHK or BHK-σNS cells with T3D and quantified viral progeny by plaque assay at 24 h post-adsorption (Figure III-1A). Viral yields in BHK- and BHK-σNS-infected cells were comparable, suggesting that overexpression of σNS does not affect viral replication.

To assess whether σNS overexpression alters steady-state levels of viral RNA during infection, I adsorbed BHK and BHK-σNS cells with T3D and quantified s4 RNA at various intervals post-adsorption by RT-qPCR (Figure III-1B). s4 RNA levels in BHK- and BHK-σNS-infected cells increased at a similar rate over the time course of infection. Between 3 and 6 h post-adsorption, which corresponds to the interval of primary transcription (Figure II-6) (143), mRNA levels increased at a lower rate compared with the rate between 6 and 12 h post-adsorption, which likely reflects secondary rounds of transcription (Figure II-6) (143). From 12 to 24 h post-adsorption, viral s4 RNA levels

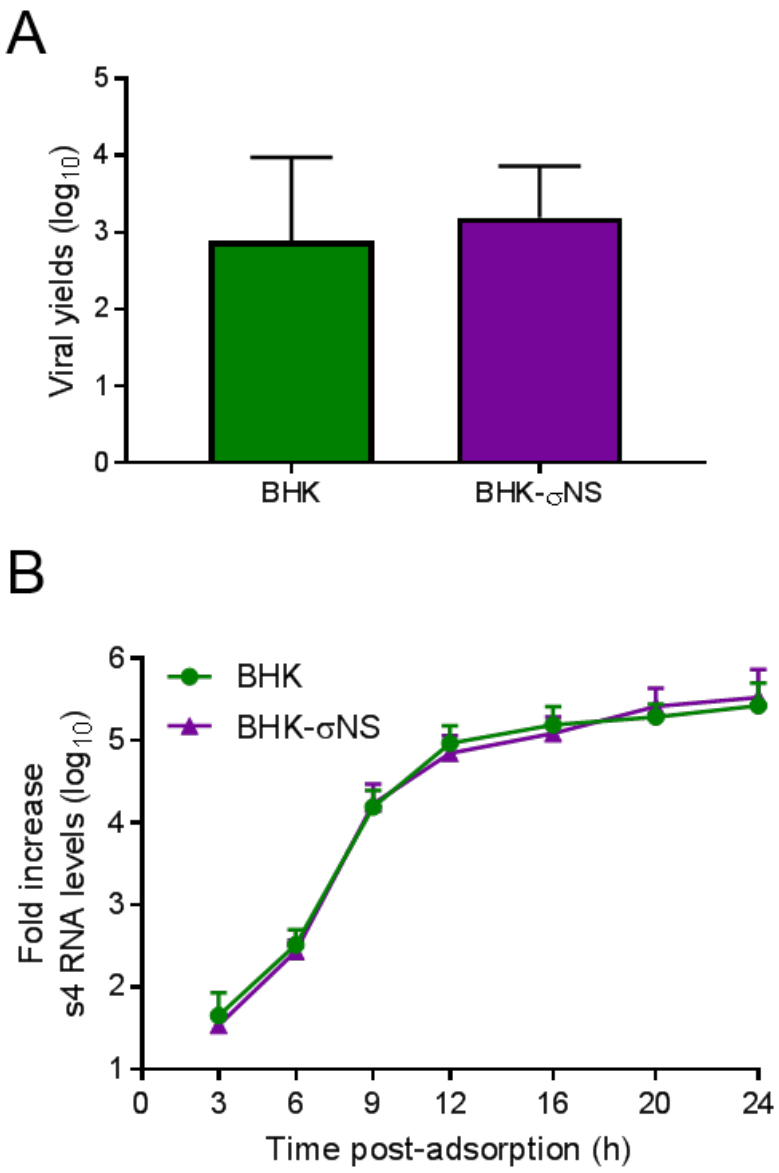

Figure III-1. Overexpression of σNS does not alter reovirus replication. BHK and BHK-σNS cells were adsorbed with T3D at an MOI of 10 PFU/cell. (A) Viral yields at 24 h post-adsorption were determined by plaque assay. Results are presented as mean ± SD for triplicate experiments. (B) Cells were lysed at the intervals shown, and s4 RNA was quantified by RT-qPCR. Results are presented as mean RNA levels normalized to the RNA levels at 0 h for three independent experiments. Error bars indicate SD.

were maintained. These results suggest that overexpression of σNS does not alter steady-state levels of viral RNA.

To determine the influence of σNS on viral mRNA levels during infection, I conducted similar experiments as those described above but in the presence of cycloheximide (CHX). CHX is an inhibitor of protein synthesis that acts by blocking translation elongation (154). BHK and BHK-σNS cells were treated with 5 μg/ml of CHX for 2 h, followed by adsorption with T3D in the absence of CHX for 1 h, and incubation in the presence of CHX for various intervals. s4 RNA levels were assessed by RT-qPCR (Figure III-2B). To confirm translation inhibition, σNS protein levels were assessed by immunoblotting at 24 h (Figure III-2A). In the presence of CHX, incoming virions enter cells and mediate primary transcription (Figure I-8 and II-11), but any further replication cycle steps would be impaired. s4 RNA levels increased comparably in CHX-treated BHK and BHK-σNS cells until 9 h post-adsorption. However, infected-BHK-σNS cells produced increased levels of s4 RNA later in infection. As primary transcription likely is constantly occurring throughout the experiment, these results suggest two possibilities: (1) σNS improves the stability of viral RNAs or (2) σNS increases primary transcription rates.

The σNS protein protects viral RNA from degradation

To test the effect of σNS on viral RNA stability, I used an infection-independent cell-based assay to quantify RNA half-life. HEK293T cells were transfected with a plasmid encoding σNS. At 20 h post-transfection, cells were transfected again with a plasmid encoding σ3, incubated for 4 h, and treated with actinomycin D to inhibit further

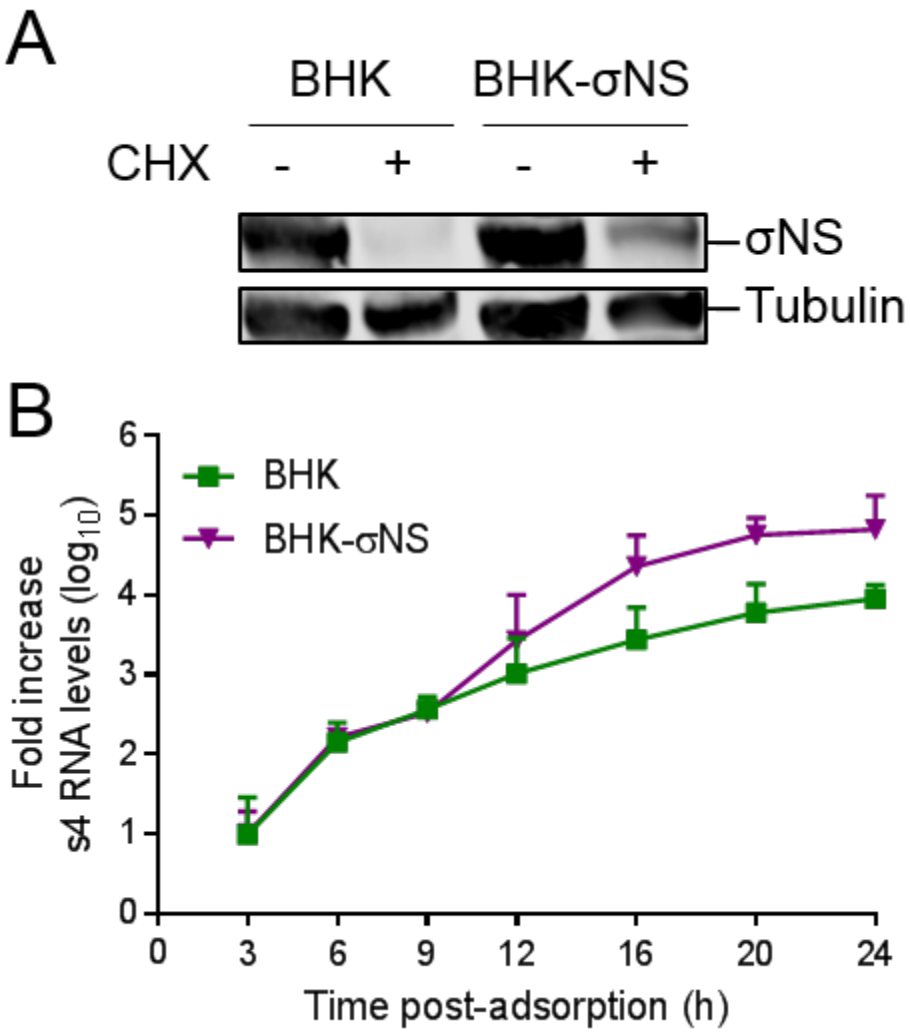

Figure III-2. σNS expression increases viral RNA levels during infection. BHK and BHK-σNS cells were treated with 5 μg/ml of cycloheximide (CHX) for 2 h, followed by adsorption with T3D at an MOI of 10 PFU/cell. Cells were incubated in medium containing CHX. (A) Cells were lysed at 24 h post-adsorption, resolved by SDS-PAGE and immunoblotted using antibodies specific for σNS and α-tubulin. Representative immunoblots from triplicate experiments are shown. (B) Cells were lysed at the intervals shown, and s4 RNA was quantified by RT-qPCR. Results are presented as mean RNA levels normalized to the RNA levels at 0 h for at least three independent experiments. Error bars indicate SD.

transcription. Transcription derived from the σ3-encoding plasmid produces RNAs that are capped and polyadenylated (155). At various times following actinomycin D treatment, I quantified total σ3-encoding s4 RNA by RT-qPCR (Figure III-3). As actinomycin D inhibits transcription, this approach allowed me to determine RNA half-life. Transfection of cells with σNS led to the maintenance of s4 RNA levels throughout the time course of actinomycin D treatment. At 8 h after treatment initiation, I detected only a 10% reduction in s4 RNA levels. These results suggest that expression of σNS increases the half-life of a viral RNA.

As a control, I used a σNS construct lacking the first 38 amino acids (Δ38 σNS). Δ38 σNS was identified in a limited proteolysis assay, in which purified WT σNS was incubated with trypsin. Digestion products were identified using mass spectrometry. This deletion mutant was anticipated to be impaired in RNA binding, as it lacks a series of positively-charged residues predicted to be required for this activity (116, 129). Using the same assay system, I observed that transfection of cells with a plasmid encoding Δ38 σNS did not increase s4 RNA half-life (Figure III-3). Thus, σNS requires its amino-terminal 38 amino acids to increase RNA stability.

To test in a more direct manner whether σNS protects RNA from degradation, I developed an *in vitro* cell-free RNA protection assay. I incubated purified, recombinant WT or Δ38 σNS with internally radiolabeled uncapped and nonpolyadenylated s4 RNA. σNS-RNA complexes were incubated with HeLa S100 cytoplasmic lysates for various intervals. RNA was resolved by electrophoresis and quantified by phosphorimaging (Figure III-4A and 4B). Incubation with WT σNS protected RNA from degradation in a

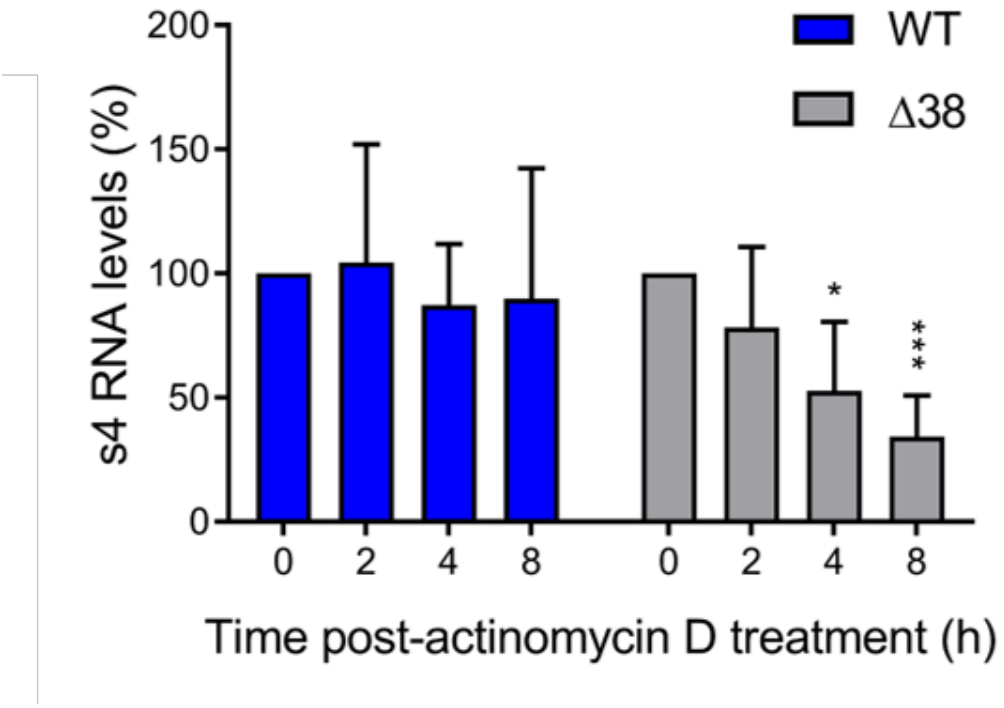

Figure III-3. The σNS protein protects viral RNA from degradation in transfected cells. HEK293T cells were transfected with plasmids encoding either WT or Δ38 σNS and incubated for 20 h, followed by a second transfection with a σ3-encoding plasmid and incubation for 4 h. Cells were treated with 10 μg/ml of actinomycin D, lysed at the intervals shown, and σ3-encoding s4 RNA was quantified by RT-qPCR. Results are presented as mean RNA levels normalized to the RNA levels at 0 h for at least three independent experiments. Error bars indicate SD. Values that differ significantly from the values at the start of the time course by one-sample t test for each time point are indicated (*, $P < 0.05$; ***, $P < 0.001$).

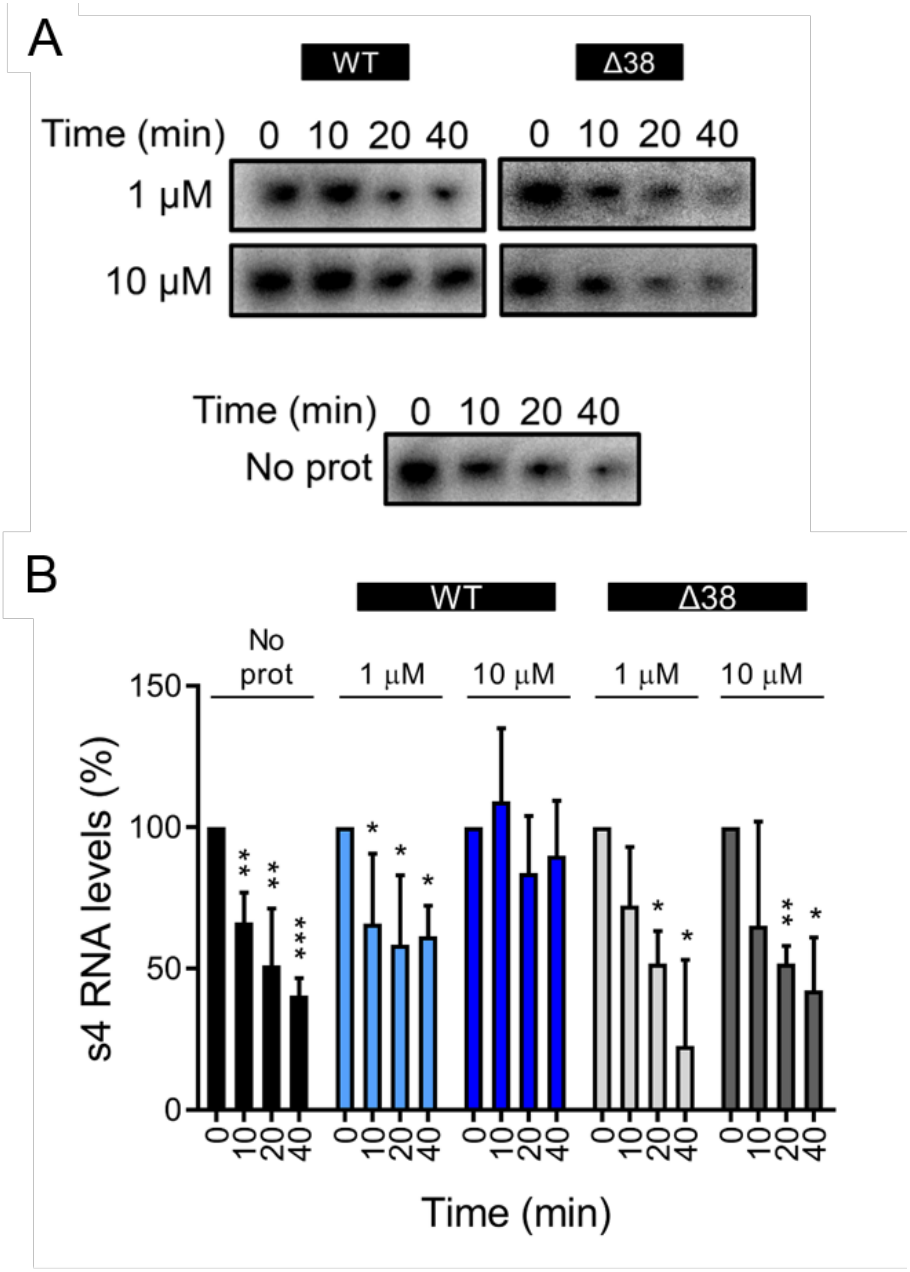

Figure III-4. The σNS protein protects viral RNA from degradation in a cell-free assay. (A) and (B) Radiolabeled uncapped and nonpolyadenylated s4 RNA was incubated without protein (no prot) or with 1 or 10 μM of purified, recombinant WT or Δ38 σNS at RT for 10 minutes, followed by addition of HeLa S100 lysates. RNA was purified at the intervals shown, resolved by electrophoresis, and visualized by phosphorimaging. (B) Pixel intensity analysis of the s4 RNA bands. Results are presented as mean RNA levels normalized to the RNA levels at 0 min for three independent experiments. Error bars indicate SD. Values that differ significantly from the values at the start of the time course by one-sample t test for each time point are indicated (*, $P < 0.05$; **, $P < 0.01$; ***, $P < 0.001$).

concentration-dependent manner. At a concentration of 1 μM, σNS did not protect s4 RNA from degradation in HeLa S100 lysates, and similar results were obtained in the presence of Δ38 σNS or in the absence of any additional protein. However, 10 μM σNS protected the s4 RNA such that by 40 min of incubation, only 10% of the input s4 RNA was lost. Thus, σNS protects viral RNA from degradation.

σNS and RNAs organize in filamentous structures

To better understand how σNS interacts with RNA, we used cryo-EM to visualize σNS-RNA complexes. We incubated purified, recombinant WT or Δ38 σNS with uncapped and nonpolyadenylated s4 RNA at a molar ratio of 50:1 on ice for 1 h and imaged σNS-RNA complexes by cryo-EM (Figure III-5). In the absence of RNA, WT σNS appears to form higher-order structures, as demonstrated by large electron-dense configurations. In contrast, Δ38 σNS appeared smaller and scattered throughout the EM grids. Following incubation with s4 RNA, WT σNS organized into long, filamentous structures approaching 200 nm in length. As expected, we did not observe interactions of Δ38 σNS with s4 RNA. These data suggest that WT σNS coats RNA and that these complexes arrange into long, filamentous structures.

The σNS protein forms higher-order complexes with viral and nonviral ssRNAs

To examine σNS-RNA complexes in detail, I sought to determine whether σNS exists in an RNA-bound complex in infected cells. I adsorbed HEK293T cells with reovirus T3D and, at 24 h post-adsorption, I lysed cells using mild conditions to preserve protein-RNA interactions. Samples were treated with RNase A and resolved by native and SDS-PAGE followed by immunoblotting using σNS-specific polyclonal

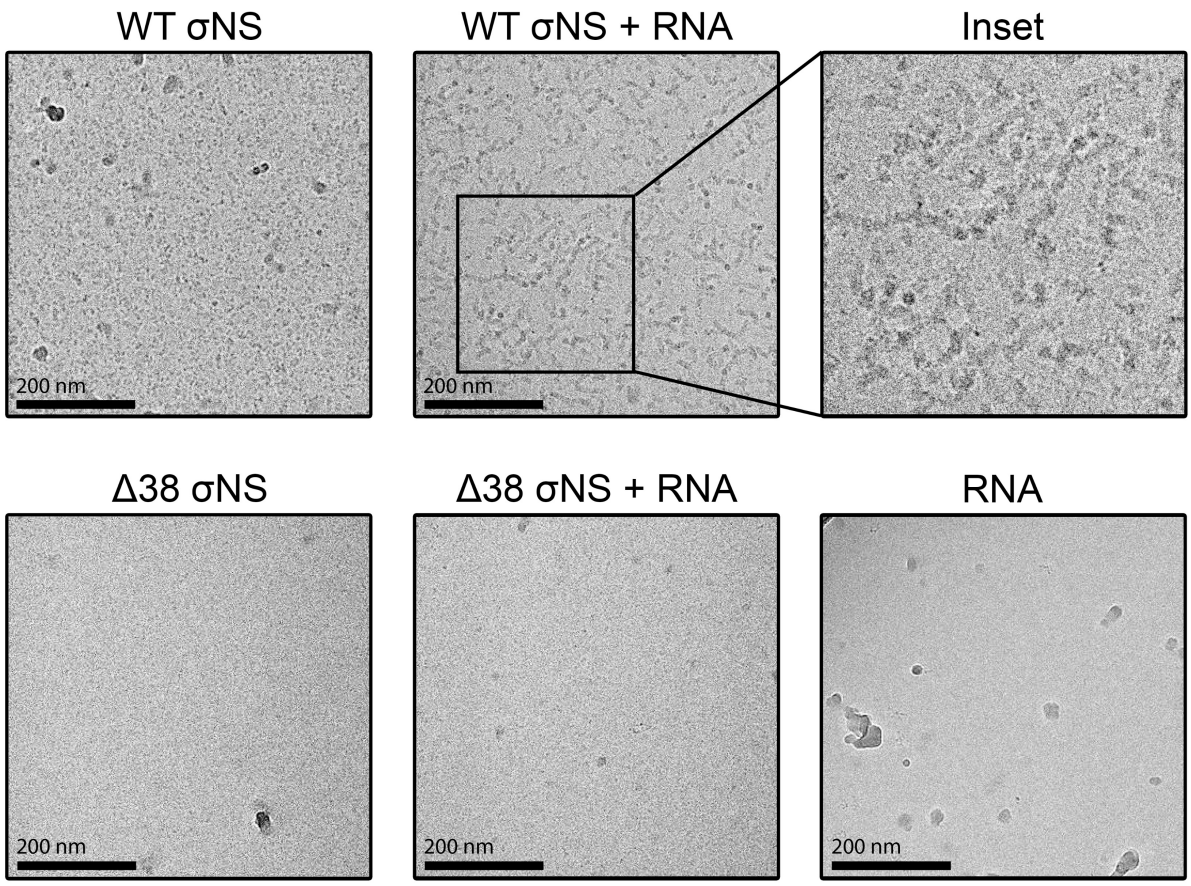

Figure III-5. The σNS protein forms filamentous structures in the presence of RNA. Uncapped and nonpolyadenylated s4 RNA was incubated with 50X molar excess of purified, recombinant WT or Δ38 σNS on ice for 1 h followed by plunge-freezing. Frozen specimens were imaged at 40,000X magnification with defocus levels ranging from -2.0 μm to -3.5 μm. Representatives images for WT σNS, WT σNS complexed with s4 RNA, inset of WT σNS and s4 RNA filaments, Δ38 σNS, Δ38 σNS incubated with s4 RNA, and s4 RNA alone are shown. Scale bars, 200 nm.

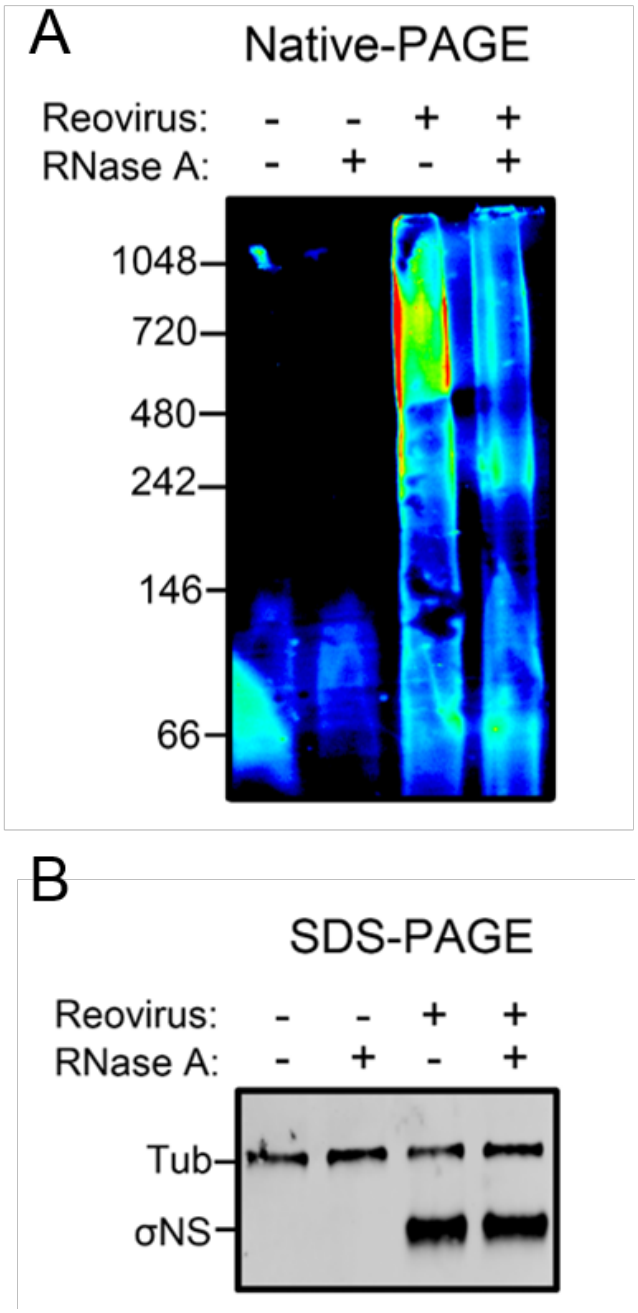

Figure III-6. The σNS protein exists as an RNA-bound complex in infected cells. HEK293T cells were adsorbed with reovirus T3D at an MOI of 100 PFU/cell and incubated for 24 h. Cells were lysed and treated with 0.25 μg/ml of RNase A at 30ºC for 1 h. Proteins were resolved by native PAGE (A) or SDS-PAGE (B), followed by immunoblotting using antibodies specific for σNS and α-tubulin (SDS-PAGE only). Representative immunoblots from triplicate experiments are shown. Pixel intensity is depicted in a rainbow scale (native-PAGE only).

serum (Figure III-6A and 6B). In the absence of RNase A treatment, σNS migrated predominantly as a high-molecular weight complex of ~500 kDa to 1 MDa. Following RNase A treatment, levels of these high-molecular weight complexes diminished. Thus, σNS appears to exist as a complex with RNA in infected cells.

We next tested the effect of RNase A treatment on the electrophoretic mobility of WT and Δ38 σNS from reovirus strains type 1 Lang (T1L) and T3D produced by coupled *in vitro* transcription and translation using rabbit reticulocyte lysates in the presence of ^{35}S-methionine. Transcription derived from these σNS-encoding plasmids yields RNAs that are uncapped and nonpolyadenylated. Following translation, samples were treated with RNase A, denatured with SDS and heat, or left untreated, resolved by native and SDS-PAGE, and imaged by phosphorimaging (Figure III-7A, 7B, 7C and 7D). In the absence of RNase A, WT σNS migrated as higher-order structures ranging from ~250 kDa to ~900 kDa, suggesting that several distinct oligomeric forms of σNS bind RNA. The migration pattern appeared to be regularly spaced, suggesting a specific stoichiometry of σNS-RNA binding. Treatment with RNase A disassembled σNS-RNA complexes. Intermediate molecular weight bands became undetectable, and bands with estimated sizes of ~900 kDa and ~80 kDa predominated. SDS and heat also disrupted higher-order structures. As expected, Δ38 σNS did not form higher-order species with RNA. Lastly, we did not observe differences in the migration patterns of T1L and T3D σNS, suggesting that the σNS proteins of both strains interact similarly with RNA. Thus, multiple subunits of σNS bind RNA with an apparent defined stoichiometry.

In a complementary approach, we used electrophoretic mobility shift assays (EMSAs) to examine σNS-RNA complexes. Purified, recombinant WT and Δ38 σNS

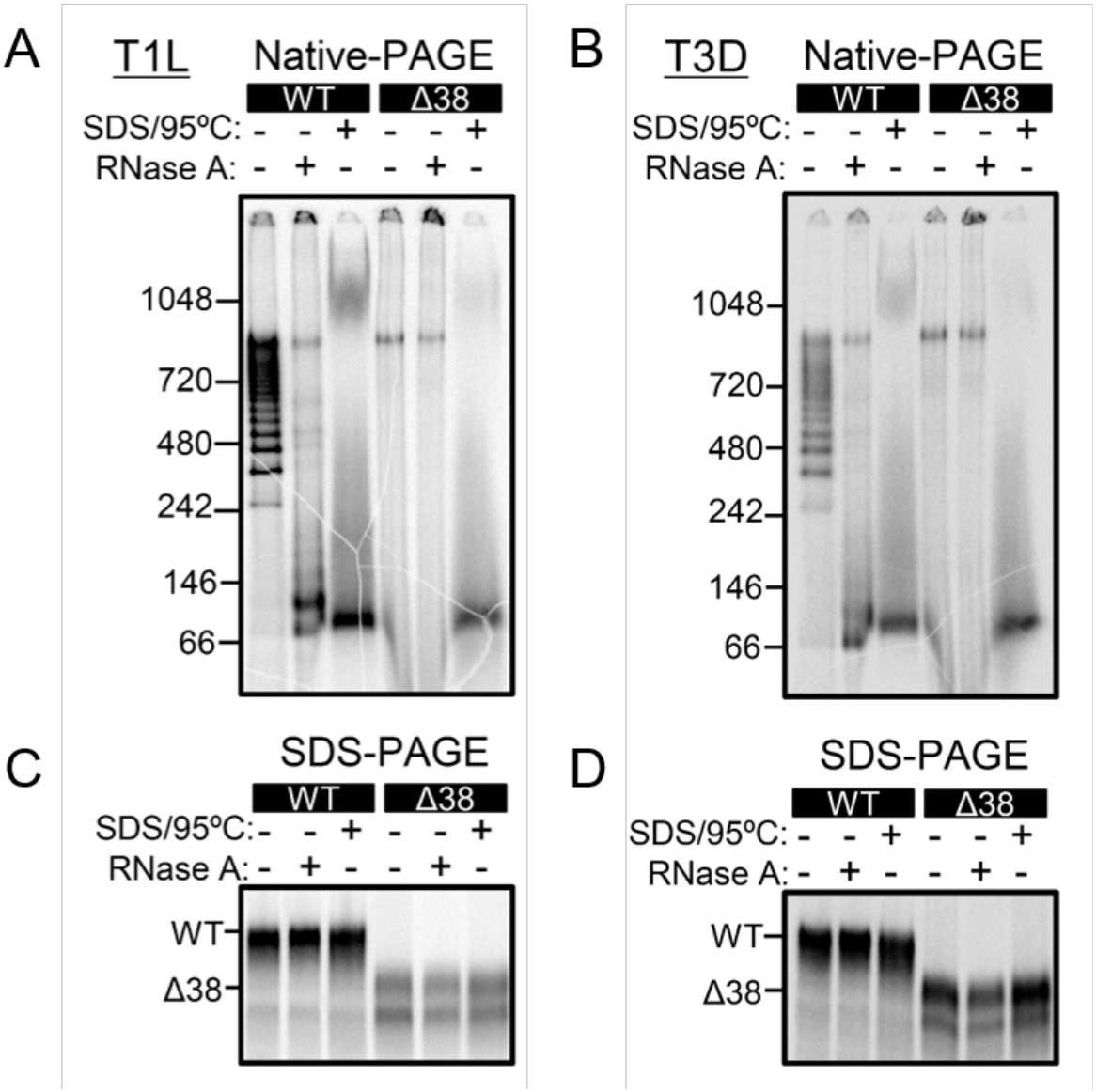

Figure III-7. The σNS protein forms higher-order complexes when incubated with RNA. (A and C) T1L and (B and D) T3D WT and Δ38 σNS were translated in vitro in the presence of ^{35}S-methionine and incubated with 0.25 µg/ml of RNase A at 30ºC for 1 h after translation, heated at 95 ºC for 10 min in SDS-PAGE sample buffer, or left untreated. Samples were resolved by native PAGE (A and B) or SDS-PAGE (C and D), and visualized by phosphorimaging. Representative gels from triplicate experiments are shown.

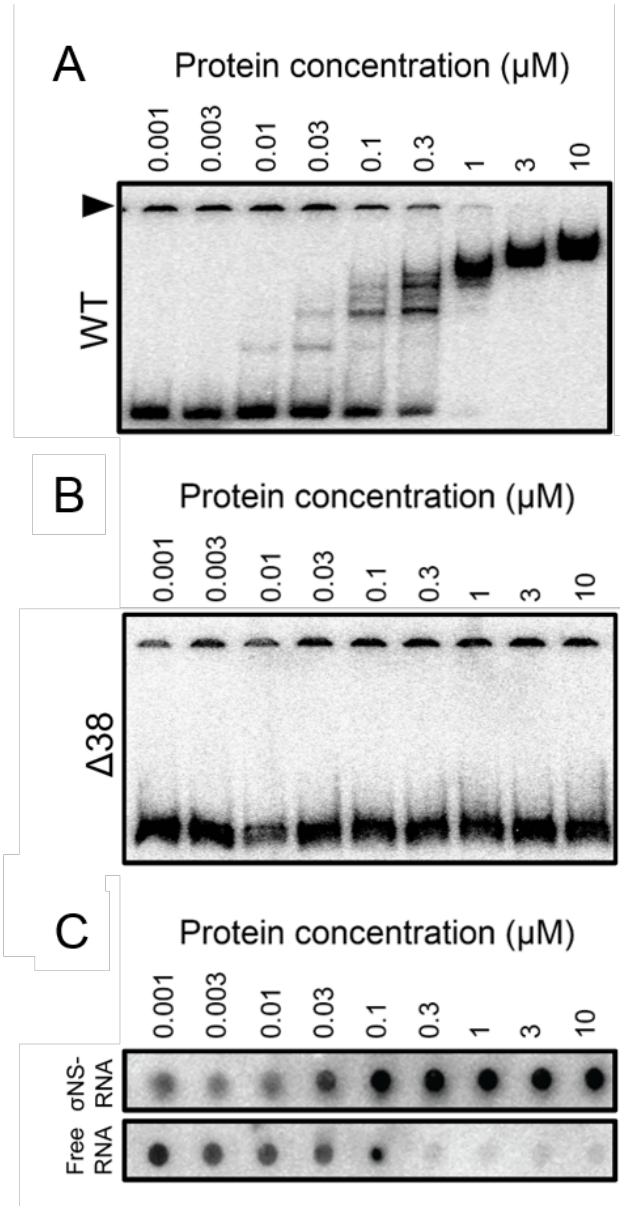

Figure III-8. The σNS protein binds viral and nonviral ssRNAs. (A and B) Increasing concentrations of purified, recombinant WT (A) or Δ38 σNS (B) were incubated with radiolabeled uncapped and nonpolyadenylated 7SK stem I RNA at RT for 10 minutes, followed by native electrophoresis and visualization by phosphorimaging. Arrowhead indicates RNA that fails to enter the gel. (C) Increasing concentrations of purified, recombinant WT σNS protein were incubated with radiolabeled uncapped and nonpolyadenylated s4 RNA at RT for 10 minutes. σNS-RNA complexes were spotted onto nitrocellulose membranes, and unbound free RNA was collected on nylon membranes. Membranes were visualized by phosphorimaging. Representative gels from experiments replicated at least three times are shown.

were equilibrated with terminally radiolabeled uncapped and nonpolyadenylated stem I 7SK small nuclear RNA (snRNA). The 7SK snRNA is a highly-structured RNA that functions to regulate transcription in metazoans (156). Stem I of the 7SK snRNA encompass the first 108 nucleotides, which organize as a GC-rich stem-loop (157). We chose this RNA as a surrogate for a nonviral RNA. Increasing concentrations of WT and Δ38 σNS were incubated with 7SK stem I RNA, and σNS-RNA complexes were resolved by native electrophoresis and quantified by phosphorimaging (Figure III-8A and 8B). WT σNS slowed the migration of the 7SK stem I RNA in a concentration-dependent manner, whereas Δ38 σNS was unable to form detectable σNS-RNA complexes. We observed at least four distinct σNS-RNA complexes following incubation of RNA with WT σNS, suggesting that each σNS unit binds ~27 nucleotides at saturation. Langmuir isotherm curve-fitting yielded an estimated K_D value of 260 nM for the interaction of σNS and 7SK stem I RNA (Figure III-9A and 9B). Increasing concentrations of WT σNS decreased the amount of free RNA and, at a concentration of 3 μM, no free RNA was detected, suggesting that at this concentration, the 7SK stem I RNA is saturated with σNS. Increasing concentrations of σNS also decreased the amount of aggregated RNA incapable of entering a polyacrylamide gel (Figure III-8A, arrowhead), suggesting that σNS has a function in unwinding RNAs.

To determine the affinity of σNS for viral RNA, we conducted a filter-binding assay using purified, recombinant WT σNS and terminally radiolabeled uncapped and nonpolyadenylated s4 RNA. Increasing concentrations of WT σNS were incubated with s4 RNA. σNS-RNA complexes were spotted on a nitrocellulose membrane, and the unbound RNA was collected on a nylon membrane. The radiolabeled RNA on each

membrane was quantified by phosphorimaging (Figure III-8C). Increasing concentrations of σNS increased the levels of RNA retained on the nitrocellulose membrane and decreased the free RNA collected on the nylon membrane. Langmuir isotherm curve-fitting yielded a K_D value of 290 nM for the σNS-s4 RNA interaction, which is comparable to the estimated K_D value for the σNS-stem I 7SK RNA interaction (Figure III-9A and 9B). Collectively, these data indicate that σNS binds a viral RNA with similar affinity as a nonviral RNA, suggesting that σNS does not recognize a specific RNA sequence.

The σNS protein impairs translation of viral and nonviral RNAs

As σNS is an ssRNA-binding protein, I hypothesized that it might alter the translation of RNAs. To test whether σNS affects translation, I co-transfected HEK293T cells with increasing concentrations of plasmids encoding either WT or Δ38 σNS and a fixed concentration of a luciferase-encoding plasmid (Figure III-10A). Transcription derived from these plasmids yields RNAs that are capped and polyadenylated (155). Increasing concentrations of WT σNS plasmid decreased luciferase activity, a marker for luciferase translation. In contrast, transfection of Δ38 σNS did not decrease luciferase activity. These data indicate that σNS impairs translation of a nonviral, capped and polyadenylated RNA and that this inhibition depends on the amino-terminal 38 amino acids of σNS.

To test whether σNS displays a broad-spectrum inhibitory effect on translation, I conducted *in vitro* translation assays using an uncapped and polyadenylated RNA in the presence or absence of σNS. Increasing concentrations of purified, recombinant

A

RNA	K_D	SD	R^2
7SK Stem I	260 nM	+/- 21 nM	0.993
s4	290 nM	+/- 17 nM	0.984

B

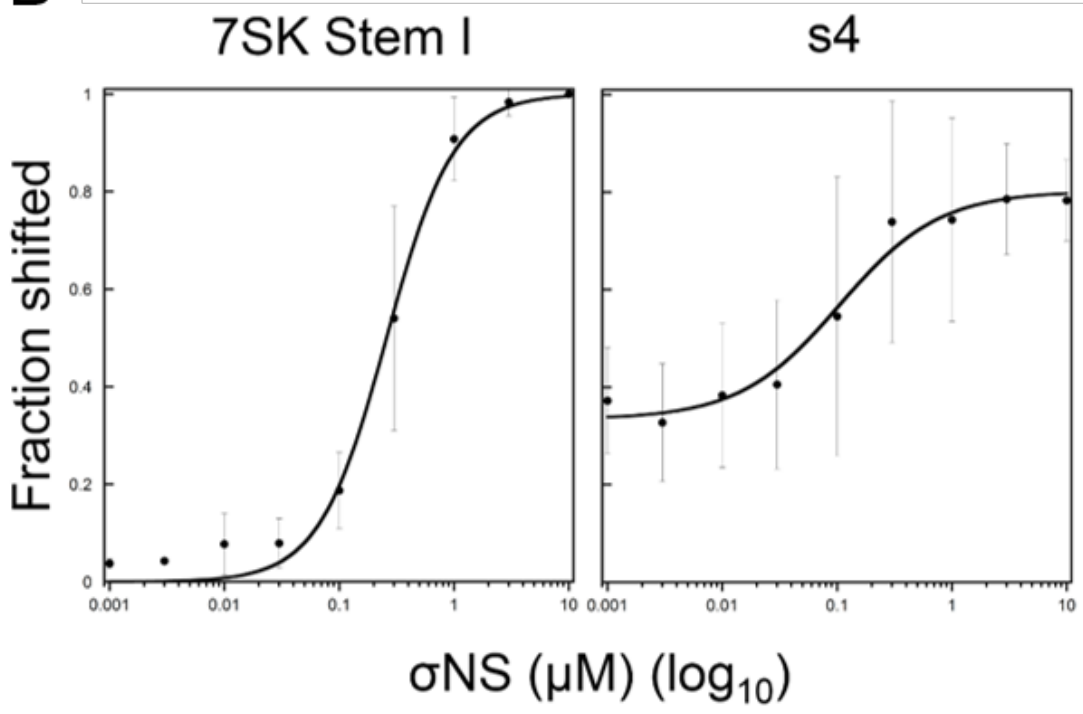

Figure III-9. The σNS protein binds viral and nonviral ssRNAs with similar affinity. (A) KD, SD, and R2 values for WT σNS and 7SK stem I (Figure III-8A) or s4 RNA (Figure III-8C) were determined using KaleidaGraph. (B) Langmuir isotherm curve fitting for WT σNS and 7SK stem I (left) or s4 RNA (right). Results are presented as mean percentage shift at each concentration of σNS for at least three independent experiments. Error bars indicate SD.

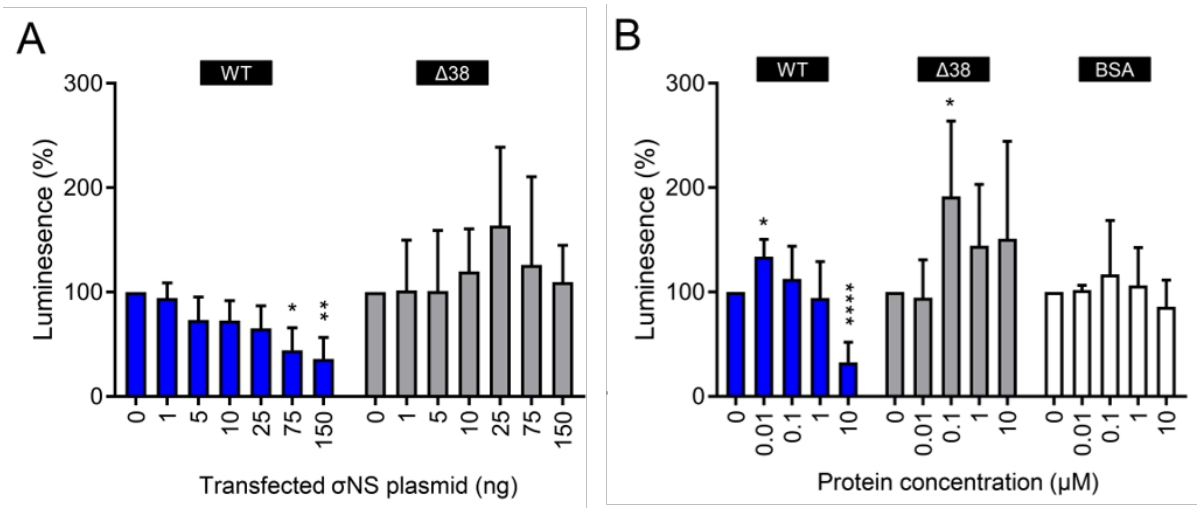

Figure III-10. The σNS protein diminishes translation of nonviral RNAs. (A) HEK293T cells were transfected with increasing amounts of plasmids encoding either WT or Δ38 σNS and a fixed amount of renilla luciferase-encoding plasmid, and incubated for 24 h. Cells were lysed, and luciferase levels were quantified. Results are presented as mean luminescence percentage normalized to luciferase levels in the absence of σNS plasmid for at least three independent experiments. Error bars indicate SD. (B) Firefly luciferase uncapped and polyadenylated RNA was incubated with increasing concentrations of purified, recombinant WT or Δ38 σNS or BSA at RT for 10 min. Protein-RNA complexes were added to wheat germ extracts and incubated at 25 ºC for 1 h. Luciferase synthesis was quantified by luciferase assay. Results are presented as mean luminescence percentage normalized to luciferase levels in the absence of protein for at least three independent experiments. Error bars indicate SD. Values that differ significantly from the no protein condition values by one-sample t test for each time point are indicated (*, $P < 0.05$; **, $P < 0.01$; and ****, $P < 0.0001$).

WT or Δ38 σNS or bovine serum albumin (BSA) as a control were incubated with uncapped and polyadenylated luciferase RNA prior to incubation with wheat germ extracts to initiate translation. Wheat germ extracts were chosen for these experiments instead of rabbit reticulocyte lysates because of their higher stringency and dependency on the type of RNA and reaction conditions for efficient translation (114). After incubation, I quantified luciferase activity (Figure III-10B). WT σNS at a concentration of 10 μM (~100:1 molar excess) decreased translation of luciferase RNA by 67%, corroborating the observations made in experiments using HEK293T cells. In contrast, Δ38 σNS and the BSA control did not diminish translation efficiency.

I examined the effect of σNS on translation of a viral RNA. I incubated increasing concentrations of purified, recombinant WT or Δ38 σNS with capped, 2'O-methylated and nonpolyadenylated s4 RNA prior to incubation with wheat germ extracts to initiate translation in the presence of ^{35}S-methionine. Protein products were resolved by SDS-PAGE and quantified by phosphorimaging (Figure III-11A and 11B). Similar to findings made in the luciferase experiments, 10 μM WT σNS (~80:1 molar excess) significantly impaired translation of the s4 RNA. Thus, when present at high concentrations, σNS inhibits translation of different types of RNAs.

The σNS protein does not have NTPase activity

The σNS homolog NSP2 from rotavirus has been hypothesized to mediate genome replication by acting as a motor using NTP hydrolysis to package RNAs (135). To test whether σNS has NTPase activity, I conducted thin-layer chromatography (TLC) assays and assessed GTP hydrolysis. Purified, recombinant WT σNS or rotavirus NSP2 was incubated with radiolabeled GTP and varying concentrations of $MgCl_2$ at 37°C for 1

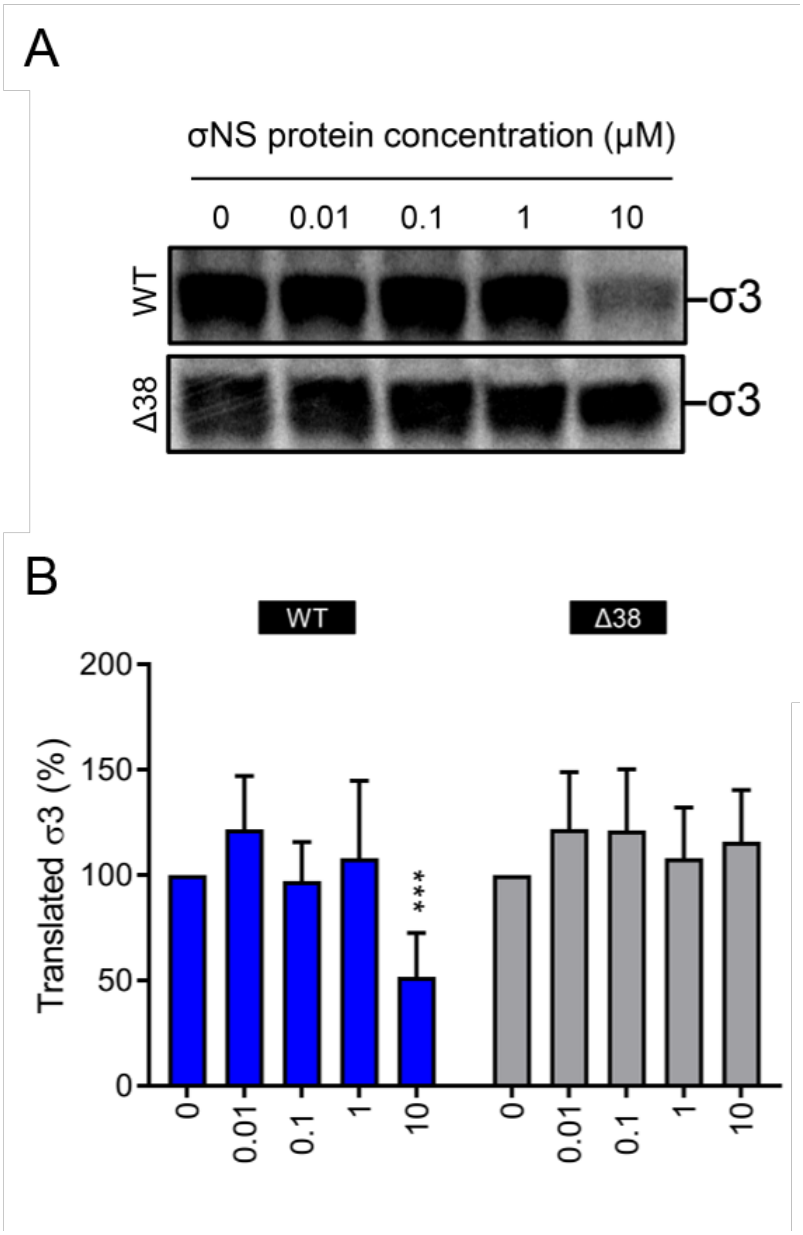

Figure III-11. The σNS protein diminishes translation of viral RNAs. (A) Capped, 2'O-methylated and nonpolyadenylated s4 RNA was incubated with increasing concentrations of purified, recombinant WT or Δ38 σNS at RT for 10 min. Protein-RNA complexes were added to wheat germ extracts and incubated at 25ºC for 1 h in the presence of 35S-methionine. Samples were resolved by SDS-PAGE and visualized by phosphorimaging. (B) Pixel intensity analysis of the σ3 protein band for at least three independent experiments. Error bars indicate SD. Values that differ significantly from the no protein condition values by one-sample t test for each time point are indicated (***, $P < 0.001$).

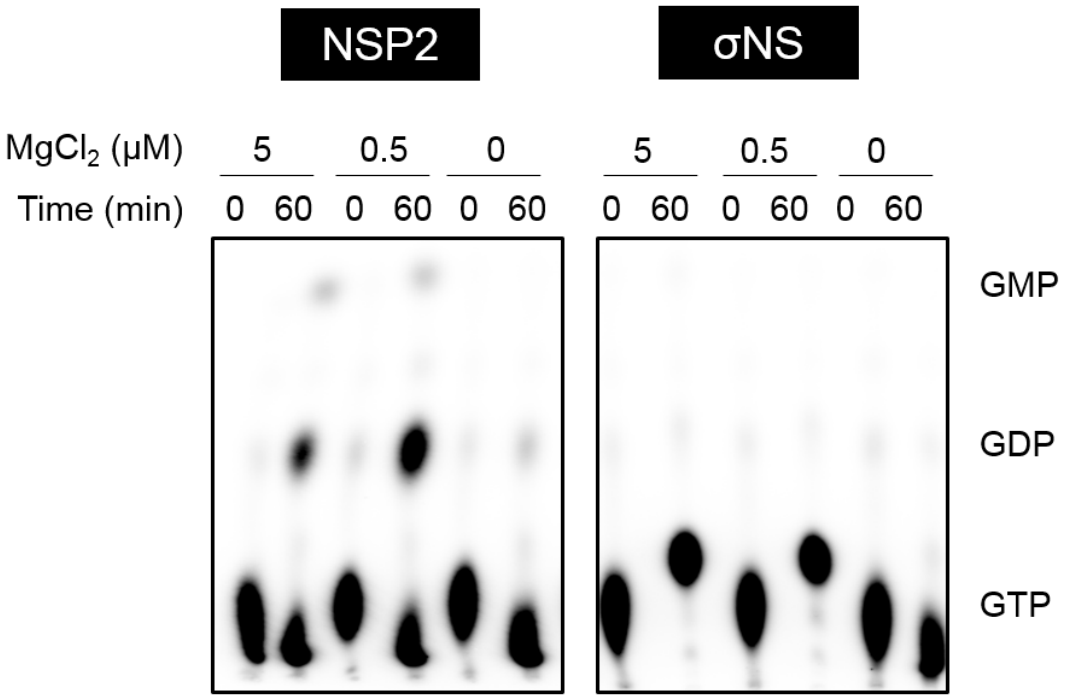

Figure III-12. The σNS protein does not have detectable NTPase activity. Recombinant, purified NSP2 and σNS protein (2 μg of protein per reaction) were incubated with α-^{32}P[GTP] and 0, 0.5, and 5 μM $MgCl_2$ at 37ºC for 0 or 60 min. Reactions were terminated with 1 N formic acid, spotted onto PEI-cellulose sheets, and resolved by TLC using 1.2 M LiCl. Sheets were dried and visualized by phosphorimaging. GTP, GDP, and GMP species were detected by UV shadowing. Representative TLC sheets from experiments replicated at least three times are shown.

h. Reactions were terminated by adding formic acid and resolved using TLC (Figure III-12). Rotavirus NSP2 hydrolyzed GTP when the incubation conditions included $MgCl_2$, as previously described (135, 137). In contrast, reovirus σNS did not hydrolyze GTP, suggesting that σNS has activities that differ from those of NSP2.

Discussion

Using *in vitro* and cell-based approaches, we discovered that σNS forms complexes with RNA that organize into long, filamentous structures. In addition, I observed that σNS increases RNA half-life and protects RNA from degradation. These results suggest a function for σNS as an RNA-binding protein that prepares RNA transcripts for dsRNA replication. This preparation could include increasing RNA stability (Figures III-3 and III-4), protecting RNAs from RNases (126), or folding RNAs into a conformation required for assortment (42).

In experiments using purified σNS and stem I 7SK RNA, a nucleic acid that is 108 nucleotides in length, we observed that at least four units of σNS bind stem I 7SK RNA at saturation (Figure III-8A). These data suggest that σNS covers a length of ~27 nucleotides, consistent with previous results (126). Residues 2 to 11 of σNS contribute to RNA-binding, although Δ2-11 σNS mutants retain the capacity to bind RNA, albeit poorly (116). Using a σNS mutant lacking the amino-terminal 38 amino acids, we found that these residues are absolutely required for RNA-binding (Figure III-8B).

Previous competition assays indicate that σNS does not preferentially bind viral over nonviral RNA (126). Our findings corroborate these results, as we calculated similar K_D values for σNS binding to viral s4 RNA and nonviral stem I 7SK RNA (290 nM and 260 nM, respectively) (Figure III-9A and 9B). Studies to quantify the affinity of a protein for RNA are usually conducted *in vitro*, and it is possible that during infection, other factors contribute to the affinity and specificity of σNS-RNA interactions. For example, sequestration of σNS in discrete cellular environments (110) might account for increased specificity for viral RNAs. In addition, μNS and μ2, which each interact with

σNS in reovirus inclusions (105, 107, 111, 158), also display affinity for RNA (108, 159). A complex of these proteins and σNS might be responsible for binding viral RNAs. It also is possible that σNS binds cellular RNAs to promote the translation of cellular proteins within these structures (122), as several host proteins are found within inclusions, for example Hsc70 (93) and the TRiC chaperonin (92).

In the EMSA experiments conducted in our study, we observed an interesting feature of σNS-RNA interactions (Figure III-8A, arrowhead). Increasing concentrations of σNS resulted in a reduction of aggregated RNA that did not enter the gel. These results suggest that σNS binding to RNA leads to RNA rearrangements allowing the RNA to migrate through the gel matrix. RNA remodeling proteins that resolve RNA structures are called RNA chaperones (131), which are encoded by some RNA viruses (132). There are three lines of evidence from our study and others suggesting that σNS is an RNA chaperone. First, RNA chaperones differ from other RNA-folding proteins by binding nucleic acids nonspecifically (Figure III-8 and III-9) and acting in an ATP-independent manner, which has been demonstrated for σNS in strand-displacement experiments (126). Second, the avian reovirus σNS protein, which is functionally homologous to mammalian reovirus σNS (160, 161), acts as an RNA chaperone *in vitro* (133), as does the rotavirus NSP2 nonstructural protein (42, 132). Third, our cryo-EM analysis demonstrates that σNS coats RNAs and forms filamentous structures (Figure III-5). Coating of RNAs by viral proteins has been suggested to mediate the activity of some viral RNA chaperones, and this activity ensures protection and folding of their target RNAs. This is the case for HIV-1 NCp7 (162, 163), poliovirus 3AB (164), and tomato bushy stunt virus p33 (165). Therefore, it is likely that *Reoviridae* family viruses

encode RNA chaperones to resolve kinetically trapped RNA conformations and facilitate replication.

Coating of RNAs also might account for the impairment in translation observed when σNS is incubated with RNAs at molar excess, as it might sterically hinder effective ribosome scanning (Figure III-10 and III-11) (166). In this regard, I envision a bimodal function for σNS in the regulation of translation. At low concentrations of σNS before RNAs become saturated, translation is enhanced, as our *in vitro* luciferase translation experiments suggest (Figure III-10B). It is possible that σNS directly stimulates translation of viral mRNAs via interactions with a domain that differs from that responsible for RNA-binding, as our experiments also showed a tendency for Δ38 σNS to increase translation (Figure III-10B). At high concentrations of σNS, translation is impaired in a mechanism dependent on the amino-terminal 38 amino acids of the protein (Figure III-10). Concentration-dependent inhibition of translation is a property of other viral proteins, like HIV Gag, which inhibits translation of its own RNA at high concentrations (167), and the coat protein from potato virus A (168).

Collectively, our findings indicate that σNS functions as an RNA-binding protein that increases viral RNA half-life. Additionally, our research suggests that the mechanism by which σNS promotes genome replication differs from that hypothesized for NSP2. Future studies will aim to translate our *in vitro* findings, including the importance of the amino terminal domain of σNS in RNA-stability, to the context of reovirus infection.

CHAPTER IV

REOVIRUS σNS INDUCES REMODELING OF THE ENDOPLASMIC RETICULUM

Introduction

Viruses that replicate in the cytoplasm use neoorganelles called inclusions, factories, or viroplasms. To build these organelles, viruses remodel host membranes using specific viral proteins. Most of the knowledge regarding viral inclusions comes from imaging studies using (+) RNA viruses (81, 169). Depending on the virus, host membranes that are used to build replication organelles are derived from the endoplasmic reticulum (ER), mitochondria, Golgi, peroxisomes, or other vesicular compartments such as autophagosomes (170). The only evidence of cellular reorganization during dsRNA virus infection comes from studies using rotavirus, for which nonstructural proteins are used to recruit lipid droplets and scaffold inclusions (171, 172). To enhance knowledge about the morphogenesis and architecture of inclusions formed during mammalian dsRNA virus infection, we used reovirus to understand organelle remodeling during infection.

The following experiments in this chapter involved optical and electron microscopy and were conducted in collaboration with Cristina Risco's laboratory at the National Center for Biotechnology in Madrid, Spain. I conducted the experiments shown in Figure IV-1, made reagents, and assisted in the experimental design and interpretation for the experiments shown in Figures IV-2, IV-3 and IV-4.

Results

Reovirus infection induces ER reorganization

Considering that the ER is the largest organelle in the cell (173) and is remodeled during infection with several (+) RNA viruses (170), we aimed to investigate rearrangements of this organelle during reovirus infection. HeLa cells were adsorbed with a reovirus reassortant strain, T3-T1M1, which is a type 3 reovirus containing the M1 gene from reovirus strain type 1 Lang. In some cell lines, T3-T1M1 replicates more efficiently than its counterpart T3D, likely due to events that occur within inclusions that favor replication of T3-T1M1 vs. T3D (143). At 24 h post-adsorption, cells were fixed and processed for confocal microscopy (Figure IV-1). The ER was detected by staining cells using antibodies specific for protein disulfide isomerase (PDI). PDI is an enzyme expressed in the lumen of the ER that catalyzes the formation of disulfide bonds. In infected cells, the ER localized around inclusions and appeared expanded compared with uninfected cells. Some regions of the ER co-localized with σNS. These data suggest that ER is reorganized during infection.

To confirm that the membrane rearrangements are specific to the ER, I tested whether reovirus rearranges the Golgi during infection (Figure IV-1). Cells were stained with antibodies specific for giantin, a protein that resides in the *cis* and *medial* Golgi and functions in its organization and biosynthetic trafficking (174). *Trans*-Golgi was marked using fluorescently-labeled wheat germ agglutinin (WGA), a lectin that binds sialic acids and N-acetylglucosaminyl residues, which are abundant in the Golgi. The Golgi was not associated with inclusions during infection, and the staining pattern did not differ between infected and uninfected cells. These results suggest that reovirus specifically

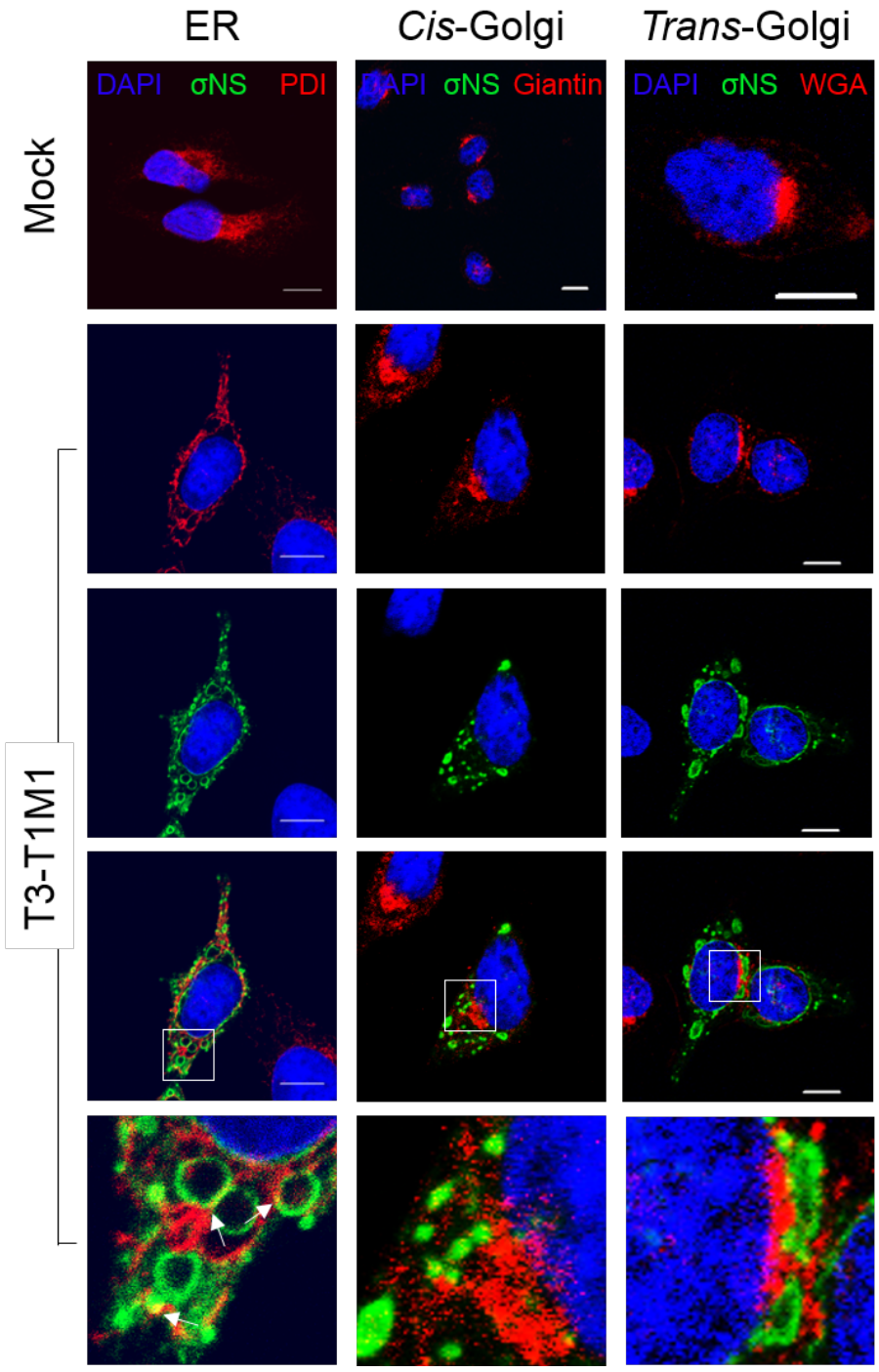

Figure IV-1. ER reorganization during reovirus infection. HeLa cells were infected with T3-T1M1 for 24 h. Cells were fixed, permeabilized, stained for σNS (green), PDI (red), giantin (red), WGA (red), or nuclei (blue), and visualized by confocal microscopy. Boxes indicate enlarged regions. Arrows point to inclusions associated with the ER. Scale bars, 10 μm.

hijacks the ER during infection.

Reovirus inclusions are embedded with membranes

As ER membranes are reorganized during infection and appear to surround viral inclusions, we hypothesized that these neoorganelles have a membranous nature. To define the ultrastructure of reovirus inclusions, we conducted three-dimensional (3D) image reconstructions of transmission electron microscopy (TEM) micrographs of HeLa cells infected with T3-T1M1 at 12 h post-adsorption (Figure IV-2). We used 3D image reconstructions because previous studies using conventional TEM had not detected membranes associated with inclusions (24). The 3D reconstructions showed that viral inclusions are membranous webs surrounded by mitochondria. The membranes derived from the RER were notable and contacted viral inclusions. Empty and full viral particles were present inside the membranous network, indicating that viral inclusions contain membranes.

To better understand the membrane rearrangements occurring within inclusions, we conducted electron tomography of Tokuyasu cryosections. Tokuyasu cryosectioning is a methodology in which cryosections are processed without dehydration, providing optimal preservation of intracellular membranes (175, 176). HeLa cells infected with T1 M1-P208S were imaged at 14 h post-adsorption (Figure IV-3). Reovirus T1 M1-P208S is a strain identical to the prototype T1L strain except for a proline-to-serine substitution at position 208 of the μ2 protein (M1 gene). This mutation changes inclusion morphology from filamentous to globular (83). The tomographic volumes of infected cells revealed that viral inclusions consist of groups of thin tubules and vesicles, with mitochondria and ER adjacent these structures. These results confirm that membranes

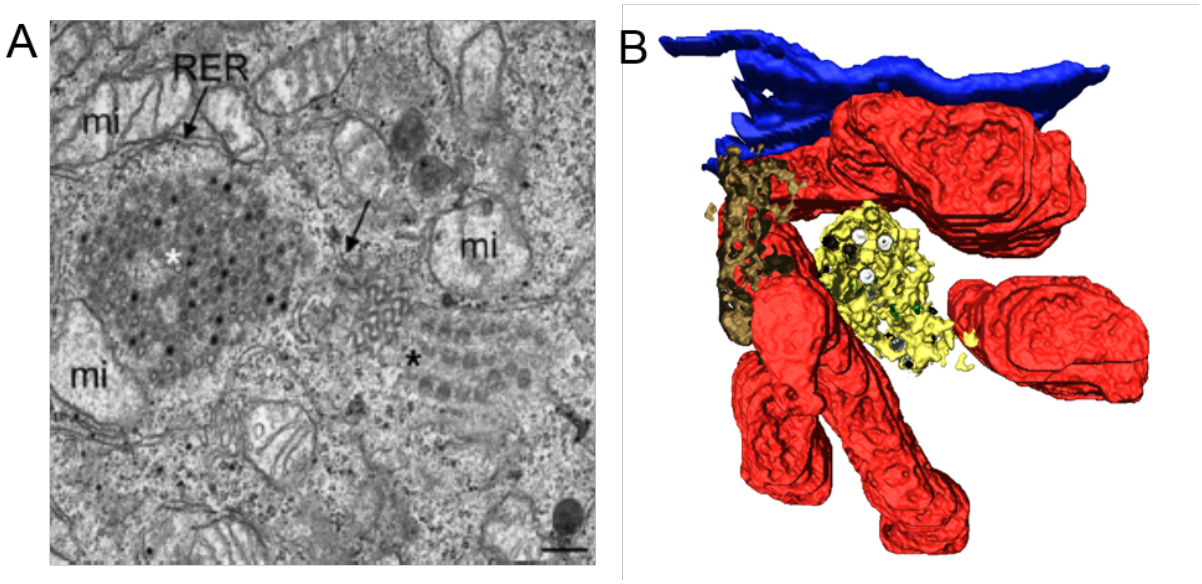

Figure IV-2. Reovirus inclusions are membranous webs. HeLa cells were infected with T3-T1M1 for 12 h. (A) TEM of viral inclusion (white asterisk) surrounded by mitochondria (mi) and ER membranes (RER). Some RER elements close to the inclusions (arrow on the right) appear to be connected to a sheet of cubic membranes (black asterisk). (B) 3D model of reovirus inclusions. Mitochondria (red) surround a membranous web (yellow). RER (brown) and nuclear envelope (blue) are adjacent to the inclusions. Filled particles (black) and empty particles (white) are integrated in the membranous network.

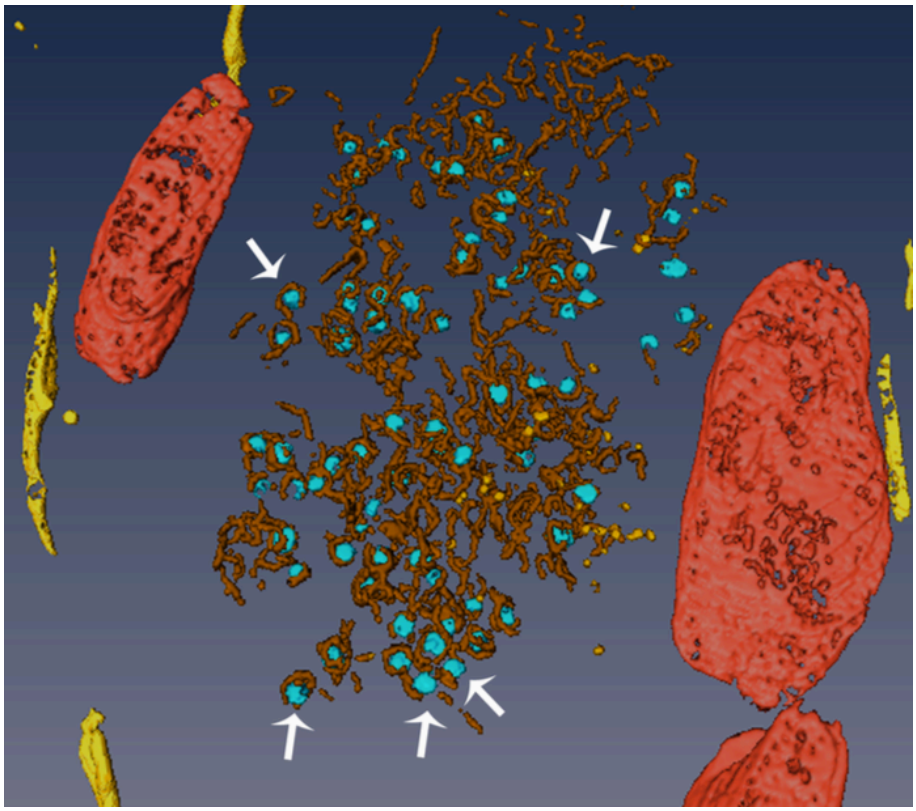

Figure IV-3. Reovirus inclusions are formed by thin tubules and vesicles. HeLa cells were infected with T1 M1-P208S for 14 h. Cells were frozen and sectioned at -120°C. Thawed cryosections were processed for electron tomography. RER (yellow) and mitochondria (red) surround the inclusion. Viral particles (light blue) appear attached to tubules (brown) and vesicles (orange) inside the inclusion.

are present inside reovirus inclusions and suggest that a viral determinant is responsible for the reorganization of the ER.

The nonstructural proteins σNS is responsible for ER remodeling

As viral nonstructural proteins are often responsible for the formation of viral inclusions and reorganization of cellular organelles (97), we hypothesized that σNS modulates changes in ER morphology. To test this hypothesis, we transfected HeLa cells with plasmids encoding either σNS or mCherry-KDEL (Figure IV-4). KDEL is a peptide sequence that localizes a protein to the ER. Cells were processed for confocal microscopy at 24 h post-transfection. Cells transfected with σNS exhibited disrupted ER morphology compared with cells transfected with mCherry-KDEL alone. The ER appeared thin and branched when σNS was present. σNS concentrated in the gaps between the tubules, generating a ring-like pattern. These results indicate that σNS is capable of inducing ER rearrangements and suggest that this viral protein contributes to the membrane reorganization observed during infection.

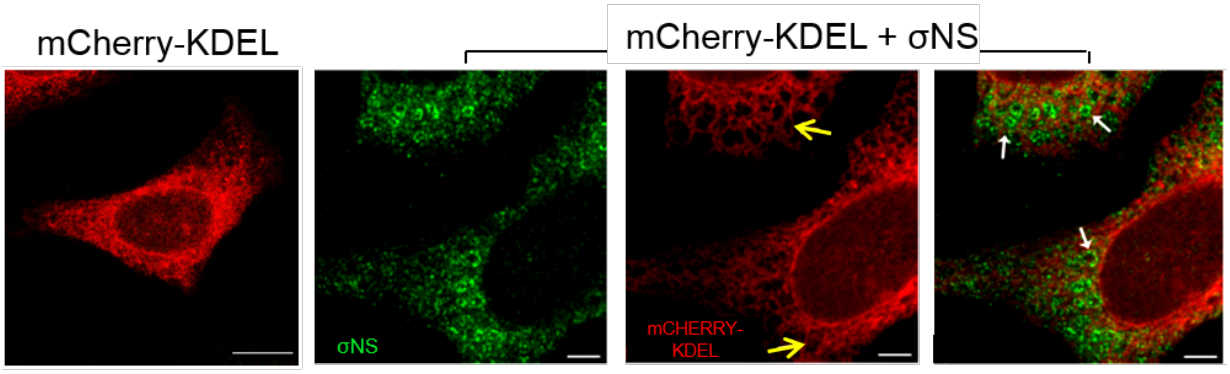

Figure IV-4. The σNS protein modifies ER morphology. HeLa cells were transfected with plasmids encoding mCherry-KDEL and σNS. At 24 h post-transfection, cells were processed for confocal microscopy. σNS was detected using a σNS-specific antibody. Cells expressing σNS show alter ER morphology, with long, separated, branched thin tubules (yellow arrows). σNS concentrates in the gaps between the tubules, producing a ring-like pattern (white arrows).

Discussion

In this chapter, I showed data suggesting that reovirus infection induces remodeling of the ER. In infected cells, the ER expands and reorganizes around reovirus inclusions (Figure IV-1). We also found that inclusions are membranous webs surrounded by RER and mitochondria (Figure IV-2 and IV-3). Although multiple viral components could be responsible for the membrane reorganizations that occur during infection, σNS likely is one of them, as cells transfected with σNS-expression plasmids show altered ER morphology (Figure IV-4).

Our study is the first report indicating that reovirus inclusions are associated with membranes. Previous studies failed to demonstrate the presence of membranes associated with these structures. This difference is probably because of the different techniques used. In conventional TEM, images are taken from ultrathin sections. These two-dimensional (2D) images represent single planes from larger volumes, limiting an analysis of the cellular architecture. In our experiments, consecutive serial sections were obtained, oriented, and aligned, providing 3D visual information of the cell.

Several viruses reorganize the ER to build their replication organelles. For example, flaviviruses form clusters of vesicles derived from the ER. These clusters are embedded in a membranous matrix inside their replication factories (177). Coronaviruses and picornaviruses also remodel the ER to form neoorganelles called double-membrane vesicles, which are sites of viral RNA replication (178). Considering that the ER is the largest organelle in the cell (173), it is not surprising that viruses use ER membranes to anchor replication machinery.

During this research, we also discovered that σNS functions as a membrane remodeler. We still do not understand the mechanism by which σNS alters the ER. σNS does not have reported or predicted transmembrane domains or any known post-translational modifications that could account for membrane interactions. Thus, we hypothesize that σNS modulates the function of ER-shaping proteins to produce changes in the ER. Some of these proteins could be reticulons, which are important for inducing tubules and vesicles of positive curvature (179), atlastins, proteins that mediate fusion of ER tubules (180), and lunapark, which stabilizes ER three-way junctions (181). Future studies will determine the mechanism by which σNS tubulates the ER, including specific domains or motifs of the protein responsible for this function.

Collectively, our results indicate that reovirus remodels the ER, likely through the function of σNS. These data enhance our understanding of how reovirus interacts with its host and reveal a new function for σNS.

CHAPTER V

SUMMARY AND FUTURE DIRECTIONS

Thesis Summary

Viruses with dsRNA genomes share mechanisms of replication. All known dsRNA viruses confine their genomes inside a protein shell, which also contains the RdRp and polymerase cofactors. These viruses use (+) RNA as a template for translation and genome replication. Members of the *Reoviridae* family have large genomes divided in 9 to 12 segments (1), which distinguishes them from other dsRNA virus families. Having a segmented genome offers some advantages, including reassortment capacity during co-infection with different strains. However, a segmented genome confers a problem in terms of packaging of genetic material. How *Reoviridae* viruses ensure that equimolar quantities of each gene segment are found within progeny particles is a question that remains unanswered. Viruses that infect vertebrates encounter additional difficulties. How do these viruses protect their transcripts from the host antiviral response and RNA decay machinery? Reoviruses are a tractable model to test hypotheses related to these questions. These viruses have a wide host range and varied tropism, replicate at high titers in mammalian cells, and can be manipulated using reverse genetics.

Most viruses encode proteins that are not packaged into virions but have functions in post-entry replication steps. These proteins are called nonstructural proteins. Reovirus encodes three nonstructural proteins: σ1s, μNS, and σNS. σ1s

enhances viral translation (95), reovirus-induced cell death (103), and dissemination in the host (182). μNS and σNS have functions in reovirus inclusion formation (110). σNS binds ssRNAs and displays nonclassical helicase activity (126). Additionally, temperature-sensitive viruses with mutations in σNS are impaired in dsRNA synthesis (117, 120, 121, 142).

In this thesis, I aimed to increase our understanding of functions of σNS during reovirus infection. I used HEK293T cells stably expressing an siRNA against the σNS-encoding S3 gene (σNS-siRNA cells) and a virus expressing synonymous mutations within the S3 gene siRNA target site of T3D (T3D-R) and tested how the absence of σNS expression affected various replication cycle steps. I found that infection of σNS-siRNA cells with T3D results in σNS knockdown, whereas infection with T3D-R yields σNS levels compared to those following infection of cells expressing a nontargeting siRNA (Figure II-3). I concluded that σNS-siRNA cells effectively and specifically diminish σNS expression when infected with T3D but not T3D-R.

By conducting time courses of infection, in which I adsorbed σNS-siRNA cells with either T3D or T3D-R, quantified viral titers by plaque assay, and evaluated inclusion morphology by confocal microscopy, I confirmed that σNS is required for progeny particle production (Figure II-4) and maturation of viral inclusions (Figure II-5). In similar infection courses, I determined that σNS is required for replication steps leading to viral protein synthesis (Figure II-9). In particular, σNS functions at a step in replication that occurs immediately before dsRNA synthesis (Figure II-10), suggesting that σNS is dispensable for primary but not secondary rounds of transcription (Figures II-6, II-7, II-8, and II-11).

Due to the pleiotropic nature of nonstructural proteins, teasing out individual activities poses challenges, especially in the context of a viral infection, in which different steps are interconnected. Therefore, in Chapter III, I used infection-independent systems to study σNS functions. I focused on understanding the biochemistry of σNS-RNA interactions, and I hypothesized that at least one of the mechanisms by which σNS promotes dsRNA synthesis is by increasing RNA stability. As a control, I used a mutant version of σNS lacking the first 38 amino acids, which are required for RNA-binding (Figure III-8). In collaboration with Liya Hu, this region was identified using limited proteolysis, suggesting that the first 38 amino acids fold as an independent domain within the structure of σNS. Using secondary structure prediction algorithms, the amino terminal region of σNS is predicted to form an α-helix with amphipathic character (Figure V-1), similar to other RNA-binding proteins (183).

To study the function of σNS in RNA stability, I determined the half-life of a viral RNA in cells transfected with either WT or Δ38 σNS and a plasmid encoding s4 RNA (Figure III-3). I found that cells expressing WT σNS had higher s4 RNA levels than cells expressing Δ38 σNS over an 8 h interval, suggesting that WT σNS increases viral mRNA half-life. I confirmed these results using an *in vitro* cell-free degradation assay, in which σNS-RNA complexes were incubated with cytoplasmic extracts from HeLa cells (Figure III-4). These extracts contain multiple cellular nucleases and are used to study RNA processing (184). A concentration of 10 μM WT σNS protected the s4 RNA from HeLa extracts, whereas smaller concentrations or any tested concentration of Δ38 σNS did not confer protection. These data indicate that σNS protects RNA from degradation.

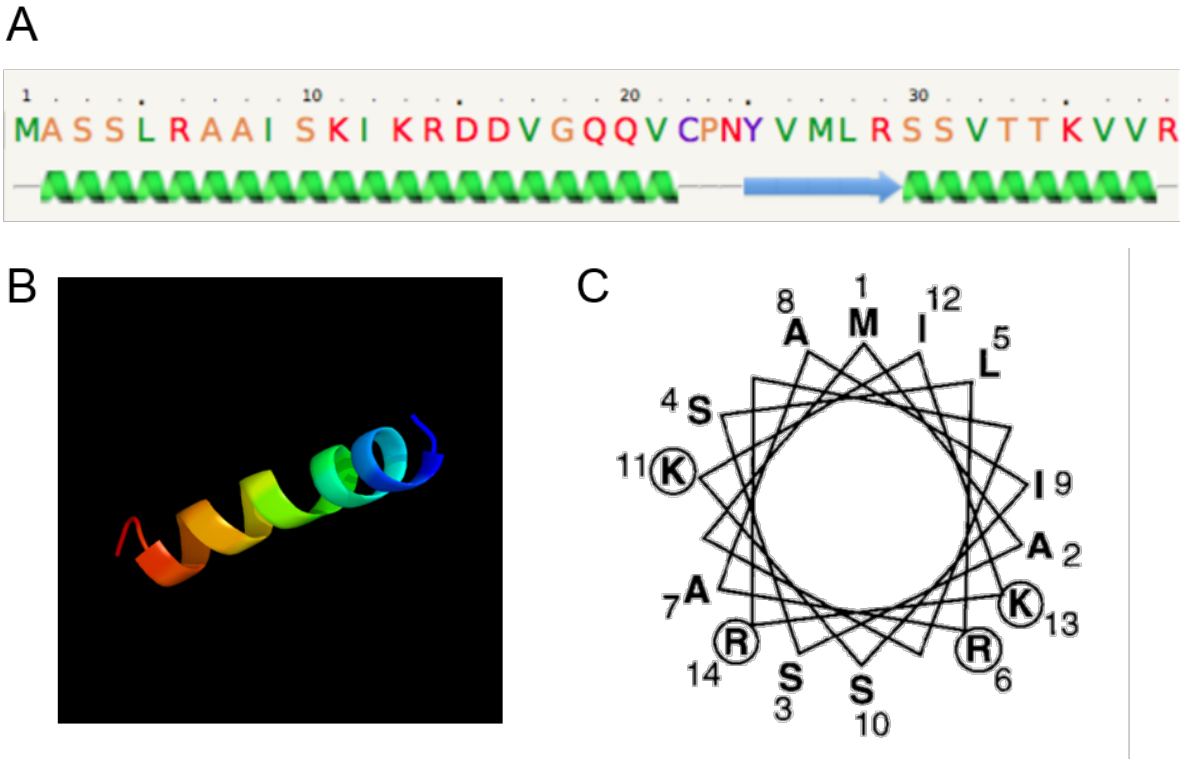

Figure V-1. Secondary structure prediction for the amino-terminal region of σNS. (A) Sequence of the first 38 amino acids of σNS and its predicted secondary structure are shown in a ribbon trace diagram. Amino acid colors indicate properties (green: hydrophobic, orange: small/polar, red: charged, purple: aromatic or cysteine). Approximately 74% of this region is predicted to fold as α-helix, and 13% folds as β-strands; 39% is predicted to be disordered. (B) Model of the amino-terminal region of σNS, including 21 residues of the protein showing 63.5% sequence identity with maltose-binding periplasmic protein, a lipid-binding protein. Rainbow colors depict N → C terminus. (C) Helical-wheel projection for amino acids 1-14 of σNS, which are predicted to fold as an α-helix with amphipathic character. Circles highlight basic residues. (Figure adapted from Gillian *et. al.* 1998 (116), predictions were generated in Phyre2 (185)).

σNS binds viral and nonviral RNAs with similar affinity (Figure III-8 and III-9) and coalesces on RNAs to form long, filamentous structures (Figure III-5). Several units of σNS bind RNA, resulting in high-molecular weight complexes (Figure III-7) (126). Large complexes also are observed in infected cells (Figure III-6). T1L and T3D σNS proteins interact similarly with RNAs (Figure III-7), which is predictable considering that these proteins share 97% identity in protein sequence.

In our EM images, σNS covers viral RNA, and I thought that σNS might protect RNAs from degradation by masking nuclease target sites. If so, I hypothesized that σNS-RNA complexes would be impaired in translation, as ribosome scanning would be blocked. I used three assays to test σNS functions in translation: a luciferase cell-based assay, an *in vitro* luciferase translation assay, and an *in vitro* σ3 translation assay using radioactive methionine (Figures III-10 and III-11). I found in all assays that high concentrations of σNS decreased luciferase translation, whereas Δ38 σNS did not. Thus, when present at high concentrations, σNS inhibits translation of different types of RNAs.

In the last data chapter of my thesis, I described experiments to study inclusion morphogenesis and interactions of σNS with the host. These experiments were conducted in collaboration with Dr. Cristina Risco's laboratory and were based on confocal and electron microscopy. During infection, the ER expands and interacts with inclusions (Figure IV-1), whereas the Golgi remains unaltered. Inclusions are surrounded by mitochondria and localize close to the nuclear envelope (Figure IV-2). Using 3D reconstructions, we discovered that reovirus inclusions are membranous webs, in which particles are attached to tubules (Figure IV-3). To identify the viral

components responsible for the membrane rearrangements, we conducted experiments to test whether σNS is capable of remodeling the ER (Figure IV-4). Although σNS does not have transmembrane domain or post-translational modifications, its amino-terminal domain is predicted to fold similarly to lipid-binding proteins (Figure V-1). Cells transfected with plasmids encoding σNS and mCherry-KDEL displayed changes in ER morphology to produce thinner ER tubules and ring-like structures that are absent in cells transfected with mCherry-KDEL alone. These findings suggest that σNS contributes to reovirus inclusion morphogenesis.

Collectively, my thesis contributes new knowledge about functions of σNS in the reovirus life cycle. It also provides new information about σNS biochemical properties and sheds light on σNS contributions to viral inclusion scaffolding. These findings enhance our understanding of *Reoviridae* nonstructural proteins and mechanisms of dsRNA virus replication and provide a foundation for future studies to determine the mechanism by which σNS influences assortment and the replication of the reovirus genome.

Future Directions

Elucidating the function of the amino-terminal region of σNS during infection

In Chapter II, I provided evidence about a function of σNS leading to genome replication. In Chapter III, I demonstrated using a series of *in vitro* assays that σNS increases mRNA stability, whereas a mutant lacking the amino-terminal 38 amino acids does not. For next steps, my *in vitro* observations about a function for σNS in RNA-stability should be tested in the context of viral infection. To examine the function of the amino-terminal 38 amino acids of σNS in infected cells, we will engineer viruses encoding point mutations in this region using reverse genetics. Charged residues will be mutated to alanine or residues with polar side chains if the alanine mutations are too disruptive and the resultant viruses are not viable. If these strategies are not successful, the mutant viruses might be recovered using cells expressing σNS in *trans.* If the latter also are not viable, virus recovery efficiency can be increased by transfecting cells with plasmids encoding vaccinia capping enzyme and FAST protein, which increase the efficiency of rotavirus reverse genetics (186). Using these viruses, we will study replication cycle steps over time courses of infection to identify the steps at which these viruses are impaired. Thus, results from these experiments will shed light on the function of the amino-terminal σNS domain in reovirus replication.

Determining sequence specificity between σNS and viral RNAs

Although EMSA experiments suggest that σNS has similar affinity for viral and nonviral RNAs (Figure III-8 and III-9), σNS must selectively bind viral RNAs during infection to ensure genome replication and particle formation. Therefore, I hypothesize

that σNS binds viral RNAs in infected cells and has higher affinity for certain regions of viral RNAs. To test whether σNS binds predominantly viral RNAs, RNA sequences bound by σNS in infected cells should be identified using high-throughput sequencing of RNA purified by cross-linking immunoprecipitation (HITS-CLIP). HITS-CLIP is a technique in which RNA-protein complexes are UV-crosslinked and immunoprecipitated (187, 188). The RNA is then extracted from the complexes, reverse-transcribed, and deep-sequenced to identify bound sequences (Figure V-2).

Cells should be infected with T3D reovirus for 9 and 24 h. These time points reflect the times at which I first detected a function for σNS (Chapter II) and a late time point, respectively. Protein-RNA complexes in cells can be crosslinked using UV irradiation. Cells will be lysed, and protein-RNA complexes will be immunoprecipitated using a monoclonal antibody specific for σNS. Linkers will be added to the ends of the RNAs, σNS-RNA complexes will be resolved by SDS-PAGE, and isolated. Protein will be digested using proteinase K, RNA will be precipitated and reverse transcribed. cDNAs will be gel purified, PCR-amplified, and HTS adapters will be ligated, followed by high-throughput sequencing using an Illumina instrument. Data will be analyzed by aligning reads to the reovirus genome. These experiments will determine whether σNS has higher affinity for certain sequences within reovirus RNAs and contribute to our understanding of the functions of σNS in reovirus assortment and dsRNA replication.

Developing an in vitro genome replication assay

The major hypothesis of my thesis work was related to a function for σNS in genome replication. However, because we lack an *in vitro* genome replication assay, I

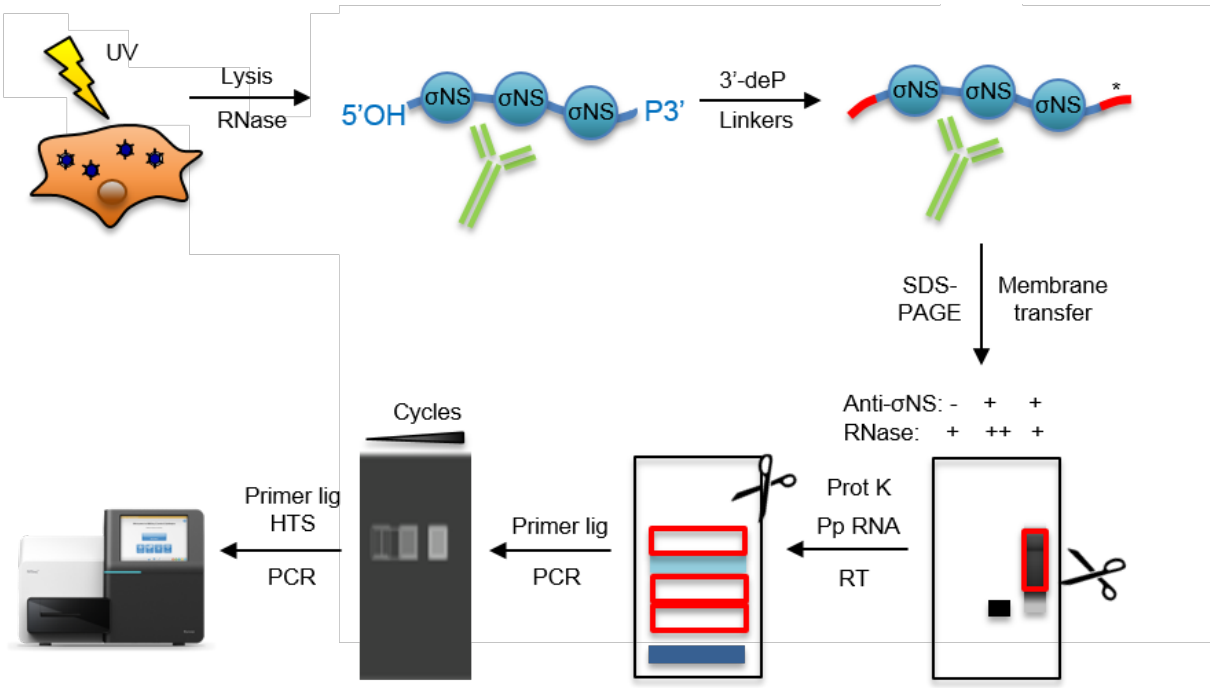

Figure V-2. HITS-CLIP strategy. Infected cells will be irradiated with UV light to induce protein-RNA crosslinks. Cells will be lysed, and RNAs will be partially digested using RNase A. σNS-RNA complexes will be immunoprecipitated using a monoclonal antibody specific for σNS (cite), followed by alkaline phosphatase treatment (3'-deP) to remove 3'-hydroxil groups and allow 3'-linker ligation. 5'- and 3'-linkers will be added, the latter being radiolabeled. Complexes will be eluted from beads and separated by SDS-PAGE. After transfer to nitrocellulose membranes, complexes will be visualized using phosphorimaging. Complexes will be isolated from the membrane and proteinase K (Prot K) treated to remove proteins, RNA will be precipitated (Pp RNA) and reverse transcribed (RT). cDNAs will be resolved in TBE-urea gels and size-selected. These cDNAs will be ligated to a 5'-primer (primer lig) and amplified. Sequencing primers will be ligated (Primer lig HTS) in a second PCR step, and samples will be sequenced using an Illumina platform. (Figure adapted from Moore et. al., 2014 (188))

was unable to directly test whether the σNS increases dsRNA synthesis. Therefore, we plan to develop an *in vitro* genome replication assay. There are three major lines of evidence suggesting that an *in vitro* genome replication assay is feasible for reovirus. First, synthesis of reovirus dsRNA in cell-free system is possible when lysates derived from infected cells are used (189, 190). However, these lysates only are active for 10 minutes. In addition, entire cell lysates are used in these assays, making it difficult to precisely alter the experimental conditions. Second, synthesis of dsRNA has been observed in crystalized λ3, suggesting that polymerase activity can be recapitulated *in vitro* (16). Third, a rotavirus genome replication assay exists that supports *de* novo synthesis of genomic RNA from exogenous RNA templates, making it the ideal *in vitro* system because the experimental conditions can be controlled. In this system, rotavirus cores are dialyzed in hypotonic buffer, resulting in the disruption of the VP2 shell (λ1 homolog). This treatment causes the dsRNA to be released from cores. Viral (+) RNA and NTPs are supplemented to these “open cores”, and dsRNA replication occurs (191).

Systems analogous to the rotavirus system have not been successful for reovirus. Although cores of both viruses are structurally similar, reovirus cores are turreted at the vertices, whereas rotavirus cores are not. Thus, it is likely that reovirus capsomeres are unstable relative to those of rotavirus, and the hypotonic treatment might dissociate these structures. To develop an *in vitro* reovirus genome replication assay, reovirus core proteins should be translated using rabbit reticulocyte lysates, and formation of capsomeres should be analyzed using native-PAGE. If capsomeres are formed, reactions can be supplemented with viral (+) RNAs, nonstructural proteins, and

radiolabeled nucleotides. Synthesis of dsRNA will be quantified following by TCA precipitation of reovirus cores and scintillation counting. A reovirus genome replication assay will allow us to directly test hypotheses related to σNS functions in synthesis of dsRNA.

Studying interactions between λ3 and σNS

My thesis shows that σNS promotes genome replication likely by increasing viral mRNA stability. However, σNS also could directly interact with λ3 to enhance its polymerization capacity. In preliminary studies conducted in collaboration with a graduate student in our laboratory, Christopher Lee, we determined that σNS co-immunoprecipitates with λ3 in infected cells (Figure V-3). To determine whether σNS and λ3 can directly interact, we will conduct similar co-immunoprecipitation studies using cell lysates derived from cells transfected with σNS, λ3, and μNS, the latter to nucleate inclusion-like structures (88). Additionally, we will study whether σNS-λ3 interactions are dependent on RNA by conducting similar experiments but in the presence of RNase A. These studies should be complemented with proximity-ligation assays in infected cells. If we determine that both proteins interact, K_D values should be defined for their interaction using surface plasmon resonance in collaboration with BVV Prasad's laboratory at Baylor College of Medicine. Results from these experiments will determine whether σNS can directly interact with λ3 and provide mechanistic information about σNS contributions to reovirus genome replication.

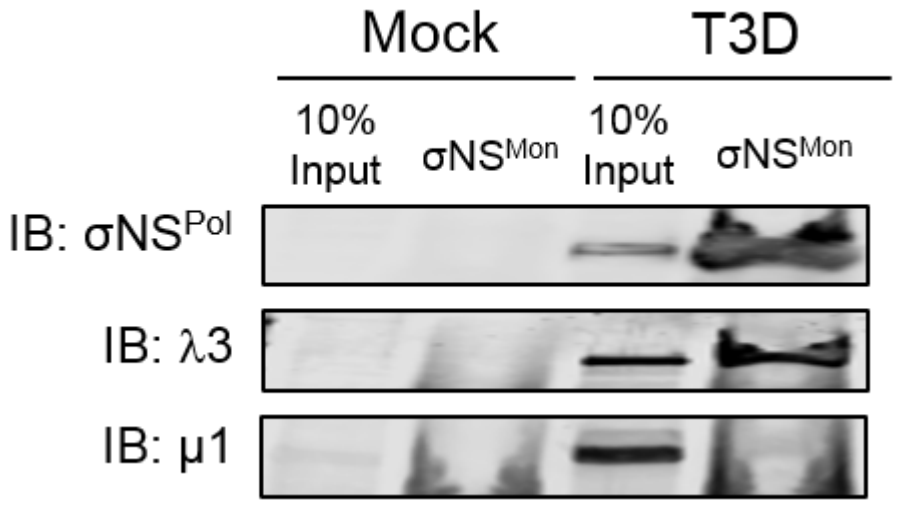

Figure V-3. Co-immunoprecipitation of σNS and λ3. HEK293T cells were adsorbed with T3D at an MOI of 100 PFU/cell. At 24 h post-adsorption, cells were lysed using NP-40 buffer, and σNS protein complexes were immunoprecipitated using a monoclonal antibody specific for σNS (σNS^{Mon}) (110). Immunoprecipitated proteins were resolved by SDS-PAGE, transferred to nitrocellulose membranes, and immunoblotted using polyclonal antibodies specific for σNS (σNS^{Pol}), λ3, or μ1, the latter being immunoblotted as a control for the specificity of the σNS and λ3 interaction.

Elucidating the mechanism by which σNS induces ER-membrane remodeling

When transfected alone, σNS induces thinning of the ER. However, σNS does not contain any predicted transmembrane domain or post-translational modifications. Therefore, I hypothesize that σNS engages ER-shaping proteins to mediate membrane reorganization and aid in viral inclusion formation. The most important proteins that regulate ER tubulation are reticulons, atlastins, and lunapark (Figure V-4). Reticulons are proteins that have hydrophobic hairpin domains that shape high-curvature ER tubules and mediate intramembrane protein interactions (179, 192). Atlastins are a family of dynamin-related GTPases that mediate homotypic fusion of ER membranes(180, 192). Lunapark proteins have several hydrophobic domains and regulate the function of reticulons and atlastins (181, 193). Besides these proteins, there are several others that regulate ER-organelle contact sites, including proteins involved in the regulation of cholesterol metabolism such as Niemann-Pick disease, type C (NPC1), oxysterol-binding protein-related protein 1L (ORP1L), and oxysterol-binding protein 1 (OSBP) (194). Thus, there are several candidate proteins that σNS could coopt to remodel the ER.

To test whether σNS interacts with ER-shaping proteins, it would be fruitful to use an unbiased approach based on mass spectrometry. Host proteins that interact with σNS can be identified using proximity-dependent biotin identification (BioID). We will engineer cells to stably express a σNS construct consisting of the σNS ORF and biotin ligase (BirA) from *Escherichia coli*. BirA is a 35-kD DNA-binding biotin protein ligase that biotinylates proteins that are in a proximity of 10 nm or less to the target protein (195). Cells will be lysed, and σNS-interacting partners will be precipitated with streptavidin followed by identification using mass spectrometry. We will conduct similar experiments

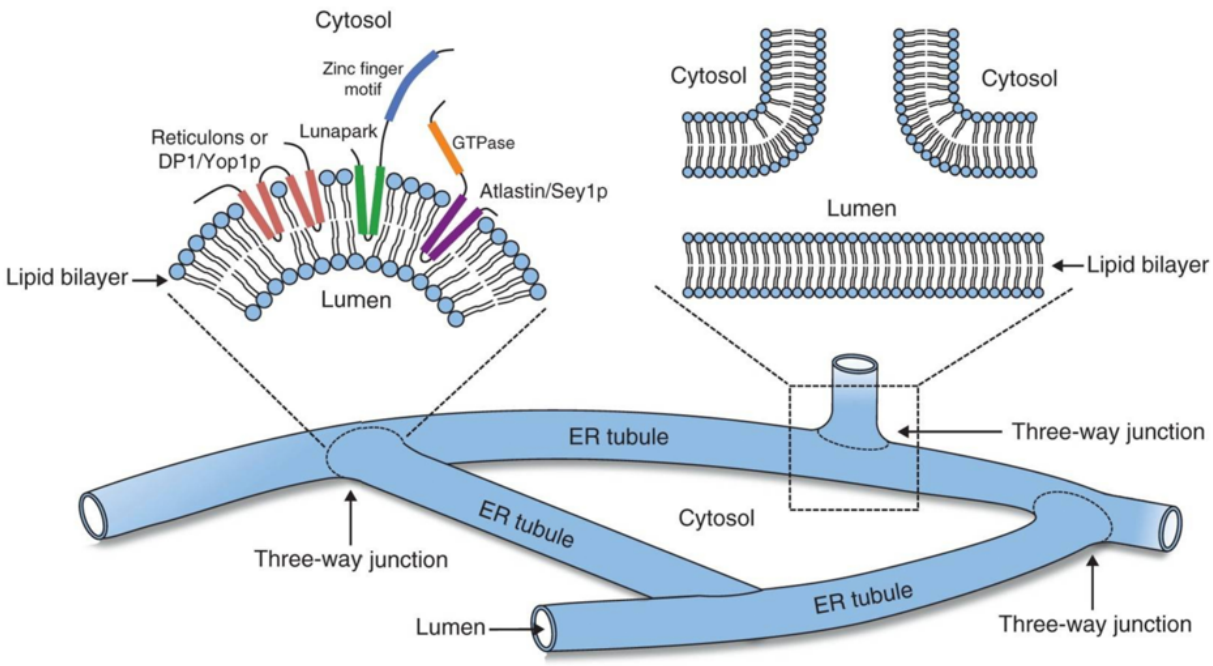

Figure V-4. ER-shaping proteins in tubules. The shape of the ER is maintained by several proteins, including reticulons, atlastins, and lunapark. Reticulons are a family of proteins that stabilize the high-curvature of tubules by forming wedges in the cytoplasmic leaflet of the lipid bilayer and oligomerizing into arc-like scaffolds around the tubules (196). Atlastins are GTPases of the dynamin family that mediate homotypic fusion of ER membranes (180). They fuse opposing ER membranes using GTP hydrolysis. Lunapark is component of a ubiquitin ligase complex that localizes and stabilizes three-way junctions (193). Other proteins involved in maintaining ER morphology are Climp-63, kinectin, p180, protrudin, Rab10, and Rab18 (194). These proteins interact to modulate ER-shape. (Figure adapted from Chen *et. al*., 2013 (192)).

in the presence of co-transfected μNS to nucleate inclusion-like structures (88). This technique has been used to identify HIV-1 Gag-interacting partners, among others (197).

Once σNS-interacting protein candidates are identified, we will validate them in several assays using infected cells, including colocalization by confocal microscopy, co-immunoprecipitation, and proximity-ligation assays. Results from these studies will provide information about the function of σNS in reovirus inclusion formation.

Collectively, these new approaches, based on the foundation provided by my thesis research, will begin to link σNS biochemical properties with known function in viral replication.

Conclusions

Viruses encode nonstructural proteins that aid in post-entry replication steps. *Reoviridae* viruses replicate their genomes within viral inclusions using a mechanism that is not understood. Viruses from this family divide their genomes in multiple segments, which must be assorted prior to genome replication. My thesis work defines σNS as a protein necessary for reovirus replication that functions at a step leading to genome replication. I provide evidence that σNS is required for viral transcript stability. Our studies establish a foundation for future work to determine mechanisms by which σNS interacts with viral transcripts to promote genome replication in the context of infection. This work sets the stage to better understand reovirus RNA assortment and packaging.

CHAPTER VI

MATERIALS AND METHODS

Cells and viruses

HEK293T cells engineered to express an siRNA against the σNS-encoding S3 gene of reovirus strain T3D (119) were single-cell sorted at the Vanderbilt University Medical Center Flow Cytometry Shared Resource. Single-cell sorting was conducted by resuspending ~2.5 x 10^6 cells in PBS supplemented to contain 2% fetal bovine serum (FBS) (Gibco) in a volume of 500 µl. Propidium iodide (Sigma) was added at a concentration of 1 µg/ml, and single cells were sorted into wells of a 96-well plate and maintained in 100 µl of Dulbecco's Modified Eagle Medium (DMEM) (Life Technologies) supplemented to contain 5% FBS, 2 mM L-glutamine (Life Technologies), 100 U/ml of penicillin, 100 µg/ml of streptomycin (Life Technologies), 0.25 mg/ml of amphotericin B (Sigma), and 5 µg/ml of puromycin (Sigma). Cell clones were propagated for approximately two weeks, after which time, cells were divided into two plates: one was maintained in supplemented DMEM, and the other was infected with reovirus T3D for 18 h. Infection was scored by fluorescent focus assay using guinea pig σNS polyclonal antiserum (141) as described (198). Clones with high knockdown efficiency were selected and passaged. HEK293T cells (ATCC CRL-3216), HEK293T cells expressing an S3-specific siRNA (σNS-siRNA cells), HEK293T cells expressing a GFP-specific siRNA (GFP-siRNA cells) (119), HeLa CCL2 cells, and BHK cells were maintained in DMEM supplemented to contain 5% FBS, 2 mM L-glutamine, 100 U/ml of penicillin, 100

μg/ml of streptomycin, 0.25 mg/ml of amphotericin B, and 5 μg/ml of puromycin (for σNS-siRNA and GFP-siRNA cells). Spinner-adapted murine L929 fibroblast cells were maintained in Joklik's modified Eagle's minimal essential medium (JMEM) (Lonza) as described (62). HBMECs were provided by Kwang Sik Kim (199) (Johns Hopkins University) and cultured in RPMI 1640 medium (Gibco) as described.

Reoviruses were recovered using plasmid-based reverse genetics (49, 87) and purified as described (46, 200). For generation of T3D-R virus, plasmid pT7-S3T3D (Addgene #33284) was altered by QuikChange (Stratagene) site-directed mutagenesis to contain synonymous mutations C632T, A635C, A642G, and, A649G using T3D_R_QC primers (Table VI-1). Primers T3D_2_QC were used to engineer the virus contain mutations A635C and A642G. To confirm mutations, viral RNA was extracted from purified virions and subjected to OneStep RT-PCR (Qiagen) using T3D_S3 primers (Table VI-1). Purified PCR products were analyzed by Sanger sequencing. Viral titers were determined by plaque assay using L929 cells (201).

Plasmid cloning, DNA transfections, and lentivirus generation

Plasmids for *in vitro* translation of the T3D s4 mRNA were engineered by introducing an EagI restriction site at the 3'-end of the S4 cDNA in pT7-S4T3D (Addgene #33285) using QuikChange site-directed mutagenesis and primers T3D_S4_EagI (Table VI-1). Plasmids for coupled *in vitro* transcription and translation of strain T1L σNS were generated by subcloning the ORF of the T1L S3 cDNA into pcDNA3.1+ using PCR amplification and primers T1L_S3_RS (Table VI-1). T1L S3 Δ38

Table VI-1. List of PCR primers.

Name	F Primer (5' → 3')	R primer (5' → 3')
T3D_R_QC	AGATATCCATGCATGCCAATCCCTTGAGG CCATCGTCCAGAAGCTGTTCCG	CGGAACAGCTTCTGGACGATGGCCTCAAG GGATTGGCATGCATGGATATCT
T3D_T7S4	GCGGGTTAATACGACTCACTATAGCTATT	GATGAATGAAGCCTGTCCCACGT
T3D_S3	CCTGATGCGCCAATGTCTAA	CTGTCTCCTCGCAATACAACTC
T3D_S4	GAAGCATTTGCCTCACCATAG	GATCTGTCCAACTTGAGTGTATTG
human_GADPH	CCCATCACCATCTTCCAG	ATGACCTTGCCCACAGCC
T3D_S4_EagI	AGATGCCATGCCGACGGCCGATGAATGAA GCC	GGCTTCATTCATCGGCCGTCGGCATGGCA TCT
T1L_S3_RS	CGACGGATCCATGGCTTCCTCACTCAGGG C	ATCACAGGCGGCCGCTTACACGCGAATTG GAAACACCAGC
T1L_S3del38	AACGTTGTTGAGTATCAAATCCGTACAGG	CATGGATCCGAGCTCGGTACCAA
T3D_S3_GA	TTGGTACCGAGCTCGGATCCATGGCTTCC TCACTCAGAG	TCTAGACTCGAGCGGCCGCCTTACACGCG AATCGGAAAAAC
pcDNA3.1_GA	GGCGGCCGCTCGAGTCTA	GGATCCGAGCTCGGTACC
T3D_S3del38_GA	CATGGATCCGAGCTCGGTACC	TTGGTACCGAGCTCGGATCCATGAATGTG GTTGAGTATCAAATTCG
T3D_S4_qPCR	CGCTTTTGAAGGTCGTGTATCA	CTGGCTGTGCTGAGATTGTTTT

plasmid was engineered by PCR amplification of the S3 cDNA from pcDNA3.1+ T1L S3 plasmid using primers T1L_S3del38. Plasmids for coupled *in vitro* transcription and translation and transient expression of strain T3D WT and Δ38 σNS were generated by subcloning the full-length ORF and Δ38 ORF of the T3D S3 cDNA into pcDNA3.1+ by Gibson assembly (New England Biolabs) using primers T3D_S3_GA, pcDNA3.1_GA, and T3D_S3del38_GA (Table VI-1). Plasmids for bacterial expression of WT and Δ38 σNS were engineered by Epoch Life Science, Inc. T7-FLuc plasmid encoding firefly luciferase was purchased from New England Biolabs, and SV40-RLuc plasmid encoding renilla luciferase, pVSVG, pCMV Lenti 8.92 Gag/Pol, and pBABE-puro-σNS were provided by Bernardo Mainou (Emory University). mCherry-KDEL was purchased from Addgene (Addgene # 55041).

Plasmids for transient protein expression were transfected using FuGene 6 transfection reagent (Promega) according to the manufacturer's instructions. Plasmids for recovering viruses using reverse genetics were transfected using TransIT-LT1 transfection reagent (Mirus) as described (46, 200).

HEK293T cells were co-transfected with pVSVG, pCMV Lenti 8.92 Gag/Pol, and pBABE-puro-σNS using FuGene 6. The culture medium was replaced 24 h post-transfection and cells were incubated at 37°C for 48 h. Medium containing packaged lentiviral particles was clarified by centrifugation and stored at -80°C. BHK cells were transduced using 2 ml of lentivirus-containing cell culture medium combined with 2 µl of polybrene (Millipore). After incubation overnight, the culture medium was supplemented to contain 1 µg/ml puromycin. Expression of σNS was confirmed by immunoblotting.

Preparation of rabbit λ3-specific polyclonal antiserum

T3D λ3 was expressed in Sf21 cells using a recombinant baculovirus (16)at the Baculovirus/Monoclonal Antibody Advanced Technology Core Laboratory at Baylor College of Medicine and purified as described (16). A rabbit was immunized with 100 μg of λ3 protein in complete Freund's adjuvant at Cocalico Biologicals. Antigen boosts containing 50 μg of λ3 protein in incomplete Freund's adjuvant were administered at days 14, 21, 49, and 134 following the initial inoculation. Antigen boosts containing 100 μg of λ3 protein in incomplete Freund's adjuvant were administered at days 120, 183, and 211 following the initial inoculation. Serum samples were obtained at days 35, 56, 148, and 197 following the initial inoculation and tested for reactivity against purified T3D virions by immunoblotting. Final exsanguination was conducted 225 days after the initial inoculation.

Immunoprecipitations

Samples for immunoprecipitation were obtained by lysing cells in lysis buffer containing 20 mM Tris-HCl pH 8, 137 mM NaCl, 1% Nonidet-P40, 2 mM EDTA, and protease inhibitor (Sigma). Samples were precleared to remove nonspecific interactions by incubating with 1 μg of isotype control (mouse IgG2a, Invitrogen) at 4ºC for 1 h, followed by incubation with Protein G Dynabeads (ThermoFisher) for 30 min and immunoprecipitation. To immunoprecipitate σNS and its interacting partners, 2 μg of mouse 3E10 σNS monoclonal antibody (110) were added to precleared lysates and incubated at 4ºC for 16 h. Protein G Dynabeads were added 4ºC for 4 h, followed by

immunoprecipitation. Samples were washed 5 times in TBS including 0.05% of NP-40 with protease inhibitor, resuspended in 5X SDS-PAGE sample buffer, incubated at 95°C for 10 min, and eluted proteins were collected and stored at -20°C.

Native-PAGE, SDS-PAGE, immunoblotting, and phosphorimaging

Samples for native PAGE were diluted in 4X Native-PAGE Sample Buffer (ThermoFisher) and resolved in 4-16% Native-PAGE Bis-Tris acrylamide gels (ThermoFisher) using the Blue Native-PAGE Novex Bis-Tris Gel System (ThermoFisher) as described (92).

Samples for denaturating SDS-PAGE were diluted in 5X SDS-PAGE sample buffer, incubated at 95°C for 5 min, and resolved in 10% Mini-Protean TGX gels (BioRad).

Native-PAGE and SDS-PAGE gels were transferred to PVDF and nitrocellulose membranes, respectively (92). The following antibodies were used for immunoblotting: guinea pig σNS polyclonal antiserum (141), chicken μNS polyclonal antiserum (122), mouse 8H6 μ1/μ1δ monoclonal antibody (202), mouse 3E10 σNS monoclonal antibody (110), rabbit λ3 polyclonal antiserum, and mouse α-tubulin monoclonal antibody (Cell Signaling Technology). The following antibodies were used as detection reagents: IRDye®800CW donkey anti-guinea pig, IRDye®680RD donkey anti-chicken, IRDye®800CW goat anti-rabbit, and IRDye®680LT goat anti-mouse (LI-COR).

Membranes were scanned using an Odyssey CLx imaging system (LI-COR). Pixel intensity of bands for all gels and membranes was quantified using Image Studio Software (LI-COR).

Native-PAGE and SDS-PAGE gels containing radiolabeled products were incubated in 40% methanol, 10% acetic acid at room temperature (RT) for 1 h, washed, and dried. Dried gels were exposed on a phosphorimaging screen and imaged using a Perkin Elmer Cyclone Phosphor System Scanner.

Purification of recombinant σNS protein

BL21(DE3)pLysS *Escherichia coli* (Promega) cultures were transformed with T3D WT or Δ38 σNS-encoding plasmids and induced with 0.5 mM isopropyl β-D-1-thiogalactopyranoside (IPTG) (Sigma) after reaching an optical density (600 nm) of 0.6–0.7. Cells were resuspended in 50 mM Tris-HCl (pH 8), 500 mM NaCl, 10 mM imidazole, and 1 mM DTT, and supplemented with protease inhibitor cocktail (Roche). Cells were lysed using a microfludizer, followed by removal of cell debris by centrifugation. Clarified cell lysates were loaded onto Ni-NTA columns (Qiagen), and σNS was eluted using a gradient of 50 mM Tris-HCl (pH 8), 0.5 M NaCl, 0.5 M imidazole, and 1 mM DTT. Elution fractions were dialyzed against 20 mM Tris-HCl (pH 8), 100 mM NaCl, 10 mM imidazole, 1 mM EDTA, and 1 mM DTT. Eluted protein was incubated with thrombin (1 U per 100 g of recombinant protein) at 4ºC for 12 h to remove the His-tag. Protein samples were re-loaded onto a Ni-NTA column to remove uncleaved His-tagged σNS. The flow-though was loaded onto a Superose 6 10/300 GL column (GE Healthcare) in 10 mM Tris-HCl (pH 7.4), 100 mM NaCl, and 1 mM DTT. Eluted fractions were concentrated using a 30 kDa centrifugal filter unit (Millipore).

Immunofluorescence microscopy

Transfected or infected cells (MOI 100 PFU/cell) were fixed in 4% paraformaldehyde (PFA) (Electron Microscopy Sciences) in PBS at RT for 20 min, permeabilized with 1% Triton X-100 in PBS at RT for 5 min, blocked with 0.5% BSA, 0.1% glycine, and 0.05% Tween 20, and stained with chicken μNS polyclonal antiserum, guinea pig σNS polyclonal antiserum, PDI-specific antibody DL-11 (Sigma), giantin-specific antibody ab24586 (Abcam), or WGA conjugated with Alexa Fluor555 (Invitrogen), Alexa-Fluor secondary antibodies (Invitrogen), and 4',6-diamidino-2-phenylindole (DAPI) (Invitrogen) to visualize nuclei. Images were captured using a Zeiss LSM 710 laser scanning confocal microscope and analyzed using Zeiss LSM5 Series Image Browser.

Transmission electron microscopy and image reconstructions

In the Risco laboratory, HeLa cells were adsorbed at an MOI of 20 PFU/cell. Following incubation at 37°C for 12 h, cells were fixed at RT for 1 h with a mixture of 4% paraformaldehyde and 1% glutaraldehyde in PBS (pH 7.4), post-fixed with 1% osmium tetroxide, dehydrated in increasing concentrations of acetone, and processed for embedding in epoxy resin EML-812 (TAAB Laboratories) as previously described (203, 204). Ultrathin (~60 to 70 nm) sections were collected on uncoated 300-mesh copper grids (TAAB Laboratories), stained with uranyl acetate and lead citrate, and imaged by TEM. Images were acquired with a JEOL JEM 1011 electron microscope operating at 100 kV. To generate 3D models, Images were aligned by selected tracers between two

consecutive sections with the free editor for serial section microscopy Reconstruct (205). Segmentation and 3D visualization were performed with Amira.

RNA extraction and purification

To purify cellular RNA, cells were lysed using TRIzol reagent (ThermoFisher), and RNA was extracted with chloroform. To purify RNA from *in vitro* transcription reactions, samples were combined with an equal volume of lysis buffer (ThermoFisher) supplemented to contain 1% β-mercaptoethanol (BME).

An equal volume of 70% ethanol was added, and RNA was purified using a PureLink RNA Mini Kit (ThermoFisher) according to the manufacturer's instructions.

S4 quantitative reverse transcription (RT)-PCR

Total and single-strand negative-sense s4 RNA was quantified using qScript XLT One-Step RT-qPCR ToughMix, Low ROX (Quanta Bioscience), and primers T3D_S4_qPCR (Table VI-1) according to the manufacturer's instructions. The following RT-qPCR cycling protocol was used: cDNA synthesis (50°C for 10 min), initial denaturation (95°C for 1 min), and 40 PCR cycles (95°C for 10 s followed by a data collection step at 60°C for 1 min). S4 cDNA was detected using a fluorogenic probe (5′-dFAM-AGCGCGCAAGAGGGATGGGA-BHQ-1-3′, Biosearch Technologies). For the single-strand RT-qPCR, the following modifications were included: RNA was incubated at 95°C for 3 min and immediately placed on ice. Reverse transcription was conducted

using only the forward primer T3D_S4_qPCR, and for the quantitative PCR step, the reverse T3D_S4_qPCR primer was included (143).

NanoString RNA quantification and analysis

Probes specific for each reovirus gene segment positive-sense RNA were designed by NanoString Technologies using proprietary software (Table III-1) (144). RNA was purified from infected cells and incubated with probes in hybridization buffer according to the manufacturer's instructions. Following hybridization, excess probe was removed using a nCounter Prep Station automated liquid handler. Probe-target complexes were transferred to an nCounter cartridge for immobilization and loaded onto an nCounter Digital Analyzer for imaging and quantification of each target RNA. Quantified expression data were analyzed using nSolver analysis software, including image quality controls and background subtraction (206). Counts for each probe were normalized using the geometric mean of four cellular transcripts (GUSB, HPRT, SARM1, and RSP6).

In vitro transcription reactions

Templates for *in vitro* transcription of the T3D S4 gene segment were generated from pT7-S4T3D by PCR amplification using primers T3D_T7S4 (Table VI-1). Templates were transcribed *in vitro* using a HiScribe T7 High Yield RNA Synthesis Kit (New England Biolabs) according to the manufacturer's instructions with the following modifications. For synthesis of radiolabeled RNA, 125 ng of PCR product was used in

the presence of radiolabeled [α-32P]-UTP (PerkinElmer) in 20 µl reactions at RT for 2 h. For synthesis of non-radiolabeled RNA, 2 µg of plasmid DNA template was used in 40 µl reactions at 37°C for 2 h. DNA templates were degraded by on-column incubation with PureLink® DNase (ThermoFisher). For some experiments, RNA was capped using vaccinia capping enzyme (New England Biolabs) and 2'-O-methyltransferase (New England Biolabs) in one-step reactions according to the manufacturer's instructions.

Stem I of 7SK RNA (5'-GGAUGUGAGGGCGAUCUGGCUGCGACAUCUGUCA CCCCAUUGAUCGCCAGGGUUGAUUCGGCUGAUCUGGCUGGCUAGGCGGGUGU CCCCUUCCUCCCUCACCGCUCC-3') was synthesized using T7 RNA polymerase from PCR-generated DNA templates. The RNA was gel purified on a 7M urea/1X TBE/6% 29:1 polyacrylamide gel.

In vitro cell-free RNA degradation assay and electrophoresis

s4 RNA transcripts (<10 pM; 5 x 10^5 cpm) were incubated with various concentrations of σNS in a volume of 10 µl at RT for 10 min. σNS-RNA complexes were incubated with 26 µl of a 6 mg/ml stock of HeLa S100 cytoplasmic extracts (Speed Biosystems). At various intervals, RNA was purified from 8 µl aliquots of the treatment mixtures. RNA was diluted in 2X Novex TBE-urea sample buffer (ThermoFisher), resolved in 6% TBE-urea gels (ThermoFisher), exposed on a phosphorimaging screen, and visualized using a Perkin Elmer Cyclone Phosphor System Scanner.

RNA degradation assay in cells

HEK293T cells seeded in 12-well plates were transfected using FuGene 6 with 500 ng of plasmid encoding either WT or Δ38 σNS and incubated for 20 h. Cells were transfected a second time using FuGene 6 with 50 ng of pCAG_S4T3D plasmid (46) and incubated for 4 h. Cells were treated with 10 μg/ml of actinomycin D (Sigma) and lysed at various intervals prior to RNA extraction. Expression of s3, s4, and human GADPH RNA was confirmed by RT-PCR amplification using primers T3D_S3, T3D_S4, and human_GADPH.

In vitro translation reactions

RNAs were translated *in vitro* using wheat germ extracts (Promega) according to the manufacturer's instructions with the following modifications. RNAs at a concentration of 10 μg/ml were incubated at 65°C for 3 min, placed immediately on ice, and incubated with various concentrations of WT or Δ38 σNS at RT for 10 min. Protein-RNA complexes were incubated with wheat germ extracts supplemented with 80 μM of Amino Acid Mixture Minus Methionine (Promega) and 0.8 U/μl of RNasin (Promega). To synthesize nonradioactive and radioactive proteins, 80 μM of Amino Acid Mixture Minus Leucine (Promega) or 0.7 μCi/μl of [35S]-methionine (PerkinElmer) was added, respectively. Translation reactions were incubated at 25°C for 1 h, followed by freezing at -20°C.

Coupled *in vitro* transcription and translation reactions

Coupled *in vitro* transcription and translation reactions were conducted using the TNT coupled rabbit reticulocyte lysate system (Promega) according to the manufacturer's instructions. Reactions were incubated at 30°C for 1 h and terminated by four-fold dilution in stop buffer (20 mM HEPES-KOH (pH 7.4), 100 mM potassium acetate, 5 mM magnesium acetate, 5 mM EDTA, 2 mM methionine) supplemented to contain a final concentration of 1 mM DTT and 2 mM puromycin. Protein samples were incubated with RNase A (Qiagen) in variable treatment conditions depending on the experiment.

5'-labeling of RNA

RNAs were dephosphorylated using calf intestinal alkaline phosphatase (CIP) (New England Biolabs) according to the manufacturer's instructions with the following modifications. CIP was used at a concentration of 0.5 U per 1 µg of RNA in 20 µl reactions. Following incubation at 37°C for 30 min, RNA was precipitated using phenol/chloroform (s4 RNAs) or gel-purified (7SK stem I RNA) and labeled using T4 polynucleotide kinase (New England Biolabs) and [γ^{32}P]-ATP (PerkinElmer). RNAs were purified using a G25 desalting column (GE Healthcare).

Luciferase assays

To quantify RLuc activity in transfected cells, HEK293T cells seeded in 96-well plates were transfected with increasing amounts of WT or Δ38 σNS plasmids (0 to 150 ng), decreasing amounts of a non-coding plasmid (pT7-S2T3D, Addgene #33283) (150 to 0 ng), and 50 ng of SV40 renilla luciferase plasmid, achieving a final DNA amount of 200 ng/well and incubated for 24 h. Cells were lysed with 20 µl of Renilla Luciferase Lysis Buffer (Promega) at RT for 20 min, followed by addition of 50 µl of Renilla Luciferase Assay Reagent (Promega) to each well.

To quantify FLuc activity in *in vitro* translation reactions, 10 ng of luciferase RNA was incubated with various concentrations of either WT or Δ38 σNS at RT for 10 min, followed by incubation with wheat germ extracts at 25°C for 1 h. Two and a half µl aliquots from the translation reaction mixtures were added to 50 µl of Luciferase Assay Reagent (Promega) in 96-well plates.

For FLuc and RLuc reactions, luminescence was quantified immediately following addition of the respective luciferase assay reagent with a Synergy H1 BioTek plate reader.

Electrophoretic mobility shift assays (EMSA)

Snap-cooled 7SK stem I RNA (<10 pM; 500 cpm) was incubated with increasing concentrations of either WT or Δ38 σNS in 100 mM NaCl, 50 mM HEPES (pH 7.2), 10% glycerol, and 1 µg BSA at RT for 10 min as described (207, 208). Reactions were loaded into wells of 0.5% native TBE polyacrylamide gels and resolved at 120V at 4°C

for 45 min. Gels were dried, exposed to phosphorimaging screens, visualized using ImageQuant TL (GE), and graphed using KaleidaGraph (Synergy Software).

Filter binding assay

s4 RNA (<10 pM; 500 cpm) was incubated with increasing concentrations of WT σNS in 100 mM NaCl, 50 mM HEPES (pH 7.2), 10% glycerol, and 1 µg BSA at RT for 10 min. Pre-soaked nitrocellulose (top) and nylon (bottom) membranes (GE) were used in a 96-well hybrid dot manifold assembly as described (209). After filtration, membranes were air-dried, exposed to phosphorimaging screens, visualized using ImageQuant TL (GE), and graphed using KaleidaGraph (Synergy Software).

GTP hydrolysis assay

Purified recombinant WT σNS or NSP2 (2 µg per reaction) was incubated with 10 µCi [α ^{32}P]-GTP (PerkinElmer) in buffer containing 10 mM Tris-HCl (pH 7.4) and 1 mM DTT. $MgCl_2$ was supplemented at 0.5, or 5 µM, or was not included. Samples were incubated at 37°C for 0 or 60 min. At each time, 10 µl of the reaction mixture were combined with 5 µl of 1 N formic acid. PEI-cellulose (GE Healthcare) sheets were spotted with 1.5 µl of each sample. After drying, sheets were positioned in TLC developing chambers pre-equilibrated with 1.2 M LiCl. Samples were resolved using 1.2 M LiCl as mobile phase solvent until the solvent reached 1-1.5 cm from the top of the plate. Sheets were air-dried and exposed to phosphorimaging screens.

Electron microscopy of σNS-RNA complexes

s4 RNA was incubated with either WT or Δ38 σNS at a molar ratio of 50:1 on ice for 1 h before plunge-freezing using a Vitribot (MIV). The frozen specimens were imaged at 40,000X magnification with defocus levels ranging from −2.0 to −3.5 μm using a JEM2010 (200 KV) cryo-electron microscope equipped with a CCD camera at the CryoEM Center at Baylor College of Medicine.

Electron Tomography of Tokuyasu Cryosections

Semi-thick (~ 300nm) Tokuyasu cryosections of reovirus-infected cells were collected on copper grids with parallel bars. Four single axis tilt series were obtained automatically between −63° to +60° with an angular interval of 1.5°. Images were recorded on an Eagle 4k x 4k slow-scan charged coupled device (FEI) using FEI software and a Tecnai G2 microscope (FEI) operating at 200 kV. Images were aligned and tomograms reconstructed using the IMOD software package. The tomogram with best contrast was segmented and processed for 3D visualization with Amira. Tomograms were subjected to noise filtering and automated segmentation to visualize membranes.

Statistical methods

All experiments were conducted independently at least three times. Data are presented as the mean ± SD. All statistical analyses were conducted using GraphPad Prism 7.00 data analysis software.

REFERENCES

1. International Committee on Taxonomy of Viruses. 2011. ICTV 9th Report . dsRNA Viruses (2011). https://talk.ictvonline.org/ictvreports/ictv_9th_report/dsrna-viruses-2011/

2. Mertens P. 2004. The dsRNA viruses. Virus Res 101:3-13.

3. Clark A, Black R, Tate J, Roose A, Kotloff K, Lam D, Blackwelder W, Parashar U, Lanata C, Kang G, Troeger C, Platts-Mills J, Mokdad A, Global Rotavirus Surveillance N, Sanderson C, Lamberti L, Levine M, Santosham M, Steele D. 2017. Estimating global, regional and national rotavirus deaths in children aged <5 years: Current approaches, new analyses and proposed improvements. PLoS One 12:e0183392.

4. Samy AM, Peterson AT. 2016. Climate change influences on the global potential distribution of Bluetongue Virus. PLoS One 11:e0150489.

5. Wu J, Ni Y, Liu H, Rao L, Zhou Y, Zhou X. 2013. Development and use of three monoclonal antibodies for the detection of rice black-streaked dwarf virus in field plants and planthopper vectors. Virol J 10:114.

6. McDonald SM, Patton JT. 2009. Core-associated genome replication mechanisms of dsRNA viruses, p 201-224. *In* Cameron CE, Gotte M, Raney K (ed), Viral Genome Replication doi:DOI:10.1007/b135974. Springer, Boston, MA.

7. Ahlquist P. 2006. Parallels among positive-strand RNA viruses, reverse-transcribing viruses and double-stranded RNA viruses. Nat Rev Microbiol 4:371-82.

8. McDonald SM, Tao YJ, Patton JT. 2009. The ins and outs of four-tunneled Reoviridae RNA-dependent RNA polymerases. Curr Opin Struct Biol 19:775-82.

9. Icho T, Wickner RB. 1989. The double-stranded RNA genome of yeast virus L-A encodes its own putative RNA polymerase by fusing two open reading frames. J Biol Chem 264:6716-23.

10. Sen A, Heymann JB, Cheng N, Qiao J, Mindich L, Steven AC. 2008. Initial location of the RNA-dependent RNA polymerase in the bacteriophage Phi6 procapsid determined by cryo-electron microscopy. J Biol Chem 283:12227-31.

11. Zhang X, Walker SB, Chipman PR, Nibert ML, Baker TS. 2003. Reovirus polymerase lambda 3 localized by cryo-electron microscopy of virions at a resolution of 7.6 A. Nat Struct Biol 10:1011-8.

12. Butcher SJ, Grimes JM, Makeyev EV, Bamford DH, Stuart DI. 2001. A mechanism for initiating RNA-dependent RNA polymerization. Nature 410:235-40.

13. Pan J, Vakharia VN, Tao YJ. 2007. The structure of a birnavirus polymerase reveals a distinct active site topology. Proc Natl Acad Sci U S A 104:7385-90.

14. Collier AM, Lyytinen OL, Guo YR, Toh Y, Poranen MM, Tao YJ. 2016. Initiation of RNA polymerization and Polymerase encapsidation by a small dsRNA virus. PLoS Pathog 12:e1005523.

15. Lu X, McDonald SM, Tortorici MA, Tao YJ, Vasquez-Del Carpio R, Nibert ML, Patton JT, Harrison SC. 2008. Mechanism for coordinated RNA packaging and genome replication by rotavirus polymerase VP1. Structure 16:1678-88.

16. Tao Y, Farsetta DL, Nibert ML, Harrison SC. 2002. RNA synthesis in a cage--structural studies of reovirus polymerase lambda3. Cell 111:733-45.

17. Venkataraman S, Prasad B, Selvarajan R. 2018. RNA dependent RNA polymerases: Insights from structure, function and evolution. Viruses 10:e76.

18. Gantier MP, Williams BR. 2007. The response of mammalian cells to double-stranded RNA. Cytokine Growth Factor Rev 18:363-71.

19. McDonald SM, Patton JT. 2011. Assortment and packaging of the segmented rotavirus genome. Trends Microbiol 19:136-44.

20. Qiao X, Qiao J, Mindich L. 2003. Analysis of specific binding involved in genomic packaging of the double-stranded-RNA bacteriophage phi6. J Bacteriol 185:6409-14.

21. Roner MR, Bassett K, Roehr J. 2004. Identification of the 5 ' sequences required for incorporation of an engineered ssRNA into the Reovirus genome. Virology 329:348-360.

22. Roner MR, Roehr J. 2006. The 3' sequences required for incorporation of an engineered ssRNA into the Reovirus genome. Virol J 3:1.

23. Roner MR, Steele BG. 2007. Localizing the reovirus packaging signals using an engineered m1 and s2 ssRNA. Virology 358:89-97.

24. Dermody TS, Parker JS, Sherry B. 2013. Orthoreoviruses, p 1304-1346. *In* Knipe DM, Howley PM (ed), Fields Virology, Sixth ed, vol 2. Lippincott Williams & Wilkins, Philadelphia.

25. Patton JT, Spencer E. 2000. Genome replication and packaging of segmented double-stranded RNA viruses. Virology 277:217-25.

26. McDonald SM, Nelson MI, Turner PE, Patton JT. 2016. Reassortment in segmented RNA viruses: Mechanisms and outcomes. Nat Rev Microbiol 14:448-60.

27. van Dijk AA, Makeyev EV, Bamford DH. 2004. Initiation of viral RNA-dependent RNA polymerization. J Gen Virol 85:1077-93.

28. Kao CC, Singh P, Ecker DJ. 2001. De novo initiation of viral RNA-dependent RNA synthesis. Virology 287:251-60.

29. Laurila MR, Salgado PS, Stuart DI, Grimes JM, Bamford DH. 2005. Back-priming mode of phi6 RNA-dependent RNA polymerase. J Gen Virol 86:521-6.

30. Beachboard DC, Horner SM. 2016. Innate immune evasion strategies of DNA and RNA viruses. Curr Opin Microbiol 32:113-119.

31. Schneider WM, Chevillotte MD, Rice CM. 2014. Interferon-stimulated genes: A complex web of host defenses. Annu Rev Immunol 32:513-45.

32. Dauber B, Wolff T. 2009. Activation of the antiviral kinase PKR and viral countermeasures. Viruses 1:523-44.

33. Zurney J, Kobayashi T, Holm GH, Dermody TS, Sherry B. 2009. Reovirus mu2 protein inhibits interferon signaling through a novel mechanism involving nuclear accumulation of interferon regulatory factor 9. J Virol 83:2178-87.

34. Yue Z, Shatkin AJ. 1997. Double-stranded RNA-dependent protein kinase (PKR) is regulated by reovirus structural proteins. Virology 234:364-371.

35. Arnold MM, Patton JT. 2011. Diversity of interferon antagonist activities mediated by NSP1 proteins of different rotavirus strains. J Virol 85:1970-9.

36. Holloway G, Dang VT, Jans DA, Coulson BS. 2014. Rotavirus inhibits IFN-induced STAT nuclear translocation by a mechanism that acts after STAT binding to importin-alpha. J Gen Virol 95:1723-33.

37. den Boon JA, Ahlquist P. 2010. Organelle-like membrane compartmentalization of positive-strand RNA virus replication factories. Annu Rev Microbiol 64:241-56.

38. Mendez F, Romero N, Cubas LL, Delgui LR, Rodriguez D, Rodriguez JF. 2017. Non-lytic egression of infectious bursal disease virus (IBDV) particles from infected cells. PLoS One 12:e0170080.

39. Fernandez de Castro I, Zamora PF, Ooms L, Fernandez JJ, Lai CM, Mainou BA, Dermody TS, Risco C. 2014. Reovirus forms neo-organelles for progeny particle assembly within reorganized cell membranes. MBio 18:e00931-13.

40. Criglar JM, Hu L, Crawford SE, Hyser JM, Broughman JR, Prasad BV, Estes MK. 2014. A novel form of rotavirus NSP2 and phosphorylation-dependent NSP2-NSP5 interactions are associated with viroplasm assembly. J Virol 88:786-98.

41. Roy P, Noad R. 2006. Bluetongue virus assembly and morphogenesis. Curr Top Microbiol Immunol 309:87-116.

42. Borodavka A, Dykeman EC, Schrimpf W, Lamb DC. 2017. Protein-mediated RNA folding governs sequence-specific interactions between rotavirus genome segments. Elife 6:e27453.

43. Fajardo T, Sung PY, Celma CC, Roy P. 2017. Rotavirus genomic RNA complex forms via specific RNA-RNA interactions: Disruption of RNA complex inhibits virus infectivity. Viruses 9:e167.

44. Sung PY, Roy P. 2014. Sequential packaging of RNA genomic segments during the assembly of Bluetongue virus. Nucleic Acids Res 42:13824-38.

45. Fajardo T, Jr., Sung PY, Roy P. 2015. Disruption of specific RNA-RNA interactions in a double-stranded RNA virus inhibits genome packaging and virus infectivity. PLoS Pathog 11:e1005321.

46. Kobayashi T, Antar AA, Boehme KW, Danthi P, Eby EA, Guglielmi KM, Holm GH, Johnson EM, Maginnis MS, Naik S, Skelton WB, Wetzel JD, Wilson GJ, Chappell JD, Dermody TS. 2007. A plasmid-based reverse genetics system for animal double-stranded RNA viruses. Cell Host Microbe 1:147-57.

47. Demidenko AA, Blattman JN, Blattman NN, Greenberg PD, Nibert ML. 2013. Engineering recombinant reoviruses with tandem repeats and a tetravirus 2A-like element for exogenous polypeptide expression. Proc Natl Acad Sci U S A 110:e1867-76.

48. Tuplin A. 2015. Diverse roles and interactions of RNA structures during the replication of positive-stranded RNA viruses of humans and animals. J Gen Virol 96:1497-503.

49. Gamarnik AV, Andino R. 1998. Switch from translation to RNA replication in a positive-stranded RNA virus. Genes Dev 12:2293-304.

50. King AMQ, Lefkowitz EJ, Mushegian AR, Adams MJ, Dutilh BE, Gorbalenya AE, Harrach B, Harrison RL, Junglen S, Knowles NJ, Kropinski AM, Krupovic M, Kuhn JH, Nibert ML, Rubino L, Sabanadzovic S, Sanfacon H, Siddell SG,

Simmonds P, Varsani A, Zerbini FM, Davison AJ. 2018. Changes to taxonomy and the International Code of Virus Classification and Nomenclature ratified by the International Committee on Taxonomy of Viruses (2018). Arch Virol doi:10.1007/s00705-018-3847-1.

51. Chappell JD, Dermody TS. 2011. Reoviruses, p 225-236. *In* Acheson NH (ed), Fundamentals of Molecular Virology, Second ed. Wiley & Sons, New York.

52. Bouziat R, Hinterleitner R, Brown JJ, Stencel-Baerenwald JE, Ikizler M, Mayassi T, Meisel M, Kim SM, Discepolo V, Pruijssers AJ, Ernest JD, Iskarpatyoti JA, Costes LM, Lawrence I, Palanski BA, Varma M, Zurenski MA, Khomandiak S, McAllister N, Aravamudhan P, Boehme KW, Hu F, Samsom JN, Reinecker HC, Kupfer SS, Guandalini S, Semrad CE, Abadie V, Khosla C, Barreiro LB, Xavier RJ, Ng A, Dermody TS, Jabri B. 2017. Reovirus infection triggers inflammatory responses to dietary antigens and development of celiac disease. Science 356:44-50.

53. Brown JJ, Short SP, Stencel-Baerenwald J, Urbanek K, Pruijssers AJ, McAllister N, Ikizler M, Taylor G, Aravamudhan P, Khomandiak S, Jabri B, Williams CS, Dermody TS. 2018. Reovirus-induced apoptosis in the intestine limits establishment of enteric infection. J Virol 92:e02062-17.

54. Chakrabarty R, Tran H, Selvaggi G, Hagerman A, Thompson B, Coffey M. 2015. The oncolytic virus, pelareorep, as a novel anticancer agent: A review. Invest New Drugs 33:761-74.

55. Nason EL, Wetzel JD, Mukherjee SK, Barton ES, Prasad BVV, Dermody TS. 2001. A monoclonal antibody specific for reovirus outer-capsid protein σ3 inhibits σ1-mediated hemagglutination by steric hindrance. Journal of Virology 75:6625-6634.

56. Dietrich MH, Ogden KM, Long JM, Ebenhoch R, Thor A, Dermody TS, Stehle T. 2018. Structural and functional features of the reovirus sigma1 tail. J Virol doi:10.1128/JVI.00336-18.

57. Barton ES, Forrest JC, Connolly JL, Chappell JD, Liu Y, Schnell FJ, Nusrat A, Parkos CA, Dermody TS. 2001. Junction adhesion molecule is a receptor for reovirus. Cell 104:441-451.

58. Campbell JA, Schelling P, Wetzel JD, Johnson EM, Forrest JC, Wilson GAR, Aurrand-Lions M, Imhof BA, Stehle T, Dermody TS. 2005. Junctional adhesion molecule a serves as a receptor for prototype and field-isolate strains of mammalian reovirus. J Virol 79:7967-7978.

59. Forrest JC, Campbell JA, Schelling P, Stehle T, Dermody TS. 2003. Structure-function analysis of reovirus binding to junctional adhesion molecule 1.

Implications for the mechanism of reovirus attachment. J Biol Chem 278:48434-44.

60. Konopka-Anstadt JL, Mainou BA, Sutherland DM, Sekine Y, Strittmatter SM, Dermody TS. 2014. The Nogo receptor NgR1 mediates infection by mammalian reovirus. Cell Host Microbe 15:681-91.

61. Sutherland DM, Aravamudhan P, Dermody TS. 2018. An orchestra of reovirus receptors: Still searching for the conductor. Adv Virus Res 100:223-246.

62. Barton ES, Connolly JL, Forrest JC, Chappell JD, Dermody TS. 2001. Utilization of sialic acid as a coreceptor enhances reovirus attachment by multistep adhesion strengthening. J Biol Chem 276:2200-2211.

63. Reiss K, Stencel JE, Liu Y, Blaum BS, Reiter DM, Feizi T, Dermody TS, Stehle T. 2012. The GM2 glycan serves as a functional co-receptor for serotype 1 reovirus. PLoS Pathog 8:e1003078.

64. Schulz WL, Haj AK, Schiff LA. 2012. Reovirus uses multiple endocytic pathways for cell entry. J Virol 86:12665-75.

65. Maginnis MS, Forrest JC, Kopecky-Bromberg SA, Dickeson SK, Santoro SA, Zutter MM, Nemerow GR, Bergelson JM, Dermody TS. 2006. β1 integrin mediates internalization of mammalian reovirus. J Virol 80:2760-2770.

66. Mainou BA, Dermody TS. 2012. Transport to late endosomes is required for efficient reovirus infection. J Virol 86:8346-58.

67. Mainou BA, Zamora PF, Ashbrook AW, Dorset DC, Kim KS, Dermody TS. 2013. Reovirus cell entry requires functional microtubules. MBio 4:e00405-13.

68. Baer GS, Dermody TS. 1997. Mutations in reovirus outer-capsid protein σ3 selected during persistent infections of L cells confer resistance to protease inhibitor E64. J Virol 71:4921-4928.

69. Sturzenbecker LJ, Nibert ML, Furlong DB, Fields BN. 1987. Intracellular digestion of reovirus particles requires a low pH and is an essential step in the viral infectious cycle. J Virol61:2351-2361.

70. Ebert DH, Deussing J, Peters C, Dermody TS. 2002. Cathepsin L and cathepsin B mediate reovirus disassembly in murine fibroblast cells. J Biol Chem 277:24609-17.

71. Chandran K, and Max L. Nibert. In Vitro Membrane Permeabilization by Mammalian Reovirus ISVPs is Accompanied by Dramatic Changes in Particle Structure and Enzymatic Activities, p. *In* (ed),

72. Chandran K, Farsetta DL, Nibert ML. 2002. Strategy for nonenveloped virus entry: a hydrophobic conformer of the reovirus membrane penetration protein micro 1 mediates membrane disruption. J Virol 76:9920-33.

73. Chandran K, Parker JS, Ehrlich M, Kirchhausen T, Nibert ML. 2003. The delta region of outer-capsid protein micro 1 undergoes conformational change and release from reovirus particles during cell entry. J Virol 77:13361-75.

74. Gillies S, Bullivant S, Bellamy AR. 1971. Viral RNA polymerases: electron microscopy of reovirus reaction cores. Science 174:694-6.

75. Bartlett NM, Gillies SC, Bullivant S, Bellamy AR. 1974. Electron microscope study of reovirus reaction cores. J Virol 14:315-326.

76. Furuichi Y, Muthukrishnan S, Shatkin AJ. 1975. 5´-Terminal $M^7G(5´)ppp(5´)G^mp$ in vivo: identification in reovirus genome RNA. Proc Natl Acad Sci U S A 72:742-745.

77. Furuichi Y, Morgan M, Muthukrishnan S, Shatkin AJ. 1975. Reovirus messenger RNA contains a methylated, blocked 5'-terminal structure: m-7G(5')ppp(5')G-MpCp. Proc Natl Acad Sci U S A 72:362-366.

78. Skup D, Millward S. 1980. mRNA capping enzymes are masked in reovirus progeny subviral particles. J Virol 34:490-6.

79. Lai CM, Mainou BA, Kim KS, Dermody TS. 2013. Directional release of reovirus from the apical surface of polarized endothelial cells. MBio 4:e00049-13.

80. Excoffon KJDA, Guglielmi KM, Wetzel JD, Gansemer ND, Campbell JA, Dermody TS, Zabner J. 2008. Reovirus preferentially infects the basolateral surface and is released from the apical surface of polarized human respiratory epithelial cells. Journal of Infectious Diseases 197:1189-1197.

81. de Castro IF, Volonte L, Risco C. 2013. Virus factories: biogenesis and structural design. Cell Microbiol 15:24-34.

82. Shah PNM, Stanifer ML, Hohn K, Engel U, Haselmann U, Bartenschlager R, Krausslich HG, Krijnse-Locker J, Boulant S. 2017. Genome packaging of reovirus is mediated by the scaffolding property of the microtubule network. Cell Microbiol 19.

83. Parker JS, Broering TJ, Kim J, Higgins DE, Nibert ML. 2002. Reovirus core protein mu2 determines the filamentous morphology of viral inclusion bodies by interacting with and stabilizing microtubules. J Virol 76:4483-96.

84. Bussiere LD, Choudhury P, Bellaire B, Miller CL. 2017. Characterization of a replicating mammalian orthoreovirus with tetracysteine-tagged muNS for live-cell visualization of viral factories. J Virol 91:01371.

85. Ooms LS, Jerome WG, Dermody TS, Chappell JD. 2012. Reovirus replication protein mu2 influences cell tropism by promoting particle assembly within viral inclusions. J Virol 86:10979-87.

86. Wheeler JR, Matheny T, Jain S, Abrisch R, Parker R. 2016. Distinct stages in stress granule assembly and disassembly. Elife 5:e18413.

87. Qin Q, Hastings C, Miller CL. 2009. Mammalian orthoreovirus particles induce and are recruited into stress granules at early times postinfection. J Virol 83:11090-101.

88. Broering TJ, Arnold MM, Miller CL, Hurt JA, Joyce PL, Nibert ML. 2005. Carboxyl-proximal regions of reovirus nonstructural protein muNS necessary and sufficient for forming factory-like inclusions. J Virol 79:6194-206.

89. Carroll K, Hastings C, Miller CL. 2014. Amino acids 78 and 79 of mammalian orthoreovirus protein microNS are necessary for stress granule localization, core protein lambda2 interaction, and de novo virus replication. Virology 448:133-45.

90. Choudhury P, Bussiere L, Miller CL. 2017. Mammalian orthoreovirus factories modulate stress granule protein localization by interaction with G3BP1. J Virol doi:10.1128/JVI.01298-17.

91. Eichwald C, Ackermann M, Nibert ML. 2018. The dynamics of both filamentous and globular mammalian reovirus viral factories rely on the microtubule network. Virology 518:77-86.

92. Knowlton JJ, Fernandez de Castro I, Ashbrook AW, Gestaut DR, Zamora PF, Bauer JA, Forrest JC, Frydman J, Risco C, Dermody TS. 2018. The TRiC chaperonin controls reovirus replication through outer-capsid folding. Nat Microbiol 3:481-493.

93. Kaufer S, Coffey CM, Parker JS. 2012. The cellular chaperone hsc70 is specifically recruited to reovirus viral factories independently of its chaperone function. J Virol 86:1079-89.

94. Ivanovic T, Boulant S, Ehrlich M, Demidenko AA, Arnold MM, Kirchhausen T, Nibert ML. 2011. Recruitment of cellular clathrin to viral factories and disruption of clathrin-dependent trafficking. Traffic 12:1179-95.

95. Phillips MB, Stuart JD, Simon EJ, Boehme KW. 2018. Non-structural protein sigma1s is required for optimal reovirus protein expression. J Virol doi:10.1128/JVI.02259-17.

96. Hu L, Crawford SE, Hyser JM, Estes MK, Prasad BV. 2012. Rotavirus non-structural proteins: Structure and function. Curr Opin Virol 2:380-8.

97. Patton JT, Silvestri LS, Tortorici MA, Vasquez-Del Carpio R, Taraporewala ZF. 2006. Rotavirus genome replication and morphogenesis: role of the viroplasm. Curr Top Microbiol Immunol 309:169-87.

98. Stanifer ML, Kischnick C, Rippert A, Albrecht D, Boulant S. 2017. Reovirus inhibits interferon production by sequestering IRF3 into viral factories. Sci Rep 7:10873.

99. Holmes EC. 2003. Error thresholds and the constraints to RNA virus evolution. Trends Microbiol 11:543-6.

100. Faust TB, Binning JM, Gross JD, Frankel AD. 2017. Making sense of multifunctional proteins: Human immunodeficiency virus type 1 accessory and regulatory proteins and connections to transcription. Annu Rev Virol 4:241-260.

101. Boehme KW, Lai CM, Dermody TS. 2013. Mechanisms of reovirus bloodstream dissemination. Adv Virus Res 87:1-35.

102. Poggioli GJ, Keefer CJ, Connolly JL, Dermody TS, Tyler KL. 2000. Reovirus-induced G2/M cell cycle arrest requires σ1s and occurs in the absence of apoptosis. J Virol 74:9562-9570.

103. Boehme KW, Hammer K, Tollefson WC, Konopka-Anstadt JL, Kobayashi T, Dermody TS. 2013. Nonstructural protein sigma1s mediates reovirus-induced cell cycle arrest and apoptosis. J Virol 87:12967-79.

104. Sharpe AH, Fields BN. 1981. Reovirus inhibition of cellular DNA synthesis: role of the S1 gene. J Virol 38:389-92.

105. Broering TJ, Parker JS, Joyce PL, Kim J, Nibert ML. 2002. Mammalian reovirus nonstructural protein microNS forms large inclusions and colocalizes with reovirus microtubule-associated protein micro2 in transfected cells. J Virol 76:8285-97.

106. Arnold MM, Murray KE, Nibert ML. 2008. Formation of the factory matrix is an important, though not a sufficient function of nonstructural protein mu NS during reovirus infection. Virology 375:412-23.

107. Miller CL, Arnold MM, Broering TJ, Hastings CE, Nibert ML. 2010. Localization of mammalian orthoreovirus proteins to cytoplasmic factory-like structures via nonoverlapping regions of microNS. J Virol 84:867-82.

108. Antczak JB, Joklik WK. 1992. Reovirus genome segment assortment into progeny genomes studied by the use of monoclonal-antibodies directed against reovirus proteins. Virology 187:760-776.

109. Broering TJ, McCutcheon AM, Centonze VE, Nibert ML. 2000. Reovirus nonstructural protein muNS binds to core particles but does not inhibit their transcription and capping activities. J Virol 74:5516-24.

110. Becker MM, Goral MI, Hazelton PR, Baer GS, Rodgers SE, Brown EG, Coombs KM, Dermody TS. 2001. Reovirus σNS protein is required for nucleation of viral assembly complexes and formation of viral inclusions. J Virol 75:1459-1475.

111. Miller CL, Broering TJ, Parker JS, Arnold MM, Nibert ML. 2003. Reovirus sigma NS protein localizes to inclusions through an association requiring the mu NS amino terminus. J Virol 77:4566-76.

112. Kobayashi T, Ooms LS, Chappell JD, Dermody TS. 2009. Identification of functional domains in reovirus replication proteins muNS and mu2. J Virol 83:2892-906.

113. Gomatos PJ, Prakash O, Stamatos NM. 1981. Small Reovirus Particles Composed Solely of Sigma-Ns with Specificity for Binding Different Nucleic-Acids. J Virol 39:115-124.

114. Mcdowell MJ, Villakom.L, Lodish HF, Joklik WK. 1972. Translation of Reovirus Messenger Rnas Synthesized in-Vitro into Reovirus Polypeptides by Several Mammalian Cell-Free Extracts. Proc Natl Acad Sci U S A 69:2649-53.

115. Gomatos PJ, Stamatos NM, Sarkar NH. 1980. Small reovirus-specific particle with polycytidylate-dependent RNA polymerase activity. J Virol 36:556-65.

116. Gillian AL, Nibert ML. 1998. Amino terminus of reovirus nonstructural protein σNS is important for ssRNA binding and nucleoprotein complex formation. Virology 240:1-11.

117. Wiener JR, Joklik WK. 1987. Comparison of the reovirus serotype 1, 2, and 3 S3 genome segments encoding the nonstructural protein σNS. Virology 161:332-339.

118. Goral MI, MochowGrundy M, Dermody TS. 1996. Sequence diversity within the reovirus S3 gene: Reoviruses evolve independently of host species, geographic locale, and date of isolation. Virology 216:265-271.

119. Kobayashi T, Chappell JD, Danthi P, Dermody TS. 2006. Gene-specific inhibition of reovirus replication by RNA interference. J Virol 80:9053-63.

120. Ramig RF, Mustoe TA, Sharpe AH, Fields BN. 1978. A genetic map of reovirus. II. Assignment of the double-stranded RNA-negative mutant groups C, D, and E to genome segments. Virology 85:531-4.

121. Cross RK, Fields BN. 1972. Temperature-sensitive mutants of reovirus type 3: studies on the synthesis of viral RNA. Virology 50:799-809.

122. Desmet EA, Anguish LJ, Parker JS. 2014. Virus-mediated compartmentalization of the host translational machinery. MBio 5:e01463-14.

123. Buchan JR, Parker R. 2009. Eukaryotic stress granules: The ins and outs of translation. Mol Cell 36:932-41.

124. Matsuki H, Takahashi M, Higuchi M, Makokha GN, Oie M, Fujii M. 2013. Both G3BP1 and G3BP2 contribute to stress granule formation. Genes Cells 18:135-46.

125. Shelton IH, Kasupski GJ, Jr., Oblin C, Hand R. 1981. DNA binding of a nonstructural reovirus protein. Can J Biochem 59:122-30.

126. Gillian AL, Schmechel SC, Livny J, Schiff LA, Nibert ML. 2000. Reovirus protein sigmaNS binds in multiple copies to single-stranded RNA and shares properties with single-stranded DNA binding proteins. J Virol 74:5939-48.

127. Stamatos NM, Gomatos PJ. 1982. Binding to selected regions of reovirus mRNAs by a nonstructural reovirus protein. Proc Natl Acad Sci U S A 79:3457-61.

128. Richardson MA, Furuichi Y. 1985. Synthesis in *Escherichia coli* of the reovirus nonstructural protein σNS. J Virol 56:527-533.

129. Richardson MA, Furuichi Y. 1983. Nucleotide sequence of reovirus genome segment S3, encoding non-structural protein σNS. Nucleic Acids Res 11:6399-6408.

130. Moras D, Poterszman A. 1995. RNA-protein interactions. Diverse modes of recognition. Curr Biol 5:249-51.

131. Rajkowitsch L, Chen D, Stampfl S, Semrad K, Waldsich C, Mayer O, Jantsch MF, Konrat R, Blasi U, Schroeder R. 2007. RNA chaperones, RNA annealers and RNA helicases. RNA Biol 4:118-30.

132. Yang J, Xia H, Qian Q, Zhou X. 2015. RNA chaperones encoded by RNA viruses. Virol Sin 30:401-9.

133. Borodavka A, Ault J, Stockley PG, Tuma R. 2015. Evidence that avian reovirus sigmaNS is an RNA chaperone: Implications for genome segment assortment. Nucleic Acids Res 43:7044-57.

134. Ramig RF, Petrie BL. 1984. Characterization of temperature-sensitive mutants of simian rotavirus SA11: protein synthesis and morphogenesis. J Virol 49:665-73.

135. Taraporewala ZF, Patton JT. 2004. Nonstructural proteins involved in genome packaging and replication of rotaviruses and other members of the Reoviridae. Virus Res 101:57-66.

136. Jayaram H, Taraporewala Z, Patton JT, Prasad BV. 2002. Rotavirus protein involved in genome replication and packaging exhibits a HIT-like fold. Nature 417:311-5.

137. Carpio RV, Gonzalez-Nilo FD, Jayaram H, Spencer E, Prasad BV, Patton JT, Taraporewala ZF. 2004. Role of the histidine triad-like motif in nucleotide hydrolysis by the rotavirus RNA-packaging protein NSP2. J Biol Chem 279:10624-33.

138. Kumar M, Jayaram H, Vasquez-Del Carpio R, Jiang X, Taraporewala ZF, Jacobson RH, Patton JT, Prasad BV. 2007. Crystallographic and biochemical analysis of rotavirus NSP2 with nucleotides reveals a nucleoside diphosphate kinase-like activity. J Virol 81:12272-84.

139. Netherton C, Moffat K, Brooks E, Wileman T. 2007. A guide to viral inclusions, membrane rearrangements, factories, and viroplasm produced during virus replication. Adv Virus Res 70:101-82.

140. Netherton CL, Wileman T. 2011. Virus factories, double membrane vesicles and viroplasm generated in animal cells. Curr Opin Virol 1:381-7.

141. Becker MM, Peters TR, Dermody TS. 2003. Reovirus sigma NS and mu NS proteins form cytoplasmic inclusion structures in the absence of viral infection. J Virol 77:5948-63.

142. Fields BN, Joklik WK. 1969. Isolation and preliminary genetic and biochemical characterization of temperature-sensitive mutants of reovirus. Virology 37:335-42.

143. Ooms LS, Kobayashi T, Dermody TS, Chappell JD. 2010. A post-entry step in the mammalian orthoreovirus replication cycle is a determinant of cell tropism. J Biol Chem 285:41604-13.

144. NanoString Technologies. 2017. Innovation After Innovation... and Counting. http://www.nanostring.com/applications/technology. Accessed 3 Feb.

145. Chappell JD, Goral MI, Rodgers SE, Depamphilis CW, Dermody TS. 1994. Sequence diversity within the reovirus S2 gene - Reovirus genes reassort in nature, and their termini are predicted to form a panhandle motif. J Virol 68:750-756.

146. Arnoldi F, Campagna M, Eichwald C, Desselberger U, Burrone OR. 2007. Interaction of rotavirus polymerase VP1 with nonstructural protein NSP5 is stronger than that with NSP2. J Virol 81:2128-37.

147. Stoltzfus CM, Shatkin AJ, Banerjee AK. 1973. Absence of polyadenylic acid from reovirus messenger ribonucleic acid. J Biol Chem 248:7993-8.

148. Zarbl H, Skup D, Millward S. 1980. Reovirus progeny subviral particles synthesize uncapped mRNA. J Virol 34:497-505.

149. Sokoloski KJ, Wilusz CJ, Wilusz J. 2006. Viruses: Overturning RNA turnover. RNA Biol 3:140-4.

150. Meng Z, King PH, Nabors LB, Jackson NL, Chen CY, Emanuel PD, Blume SW. 2005. The ELAV RNA-stability factor HuR binds the 5'-untranslated region of the human IGF-IR transcript and differentially represses cap-dependent and IRES-mediated translation. Nucleic Acids Res 33:2962-79.

151. Peng SS, Chen CY, Xu N, Shyu AB. 1998. RNA stabilization by the AU-rich element binding protein, HuR, an ELAV protein. EMBO J 17:3461-70.

152. Johnston JM, Denning G, Moot R, Whitehead D, Shields J, Le Doux JM, Doering CB, Spencer HT. 2014. High-throughput screening identifies compounds that enhance lentiviral transduction. Gene Ther 21:1008-20.

153. Muazzam MG, Sneddon M. 1970. Sensitivity of baby hamster kidney (BHK 21-C 13) cells to enteric viruses. Brief report. Arch Gesamte Virusforsch 30:405-7.

154. Schneider-Poetsch T, Ju J, Eyler DE, Dang Y, Bhat S, Merrick WC, Green R, Shen B, Liu JO. 2010. Inhibition of eukaryotic translation elongation by cycloheximide and lactimidomycin. Nat Chem Biol 6:209-217.

155. Cho EJ, Takagi T, Moore CR, Buratowski S. 1997. mRNA capping enzyme is recruited to the transcription complex by phosphorylation of the RNA polymerase II carboxy-terminal domain. Genes Dev 11:3319-26.

156. Egloff S, Studniarek C, Kiss T. 2018. 7SK small nuclear RNA, a multifunctional transcriptional regulatory RNA with gene-specific features. Transcription 9:95-101.

157. Bourbigot S, Dock-Bregeon AC, Eberling P, Coutant J, Kieffer B, Lebars I. 2016. Solution structure of the 5'-terminal hairpin of the 7SK small nuclear RNA. RNA 22:1844-1858.

158. Broering TJ, Kim J, Miller CL, Piggott CD, Dinoso JB, Nibert ML, Parker JS. 2004. Reovirus nonstructural protein μNS recruits viral core surface proteins and entering core particles to factory-like inclusions. J Virol 78:1882-1892.

159. Brentano L, Noah DL, Brown EG, Sherry B. 1998. The reovirus protein mu 2, encoded by the M1 gene, is an RNA-binding protein. J Virol 72:8354-8357.

160. Touris-Otero F, Martinez-Costas J, Vakharia VN, Benavente J. 2004. Avian reovirus nonstructural protein microNS forms viroplasm-like inclusions and recruits protein sigmaNS to these structures. Virology 319:94-106.

161. Touris-Otero F, Martinez-Costas J, Vakharia VN, Benavente J. 2005. Characterization of the nucleic acid-binding activity of the avian reovirus non-structural protein sigma NS. J Gen Virol 86:1159-69.

162. Darlix JL, Godet J, Ivanyi-Nagy R, Fosse P, Mauffret O, Mely Y. 2011. Flexible nature and specific functions of the HIV-1 nucleocapsid protein. J Mol Biol 410:565-81.

163. Ivanyi-Nagy R, Davidovic L, Khandjian EW, Darlix JL. 2005. Disordered RNA chaperone proteins: From functions to disease. Cell Mol Life Sci 62:1409-17.

164. DeStefano JJ, Titilope O. 2006. Poliovirus protein 3AB displays nucleic acid chaperone and helix-destabilizing activities. J Virol 80:1662-71.

165. Stork J, Kovalev N, Sasvari Z, Nagy PD. 2011. RNA chaperone activity of the tombusviral p33 replication protein facilitates initiation of RNA synthesis by the viral RdRp in vitro. Virology 409:338-47.

166. Sagar V, Murray KE. 2014. The mammalian orthoreovirus bicistronic M3 mRNA initiates translation using a 5' end-dependent, scanning mechanism that does not require interaction of 5'-3' untranslated regions. Virus Res 183:30-40.

167. Anderson EC, Lever AM. 2006. Human immunodeficiency virus type 1 Gag polyprotein modulates its own translation. J Virol 80:10478-86.

168. Besong-Ndika J, Ivanov KI, Hafren A, Michon T, Makinen K. 2015. Cotranslational coat protein-mediated inhibition of potyviral RNA translation. J Virol 89:4237-48.

169. Risco C, Fernandez de Castro I. 2013. Virus morphogenesis in the cell: methods and observations. Subcell Biochem 68:417-40.

170. Romero-Brey I, Bartenschlager R. 2016. Endoplasmic reticulum: The favorite intracellular niche for viral replication and assembly. Viruses 8:e160.

171. Cheung W, Gill M, Esposito A, Kaminski CF, Courousse N, Chwetzoff S, Trugnan G, Keshavan N, Lever A, Desselberger U. 2010. Rotaviruses associate with cellular lipid droplet components to replicate in viroplasms, and compounds disrupting or blocking lipid droplets inhibit viroplasm formation and viral replication. J Virol 84:6782-98.

172. Crawford SE, Desselberger U. 2016. Lipid droplets form complexes with viroplasms and are crucial for rotavirus replication. Curr Opin Virol 19:11-5.

173. Schwarz DS, Blower MD. 2016. The endoplasmic reticulum: Structure, function and response to cellular signaling. Cell Mol Life Sci 73:79-94.

174. Bergen DJM, Stevenson NL, Skinner REH, Stephens DJ, Hammond CL. 2017. The Golgi matrix protein giantin is required for normal cilia function in zebrafish. Biol Open 6:1180-1189.

175. Tokuyasu KT. 1973. A technique for ultracryotomy of cell suspensions and tissues. J Cell Biol 57:551-65.

176. Hurbain I, Sachse M. 2011. The future is cold: cryo-preparation methods for transmission electron microscopy of cells. Biol Cell 103:405-20.

177. Neufeldt CJ, Cortese M, Acosta EG, Bartenschlager R. 2018. Rewiring cellular networks by members of the Flaviviridae family. Nat Rev Microbiol 16:125-142.

178. Shulla A, Randall G. 2016. (+) RNA virus replication compartments: A safe home for (most) viral replication. Curr Opin Microbiol 32:82-88.

179. Diaz A, Wang X, Ahlquist P. 2010. Membrane-shaping host reticulon proteins play crucial roles in viral RNA replication compartment formation and function. Proc Natl Acad Sci U S A 107:16291-6.

180. Farhan H, Hauri HP. 2009. Membrane biogenesis: Networking at the ER with atlastin. Curr Biol 19:R906-8.

181. Wang S, Tukachinsky H, Romano FB, Rapoport TA. 2016. Cooperation of the ER-shaping proteins atlastin, lunapark, and reticulons to generate a tubular membrane network. Elife 5:e18605.

182. Boehme KW, Frierson JM, Konopka JL, Kobayashi T, Dermody TS. 2011. The reovirus sigma1s protein is a determinant of hematogenous but not neural virus dissemination in mice. J Virol 85:11781-90.

183. Wang W, Riedel K, Lynch P, Chien CY, Montelione GT, Krug RM. 1999. RNA binding by the novel helical domain of the influenza virus NS1 protein requires its dimer structure and a small number of specific basic amino acids. RNA 5:195-205.

184. Tran H, Schilling M, Wirbelauer C, Hess D, Nagamine Y. 2004. Facilitation of mRNA deadenylation and decay by the exosome-bound, DExH protein RHAU. Mol Cell 13:101-11.

185. Kelley LA, Mezulis S, Yates CM, Wass MN, Sternberg MJ. 2015. The Phyre2 web portal for protein modeling, prediction and analysis. Nat Protoc 10:845-58.

186. Kanai Y, Komoto S, Kawagishi T, Nouda R, Nagasawa N, Onishi M, Matsuura Y, Taniguchi K, Kobayashi T. 2017. Entirely plasmid-based reverse genetics system for rotaviruses. Proc Natl Acad Sci U S A 114:2349-2354.

187. Darnell RB. 2010. HITS-CLIP: Panoramic views of protein-RNA regulation in living cells. Wiley Interdiscip Rev RNA 1:266-86.

188. Moore MJ, Zhang C, Gantman EC, Mele A, Darnell JC, Darnell RB. 2014. Mapping Argonaute and conventional RNA-binding protein interactions with RNA at single-nucleotide resolution using HITS-CLIP and CIMS analysis. Nat Protoc 9:263-93.

189. Watanabe Y, Sakuma S, Shames R. 1974. In vitro synthesis of reovirus genomic segments. Jpn J Microbiol 18:253-8.

190. Acs G, Klett H, Schonberg M, Christman J, Levin DH, Silverstein JC. 1971. Mechanism of reovirus double-stranded RNA synthesis in vivo and in vitro. Journal of Virology 8:684-689.

191. Chen D, Zeng CQ, Wentz MJ, Gorziglia M, Estes MK, Ramig RF. 1994. Template-dependent, in vitro replication of rotavirus RNA. J Virol 68:7030-9.

192. Chen S, Novick P, Ferro-Novick S. 2013. ER structure and function. Curr Opin Cell Biol 25:428-33.

193. Zhao Y, Zhang T, Huo H, Ye Y, Liu Y. 2016. Lunapark is a component of a ubiquitin ligase complex localized to the endoplasmic reticulum three-way junctions. J Biol Chem 291:18252-62.

194. Zhang H, Hu J. 2016. Shaping the endoplasmic reticulum into a social network. Trends Cell Biol 26:934-943.

195. Varnaite R, MacNeill SA. 2016. Meet the neighbors: Mapping local protein interactomes by proximity-dependent labeling with BioID. Proteomics 16:2503-2518.

196. Shemesh T, Klemm RW, Romano FB, Wang S, Vaughan J, Zhuang X, Tukachinsky H, Kozlov MM, Rapoport TA. 2014. A model for the generation and interconversion of ER morphologies. Proc Natl Acad Sci U S A 111:E5243-51.

197. Le Sage V, Cinti A, Valiente-Echeverria F, Mouland AJ. 2015. Proteomic analysis of HIV-1 Gag interacting partners using proximity-dependent biotinylation. Virol J 12:138.

198. Ashbrook AW, Lentscher AJ, Zamora PF, Silva LA, May NA, Bauer JA, Morrison TE, Dermody TS. 2016. Antagonism of the sodium-potassium ATPase impairs Chikungunya virus infection. MBio 24:00693-16.

199. Stins MF, Gilles F, Kim KS. 1997. Selective expression of adhesion molecules on human brain microvascular endothelial cells. J Neuroimmunol 76:81-90.

200. Boehme KW, Ikizler M, Kobayashi T, Dermody TS. 2011. Reverse genetics for mammalian reovirus. Methods 55:109-13.

201. Virgin HWt, Bassel-Duby R, Fields BN, Tyler KL. 1988. Antibody protects against lethal infection with the neurally spreading reovirus type 3 (Dearing). J Virol 62:4594-604.

202. Virgin HW, IV, Mann MA, Fields BN, Tyler KL. 1991. Monoclonal antibodies to reovirus reveal structure/function relationships between capsid proteins and genetics of susceptibility to antibody action. Jf Virol 65:6772-6781.

203. Risco C, Rodriguez JR, Lopez-Iglesias C, Carrascosa JL, Esteban M, Rodriguez D. 2002. Endoplasmic reticulum-Golgi intermediate compartment membranes and vimentin filaments participate in vaccinia virus assembly. J Virol 76:1839-55.

204. Fontana J, Tzeng WP, Calderita G, Fraile-Ramos A, Frey TK, Risco C. 2007. Novel replication complex architecture in rubella replicon-transfected cells. Cell Microbiol 9:875-90.

205. Fiala JC. 2005. Reconstruct: a free editor for serial section microscopy. J Microsc 218:52-61.

206. NanoString Technologies Inc. 2018. nSolver™ 4.0: Analysis Software User Manual. https://www.nanostring.com/application/files/6415/1789/7813/MAN-C0019-08_nSolver_4.0_Analysis_Software_User_Manual.pdf. Accessed 25 May.

207. Lahr RM, Mack SM, Heroux A, Blagden SP, Bousquet-Antonelli C, Deragon JM, Berman AJ. 2015. The La-related protein 1-specific domain repurposes HEAT-like repeats to directly bind a 5'TOP sequence. Nucleic Acids Res 43:8077-88.

208. Lahr RM, Fonseca BD, Ciotti GE, Al-Ashtal HA, Jia JJ, Niklaus MR, Blagden SP, Alain T, Berman AJ. 2017. La-related protein 1 (LARP1) binds the mRNA cap, blocking eIF4F assembly on TOP mRNAs. Elife 6:e24146.

209. Rio DC. 2012. Filter-binding assay for analysis of RNA-protein interactions. Cold Spring Harb Protoc 2012:1078-81.

Reovirus Cell Entry Requires Functional Microtubules

Bernardo A. Mainou,[a,b] Paula F. Zamora,[b,c] Alison W. Ashbrook,[b,c] Daniel C. Dorset,[d] Kwang S. Kim,[e] Terence S. Dermody[a,b,c]

Departments of Pediatrics,[a] Pathology, Microbiology, and Immunology,[c] Elizabeth B. Lamb Center for Pediatric Research,[b] and Vanderbilt Technologies for Advanced Genomics,[d] Vanderbilt University School of Medicine, Nashville, Tennessee, USA; Division of Pediatric Infectious Diseases, Johns Hopkins School of Medicine, Baltimore, Maryland, USA[e]

ABSTRACT **Mammalian reovirus binds to cell-surface glycans and junctional adhesion molecule A and enters cells by receptor-mediated endocytosis in a process dependent on β1 integrin. Within the endocytic compartment, reovirus undergoes stepwise disassembly, allowing release of the transcriptionally active viral core into the cytoplasm. To identify cellular mediators of reovirus infectivity, we screened a library of small-molecule inhibitors for the capacity to block virus-induced cytotoxicity. In this screen, reovirus-induced cell killing was dampened by several compounds known to impair microtubule dynamics. Microtubule inhibitors were assessed for blockade of various stages of the reovirus life cycle. While these drugs did not alter reovirus cell attachment or internalization, microtubule inhibitors diminished viral disassembly kinetics with a concomitant decrease in infectivity. Reovirus virions colocalize with microtubules and microtubule motor dynein 1 during cell entry, and depolymerization of microtubules results in intracellular aggregation of viral particles. These data indicate that functional microtubules are required for proper sorting of reovirus virions following internalization and point to a new drug target for pathogens that use the endocytic pathway to invade host cells.**

IMPORTANCE **Screening libraries of well-characterized drugs for antiviral activity enables the rapid characterization of host processes required for viral infectivity and provides new therapeutic applications for established pharmaceuticals. Our finding that microtubule-inhibiting drugs impair reovirus infection identifies a new cell-based antiviral target.**

Received 30 May 2013 **Accepted** 10 June 2013 **Published** 2 July 2013

Citation Mainou BA, Zamora PF, Ashbrook AW, Dorset DC, Kim KS, Dermody TS. 2013. Reovirus cell entry requires functional microtubules. mBio 4(4):e00405-13. doi:10.1128/mBio.00405-13.

Editor Anne Moscona, Weill Medical College—Cornell

Address correspondence to Terence S. Dermody, terry.dermody@vanderbilt.edu.

The interplay between viruses and host cells regulates each step of the virus-host encounter. Viral tropism is restricted by the availability of cell-surface receptors and host molecules that promote viral internalization, replication, assembly, and release. Understanding the cellular components that underlie productive viral infection can illuminate new targets for development of antiviral therapies, improve viral vector design, and enhance an understanding of cellular processes at the pathogen-host interface.

Mammalian orthoreovirus (called reoviruses here) are nonenveloped, double-stranded RNA viruses that are formed from two concentric protein shells (1). Reoviruses infect most mammalian species, and although most humans are exposed during childhood, infection seldom results in disease (1, 2). The reovirus genome can now be engineered using reverse genetics, leading to the recovery of viable viruses with targeted alterations (3). Coupled with the capacity to elicit mucosal immune responses (1, 4) and natural attenuation in humans (1), this technology provides an opportunity to develop reovirus as a vaccine vector. Moreover, reovirus is currently being tested in clinical trials for efficacy as an oncolytic agent against a variety of cancers (5).

Reovirus attaches to host cells via interactions with cell-surface glycans (6, 7) and junctional adhesion molecule A (JAM-A) (8–10). Following attachment to JAM-A, reovirus is internalized in a β1 integrin-dependent manner via receptor-mediated endocytosis (11). Following internalization, reovirus activates Src kinase (12) and traverses through early and late endosomes (13). In late endosomes, virions undergo stepwise acid-dependent proteolytic disassembly catalyzed by cysteine cathepsin proteases to form infectious subvirion particles (ISVPs). ISVPs are characterized by the loss of outer-capsid protein σ3 and cleavage of outer-capsid protein μ1. The μ1 cleavage fragments mediate endosomal membrane penetration and release of the transcriptionally active viral core into the cytoplasm (14–16). ISVPs also can be generated *in vitro* by treatment of virions with a variety of proteases (14, 16). These particles bind JAM-A to initiate infection but are thought to penetrate at or near the cell surface (8, 17, 18), bypassing a requirement for acid-dependent proteolytic disassembly (16, 18). Host factors that mediate internalization and endosomal transport of reovirus virions are not completely understood.

Microtubules are long, filamentous protein polymers composed of α-tubulin and β-tubulin heterodimers (19). These structures regulate a wide variety of cellular functions, including mitosis, maintenance of cell shape, and intracellular transport (19). Posttranslational modifications of tubulin subunits and the interaction of microtubule-associated proteins with microtubules regulate polymerization dynamics (20). Because of the essential role in cell division, microtubules are targets for several anticancer chemotherapeutic agents (20, 21). For example, paclitaxel was originally developed for use against ovarian cancer but also is used

to treat other cancers, including metastatic breast cancer (20–22). Vinca alkaloids, including vindesine sulfate, are used to treat non-small-cell lung cancer, leukemia, lymphoma, and breast cancer (20, 21, 23). Microtubule-inhibiting compounds are classified into two groups based on whether the drug stabilizes or destabilizes microtubules. Stabilizing agents, such as taxanes, enhance microtubule polymerization, whereas destabilizing agents, such as vinca alkaloids and colchicine, inhibit microtubule polymerization by directly binding to microtubule subunits (20). Microtubule motors are used for bidirectional transport of cargo (24). Minus-end motors (dyneins) transport cargo toward the cell interior, whereas plus-end motors (kinesins) move cargo toward the cell periphery (24). It is not known whether microtubules or microtubule motors are required for reovirus entry.

In this study, we identified microtubule inhibitors in a high-throughput screen of small molecules for blockade of reovirus-mediated cell death. These drugs do not impede reovirus attachment or internalization but delay the intracellular transport of incoming virions, with a concomitant decrease in viral infectivity. Diminished expression of the dynein 1 heavy chain by RNA interference (RNAi) decreases reovirus infection. These findings indicate that reovirus uses microtubules and dynein 1 to efficiently enter and infect host cells, providing a potential new therapeutic option for viruses that penetrate deep into the endocytic pathway to establish infection.

RESULTS

Identification of microtubule inhibitors using a high-throughput small-molecule screen. To identify cellular factors required for reovirus cytotoxicity, we performed a high-throughput screen using small molecules from the NIH Clinical Collection (NCC), a library that contains 446 compounds that have been used in phase I, II, and III clinical trials in humans (see Fig. S1A in the supplemental material). Small molecules in the NCC were initially developed for use against a variety of diseases, including central nervous system, cardiovascular, and gastrointestinal malignancies, as well as numerous anti-infectives. HeLa S3 cells, which undergo cell death following reovirus infection (25), were incubated with dimethyl sulfoxide (DMSO) (vehicle control), 10 μM cysteine-protease inhibitor E64-d as a positive control (26), or a 10 μM concentration of each of the compounds in the NCC, adsorbed with cytopathic reovirus strain T3SA+ (6, 27), and incubated for 48 h. Cellular ATP levels were assessed as a proxy for cell viability. *Z* scores were calculated to identify compounds that significantly diminished reovirus-induced cell death (see Table S1 in the supplemental material). Eleven compounds had *Z* scores of greater than 2.0, with *Z* scores in this group ranging from 2.758 to 8.444 (Fig. S1B). Interestingly, 5 of the 11 compounds identified are drugs that influence microtubule stability and function (20) (Fig. S1C). Microtubule-inhibiting compounds constitute <1% of the total number of small molecules in the NCC, suggesting that the large number of microtubule inhibitors identified does not reflect bias within the screen. Thus, these data suggest that functional microtubules are required for reovirus-induced cytotoxicity.

Microtubule inhibitors diminish reovirus-mediated cell death and infectivity. To verify that microtubule-inhibiting drugs block cytotoxicity induced by reovirus, HeLa S3 cells were incubated with DMSO, E64-d, or NH_4Cl as positive controls, or increasing concentrations of microtubule-inhibiting drugs for 1 h prior to reovirus adsorption. Cell viability was assessed by quantifying cellular ATP levels 48 h after adsorption (Fig. 1A). Similar to the observations made using the NCC screen, we observed a dose-dependent decrease in reovirus-mediated cytotoxicity with increasing concentrations of microtubule-inhibiting compounds, E64-d, or NH_4Cl. The observed inhibition was statistically significant at concentrations of 0.1 to 1.0 μM for all compounds tested except for flubendazole, which inhibited at concentrations of 1.0 and 10 μM. These data confirm findings obtained from the small-molecule screen and provide further evidence that microtubule function is required for reovirus-induced cell death.

To determine whether microtubule function is required for reovirus infectivity in epithelial and endothelial cells, we tested the effect of microtubule-inhibiting compounds on reovirus infection of CCL2 HeLa cells, HeLa S3 cells, and human brain microvascular endothelial cells (HBMECs). Both CCL2 and S3 HeLa cells are highly susceptible to reovirus infection and have been used in studies to understand cellular mediators of reovirus cell entry (12, 13). HBMECs are highly transfectable and provide a tractable model cell line for studies of virus replication in endothelial cells (28). Cells were treated with DMSO, E64-d, NH_4Cl, or increasing concentrations of microtubule inhibitors for 1 h prior to adsorption with reovirus T3SA+, incubated in the presence of inhibitors, and scored for infection by indirect immunofluorescence (Fig. 1B). For all cell lines tested, treatment with vindesine sulfate yielded a statistically significant decrease in infectivity. While colchicine and docetaxel also decreased infectivity in the cell types tested, the effects were not as pronounced as those observed with vindesine sulfate. Interestingly, among the compounds from the NCC, we identified three vinca alkaloid compounds, vindesine sulfate, vincristine sulfate, and vinorelbine bitartrate, that impaired reovirus-mediated cytotoxicity. These data suggest that vinca alkaloids are more potent as anti-infectives against reovirus than other microtubule-inhibiting agents. Together, these data indicate that microtubule function is required for maximal reovirus infectivity and reovirus-mediated cell killing.

Vindesine sulfate blocks reovirus replication at early times of infection. To define the temporal window in which microtubule inhibitors act to impair reovirus infection, CCL2 HeLa cells were treated with DMSO, NH_4Cl, or 1 μM vindesine sulfate for 1 h prior to reovirus adsorption or in 1-h increments up to 2 h post-adsorption. Cells were then incubated in the presence or absence of inhibitors and scored for infection by indirect immunofluorescence 20 h after adsorption (Fig. 2A). Since microtubules depolymerize at cold temperatures (29), virus was adsorbed at room temperature to prevent microtubule depolymerization while also allowing sufficient time for reovirus to attach to cells. For the remainder of the descriptions of our studies, 0 min represents the initiation of infection following adsorption at room temperature. Vindesine sulfate treatment 1 h prior to or immediately following adsorption substantially decreased reovirus infection. However, addition of vindesine sulfate 1 h or more after adsorption decreased reovirus infection much less efficiently. These data indicate that vindesine sulfate is most potent in diminishing reovirus infection during the first hour of the infectious cycle, suggesting that reovirus requires microtubule function during the interval required for viral entry and uncoating. In addition, these findings demonstrate that impairment of reovirus infection by vindesine sulfate is not attributable to toxicity of the compound.

To determine whether vindesine sulfate impairs infection by

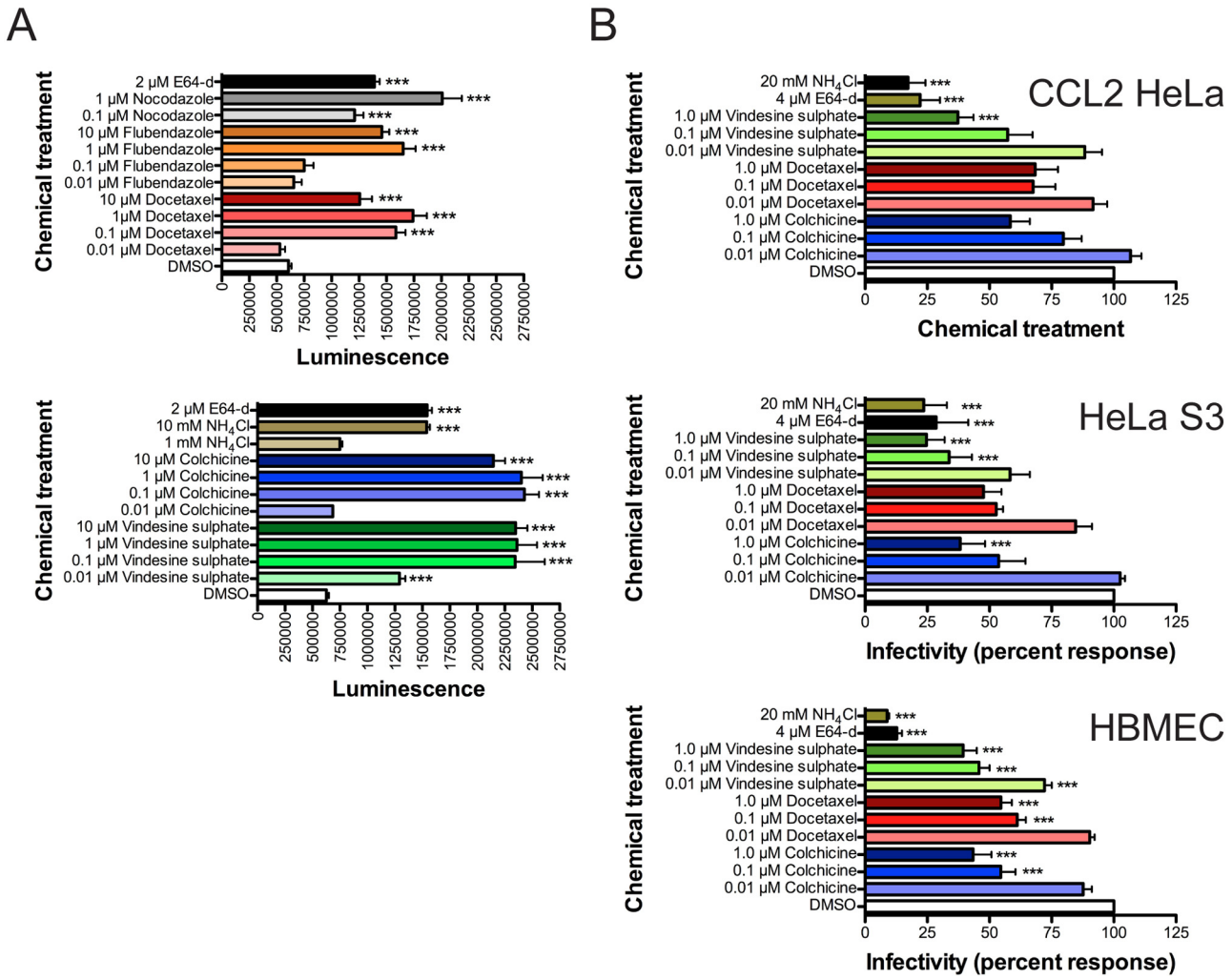

FIG 1 Microtubule-inhibiting compounds diminish reovirus-mediated cytotoxicity and inhibit reovirus infectivity. (A) HeLa S3 cells were incubated with DMSO, increasing concentrations of docetaxel, flubendazole, nocodazole, vindesine sulfate, colchicine, or NH_4Cl, or 2 μM E64-d, adsorbed with T3SA+, and incubated for 48 h. Cell viability was quantified using an ATP-dependent luminescence assay. Results are presented as total luminescence intensity values from experiments performed in quadruplicate. Error bars indicate standard deviations. (B) CCL2 HeLa cells, HeLa S3 cells, or HBMECs were incubated with DMSO or increasing concentrations of colchicine, docetaxel, vindesine sulfate, E64-d, or NH_4Cl and adsorbed with T3SA+ at an MOI of either 5 PFU/cell for HeLa S3 cells and HBMECs or 1 PFU/cell for CCL2 HeLa cells. Cells were incubated in the presence of inhibitors for 20 h and scored for infection by indirect immunofluorescence. Results are presented as percent mean fluorescence intensity compared with DMSO, normalized to cell number and background fluorescence, for quadruplicate experiments with CCL2 HeLa cells and triplicate experiments with HeLa S3 cells and HBMECs. Error bars indicate standard errors of the mean. ***, $P < 0.05$ in comparison to DMSO by one-way ANOVA with Dunnett's multiple-comparison test.

ISVPs, which bind JAM-A at the cell surface but do not require intracellular transport for infection (8, 16–18), CCL2 HeLa cells were treated with DMSO, 20 mM NH_4Cl, or increasing concentrations of vindesine sulfate for 1 h, adsorbed with reovirus virions or ISVPs, and scored for infection by indirect immunofluorescence 20 h after adsorption (Fig. 2B). As observed previously, treatment of cells with NH_4Cl or vindesine sulfate diminished infection following adsorption with virions. In contrast, treatment of cells with NH_4Cl or vindesine sulfate did not significantly alter infection following adsorption with ISVPs. These data indicate that vindesine sulfate blocks a step in reovirus replication following attachment to JAM-A but prior to viral protein synthesis.

Microtubules are required for endocytic sorting of reovirus during cell entry. To determine whether reovirus uses microtubule tracks during cell entry, CCL2 HeLa cells were treated with DMSO or 1 μM vindesine sulfate for 1 h, adsorbed with reovirus, and incubated for 0, 20, or 120 min. Cells were stained for reovirus and α-tubulin and imaged using confocal microscopy (Fig. 3). In DMSO-treated cells, virions were detected on microtubule tracks at 0, 20, and 120 min, with an increasing number of particles observed in the perinuclear area at 120 min. The perinuclear distribution of reovirus virions is consistent with access to late endosomes for disassembly by cathepsin proteases to allow productive infection (13). In vindesine sulfate-treated cells, virions were associated with depolymerized microtubules at 0 and 20 min, but by 120 min, particles appeared to form clusters in the cytoplasm. Treatment of HBMECs with vindesine sulfate also resulted in aggregation of viral particles at 120 min postadsorption, although the clusters were not as prominent as those observed in vindesine

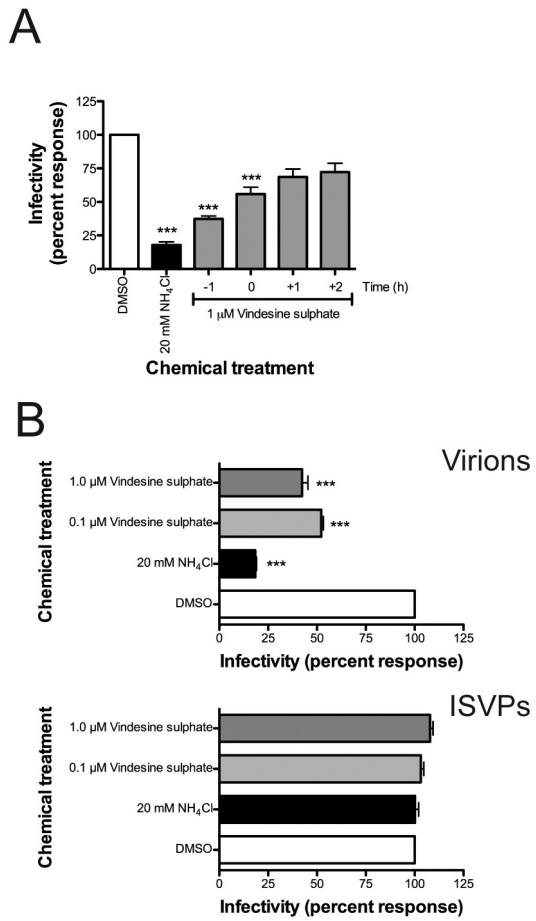

FIG 2 Vindesine sulfate blocks reovirus replication at early times of infection. (A) CCL2 HeLa cells were incubated with DMSO, 20 mM NH_4Cl, or 1 μM vindesine sulfate, adsorbed with T3SA+ at an MOI of 5 PFU/cell, and incubated in the presence of inhibitors for 20 h. Alternatively, cells were incubated with 1 μM vindesine sulfate immediately following adsorption or at 1-h intervals after adsorption. Cells were scored for infection by indirect immunofluorescence. (B) CCL2 HeLa cells were incubated with DMSO, NH_4Cl, or vindesine sulfate, adsorbed with T3SA+ virions or ISVPs at an MOI of 1.63×10^3 particles/cell, and incubated in the presence of inhibitors for 20 h. Cells were scored for infection by indirect immunofluorescence. Results are presented as percent mean fluorescence intensity compared with DMSO, normalized to cell number and background fluorescence, for triplicate experiments. ***, $P < 0.05$ in comparison to DMSO by one-way ANOVA with Dunnett's multiple-comparison test.

sulfate-treated CCL2 HeLa cells (data not shown). These observations suggest that depolymerization of microtubules by vindesine sulfate leads to missorting of reovirus virions during cell entry.

Vindesine sulfate does not affect internalization of reovirus into cells. Since depolymerization of microtubules impairs reovirus intracellular transport and infectivity, we sought to determine whether vindesine sulfate inhibits internalization of viral particles from the cell surface. CCL2 HeLa cells were treated with DMSO or 1 μM vindesine sulfate for 1 h, adsorbed with Alexa 546-labeled reovirus, and incubated for 0, 60, or 120 min. Cells were stained for extracellular virus using reovirus-specific antiserum under nonpermeabilizing conditions, and the ratio of extracellular to internalized reovirus particles was quantified by flow cytometry (Fig. 4A). Over the course of the infection, we observed a decrease in extracellular virus in the presence and absence of vindesine sulfate. These results suggest that vindesine sulfate does not significantly impede internalization of reovirus, at least up to 120 min after adsorption. Consistent with this finding, vindesine sulfate treatment did not diminish cell-surface expression of JAM-A or β1 integrin (data not shown). These results suggest that microtubule function is not required for reovirus attachment or internalization.

Vindesine sulfate impairs reovirus access to intracellular acidified compartments. To determine whether vindesine sulfate alters transport of reovirus to acidified compartments during cell entry, CCL2 HeLa cells were treated with DMSO or 1 μM vindesine sulfate for 1 h, adsorbed with reovirus labeled with a pH-sensitive dye (pHrodo), and incubated for 0, 60, or 120 min. The fluorescence intensity of intracellular virus was quantified by flow cytometry (Fig. 4B). In DMSO-treated cells, mean fluorescence intensity increased over time, indicating that virions gain access to an acidified compartment between 60 and 120 min after adsorption, consistent with prior studies of the kinetics of reovirus delivery to acidified endosomes (13, 30). In contrast, mean fluorescence intensity was dampened during the interval of reovirus entry into vindesine sulfate-treated cells. Importantly, microtubule-inhibiting drugs do not affect the intraluminal pH of endosomes (31). These data suggest that vindesine sulfate impairs reovirus infection by impeding transport of virions to acidified intracellular organelles.

During cell entry, reovirus traverses through Rab5-marked early endosomes en route to Rab7- and Rab9-marked late endosomes for proteolytic disassembly (12). To determine whether vindesine sulfate treatment leads to retention of reovirus particles in early endosomes, CCL2 HeLa cells were transfected with enhanced green fluorescent protein (EGFP)-Rab5A, incubated with DMSO or 1 μM vindesine sulfate for 1 h, adsorbed with Alexa-labeled reovirus, incubated for 120 min, and imaged by confocal microscopy. Analysis of the spectral overlap of fluorescently labeled virions and Rab5A-positive compartments showed no statistically significant difference in the percentages of virions in early endosomes in cells treated with either DMSO or vindesine sulfate (Fig. 4C). These data suggest that inhibition of microtubule function by vindesine sulfate does not lead to an accumulation of reovirus particles in early endosomes.

In a complementary experiment, CCL2 HeLa cells were incubated with DMSO or 1 μM vindesine sulfate for 1 h, adsorbed with Alexa-labeled reovirus, and incubated for 60 or 120 min. Cells were stained for lysosomal-associated membrane protein 1 (LAMP1) to identify late endosomes and lysosomes (Fig. 4D). Analysis of the spectral overlap of fluorescently labeled virions and LAMP1-positive compartments revealed a higher percentage of viral particles distributed to LAMP1-positive endosomes in control-treated cells than in those treated with vindesine sulfate (Fig. 4E). Concordant with these observations, vindesine sulfate decreased reovirus colocalization with Rab7-marked endosomes compared to that seen with control-treated cells (data not shown). Together, these data indicate that although vindesine sulfate does not inhibit reovirus internalization or lead to retention of virus in early endosomes, the drug impedes efficient transport of virions to acidified intracellular compartments where viral disassembly takes place.

Reovirus requires dynein 1 to efficiently infect cells. To determine whether reovirus uses minus-end microtubule motor dy-

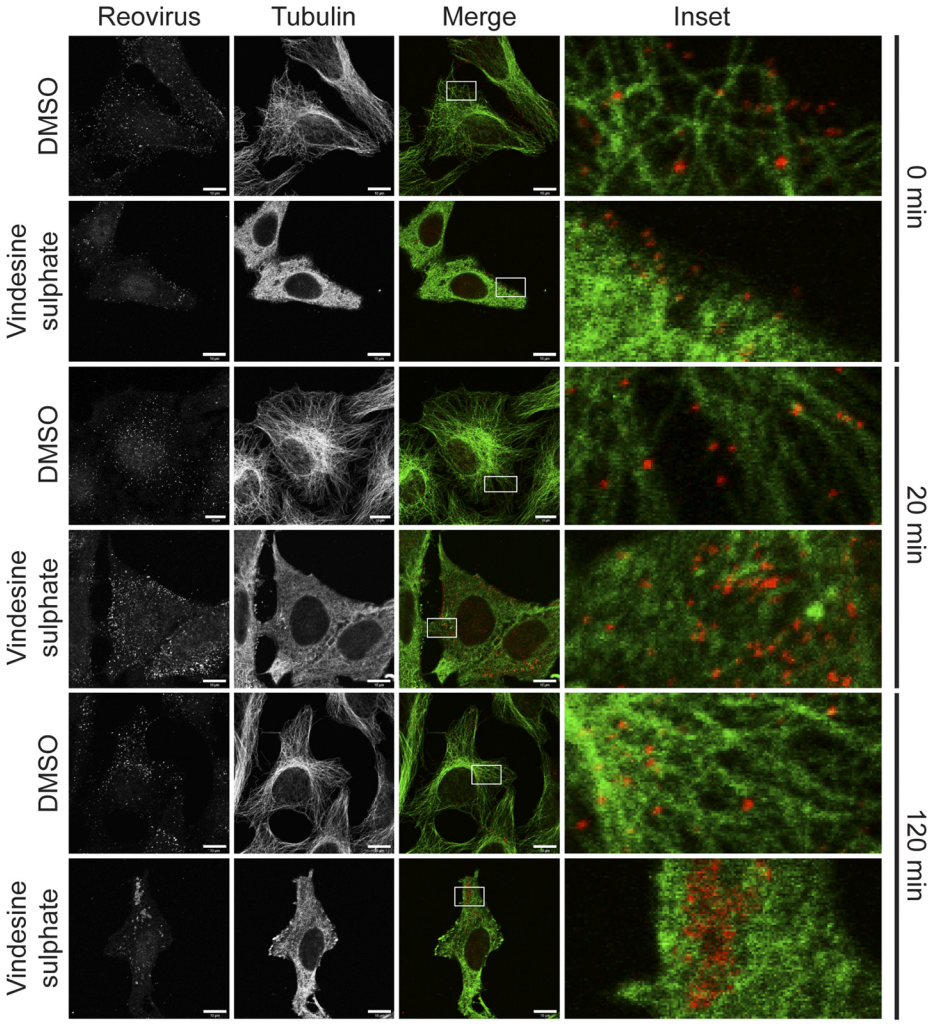

FIG 3 Reovirus uses microtubules to enter cells. CCL2 HeLa cells were adsorbed with T3SA+ at an MOI of 2×10^4 particles/cell at room temperature and incubated at 37°C for 0, 20, or 120 min. Cells were fixed in methanol, stained for reovirus (red) or α-tubulin (green), and imaged by confocal microscopy. Single sections from a Z-stack as well as a merged image are shown for each stain. Insets depict enlarged areas from boxed regions. Scale bars, 10 μm.

nein 1 for transport into the cell interior, HBMECs were transfected with small interfering RNAs (siRNAs) specific for the dynein 1 heavy chain, adsorbed with reovirus strains type 1 Lang (T1L) or type 3 Dearing (T3D), incubated for 48 h, and scored for infection by indirect immunofluorescence (Fig. 5A). Of the cell lines used in this study, diminished expression of dynein 1 caused by RNAi treatment is most efficient in HBMECs (data not shown). Consistent with a requirement for microtubule function for efficient reovirus infection, diminished dynein 1 heavy chain expression caused by RNAi treatment decreased infection by both T1L and T3D. To further define the role of dynein 1 in reovirus cell entry, cells were adsorbed with T1L, incubated for 20 min, stained for reovirus and dynein 1 heavy chain, and imaged by confocal microscopy. Virions were observed in close proximity to dynein 1 in both HBMECs (Fig. 5B) and CCL2 HeLa cells (Fig. 5C), suggesting that reovirus uses dynein 1 to promote cell entry. Together, these data indicate that reovirus requires the microtubule minus-end motor dynein 1 to efficiently infect cells.

CHKV does not require microtubules to infect cells. Chikungunya virus (CHKV), a mosquito-transmitted alphavirus that causes epidemics of arthritis (32), requires acidification to efficiently enter cells, but unlike reovirus, CHKV does not require access to late endosomes (33). To determine whether vindesine sulfate inhibits CHKV infection, BHK-21 cells, which are susceptible to CHKV, were treated with DMSO or 1 μM vindesine sulfate for 1 h, adsorbed with CHKV vaccine strain 181/25 or virulent strain SL15649, incubated for 10 h, and scored for infection by indirect immunofluorescence (Fig. 6A and B). In contrast to findings made in our studies of reovirus, vindesine sulfate did not impair CHKV infection, suggesting that CHKV does not require microtubule function to efficiently enter cells. These results are in agreement with a requirement for microtubules in the maturation of early to late endosomes (34) and provide additional evidence that the drug does not impair reovirus infection by nonspecific cytotoxic effects.

Vindesine sulfate alters reovirus disassembly kinetics. As a final experiment to define the step in reovirus replication blocked by microtubule inhibitors, we tested whether inhibition of microtubule function alters the kinetics of reovirus disassembly. CCL2 HeLa cells were treated with DMSO or 1 μM vindesine sulfate for

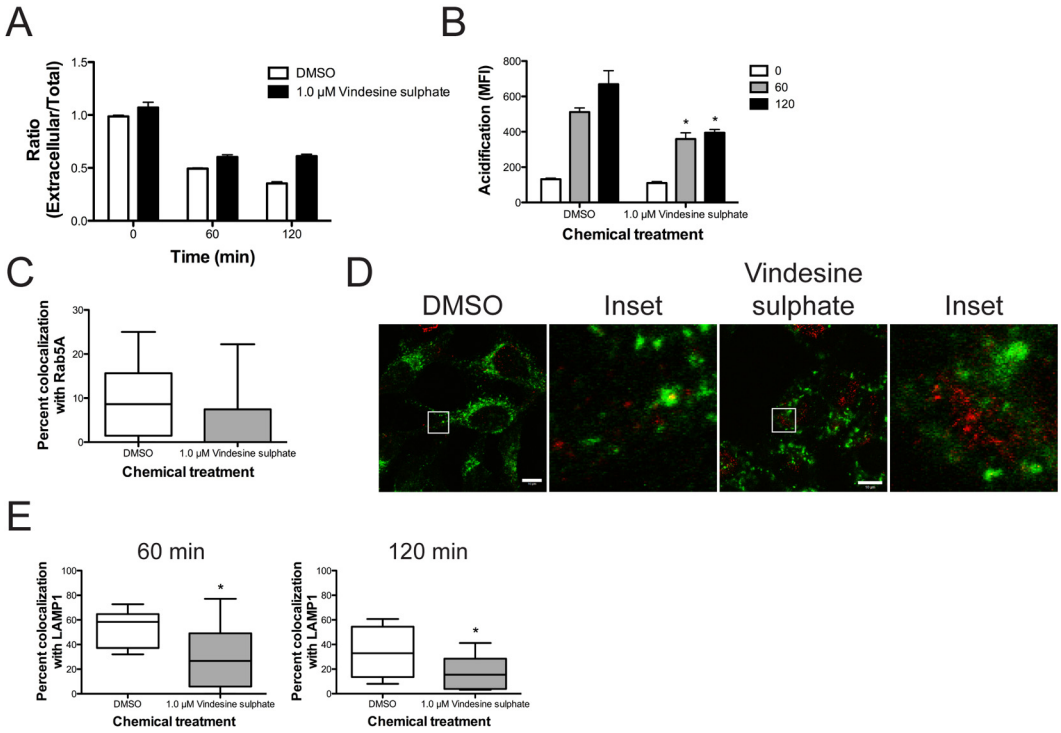

FIG 4 Vindesine sulfate impairs transport of reovirus in the endocytic pathway. (A) CCL2 HeLa cells were incubated with DMSO or 1 μM vindesine sulfate, adsorbed with A546-labeled T3SA+ at an MOI of 5×10^3 particles/cell, and incubated with DMSO or 1 μM vindesine sulfate for the times shown. Cells were stained with reovirus-specific antiserum using nonpermeabilizing conditions. Mean fluorescence intensity (MFI) was assessed by flow cytometry. Results are presented as a ratio of extracellular to total mean fluorescence intensity for triplicate samples. Error bars indicate standard deviations. (B) CCL2 HeLa cells were incubated with DMSO or 1 μM vindesine sulfate, adsorbed with pHrodo-labeled T3SA+ at an MOI of 5×10^3 particles/cell, and incubated with DMSO or 1 μM vindesine sulfate for the times shown. MFI was assessed by flow cytometry. Error bars indicate standard deviations. (C) CCL2 HeLa cells were transfected with EGFP-Rab5A, incubated with DMSO or 1 μM vindesine sulfate, adsorbed with A546-labeled T3SA+ at an MOI of 10^4 particles/cell, and incubated with DMSO or 1 μM vindesine for 120 min. Cells were fixed and imaged by confocal microscopy. Results are expressed as percent colocalization of reovirus particles with Rab5A-positive endosomes ($n = 8$ cells per condition). Error bars indicate minimum and maximum values. (D) CCL2 HeLa cells were incubated with DMSO or 1 μM vindesine sulfate, adsorbed with A546-labeled T3SA+ (red) at an MOI of 10^4 particles/cell, and incubated with DMSO or 1 μM vindesine sulfate for 60 or 120 min. Cells were fixed, stained with a LAMP1-specific antibody (green), and imaged by confocal microscopy. Representative images from 120 min shown. Insets depict enlarged areas of boxed regions. Scale bars, 10 μm. (E) Percent colocalization of reovirus particles with LAMP-1-positive endosomes ($n = 10$ cells per condition). Error bars indicate minimum and maximum values. *, $P < 0.05$ in comparison to DMSO by Student's t test.

1 h, adsorbed with reovirus, and incubated from 0 to 120 min. Whole-cell lysates were resolved by SDS-PAGE and immunoblotted using a reovirus-specific antiserum to detect viral capsid protein μ1 and its major cleavage fragment, δ (Fig. 6C). In control-treated cells, δ was detected by 20 min, with increasing band intensity noted over the experimental time course. In vindesine sulfate-treated cells, δ was not detected until 60 min after adsorption. Densitometric analysis of three independent experiments showed delayed μ1-to-δ conversion at all times tested in vindesine sulfate-treated cells in comparison to control cells (Fig. 6D). We conclude that inhibition of microtubule function leads to inefficient access to acidified endosomal compartments, which in turn delays the disassembly of internalized virions.

DISCUSSION

In this study, we found that reovirus colocalizes with microtubule tracks during cell entry and requires microtubule function and microtubule motor dynein 1 to efficiently traverse the endocytic pathway. Microtubule function is not required for internalization of reovirus virions but rather facilitates targeting of reovirus to acidified endosomes for viral disassembly. Treatment of cells with microtubule inhibitors blocks reovirus infection in a temporal window in which the virus transits from early to late endosomes. These results highlight a new function for microtubules in reovirus replication and suggest that impairment of microtubule activity might diminish infection by viruses that require access to late endosomes to establish productive infection.

Endocytic uptake of macromolecular cargo requires the coordinated action of several host factors, including receptors, Rab GTPases, and enzymes that regulate endocytic transport by modifying targets at specific intracellular sites. For some cargo, microtubules and microtubule-associated motors are required for transport to and from the cell surface. Importantly, the maturation of early to late endosomes is dependent on microtubule function (34). Rab-interacting lysosomal protein (RILP), a Rab7 adapter, recruits dynactin and dynein to late endosomes, promoting late endosome movement toward the cell interior (35). Reovirus is transported to Rab7-marked endosomes during cell entry (13), and expression of dominant-negative RILP inhibits reovirus infection (13). Thus, disruption of microtubule function appears to delay reovirus disassembly by slowing the maturation of the reovirus-containing endosomal fraction. This model is supported by the observed decrease in colocalization of reovirus with LAMP1-marked endosomes. Additional support comes from the

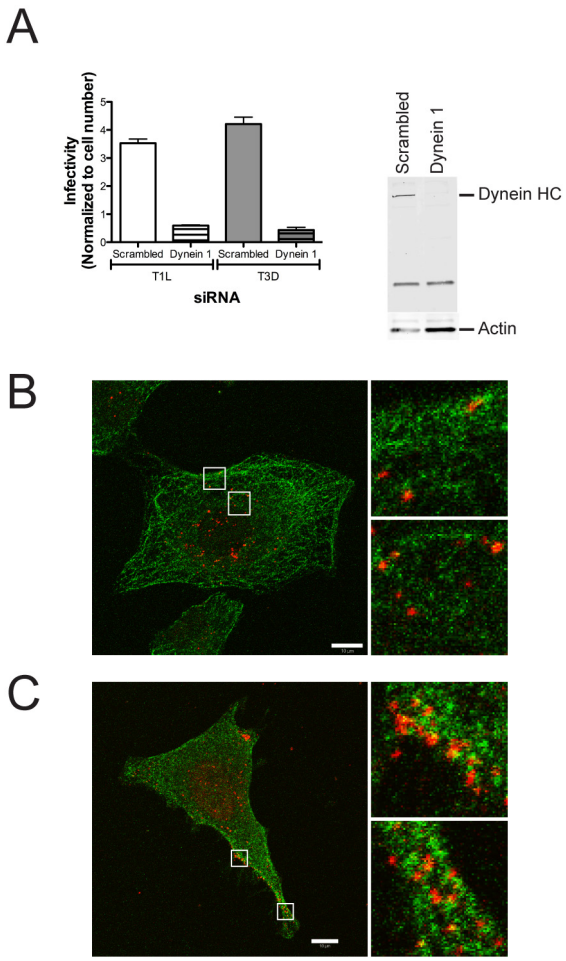

FIG 5 Reovirus uses microtubule motor dynein 1 to efficiently infect cells. (A) (Left panel) HBMECs were transfected with a nonspecific siRNA (scrambled) or an siRNA specific for dynein 1 heavy chain (dynein 1), adsorbed with reovirus strains T1L or T3D at an MOI of 15 PFU/cell, and incubated for 24 h. Cells were scored for infection by indirect immunofluorescence. Results are presented as mean fluorescence intensity normalized to cell number and background fluorescence for triplicate wells. Error bars indicate standard deviations. (Right panel) Whole-cell lysates of HBMECs transfected with nonspecific or dynein 1-specific siRNAs were analyzed by immunoblotting using dynein 1 heavy chain (HC)-specific or actin-specific antibodies. (B and C) HBMECs (B) or CCL2 HeLa cells (C) were adsorbed with T1L at an MOI of 10^4 particles/cell and incubated for 20 min. Cells were stained for reovirus (red) and dynein 1 heavy chain (green) and imaged by confocal microscopy. A single section from a Z-stack is shown. Insets depict enlarged areas from boxed regions. Scale bars, 10 μm.

observation that vindesine sulfate does not diminish infection after adsorption of ISVPs, which are uncoated *in vitro* and thus do not require access to cathepsin-containing organelles to establish infection (16–18). As an important control, vindesine sulfate does not inhibit infection by CHKV, which uncoats in early endosomes (33). Impairment of endosomal maturation might be responsible for the aggregates of reovirus particles observed in vindesine sulfate-treated cells. Interestingly, reovirus virions do not accumulate in early endosomes in cells treated with vindesine sulfate (Fig. 4C). Instead, viral particles in vindesine sulfate-treated cells aggregate in clusters in the cytoplasm. These observations suggest that in the absence of microtubule function, viral particles are missorted during cell entry and not trapped in early endosomes.

Our report highlights the potential for drugs that inhibit endosomal maturation for use as broadly active anti-infectives. Such drugs could inhibit viruses, bacteria, bacterial toxins, and parasites that require access to late endosomes and lysosomes to mediate pathological effects. Avian reovirus, a fusogenic reovirus that, unlike mammalian reovirus, enters cells via caveolin-1 and causes infected cells to form syncytia (36, 37), also uses microtubules to enter cells (36). This finding suggests that employment of microtubules by fusogenic and nonfusogenic reoviruses is a conserved cell entry mechanism despite the use of different endocytic uptake pathways. Adenovirus (38) and Borna disease virus (39) also use microtubules and microtubule motors during cell entry (40). *Enterococcus faecalis* requires microtubules for efficient internalization into cells (41). Cytotoxic necrotizing factor 1 (CNF1), a toxin produced by some pathogenic *Escherichia coli* strains, requires microtubule function to access late endosomes for the processing required for cytotoxicity (42). Flubendazole, a compound identified in our screen as impairing reovirus cytotoxicity, inhibits infection by nematodes (43). While currently available microtubule-inhibiting compounds are associated with significant adverse effects (21), it is possible that safer agents could be developed for anti-infective therapies that transiently inhibit endosomal maturation.

Reovirus strain T3D, which has been trademarked as Reolysin, is being evaluated in clinical trials for efficacy as an oncolytic agent in combination with various chemotherapeutic drugs, including the microtubule inhibitor docetaxel (5). Our findings suggest that pairing reovirus with microtubule-inhibiting agents during oncolytic therapy may limit virus-induced cell killing. Cancer treatment regimens that use reovirus and microtubule-inhibiting drugs may be more efficacious if the administration of virus and chemotherapeutic is not simultaneous. We found that addition of vindesine sulfate to reovirus-infected cells at up to 1 h after infection fails to significantly diminish infection. Thus, we think it important to assess the effects of pharmacological agents on viral infectivity when these treatments are used in combination.

The NCC screen yielded six candidate compounds that do not target microtubules. Procarbazine, which promotes DNA damage (44), and 6-azauridine, which inhibits pyrimidine synthesis (45), likely impair reovirus replication by affecting viral transcription or genome replication. The identification of nicotinic acetylcholine receptor and serotonin receptor agonists as drugs that impair reovirus-induced cytotoxicity points to interesting cellular targets. The nicotinic acetylcholine receptor is expressed in the brain (46), and serotonin receptors are expressed in both the brain and gastrointestinal tract (47). Both of these organs are sites for reovirus replication in the infected host (1). Finally, the identification of indomethacin, which inhibits cyclooxygenase 1 and 2 (48), suggests a yet-uncharacterized function for cyclooxygenases in reovirus replication. Further studies are required to determine whether these drugs inhibit reovirus replication and to define the antiviral mechanisms by which they act.

The identification of host molecules that regulate steps in viral replication enhances an understanding of how viruses use basic cellular processes to propagate and disseminate. These studies also yield new knowledge about cellular functions and illuminate new targets for antiviral drug development. In this study, we used a high-throughput screening approach to identify microtubules and microtubule motor dynein 1 as host factors required for reovirus cell entry, initiation of infection, and consequent cell death.

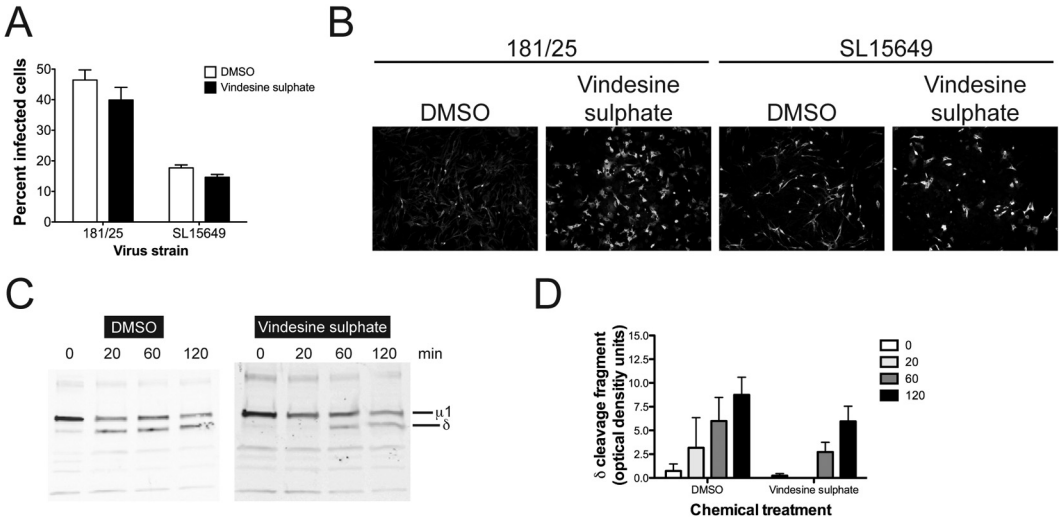

FIG 6 Vindesine sulfate does not affect CHKV infection but alters reovirus disassembly kinetics. (A) BHK-21 cells were incubated with DMSO or 1 μM vindesine sulfate, adsorbed with CHKV strain 181/25 or SL15649 at an MOI of 1 PFU/cell, and incubated with DMSO or vindesine sulfate for 10 h. Cells were stained with CHKV-specific antiserum and DAPI to detect nuclei. Infection was quantified by indirect immunofluorescence. Results are presented as percent infected cells from triplicate wells. Error bars indicate standard deviations. (B) Images of DMSO- or vindesine sulfate-treated BHK-21 cells infected with CHKV strain 181/25 or SL15659 and stained with CHKV-specific antiserum. (C) CCL2 HeLa cells were incubated with DMSO or 1 μM vindesine sulfate, adsorbed with T3SA+ at an MOI of 10 PFU/cell, and incubated with DMSO or 1 μM vindesine sulfate for the times shown. Whole-cell lysates were immunoblotted using reovirus-specific antiserum. (D) Densitometric analysis of the δ cleavage fragment of reovirus μ1 protein from triplicate experiments. Error bars indicate standard errors of the mean. The key indicates times in minutes.

Findings made in this study should contribute to the development of improved strategies for use of reovirus as an oncolytic and establish a platform for testing microtubule inhibitors as antiinfective agents.

MATERIALS AND METHODS

Cells, viruses, chemical inhibitors, and antibodies. Spinner-adapted murine L929 cells, CCL2 HeLa cells, HeLa S3 cells, and HBMECs were cultivated as previously described (13, 28). BHK-21 and Vero81 cells were cultivated in Alpha minimal essential medium (MEM) (Sigma) supplemented to contain 5% fetal bovine serum (FBS) (Vero81) or 10% FBS (BHK-21) and L-glutamine. Medium for all cells was supplemented with penicillin-streptomycin (Invitrogen) and amphotericin B (Sigma).

Purified virions of reovirus strains T1L, T3D, and T3SA+ were prepared by plaque purification and passage using L929 cells as previously described (12, 13, 28). ISVPs were generated by treating particles with α-chymotrypsin (Sigma) as previously described (12). Reovirus virions were labeled with succinimidyl ester Alexa Fluor 546 (A546) or pHrodo SE (pHrodo) (Invitrogen) as previously described (13).

CHKV strain 181/25 was provided by Robert Tesh (University of Texas Medical Branch). Viral RNA was isolated from a plaque-purified isolate, and cDNA was generated using random hexamers. Overlapping fragments were amplified, cloned into pCR2.1 TOPO (Invitrogen), and sequenced. The 5′ untranslated region was sequenced using 5′ rapid amplification of cDNA ends. An infectious clone was synthesized by GenScript (Piscataway, NJ) in four fragments. Genome fragments were assembled and subcloned into pSinRep5 low-copy-number plasmid. The CHKV strain SL15649 infectious clone was provided by Mark Heise (University of North Carolina at Chapel Hill) (49). Infectious clone plasmids for 181/25 and SL15649 were linearized and transcribed *in vitro* using an mMessage mMachine SP6 transcription kit (Ambion). BHK-21 cells were electroporated with viral RNA and incubated at 37°C for 24 h. Supernatants containing progeny virus were harvested from electroporated cells and stored at −80°C. All experiments using SL15649 were performed using biosafety level 3 conditions.

Ammonium chloride (NH_4Cl; Gibco) was resuspended in water. E64-d, colchicine, nocodazole (Sigma), docetaxel, flubendazole, and vindesine sulfate (Sequoia Research Products) were resuspended in DMSO. The immunoglobulin G (IgG) fraction of a rabbit antiserum raised against T1L or T3D was purified as previously described (6). LAMP1-specific and dynein heavy chain-specific monoclonal antibodies (Abcam), α-tubulin-specific monoclonal antibody (Cell Signaling Technology), actin-specific polyclonal antiserum (Santa Cruz Biotechnology), and CHKV-specific antiserum (ATCC) were used for indirect immunofluorescence experiments, infectivity assays, and immunoblot analyses. Alexa Fluor-conjugated antibodies (Invitrogen) were used as secondary antibodies.

Cell viability assay. HeLa S3 cells were incubated with OMEM-1 (Invitrogen) medium containing DMSO, E64-d, NH_4Cl, or microtubule inhibitors at 37°C for 1 h and adsorbed with T3SA+ at a multiplicity of infection (MOI) of 200 PFU/cell in the presence of DMSO, E64-d, NH_4Cl, or microtubule inhibitors in OMEM-I medium at 37°C for 48 h. Cell viability was quantified using the Cell Titer Glo assay.

Quantification of reovirus infectivity. Reovirus infectivity was assessed by indirect immunofluorescence (50). Cells were incubated with complete medium containing DMSO or chemical inhibitors at 37°C for 1 h, adsorbed with reovirus at room temperature for 1 h, and incubated with complete medium containing DMSO or chemical inhibitors at 37°C for 20 h. Cells were fixed and stained with reovirus-specific antiserum and goat anti-rabbit IRDye 800 (Li-COR), DRAQ5 (Cell Signaling), and Sapphire700 (Li-COR). Immunofluorescence was detected using a Li-COR Odyssey infrared imaging system (Li-COR). Infectivity was quantified using the In-Cell Western feature of the Odyssey software suite.

Confocal microscopy of reovirus-infected cells. Confocal microscopy of reovirus-infected cells was performed as previously described (12, 13). HeLa CCL2 cells were incubated with complete medium containing DMSO or vindesine sulfate at 37°C for 1 h. Cells were adsorbed with reovirus at an MOI of 2×10^4 particles/cell and either fixed with ice-cold methanol or incubated in complete medium containing DMSO or vindesine sulfate at 37°C for 120 min followed by fixation with ice-cold methanol. Cells were incubated with reovirus-specific polyclonal and α-tubulin-specific antiserum followed by Alexa Fluor IgG A488 or A546.

Coverslips were placed on slides using aqua-Poly/Mount mounting medium (Polysciences, Inc.).

Colocalization of reovirus particles with Rab5A-positive endosomes was assessed by transfecting CCL2 HeLa cells with EGFP-Rab5A (13) using Fugene 6 (Roche). Cells were incubated at 37°C for 24 h, incubated with medium containing DMSO or vindesine sulfate at 37°C for 1 h, adsorbed with A546-labeled reovirus at an MOI of 10^4 particles/cell, incubated with complete medium containing DMSO or vindesine sulfate for 120 min, fixed for 20 min with 10% formalin, quenched with 0.1 M glycine, washed with phosphate-buffered saline (PBS), and placed on slides using aqua-Poly/Mount mounting medium.

Colocalization of reovirus particles with LAMP1-positive endosomes was determined by incubating CCL2 HeLa cells with complete medium containing DMSO or vindesine sulfate at 37°C for 1 h followed by adsorption with A546-labeled reovirus at an MOI of 10^4 particles/cell and incubation with complete medium containing DMSO or vindesine sulfate for various intervals, after which the cells were fixed and stained with LAMP1-specific antibody. Colocalization of reovirus particles with dynein 1 was determined by adsorbing HBMECs or CCL2 HeLa cells with reovirus at an MOI of 10^4 particles/cell, after which the cells were incubated with complete medium for 20 min, fixed in methanol, and stained with reovirus-specific antiserum and dynein heavy chain-specific antibody.

Images were captured using a Zeiss LSM 510 Meta laser scanning confocal microscope and a 63×/1.40 numerical aperture (NA) Plan-Apochromat oil objective. Pinhole sizes were identical for all fluors. Images were normalized for pixel intensity, brightness, and contrast. Single sections of 0.39 μM thickness from a Z-stack are presented. Colocalization was determined using the Profile function of LSM Image software (Zeiss) (12, 13).

Flow cytometric analysis of reovirus internalization. CCL2 HeLa cells were treated with DMSO or vindesine sulfate in complete medium at 37°C for 1 h and adsorbed with A546-labeled reovirus at an MOI of 5×10^3 particles/cell at room temperature for 1 h. The inoculum was removed, and cells were incubated with complete medium containing DMSO or vindesine sulfate for various intervals. Cells were detached with Cellstripper (Cellgro) at 37°C for 15 min, quenched with fluorescence-activated cell sorter (FACS) buffer (PBS with 2% FBS), and stained with reovirus-specific polyclonal antiserum in FACS buffer at 4°C for 30 min. Cells were washed with FACS buffer, stained with Alexa Fluor-conjugated antibodies in FACS buffer at 4°C for 30 min, and fixed in PBS with 1% electron microscopy (EM)-grade paraformaldehyde (FACS Fix; Electron Microscopy Sciences).

Flow cytometric analysis of reovirus acidification was performed as previously described (13). Cells were treated with DMSO or vindesine sulfate in complete medium at 37°C for 1 h, adsorbed with pHrodo-labeled reovirus at an MOI of 5×10^3 particles/cell, incubated in complete medium containing DMSO or vindesine sulfate for various intervals, and fixed in FACS Fix. Cell staining was assessed using a BD LSRII flow cytometer and quantified using FlowJo software.

Knockdown of dynein 1 heavy chain by RNAi. HBMECs were transfected with 10 nM nonspecific siRNA or an siRNA specific for the dynein 1 heavy chain using Lipofectamine RNAi Max (Invitrogen) according to the manufacturer's instructions. Cells were incubated at 37°C for 48 h, adsorbed with reovirus at an MOI of 15 PFU/cell at room temperature for 1 h, and incubated at 37°C for 24 h. Cells were fixed with methanol and scored for infection by indirect immunofluorescence.

Immunoblotting for dynein 1 heavy chain. Immunoblot analysis of cell lysates was performed as previously described (12). Total cell lysates of HBMECs transfected with nonspecific or dynein 1 heavy chain-specific siRNAs were resolved by SDS-PAGE and immunoblotted with primary antibodies specific for dynein 1 heavy chain and actin. Membranes were scanned using an Odyssey imaging system, and band intensity was quantified using the Odyssey software suite.

CHKV infectivity assay. BHK-21 cells were incubated with DMSO or vindesine sulfate in complete medium at 37°C for 1 h and adsorbed with CHKV strain 181/25 or SL15649 at an MOI of 1 PFU/cell in the presence of DMSO or vindesine sulfate at 37°C for 1 h. The inoculum was removed, and cells were incubated with complete medium containing DMSO or vindesine sulfate at 37°C for 10 h. Cells were fixed with ice-cold methanol and incubated with CHKV-specific polyclonal antiserum, A488-labeled IgG, and 4′,6-diamidino-2-phenylindole (DAPI; Invitrogen). Cells were visualized using an Axiovert 200 fluorescence microscope (Zeiss). CHKV-positive cells were enumerated in three fields of view for triplicate samples and normalized to total cells per field.

Assessment of reovirus disassembly kinetics. CCL2 HeLa cells were treated with DMSO or vindesine sulfate in complete medium at 37°C for 1 h, adsorbed with reovirus at an MOI of 10 PFU/cell at room temperature for 1 h, and incubated in complete medium with DMSO or vindesine sulfate for various intervals. Total cell lysates were resolved by SDS-PAGE and immunoblotted with reovirus-specific polyclonal antiserum. Immunoblots were quantified by densitometry analysis using Odyssey software.

Statistical analysis. Mean values for at least triplicate experiments were compared using one-way analysis of variance (ANOVA) with Dunnett's multiple-comparison test (Graph Pad Prism). P values of <0.05 were considered to be statistically significant. Alternatively, samples were compared using an unpaired Student's t test (Graph Pad Prism). P values of <0.05 were considered to be statistically significant.

SUPPLEMENTAL MATERIAL

Supplemental material for this article may be found at http://mbio.asm.org/lookup/suppl/doi:10.1128/mBio.00405-13/-/DCSupplemental.

Text S1, DOCX file, 0.1 MB.
Figure S1, TIF file, 8.9 MB.
Table S1, PDF file, 0.1 MB.

ACKNOWLEDGMENTS

We thank Jennifer Konopka and Caroline Lai for critical review of the manuscript. We are grateful to members of the Dermody laboratory for useful suggestions during the course of this study. Small-molecule screening was conducted with assistance from the Vanderbilt High-Throughput Screening Facility. Confocal microscopy experiments were conducted in the Vanderbilt Cell Imaging Shared Resource. Flow cytometry experiments were performed in the Vanderbilt Cytometry Shared Resource.

This work was supported by Public Health Service awards T32 HL07751 (B.A.M. and A.W.A.), F32 A1801082 (B.A.M.), R01 AI32539 (T.S.D.), and U54 AI057157 (T.S.D.) and by the Elizabeth B. Lamb Center for Pediatric Research. Additional support was provided by Public Health Service awards P30 CA68485 for the Vanderbilt-Ingram Cancer Center and P60 DK20593 for the Vanderbilt Diabetes Research and Training Center.

REFERENCES

1. **Dermody TS, Parker J, Sherry B.** 2013. Orthoreoviruses. pp. 1304–1346. *In* Knipe DM, Howley PM (ed.), Fields virology, vol. 2, 6th ed., Lippincott Williams & Wilkins, Philadelphia, PA.
2. **Ouattara LA, Barin F, Barthez MA, Bonnaud B, Roingeard P, Goudeau A, Castelnau P, Vernet G, Paranhos-Baccalà G, Komurian-Pradel F.** 2011. Novel human reovirus isolated from children with acute necrotizing encephalopathy. Emerg. Infect. Dis. **17:**1436–1444.
3. **Kobayashi T, Antar AA, Boehme KW, Danthi P, Eby EA, Guglielmi KM, Holm GH, Johnson EM, Maginnis MS, Naik S, Skelton WB, Wetzel JD, Wilson GJ, Chappell JD, Dermody TS.** 2007. A plasmid-based reverse genetics system for animal double-stranded RNA viruses. Cell Host Microbe **1:**147–157.
4. **London SD, Cebra-Thomas JA, Rubin DH, Cebra JJ.** 1990. CD8 lymphocyte subpopulations in Peyer's patches induced by reovirus serotype 1 infection. J. Immunol. **144:**3187–3194.
5. **Maitra R, Ghalib MH, Goel S.** 2012. Reovirus: a targeted therapeutic—progress and potential. Mol. Cancer Res. **10:**1514–1525.
6. **Barton ES, Connolly JL, Forrest JC, Chappell JD, Dermody TS.** 2001.

Utilization of sialic acid as a coreceptor enhances reovirus attachment by multistep adhesion strengthening. J. Biol. Chem. **276:**2200–2211.
7. **Reiss K, Stencel JE, Liu Y, Blaum BS, Reiter DM, Feizi T, Dermody TS, Stehle T.** 2012. The GM2 glycan serves as a functional coreceptor for serotype 1 reovirus. PLoS Pathog. **8:**e1003078. doi: 10.1371/journal.ppat.1003078.
8. **Barton ES, Forrest JC, Connolly JL, Chappell JD, Liu Y, Schnell FJ, Nusrat A, Parkos CA, Dermody TS.** 2001. Junction adhesion molecule is a receptor for reovirus. Cell **104:**441–451.
9. **Campbell JA, Schelling P, Wetzel JD, Johnson EM, Wilson GA, Forrest JC, Aurrand-Lions M, Imhof BA, Stehle T, Dermody TS.** 2005. Junctional adhesion molecule-A serves as a receptor for prototype and field-isolate strains of mammalian reovirus. J. Virol. **79:**7967–7978.
10. **Forrest JC, Campbell JA, Schelling P, Stehle T, Dermody TS.** 2003. Structure-function analysis of reovirus binding to junctional adhesion molecule 1. Implications for the mechanism of reovirus attachment. J. Biol. Chem. **278:**48434–48444.
11. **Maginnis MS, Forrest JC, Kopecky-Bromberg SA, Dickeson SK, Santoro SA, Zutter MM, Nemerow GR, Bergelson JM, Dermody TS.** 2006. Beta1 integrin mediates internalization of mammalian reovirus. J. Virol. **80:**2760–2770.
12. **Mainou BA, Dermody TS.** 2011. Src kinase mediates productive endocytic sorting of reovirus during cell entry. J. Virol. **85:**3203–3213.
13. **Mainou BA, Dermody TS.** 2012. Transport to late endosomes is required for efficient reovirus infection. J. Virol. **86:**8346–8358.
14. **Ebert DH, Deussing J, Peters C, Dermody TS.** 2002. Cathepsin L and cathepsin B mediate reovirus disassembly in murine fibroblast cells. J. Biol. Chem. **277:**24609–24617.
15. **Maratos-Flier E, Goodman MJ, Murray AH, Kahn CR.** 1986. Ammonium inhibits processing and cytotoxicity of reovirus, a nonenveloped virus. J. Clin. Invest. **78:**1003–1007.
16. **Sturzenbecker LJ, Nibert M, Furlong D, Fields BN.** 1987. Intracellular digestion of reovirus particles requires a low pH and is an essential step in the viral infectious cycle. J. Virol. **61:**2351–2361.
17. **Borsa J, Morash BD, Sargent MD, Copps TP, Lievaart PA, Szekely JG.** 1979. Two modes of entry of reovirus particles into L cells. J. Gen. Virol. **45:**161–170.
18. **Boulant S, Stanifer M, Kural C, Cureton DK, Massol R, Nibert ML, Kirchhausen T.** 2013. Similar uptake but different trafficking and escape routes of reovirus virions and ISVPs imaged in polarized MDCK cells. Mol. Biol. Cell, **24:**1196–1207.
19. **Jordan MA.** 2002. Mechanism of action of antitumor drugs that interact with microtubules and tubulin. Curr. Med. Chem. Anticancer Agents **2:**1–17.
20. **Dumontet C, Jordan MA.** 2010. Microtubule-binding agents: a dynamic field of cancer therapeutics. Nat. Rev. Drug Discov. **9:**790–803.
21. **McGrogan BT, Gilmartin B, Carney DN, McCann A.** 2008. Taxanes, microtubules and chemoresistant breast cancer. Biochim. Biophys. Acta **1785:**96–132.
22. **Guéritte F.** 2001. General and recent aspects of the chemistry and structure-activity relationships of taxoids. Curr. Pharm. Des. **7:**1229–1249.
23. **Duflos A, Kruczynski A, Barret JM.** 2002. Novel aspects of natural and modified vinca alkaloids. Curr. Med. Chem. Anticancer Agents **2:**55–70.
24. **Gennerich A, Vale RD.** 2009. Walking the walk: how kinesin and dynein coordinate their steps. Curr. Opin. Cell Biol. **21:**59–67.
25. **Danthi P, Coffey CM, Parker JS, Abel TW, Dermody TS.** 2008. Independent regulation of reovirus membrane penetration and apoptosis by the mu1 phi domain. PLoS Pathog. **4:**e1000248. doi:10.1371/journal.ppat.1000248.
26. **Ebert DH, Wetzel JD, Brumbaugh DE, Chance SR, Stobie LE, Baer GS, Dermody TS.** 2001. Adaptation of reovirus to growth in the presence of protease inhibitor E64 segregates with a mutation in the carboxy terminus of viral outer-capsid protein sigma3. J. Virol. **75:**3197–3206.
27. **Connolly JL, Barton ES, Dermody TS.** 2001. Reovirus binding to cell surface sialic acid potentiates virus-induced apoptosis. J. Virol. **75:**4029–4039.
28. **Lai CM, Mainou BA, Kim KS, Dermody TS.** 2013. Directional release of reovirus from the apical surface of polarized endothelial cells. mBio **4:**e00049-13. doi: 10.1128/mBio.00049-13.
29. **Weatherbee JA, Luftig RB, Weihing RR.** 1978. In vitro polymerization of microtubules from HeLa cells. J. Cell Biol. **78:**47–57.
30. **Doyle JD, Danthi P, Kendall EA, Ooms LS, Wetzel JD, Dermody TS.** 2012. Molecular determinants of proteolytic disassembly of the reovirus outer capsid. J. Biol. Chem. **287:**8029–8038.
31. **Bayer N, Schober D, Prchl E, Murphy RF, Blaas D, Fuchs R.** 1998. Effect of bafilomycin A1 and nocodazole on endocytic transport in HeLa cells: implications for viral uncoating and infection. J. Virol. **72:**9645–9655.
32. **Pastorino B, Muyembe-Tamfum JJ, Bessaud M, Tock F, Tolou H, Durand JP, Peyrefitte CN.** 2004. Epidemic resurgence of chikungunya virus in democratic Republic of the Congo: identification of a new Central African strain. J. Med. Virol. **74:**277–282.
33. **Bernard E, Solignat M, Gay B, Chazal N, Higgs S, Devaux C, Briant L.** 2010. Endocytosis of chikungunya virus into mammalian cells: role of clathrin and early endosomal compartments. PLoS One **5:**e11479. doi: 10.1371/journal.pone.0011479.
34. **Huotari J, Helenius A.** 2011. Endosome maturation. EMBO J. **30:**3481–3500.
35. **Jordens I, Fernandez-Borja M, Marsman M, Dusseljee S, Janssen L, Calafat J, Janssen H, Wubbolts R, Neefjes J.** 2001. The Rab7 effector protein RILP controls lysosomal transport by inducing the recruitment of dynein-dynactin motors. Curr. Biol. **11:**1680–1685.
36. **Huang WR, Wang YC, Chi PI, Wang L, Wang CY, Lin CH, Liu HJ.** 2011. Cell entry of avian reovirus follows a caveolin-1-mediated and dynamin-2-dependent endocytic pathway that requires activation of p38 mitogen-activated protein kinase (MAPK) and Src signaling pathways as well as microtubules and small GTPase Rab5 protein. J. Biol. Chem. **286:**30780–30794.
37. **Salsman J, Top D, Boutilier J, Duncan R.** 2005. Extensive syncytium formation mediated by the reovirus FAST proteins triggers apoptosis-induced membrane instability. J. Virol. **79:**8090–8100.
38. **Bremner KH, Scherer J, Yi J, Vershinin M, Gross SP, Vallee RB.** 2009. Adenovirus transport via direct interaction of cytoplasmic dynein with the viral capsid hexon subunit. Cell Host Microbe **6:**523–535.
39. **Clemente R, de la Torre JC.** 2009. Cell entry of Borna disease virus follows a clathrin-mediated endocytosis pathway that requires Rab5 and microtubules. J. Virol. **83:**10406–10416.
40. **Hsieh MJ, White PJ, Pouton CW.** 2010. Interaction of viruses with host cell molecular motors. Curr. Opin. Biotechnol. **21:**633–639.
41. **Millán D, Chiriboga C, Patarroyo MA, Fontanilla MR.** 2013. Enterococcus faecalis internalization in human umbilical vein endothelial cells (HUVEC). Microb. Pathog. **57:**62–69.
42. **Contamin S, Galmiche A, Doye A, Flatau G, Benmerah A, Boquet P.** 2000. The p21 Rho-activating toxin cytotoxic necrotizing factor 1 is endocytosed by a clathrin-independent mechanism and enters the cytosol by an acidic-dependent membrane translocation step. Mol. Biol. Cell **11:**1775–1787.
43. **Hanser E, Mehlhorn H, Hoeben D, Vlaminck K.** 2003. In vitro studies on the effects of flubendazole against Toxocara canus and Ascaris suum. Parasitol. Res. **89:**63–74.
44. **Erikson JM, Tweedie DJ, Ducore JM, Prough RA.** 1989. Cytotoxicity and DNA damage caused by the azoxy metabolites of procarbazine in L1210 tumor cells. Cancer Res. **49:**127–133.
45. **Tatibana M, Kita K, Asai T.** 1982. Stimulation by 6-azauridine of carbamoyl phosphate synthesis for pyrimidine biosynthesis in mouse spleen slices. Eur. J. Biochem. **128:**625–629.
46. **Changeux JP.** 2012. The nicotinic acetylcholine receptor: the founding father of the pentameric ligand-gated ion channel superfamily. J. Biol. Chem. **287:**40207–40215.
47. **Hannon J, Hoyer D.** 2008. Molecular biology of 5-HT receptors. Behav. Brain Res. **195:**198–213.
48. **Dannhardt G, Kiefer W.** 2001. Cyclooxygenase inhibitors—current status and future prospects. Eur. J. Med. Chem. **36:**109–126.
49. **Morrison TE, Oko L, Montgomery SA, Whitmore AC, Lotstein AR, Gunn BM, Elmore SA, Heise MT.** 2011. A mouse model of chikungunya virus-induced musculoskeletal inflammatory disease: evidence of arthritis, tenosynovitis, myositis, and persistence. Am. J. Pathol. **178:**32–40.
50. **Iskarpatyoti JA, Willis JZ, Guan J, Morse EA, Ikizler M, Wetzel JD, Dermody TS, Contractor N.** 2012. A rapid, automated approach for quantitation of rotavirus and reovirus infectivity. J. Virol. Methods **184:**1–7.

RESEARCH ARTICLE

Reovirus Forms Neo-Organelles for Progeny Particle Assembly within Reorganized Cell Membranes

Isabel Fernández de Castro,[a] Paula F. Zamora,[b,c] Laura Ooms,[b] José Jesús Fernández,[d] Caroline M.-H. Lai,[b,c] Bernardo A. Mainou,[c,e] Terence S. Dermody,[b,c,e] Cristina Risco[a]

Cell Structure Laboratory, National Center for Biotechnology, National Research Council (CNB-CSIC), Campus UAM, Madrid, Spain[a]; Department of Pathology, Microbiology, and Immunology, Vanderbilt University School of Medicine, Nashville, Tennessee, USA[b]; Elizabeth B. Lamb Center for Pediatric Research, Vanderbilt University School of Medicine, Nashville, Tennessee, USA[c]; Department of Macromolecular Structures, National Center for Biotechnology, National Research Council (CNB-CSIC), Campus UAM, Madrid, Spain[d]; Department of Pediatrics, Vanderbilt University School of Medicine, Nashville, Tennessee, USA[e]

P.F.Z. and L.O. contributed equally to this work.

ABSTRACT **Most viruses that replicate in the cytoplasm of host cells form neo-organelles that serve as sites of viral genome replication and particle assembly. These highly specialized structures concentrate viral replication proteins and nucleic acids, prevent the activation of cell-intrinsic defenses, and coordinate the release of progeny particles. Despite the importance of inclusion complexes in viral replication, there are key gaps in the knowledge of how these organelles form and mediate their functions. Reoviruses are nonenveloped, double-stranded RNA (dsRNA) viruses that serve as tractable experimental models for studies of dsRNA virus replication and pathogenesis. Following reovirus entry into cells, replication occurs in large cytoplasmic structures termed inclusions that fill with progeny virions. Reovirus inclusions are nucleated by viral nonstructural proteins, which in turn recruit viral structural proteins for genome replication and particle assembly. Components of reovirus inclusions are poorly understood, but these structures are generally thought to be devoid of membranes. We used transmission electron microscopy and three-dimensional image reconstructions to visualize reovirus inclusions in infected cells. These studies revealed that reovirus inclusions form within a membranous network. Viral inclusions contain filled and empty viral particles and microtubules and appose mitochondria and rough endoplasmic reticulum (RER). Immunofluorescence confocal microscopy analysis demonstrated that markers of the ER and ER-Golgi intermediate compartment (ERGIC) codistribute with inclusions during infection, as does dsRNA. dsRNA colocalizes with the viral protein σNS and an ERGIC marker inside inclusions. These findings suggest that cell membranes within reovirus inclusions form a scaffold to coordinate viral replication and assembly.**

IMPORTANCE **Viruses alter the architecture of host cells to form an intracellular environment conducive to viral replication. This step in viral infection requires the concerted action of viral and host components and is potentially vulnerable to pharmacological intervention. Reoviruses form large cytoplasmic replication sites called inclusions, which have been described as membrane-free structures. Despite the importance of inclusions in the reovirus replication cycle, little is known about their formation and composition. We used light and electron microscopy to demonstrate that reovirus inclusions are membrane-containing structures and that the endoplasmic reticulum (ER) and the ER-Golgi intermediate compartment interact closely with these viral organelles. These findings enhance our understanding of the cellular machinery usurped by viruses to form inclusion organelles and complete an infectious cycle. This information, in turn, may foster the development of antiviral drugs that impede this essential viral replication step.**

Received 6 November 2013 **Accepted** 21 January 2014 **Published** 18 February 2014

Citation Fernández de Castro I, Zamora PF, Ooms L, Fernández JJ, Lai CM-H, Mainou BA, Dermody TS, Risco C. 2014. Reovirus forms neo-organelles for progeny particle assembly within reorganized cell membranes. mBio 5(1):e00931-13. doi:10.1128/mBio.00931-13.

Editor Anne Moscona, Weill Medical College-Cornell

Address correspondence to Cristina Risco, crisco@cnb.csic.es, or Terence S. Dermody, terry.dermody@vanderbilt.edu.

The replication and assembly of many viruses occur in specialized intracellular compartments known as virus factories, viral inclusions, or viroplasms. These neo-organelles formed during viral infection concentrate viral replication proteins and nucleic acids, prevent the activation of cell-intrinsic defenses, and coordinate the release of progeny particles (1–3). Many RNA viruses build factories by remodeling host membranes and creating new interorganelle contacts (4). Interestingly, membrane rearrangements are induced by both enveloped and nonenveloped viruses, suggesting that viral replication requires the physical support of cell membranes, even for those viruses that do not incorporate membranes into progeny particles (5). The growing interest in understanding how virus factories form, coupled with technical advances in genomics, proteomics, and cell imaging, has advanced our knowledge of the biogenesis and architecture of these unique structures. However, for many viruses, it is not known how these structures form and mediate their functions.

Mammalian orthoreoviruses (reoviruses) are nonenveloped,

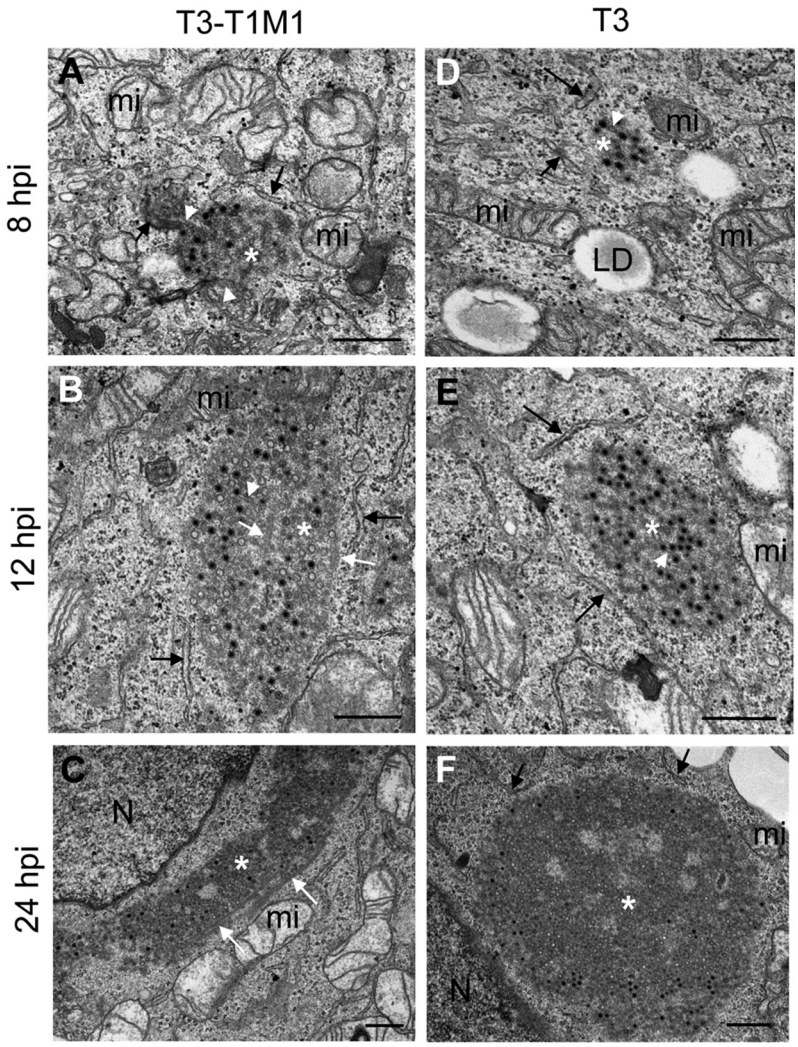

FIG 1 Ultrastructure of reovirus inclusions in HeLa cells. HeLa cells were infected with reovirus strain T3-T1M1 (A to C) or T3 (D to F) and fixed at 8, 12, or 24 hpi. Ultrathin (~60- to 70-nm) sections were imaged by TEM. Inclusions are marked with white asterisks, RER cisternae are marked with black arrows, smooth membranes inside inclusions are marked with white arrowheads, and coated microtubules are marked with white arrows. T3-T1M1 inclusions at 8 (A), 12 (B), and 24 (C) hpi and T3 inclusion at 8 (D), 12 (E), and 24 (F) hpi are shown. LD, lipid droplet; mi, mitochondria; N, nucleus. Scale bars: 0.5 μm.

double-shelled viruses that contain a genome of 10 double-stranded RNA (dsRNA) segments (6). Following the entry of reovirus into cells, the outer capsid is removed within the endocytic compartment (7–9), which allows the release of transcriptionally active core particles into the cytoplasm (10–13). These particles initiate a primary round of transcription to produce full-length, message-sense, single-stranded RNAs (ssRNAs) corresponding to each viral gene segment (14, 15). Reovirus ssRNAs can be translated and also serve as templates for minus-strand synthesis to generate nascent genomic dsRNA within replicase particles (16). These particles initiate a secondary round of transcription that fuels most viral protein synthesis (17). Particle assembly is completed by the addition of outer-capsid proteins onto nascent cores.

Viral RNA assortment, genome replication, secondary transcription, and particle assembly occur within specialized virus-derived neo-organelles, termed inclusions, which form in the host cell cytoplasm (14, 16, 18–22). Inclusions can be detected by confocal microscopy as early as 4 h postinfection (hpi) and contain viral proteins and dsRNA, as well as particles at various stages of morphogenesis (23–26). Mature viral progeny are arranged in paracrystalline arrays at late times postinfection prior to viral release (18, 21, 27). It is not thought that reovirus inclusions require membrane for their formation or function.

Most cell lines are readily infected by numerous reovirus strains (6). However, Madin-Darby canine kidney (MDCK) cells are susceptible to infection by reovirus strain type 1 Lang (T1) but not strain type 3 Dearing (T3) (28, 29). The primary determinant of this replication difference is the viral *M1* gene (29), which encodes μ2, a multifunctional replication protein. The critical μ2-dependent function in the replication cycle in MDCK cells occurs at a postentry step in the viral life cycle, following primary transcription and translation but prior to dsRNA synthesis (29). Further characterization of T3 replication in MDCK cells revealed that particle assembly is defective (30). These studies indicate that events within the inclusion involving the interaction of viral proteins and cell-type-specific factors promote the development of

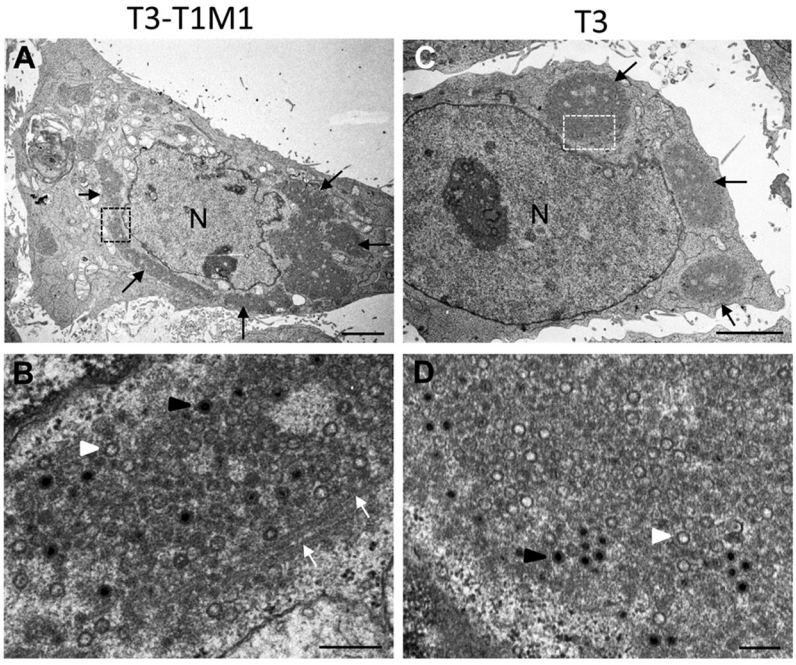

FIG 2 TEM of HeLa cells infected with reovirus strain T3-T1M1 or T3 at 24 hpi. Low (A) and high (B) magnifications of cells infected with T3-T1M1 are shown. (A) Perinuclear inclusion (black arrows). (B) Enlargement of highlighted area in panel A. The inclusion contains filled viral particles (black arrowhead), empty viral particles (white arrowhead), and coated microtubules (white arrows). (C, D) Low (C) and high (D) magnifications of cells infected with T3. In panel C, perinuclear inclusions are marked with black arrows. Panel D is an enlargement of the boxed area in panel C. The inclusion contains filled (black arrowhead) and empty (white arrowhead) particles. Scale bars: 3 μm in panels A and C, 0.25 μm in panels B and D.

inclusions with the capacity to generate fully assembled infectious virions. Thus, the formation of reovirus inclusions is a determinant of virus cell tropism.

In this study, we used transmission electron microscopy (TEM), three-dimensional (3D) image reconstructions, and immunofluorescence confocal microscopy to study the composition and organization of reovirus neo-organelles. Surprisingly, we found that reovirus inclusions formed in HeLa cells are membranous webs in which viral particles are embedded. Using organelle markers, we found that the endoplasmic reticulum (ER) and ER-Golgi intermediate compartment (ERGIC) are remodeled during infection and codistribute with inclusions. Membrane recruitment also occurs during reovirus infection of MDCK cells, suggesting a function for cellular membranes in reovirus replication in different cell types. These results suggest that reovirus inclusions are complex structures that recruit cell membranes to house functions required for viral replication.

RESULTS

Reovirus inclusions are surrounded by membranes and mitochondria. To define the organization of reovirus inclusions, we performed ultrastructural studies of infected cells. HeLa cells were infected with reovirus strain T3-T1M1 or T3, each of which establishes productive infection of this cell line (data not shown), and imaged by TEM. We observed that inclusions formed by either strain were partially surrounded by ER membranes (Fig. 1). Mitochondria and rough ER (RER) cisternae surrounded and attached to inclusions at 8 and 12 hpi (Fig. 1A and B and D and E). Quantification of imaging data from 53 randomly selected inclusions showed that RER elements associated with all of them. Smooth membranes were frequently observed to be connected with the interior of inclusions (white arrowheads in Fig. 1A). Thick, coated microtubules were detected inside and adjacent to the inclusions formed by both strains at 12 and 24 hpi but were not observed at 8 hpi (Fig. 1B and C and 2). At 24 hpi, inclusions developed into large structures that occupied extensive areas of the cytosol (Fig. 1C and F and 2A and C) with mitochondria and RER cisternae remaining closely apposed. No significant changes in mitochondrial morphology or integrity were observed during infection. Most of the viral particles within inclusions at early times (8 and 12 hpi) exhibited mature morphology, as demonstrated by dark staining inside the viral particle surrounded by lighter staining (Fig. 1A and B and D and E). However, at 24 hpi, empty particles were more numerous (Fig. 2B and D).

Imaging of cells at higher magnification showed details of the membranes and microtubules contained within reovirus inclusions (Fig. 3). RER elements were observed attached at discrete points to the inclusion periphery, but characteristic RER cisternae were rarely observed inside these structures. However, the smooth membranes associated with cytosolic viral particles and seen inside inclusions appeared to be connected to RER (Fig. 3A and B). Occasionally, RER elements on the periphery of inclusions were joined with cubic membrane sheets (Fig. 3C) reminiscent of the membranous platforms assembled by other viruses (5, 31). Coated microtubules were found to fill the inclusions at 24 hpi (Fig. 3D). Both filled and empty viral particles appeared to attach to coated microtubules but not to uncoated microtubules (Fig. 3E).

Cell membranes are associated with inclusions during nonproductive T3 infection in MDCK cells. In contrast to HeLa cells,

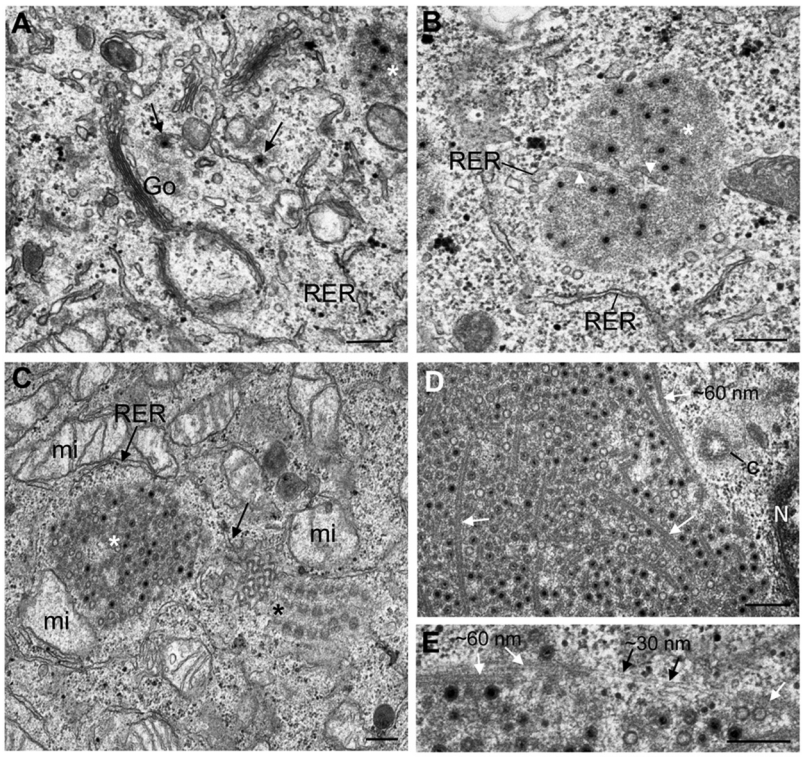

FIG 3 TEM of viral inclusions in T3-T1M1-infected HeLa cells. Inclusions are marked with white asterisks. (A) Viral particles (arrows) in small inclusions attached to membranes in a region containing RER and the Golgi compartment at 8 hpi. (B) Smooth membranes (white arrowheads) inside an inclusion surrounded by RER at 8 hpi. (C) Inclusion at 12 hpi surrounded by mitochondria and ER membranes. Some RER elements close to the inclusion (arrow on the right) appear to be connected to a sheet of cubic membranes (black asterisk). (D) Inclusion at 24 hpi filled with coated microtubules (white arrows). (E) Higher magnification of a different inclusion with viral particles attached to coated (~60 nm, white arrows) but not uncoated (~30 nm, black arrows) microtubules. N, nucleus; C, centriole. Scale bars: 0.25 μm.

reovirus strains T3 and T3-T1M1 differ in the capacity to complete a replication cycle in MDCK cells (28, 29). Although T3 can infect MDCK cells and form inclusion-like structures, yields of viral progeny in these cells are markedly less than those produced by T3-T1M1 (29, 30). To determine whether membranes are associated with the inclusions formed by reovirus in another cell type and to gain insight into the elements required for the biogenesis of functional inclusions, we imaged MDCK cells infected with either T3-T1M1 (permissive) or T3 (nonpermissive) reovirus (see Fig. S1 in the supplemental material). Inclusions formed in MDCK cells infected with T3-T1M1 at 8, 12, and 24 hpi were similar to those observed in HeLa cells. In contrast, inclusion formation was delayed in T3-infected MDCK cells, consistent with previous observations (29; data not shown). Accordingly, inclusions in T3-infected MDCK cells were scarce at 8 and 12 hpi but numerous and large at 24 hpi (data not shown). ER membranes and mitochondria were associated with inclusions formed in cells infected with either virus strain (see Fig. S1A, D, and E). Vacuoles containing fibers and a few viral particles were observed in inclusions assembled by T3 reovirus (see Fig. S1E). However, microtubules were observed only in the inclusions assembled by T3-T1M1 (see Fig. S1A and B). Inclusions formed in T3-T1M1-infected cells contained numerous mature virions and few empty particles (see Fig. S1C), whereas in cells infected by T3, the inclusions contained numerous empty particles and few mature virions (see Fig. S1F). These data corroborate previous TEM studies of reovirus infection of MDCK cells (29, 30). In addition, T3 inclusions were filled with many smaller particles, which appeared to be subassemblies of macromolecules containing nucleic acid, as shown by a density darker than that in empty particles. These particles were irregular in size and did not have a shell (see Fig. S1F). These findings suggest that reovirus recruits membranes to the inclusions formed in HeLa and MDCK cells.

Reovirus inclusions associate with ERGIC and ER elements. To elucidate the cellular source of the inclusion-associated membranes, we stained T3-T1M1-infected HeLa and MDCK cells with different organelle markers (Fig. 4; see Fig. S2 in the supplemental material). Viral inclusions were marked with an antibody specific for the σNS protein, which is an essential reovirus inclusion component (23, 25, 32). ER marker protein disulfide isomerase (PDI) distributed with inclusions in both HeLa cells (see Fig. S2A to C) and MDCK cells (data not shown). Golgi compartment markers giantin and wheat germ agglutinin (WGA) were not associated with inclusions during infection, and the staining patterns of each did not differ between infected and uninfected cells (see Fig. S2D to I). These findings make it unlikely that the Golgi compartment serves as a source of membranes associated with reovirus inclusions. Higher-magnification images showed ER marker PDI in close apposition to viral inclusions at early and late times after infection (Fig. 4A to F), whereas the PDI staining was mostly perinuclear in uninfected cells (see Fig. S2A to C). Type I transmembrane protein ERGIC-53, which has been used in previous studies

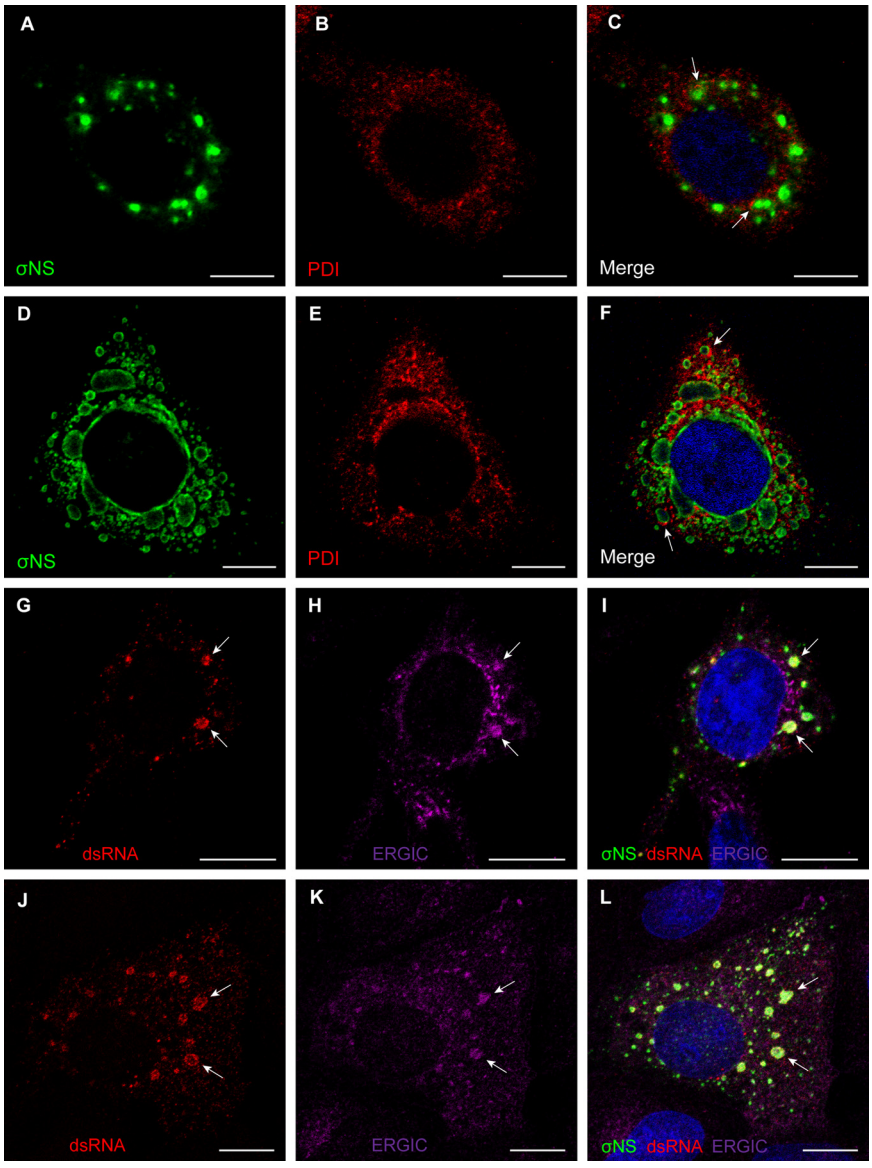

FIG 4 Reovirus inclusions codistribute with ER and ERGIC elements. (A to F) HeLa cells were infected with T3-T1M1 for 12 h (A to C) or 24 h (D to F). Cells were fixed; permeabilized; stained for σNS (green), PDI (red), or nuclei (blue); and visualized by confocal microscopy. Arrows indicate viral inclusions associated with RER elements on the periphery. (G to L) HeLa cells (G to I) and MDCK cells (J to L) were infected with T3-T1M1 for 12 h; fixed; permeabilized; stained for dsRNA (red), ERGIC-53 (magenta), σNS (green), or nuclei (blue); and visualized by confocal microscopy. Arrows indicate viral inclusions that contain dsRNA, the ERGIC, and σNS. Scale bars: 10 μm.

to mark the ERGIC (33), localized within inclusion structures in both HeLa and MDCK cells (Fig. 4G to L), as does the KDEL receptor (see Fig. S2J to L), which marks the ERGIC and Golgi compartment. Collectively, these observations suggest that the ERGIC, a membranous system that functionally links the ER and the Golgi compartment, is a source of inclusion-associated membranes, consistent with our TEM studies.

To confirm that inclusions localizing with ERGIC-53 support viral replication, T3-T1M1-infected HeLa and MDCK cells were stained with a dsRNA-specific antibody (Fig. 4G to L). Staining for dsRNA codistributed with inclusion marker σNS and ERGIC-53 inside the inclusions. These data suggest that membrane-filled inclusions are sites of reovirus RNA replication.

Serial sections and 3D reconstructions reveal that reovirus inclusions are membranous webs that contain microtubules. To understand the global architecture of inclusions and the contribution of cell membranes and specific organelles to the construction of these structures, we generated 3D reconstructions of reovirus inclusions. Oriented serial sections of reovirus-infected cells were imaged by TEM and processed for 3D reconstruction (see Fig. S3 and 4 in the supplemental material). The resulting 3D reconstructions showed that inclusions in HeLa cells are membranous webs surrounded by mitochondria (Fig. 5; see Fig. S3A and B and Fig. S5 in the supplemental material). Smooth membranes of the inclusions were observed to contact mitochondria in a variety of orientations (arrows in Fig. 5; see Movie S1 in the supplemental mate-

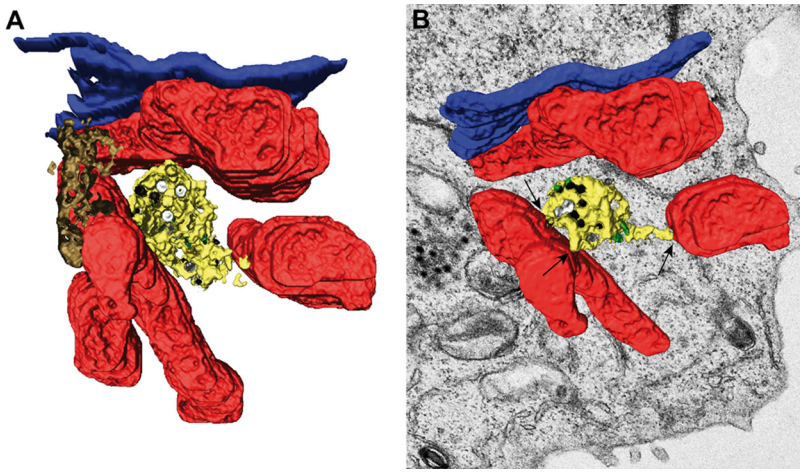

FIG 5 3D model of reovirus inclusions in HeLa cells. HeLa cells were infected with T3-T1M1 and fixed at 12 hpi. The inclusion was visualized by TEM of serial sections, 3D reconstruction, and image processing. (A) Mitochondria (red) surround a network of membranes (yellow). RER (brown) and nuclear envelope (blue) are adjacent to the inclusion. Filled viral particles (black), empty viral particles (white), and microtubules (green) are integrated into the inclusion membrane network. (B) Rotation of the same reconstruction showing contacts between the inclusion membranes and mitochondria (arrows). The volume has been superimposed onto the 2D image of one of the sections in the series.

rial). RER cisternae also were observed to contact the inclusion membranes and adjacent mitochondria (see Fig. S5 and Movie S2). Microtubules and viral particles were embedded in the inclusion membranous webs (Fig. 5; see Fig. S5A, and B). As detected by 3D TEM, viral particles appeared to be attached to microtubules (see Fig. S5C and D). These features were observed in all of the 3D reconstructions prepared from serial sections of reovirus-infected cells (data not shown).

To analyze the morphology of inclusions formed by reovirus strains that vary in the capacity to complete an infectious cycle, TEM images were processed to generate 3D reconstructions of inclusions formed in MDCK cells infected with strain T3-T1M1 or T3 (Fig. 6). Numerous mitochondria and RER cisternae were observed to surround the inclusions formed in T3-T1M1-infected cells (Fig. 6A). RER membranes appeared to contact the smooth membranes of the inclusions at 24 hpi, which are filled with mature virions, empty particles, and microtubules (Fig. 6A; see Movie S3 in the supplemental material). However, inclusions formed in T3-infected cells do not contain microtubules. In addition, most of the viral particles inside the membranous web in T3-infected cells were empty, and fewer filled particles were observed (Fig. 6B; see Movie S4). RER and mitochondria surrounded the inclusions formed by T3 reovirus. Inclusions assembled during T3-T1M1 infection were frequently observed close to the plasma membrane at 24 hpi. Image reconstructions of those inclusions showed viral particles adjacent to the plasma membrane and attached to smooth membranes, RER cisternae, and microtubules (Fig. 6C to E; see Movie S5). Together, our data indicate that reovirus inclusions are associated with ER and ERGIC membranes and mitochondria, highlighting these cellular organelles as important constituents of viral replication factories.

DISCUSSION

In this study, we demonstrated that inclusions formed by reovirus are associated with cell membranes. The participation of cell membranes within inclusions is a new finding for reoviruses, which previously had been thought to form inclusion complexes devoid of membranes. However, other *Reoviridae* viruses require membranes to replicate. *Hyposoter exiguae* reovirus (a reovirus of the parasitoid wasp *H. exiguae*) is released from infected cells exclusively by budding (34). Orbiviruses are variously described as being membranophilic (35), pseudoenveloped (36), or transiently enveloped (37). Rotavirus morphogenesis requires penetration of the ER to acquire outer-shell proteins VP4 and VP7 (38, 39). Therefore, the use of cell membranes to promote replication, assembly, or release may be a general feature of dsRNA viruses.

Previous studies of the ultrastructure of reovirus inclusions clearly demonstrate the presence of microtubules, but membranes in association with inclusions have not been described (18, 30). The discordance between our results and those obtained previously might be attributable to differences in the time postinfection chosen for analysis and the strategies used for TEM. In conventional TEM, samples must be thin, $<$100 nm, for electrons to be able to traverse them and generate a projection image. These ultrathin sections of eukaryotic cells are single planes of much larger volumes. Moreover, when analysis is restricted to random sections of cells, scarce or nonrandomly distributed elements can be missed. Oriented serial sections and 3D reconstructions avoid these limitations and allow imaging of whole cells and a comprehensive analysis of intracellular contacts (5, 40, 41). This analysis was instrumental in our finding that reovirus inclusions are embedded in membrane.

Our 3D image reconstructions have revealed the complex organization of reovirus inclusions and the participation of cell membranes (most likely derived from the ERGIC), mitochondria, and microtubules in inclusion structure. Confocal microscopy studies confirmed an association of the inclusions with the ER and ERGIC and suggest that the Golgi complex does not contribute to inclusion formation. Viral particles appear to attach to coated microtubules and membranes inside the inclusion and remain attached when reaching the plasma membrane. Microtubule coats are likely to contain the viral μ2 protein, which associates with

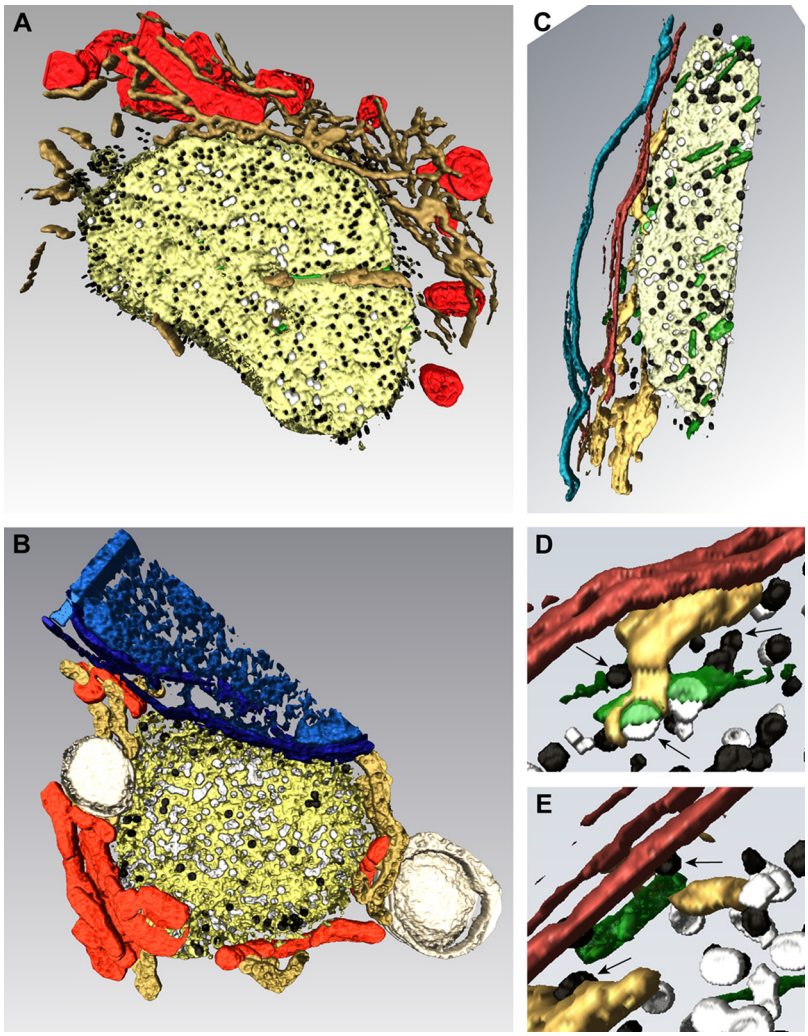

FIG 6 3D model of reovirus inclusions in MDCK cells. MDCK cells were infected with T3-T1M1 (A and C to E) or T3 (B) and fixed at 24 hpi. Membranes (yellow), mitochondria (red), RER (light brown), microtubules (green), filled viral particles (black), and empty viral particles (white) are shown. (A) Image reconstruction of an inclusion formed in T3-T1M1-infected cells. RER membranes surround and incorporate into the inclusion membrane network that contains numerous mature virions, fewer empty particles, and microtubules. (B) Image reconstruction of an inclusion formed in T3-infected cells. Most of the viral particles inside the membranous web are empty. No microtubules were observed inside or around the inclusion. Mitochondria, RER, and lipid droplets (large white structures) surround the inclusion, which is in contact with the nuclear envelope (blue). (C) Image reconstruction of an inclusion close to the plasma membrane (brown) in a cell infected with T3-T1M1. The plasma membrane from another cell is colored blue. The inclusion contains membranes (yellow) and filled (black) and empty (white) viral particles. Peripheral RER elements, microtubules, and viral particles are in contact with the cytosolic face of the plasma membrane. Enlargements of this region are shown in panels D and E. Viral particles attached to RER, microtubules, and the plasma membrane (arrows) are visible.

microtubules (42), as well as other viral and perhaps cellular proteins. When a complete analysis is performed with serial sections and 3D reconstructions, all of the inclusions identified in both HeLa and MDCK cells are associated with mitochondria, ER elements, and membranous webs. We think that the cell membranes within inclusions serve as a physical scaffold for inclusion formation and organize the reovirus nonstructural and structural proteins required for viral genome replication and progeny particle assembly. In this regard, RER cisternae make numerous contacts with reovirus inclusions but do not surround them completely. The association of RER with reovirus inclusions is reminiscent of the structures of rubella virus replication organelles (43). In rubella virus factories, RER cisternae provide a framework for newly synthesized viral proteins to incorporate into viral replication complexes (43).

Mitochondria are recruited to factories assembled by many viruses (5). In keeping with this general feature of viral replication, our 3D image reconstructions showed numerous contacts between reovirus inclusion membranes and mitochondria. Moreover, new interorganelle contacts have been visualized within reovirus factories. For example, attachment of mitochondria to ERGIC, the Golgi compartment, or lysosomes is not observed in uninfected mammalian cells (5). Mitochondria may be used as an energy source to power viral replication and also supply host factors required for viral genome synthesis and particle assembly, as reported for rubella virus and tombusviruses (5, 43). In reovirus-

infected cells, the transfer of energy and host factors likewise might be mediated by the physical contacts between mitochondria and the inclusion membranous webs. RER also might serve as the source of viral and cellular proteins required for inclusion activities.

The inclusions assembled in MDCK cells infected with strain T3, which enters these cells but does not complete an infectious cycle (28, 29), contain membrane but lack microtubules. This finding suggests that microtubules are required for the functional organization of inclusions and assembly of progeny particles. Moreover, this finding provides a potential explanation for the genetic linkage between the replication differences displayed by reovirus strains in MDCK cells and the μ2-encoding *M1* gene (28, 29). The μ2 protein interacts with microtubules and dictates inclusion morphology (42). Concordantly, microtubules are observed in inclusions assembled by both T3 and T3-T1M1 in HeLa cells, which support the replication of both strains (data not shown). Microtubule function might be required to transport essential components to inclusions, organize inclusion content, or compartmentalize inclusion activities. Microtubules also might be required to transport progeny particles to the plasma membrane for subsequent release. It is not known whether microtubules incorporate into small inclusions and enhance inclusion coalescence and growth, as reported for some other viruses (44, 45). The delay in inclusion formation during T3 infection of MDCK cells also could point to a defect in the recruitment or remodeling of cell membranes. We observed membranes in association with inclusions from the initial stages of inclusion assembly in HeLa cells infected with either T3 or T3-T1M1, suggesting that membranes could potentiate steps required for inclusion biogenesis.

An important question left unanswered by our study is the mechanism by which progeny viral particles migrate from inclusions to the cell periphery and exit infected cells. Reovirus exits some cells by lysis (28, 46, 47). However, egress of virus from polarized endothelial cells (48) and epithelial cells (49) is noncytolytic. The mechanism by which nonenveloped viral particles are released from infected cells without inducing cell lysis is not known. ER membranes could be used by reovirus to traffic to the cell periphery through some type of vesicular transport pathway that bypasses the Golgi apparatus, as suggested by our 3D reconstructions (Fig. 6). Unconventional vesicular trafficking has been suggested for rotavirus egress, which also bypasses the Golgi apparatus to reach the cell periphery (50). The rotavirus spike protein VP4 is particularly important for this process. Despite not having transmembrane domains, VP4 interacts with lipids and is enriched in lipid rafts (51). VP4 is essential for rotavirus release, as it interacts with actin filaments in infected cells (52). A homologous reovirus protein responsible for interaction with lipids is not known. All reovirus proteins lack transmembrane domains, and posttranslational modifications are not completely defined, although the μ1 protein contains a myristoyl moiety (53). Lipidation of reovirus proteins, specifically at late times after infection, might be required for membrane recruitment and particle transport to the cell periphery.

New technologies now offer access to the analysis of viruses in cells in unprecedented detail. The complexity of the interaction networks established in these contexts is changing our concept of viruses from that of inert chemicals to living entities capable of performing a wide variety of intracellular functions. Reovirus inclusions appear to assemble as membranous replication organelles that are usually associated with mitochondria. However, it is not known how the cellular organelles are recruited, how macromolecular transport operates inside the inclusions to connect viral replication and morphogenesis, and how nonenveloped viruses like reovirus exit the membranous scaffolds and leave the cell. With the information provided by this study, we now can initiate functional and mechanistic studies to identify the signals that regulate the biogenesis and activities of viral inclusions. This work will enhance our knowledge of the cell biology of virus replication and provide potential new therapeutic targets to ameliorate diseases caused by pathogenic viruses.

MATERIALS AND METHODS

Cells and viruses. Spinner-adapted murine L929 fibroblast cells were grown in either suspension or monolayer cultures as previously described (54). HeLa CCL2 cells and MDCK cells were grown in Dulbecco's modified Eagle's medium containing 4.5 g/liter glucose, L-glutamine, and sodium pyruvate (Mediatech) supplemented to contain 10% fetal bovine serum, 100 U/ml penicillin G (Gibco), 100 μg/ml streptomycin (Gibco), and 0.25 μg/ml amphotericin B (Sigma). Reovirus strains T3 and T3-T1M1 were recovered by using plasmid copies of gene segment cDNAs as previously described (29). Virus was purified by cesium gradient centrifugation as previously described (55). Viral titers were determined by plaque assay with L929 cells (56).

TEM. Virus was allowed to adsorb to monolayers of HeLa and MDCK cells at a multiplicity of infection (MOI) of 20 PFU/cell. Following incubation at 37°C for 8, 12, or 24 h, cells were fixed at room temperature for 1 h with a mixture of 4% paraformaldehyde and 1% glutaraldehyde in phosphate-buffered saline (pH 7.4), postfixed with 1% osmium tetroxide, dehydrated in increasing concentrations of acetone, and processed for embedding in epoxy resin EML-812 (TAAB Laboratories) as previously described (57, 58). Osmium tetroxide is a lipid-staining agent used in TEM to provide image contrast. Osmium(VIII) oxide binds phospholipid head groups, thus providing contrast and allowing ultrastructural identification of membranes, which are apparent as dark, flexible lines with a thickness of ~5 nm (59, 60). Ultrathin (~60- to 70-nm) sections were collected on uncoated 300-mesh copper grids (TAAB Laboratories), stained with uranyl acetate and lead citrate, and imaged by TEM. Images were acquired with a JEOL JEM 1011 electron microscope operating at 100 kV.

Confocal microscopy. Virus at an MOI of 20 PFU/cell was allowed to adsorb to HeLa CCL2 cells cultivated on untreated glass coverslips and MDCK cells cultivated on poly-L-lysine (Sigma)-treated glass coverslips in 24-well plates. Following incubation at 37°C for 12 or 24 h, cells were fixed with ice-cold methanol (−20°C), permeabilized with 1% Triton X-100, and stained with σNS-specific antibody (25) and ERGIC-53-specific antibody H-245 (Santa Cruz Biotechnology) or KDEL receptor-specific antibody FL-212 (Santa Cruz Biotechnology) for ERGIC staining, anti-giantin antibody ab24586 (Abcam) or WGA conjugated with Alexa Fluor 555 (Invitrogen) to mark the Golgi compartment, PDI-specific antibody DL-11 (Sigma) to mark the ER, or K2 antibody (40) to mark dsRNA. ToPro3 or 4′,6-diamidino-2-phenylindole (DAPI; Invitrogen) was used to stain nuclei. Alexa Fluor-conjugated antibodies (Invitrogen) were used as secondary antibodies. Images were acquired with Zeiss LSM 510 Meta and 710 Meta inverted confocal microscopes.

3D image reconstructions. Consecutive ultrathin (~60- to 70-nm) sections were collected on Formvar-coated copper slot grids (TAAB Laboratories), stained, and imaged by TEM. A total of eight series of 15 were selected and processed for 3D reconstruction as previously described (40, 61) (see Fig. S4 in the supplemental material). Photographs of reovirus inclusions were taken at a nominal magnification of ×10,000 or ×12,000. Plates were digitized as 8-bit images with a 3.39-nm final pixel size and a 600-dpi resolution with an Epson Perfection Photo 3170 scanner. Digital images were aligned by selected tracers between two consecutive sections with the free editor for serial section microscopy Reconstruct (62) (http:

//synapses.clm.utexas.edu/tools/index.stm). Segmentation and 3D visualization were performed with Amira (http://amira.zib.de). Movies were prepared from the 3D reconstructions with the Camera Rotate and Movie Maker applications of the Amira software suite.

SUPPLEMENTAL MATERIAL

Supplemental material for this article may be found at http://mbio.asm.org/lookup/suppl/doi:10.1128/mBio.00931-13/-/DCSupplemental.

Movie S1, AVI file, 9.3 MB.
Movie S2, AVI file, 11.6 MB.
Movie S3, AVI file, 14.2 MB.
Movie S4, AVI file, 11.9 MB.
Movie S5, AVI file, 8.8 MB.
Figure S1, TIF file, 14.8 MB.
Figure S2, TIF file, 3.1 MB.
Figure S3, TIF file, 4.8 MB.
Figure S4, TIF file, 3 MB.
Figure S5, TIF file, 5.1 MB.

ACKNOWLEDGMENTS

We thank members of the Risco and Dermody laboratories for many useful discussions and Jim Chappell and Jennifer Konopka for critical review of the manuscript. Confocal microscopy experiments were conducted in the Vanderbilt Cell Imaging Shared Resource.

This research was supported by an FPI Program fellowship (I.F.C.) and research grants BIO2009-07255 and BIO2012-33314 from the Spanish Ministry of Economy and Competitiveness (CR), Public Health Service awards T32 GM007347 (C.M.L.), F31 NS074596 (C.M.L.), T32 HL007751 (B.A.M.), F32 AI080108 (B.A.M.), and R01 AI032539 (T.S.D.); the Vanderbilt International Scholar Program (P.F.Z.); and the Elizabeth B. Lamb Center for Pediatric Research. Additional support was provided by Public Health Service awards P30 CA68485 for the Vanderbilt-Ingram Cancer Center and P60 DK20593 for the Vanderbilt Diabetes Research and Training Center.

REFERENCES

1. **Miller S, Krijnse-Locker J.** 2008. Modification of intracellular membrane structures for virus replication. Nat. Rev. Microbiol. **6:**363–374. http://dx.doi.org/10.1038/nrmicro1890.
2. **Paul D, Bartenschlager R.** 2013. Architecture and biogenesis of plus-strand RNA virus replication factories. World J. Virol. **2:**32–48. http://dx.doi.org/10.5501/wjv.v2.i2.32.
3. **Paul D, Hoppe S, Saher G, Krijnse-Locker J, Bartenschlager R.** 2013. Morphological and biochemical characterization of the membranous hepatitis C virus replication compartment. J. Virol. **87:**10612–10627. http://dx.doi.org/10.1128/JVI.01370-13.
4. **Novoa RR, Calderita G, Arranz R, Fontana J, Granzow H, Risco C.** 2005. Virus factories: associations of cell organelles for viral replication and morphogenesis. Biol. Cell **97:**147–172. http://dx.doi.org/10.1042/BC20040058.
5. **de Castro IF, Volonté L, Risco C.** 2013. Virus factories: biogenesis and structural design. Cell. Microbiol. **15:**24–34. http://dx.doi.org/10.1111/cmi.12029.
6. **Dermody TS, Parker JS, Sherry B.** 2013. Orthoreoviruses, p 1304–1346. *In* Knipe DM, Howley PM (ed), Fields virology, 6th ed. Lippincott Williams & Wilkins, Philadelphia, PA.
7. **Sturzenbecker LJ, Nibert M, Furlong D, Fields BN.** 1987. Intracellular digestion of reovirus particles requires a low pH and is an essential step in the viral infectious cycle. J. Virol. **61:**2351–2361.
8. **Baer GS, Ebert DH, Chung CJ, Erickson AH, Dermody TS.** 1999. Mutant cells selected during persistent reovirus infection do not express mature cathepsin L and do not support reovirus disassembly. J. Virol. **73:**9532–9543.
9. **Ebert DH, Deussing J, Peters C, Dermody TS.** 2002. Cathepsin L and cathepsin B mediate reovirus disassembly in murine fibroblast cells. J. Biol. Chem. **277:**24609–24617. http://dx.doi.org/10.1074/jbc.M201107200.
10. **Borsa J, Morash BD, Sargent MD, Copps TP, Lievaart PA, Szekely JG.** 1979. Two modes of entry of reovirus particles into L cells. J. Gen. Virol. **45:**161–170. http://dx.doi.org/10.1099/0022-1317-45-1-161.
11. **Odegard AL, Chandran K, Zhang X, Parker JS, Baker TS, Nibert ML.** 2004. Putative autocleavage of outer capsid protein μ1, allowing release of myristoylated peptide μ1N during particle uncoating, is critical for cell entry by reovirus. J. Virol. **78:**8732–8745. http://dx.doi.org/10.1128/JVI.78.16.8732-8745.2004.
12. **Agosto MA, Ivanovic T, Nibert ML.** 2006. Mammalian reovirus, a nonfusogenic nonenveloped virus, forms size-selective pores in a model membrane. Proc. Natl. Acad. Sci. U. S. A. **103:**16496–16501. http://dx.doi.org/10.1073/pnas.0605835103.
13. **Ivanovic T, Agosto MA, Zhang L, Chandran K, Harrison SC, Nibert ML.** 2008. Peptides released from reovirus outer capsid form membrane pores that recruit virus particles. EMBO J. **27:**1289–1298. http://dx.doi.org/10.1038/emboj.2008.60.
14. **Watanabe Y, Millward S, Graham AF.** 1968. Regulation of transcription of the reovirus genome. J. Mol. Biol. **36:**107–123. http://dx.doi.org/10.1016/0022-2836(68)90223-4.
15. **Shatkin AJ, LaFiandra AJ.** 1972. Transcription by infectious subviral particles of reovirus. J. Virol. **10:**698–706.
16. **Antczak JB, Joklik WK.** 1992. Reovirus genome segment assortment into progeny genomes studied by the use of monoclonal antibodies directed against reovirus proteins. Virology **187:**760–776. http://dx.doi.org/10.1016/0042-6822(92)90478-8.
17. **Skup D, Millward S.** 1980. Reovirus-induced modification of cap dependent translation in infected L cells. Proc. Natl. Acad. Sci. U. S. A. **77:**152–156. http://dx.doi.org/10.1073/pnas.77.1.152.
18. **Dales S, Omatos PJ.** 1965. The uptake and development of reovirus in strain L cells followed with labelled viral ribonucleic acid and ferritin-antibody conjugates. Virology **25:**193–211. http://dx.doi.org/10.1016/0042-6822(65)90199-6.
19. **Morgan EM, Zweerink HJ.** 1974. Reovirus morphogenesis: core-like particles in cells infected at 39 degrees with wild-type reovirus and temperature-sensitive mutants of groups B and G. Virology **59:**556–565. http://dx.doi.org/10.1016/0042-6822(74)90465-6.
20. **Morgan EM, Zweerink HJ.** 1975. Characterization of transcriptase and replicase particles isolated from reovirus infected cells. Virology **68:**455–466. http://dx.doi.org/10.1016/0042-6822(75)90286-X.
21. **Rhim JS, Jordan LE, Mayor HD.** 1962. Cytochemical, fluorescent-antibody and electron microscopic studies on the growth of reovirus (echo 10) in tissue culture. Virology **17:**342–355. http://dx.doi.org/10.1016/0042-6822(62)90125-3.
22. **Zweerink HJ, Morgan EM, Skyler JS.** 1976. Reovirus morphogenesis: characterization of subviral particles in infected cells. Virology **73:**442–453. http://dx.doi.org/10.1016/0042-6822(76)90405-0.
23. **Becker MM, Goral MI, Hazelton PR, Baer GS, Rodgers SE, Brown EG, Coombs KM, Dermody TS.** 2001. Reovirus σNS protein is required for nucleation of viral assembly complexes and formation of viral inclusions. J. Virol. **75:**1459–1475. http://dx.doi.org/10.1128/JVI.75.3.1459-1475.2001.
24. **Broering TJ, Parker JS, Joyce PL, Kim J, Nibert ML.** 2002. Mammalian reovirus nonstructural protein μNS forms large inclusions and colocalizes with reovirus microtubule-associated protein μ2 in transfected cells. J. Virol. **76:**8285–8297. http://dx.doi.org/10.1128/JVI.76.16.8285-8297.2002.
25. **Becker MM, Peters TR, Dermody TS.** 2003. Reovirus σNS and μNS proteins form cytoplasmic inclusion structures in the absence of viral infection. J. Virol. **77:**5948–5963. http://dx.doi.org/10.1128/JVI.77.10.5948-5963.2003.
26. **Broering TJ, Kim J, Miller CL, Piggott CD, Dinoso JB, Nibert ML, Parker JS.** 2004. Reovirus nonstructural protein μNS recruits viral core surface proteins and entering core particles to factory-like inclusions. J. Virol. **78:**1882–1892. http://dx.doi.org/10.1128/JVI.78.4.1882-1892.2004.
27. **Dales, S.** 1963. Association between the spindle apparatus and reovirus. Proc. Natl. Acad. Sci. U. S. A. **50:**268–275. http://dx.doi.org/10.1073/pnas.50.2.268.
28. **Rodgers SE, Barton ES, Oberhaus SM, Pike B, Gibson CA, Tyler KL, Dermody TS.** 1997. Reovirus-induced apoptosis of MDCK cells is not linked to viral yield and is blocked by Bcl-2. J. Virol. **71:**2540–2546.
29. **Ooms LS, Kobayashi T, Dermody TS, Chappell JD.** 2010. A post-entry step in the mammalian orthoreovirus replication cycle is a determinant of cell tropism. J. Biol. Chem. **285:**41604–41613. http://dx.doi.org/10.1074/jbc.M110.176255.

30. **Ooms LS, Jerome WG, Dermody TS, Chappell JD.** 2012. Reovirus replication protein M2 influences cell tropism by promoting particle assembly within viral inclusions. J. Virol. **86:**10979–10987. http://dx.doi.org/10.1128/JVI.01172-12.
31. **Deng Y, Almsherqi ZA, Ng MM, Kohlwein SD.** 2010. Do viruses subvert cholesterol homeostasis to induce host cubic membranes? Trends Cell Biol. **20:**371–379. http://dx.doi.org/10.1016/j.tcb.2010.04.001.
32. **Miller CL, Broering TJ, Parker JS, Arnold MM, Nibert ML.** 2003. Reovirus sigmaNS protein localizes to inclusions through an association requiring the μNS amino terminus. J. Virol. **77:**4566–4576. http://dx.doi.org/10.1128/JVI.77.8.4566-4576.2003.
33. **Hauri HP, Kappeler F, Andersson H, Appenzeller C.** 2000. ERGIC-53 and traffic in the secretory pathway. J. Cell Sci. **113:**587–596.
34. **Stoltz D, Makkay A.** 2000. Co-replication of a reovirus and a polydnavirus in the ichneumonid parasitoid *Hyposoter exiguae*. Virology **278:**266–275. http://dx.doi.org/10.1006/viro.2000.0652.
35. **Foster N, Alders M.** 1979. Bluetongue virus: a membraned structure, p 48–49. *In* Proc. Annu. Meet. Microsc. Soc. Am. Microscopy Society of America, Reston, VA.
36. **Els HJ, Verwoerd DW.** 1969. Morphology of bluetongue virus. Virology **38:**213–219. http://dx.doi.org/10.1016/0042-6822(69)90362-6.
37. **Hyatt AD, Zhao Y, Roy P.** 1993. Release of bluetongue virus-like particles from insect cells is mediated by BTV nonstructural protein NS3/NS3A. Virology **193:**592–603. http://dx.doi.org/10.1006/viro.1993.1167.
38. **Estes MK, Greenberg HB.** 2013. Rotaviruses, p 1347–1401. *In* Knipe DM, Howley PM (ed), Fields virology, 6th ed. Lippincott Williams & Wilkins, Philadelphia, PA.
39. **Poruchynsky MS, Maass DR, Atkinson PH.** 1991. Calcium depletion blocks the maturation of rotavirus by altering the oligomerization of virus-encoded proteins in the ER. J. Cell Biol. **114:**651–661.
40. **Fontana J, López-Montero N, Elliott RM, Fernández JJ, Risco C.** 2008. The unique architecture of Bunyamwera virus factories around the Golgi complex. Cell. Microbiol. **10:**2012–2028. http://dx.doi.org/10.1111/j.1462-5822.2008.01184.x.
41. **Risco C, Fernández de Castro I.** 2013. Virus morphogenesis in the cell: methods and observations. Subcell. Biochem. **68:**417–440. http://dx.doi.org/10.1007/978-94-007-6552-8_14.
42. **Parker JS, Broering TJ, Kim J, Higgins DE, Nibert ML.** 2002. Reovirus core protein M2 determines the filamentous morphology of viral inclusion bodies by interacting with and stabilizing microtubules. J. Virol. **76:**4483–4496. http://dx.doi.org/10.1128/JVI.76.9.4483-4496.2002.
43. **Fontana J, López-Iglesias C, Tzeng WP, Frey TK, Fernández JJ, Risco C.** 2010. Three-dimensional structure of rubella virus factories. Virology **405:**579–591. http://dx.doi.org/10.1016/j.virol.2010.06.043.
44. **Eichwald C, Arnoldi F, Laimbacher AS, Schraner EM, Fraefel C, Wild P, Burrone OR, Ackermann M.** 2012. Rotavirus viroplasm fusion and perinuclear localization are dynamic processes requiring stabilized microtubules. PLoS One **7:**e47947. http://dx.doi.org/10.1371/journal.pone.0047947.
45. **Howard AR, Moss B.** 2012. Formation of orthopoxvirus cytoplasmic A-type inclusion bodies and embedding of virions are dynamic processes requiring microtubules. J. Virol. **86:**5905–5914. http://dx.doi.org/10.1128/JVI.06997-11.
46. **Tyler KL, Squier MK, Rodgers SE, Schneider BE, Oberhaus SM, Grdina TA, Cohen JJ, Dermody TS.** 1995. Differences in the capacity of reovirus strains to induce apoptosis are determined by the viral attachment protein sigma1. J. Virol. **69:**6972–6979.
47. **Connolly JL, Barton ES, Dermody TS.** 2001. Reovirus binding to cell surface sialic acid potentiates virus-induced apoptosis. J. Virol. **75:**4029–4039. http://dx.doi.org/10.1128/JVI.75.9.4029-4039.2001.
48. **Lai CM, Mainou BA, Kim KS, Dermody TS.** 2013. Directional release of reovirus from the apical surface of polarized endothelial cells. mBio **4:**e00049–e00013. http://dx.doi.org/10.1128/mBio.00049-13.
49. **Excoffon KJ, Guglielmi KM, Wetzel JD, Gansemer ND, Campbell JA, Dermody TS, Zabner J.** 2008. Reovirus preferentially infects the basolateral surface and is released from the apical surface of polarized human respiratory epithelial cells. J. Infect. Dis. **197:**1189–1197. http://dx.doi.org/10.1086/529515.
50. **Jourdan N, Maurice M, DeLautier D, Quero AM, Servin AL, Trugnan G.** 1997. Rotavirus is released from the apical surface of cultured human intestinal cells through nonconventional vesicular transport that bypasses the Golgi apparatus. J. Virol. **71:**8268–8278.
51. **Cuadras MA, Bordier BB, Zambrano JL, Ludert JE, Greenberg HB.** 2006. Dissecting rotavirus particle-raft interaction with small interfering RNAs: insights into rotavirus transit through the secretory pathway. J. Virol. **80:**3935–3946. http://dx.doi.org/10.1128/JVI.80.8.3935-3946.2006.
52. **Gardet A, Breton M, Trugnan G, Chwetzoff S.** 2007. Role for actin in the polarized release of rotavirus. J. Virol. **81:**4892–4894. http://dx.doi.org/10.1128/JVI.02698-06.
53. **Nibert ML, Schiff LA, Fields BN.** 1991. Mammalian reoviruses contain a myristoylated structural protein. J. Virol. **65:**1960–1967.
54. **Boehme KW, Guglielmi KM, Dermody TS.** 2009. Reovirus nonstructural protein sigma1s is required for establishment of viremia and systemic dissemination. Proc. Natl. Acad. Sci. U. S. A. **106:**19986–19991. http://dx.doi.org/10.1073/pnas.0907412106.
55. **Furlong DB, Nibert ML, Fields BN.** 1988. Sigma 1 protein of mammalian reoviruses extends from the surfaces of viral particles. J. Virol. **62:**246–256.
56. **Virgin HW, IV, Bassel-Duby R, Fields BN, Tyler KL.** 1988. Antibody protects against lethal infection with the neurally spreading reovirus type 3 (Dearing). J. Virol. **62:**4594–4604.
57. **Risco C, Rodríguez JR, López-Iglesias C, Carrascosa JL, Esteban M, Rodríguez D.** 2002. Endoplasmic reticulum-Golgi intermediate compartment membranes and vimentin filaments participate in vaccinia virus assembly. J. Virol. **76:**1839–1855. http://dx.doi.org/10.1128/JVI.76.4.1839-1855.2002.
58. **Fontana J, Tzeng WP, Calderita G, Fraile-Ramos A, Frey TK, Risco C.** 2007. Novel replication complex architecture in rubella replicon-transfected cells. Cell. Microbiol. **9:**875–890. http://dx.doi.org/10.1111/j.1462-5822.2006.00837.x.
59. **Bozzola JJ, Russell LD.** 1999. Specimen preparation for transmission electron microscopy, p 21–31. *In* Bozzola JJ, Russell LD (ed), Electron microscopy: principles and techniques for biologists, 2nd ed. Jones and Bartlett Publishers, Sudbury, MA.
60. **Hayat MA.** 2000. Principles and techniques of electron microscopy: biological applications, 4th ed. Cambridge University Press, Cambridge, United Kingdom
61. **Sanz-Sánchez L, Risco C.** 2013. Multilamellar structures and filament bundles are found on the cell surface during bunyavirus egress. PLoS One **8:**e65526. http://dx.doi.org/10.1371/journal.pone.0065526.
62. **Fiala JC.** 2005. Reconstruct: a free editor for serial section microscopy. J. Microsc. **218:**52–61. http://dx.doi.org/10.1111/j.1365-2818.2005.01466.x.

Correction for Fernández de Castro et al., Reovirus Forms Neo-Organelles for Progeny Particle Assembly within Reorganized Cell Membranes

Isabel Fernández de Castro,[a] Paula F. Zamora,[b,c] Laura Ooms,[b] José Jesús Fernández,[d] Caroline M.-H. Lai,[b,c] Bernardo A. Mainou,[c,e] Terence S. Dermody,[b,c,e] Cristina Risco[a]

Cell Structure Laboratory, National Center for Biotechnology, National Research Council (CNB-CSIC), Campus UAM, Madrid, Spain[a]; Department of Pathology, Microbiology, and Immunology, Vanderbilt University School of Medicine, Nashville, Tennessee, USA[b]; Elizabeth B. Lamb Center for Pediatric Research, Vanderbilt University School of Medicine, Nashville, Tennessee, USA[c]; Department of Macromolecular Structures, National Center for Biotechnology, National Research Council (CNBCSIC), Campus UAM, Madrid, Spain[d]; Department of Pediatrics, Vanderbilt University School of Medicine, Nashville, Tennessee, USA[e]

P.F.Z. and L.O. contributed equally to this work.

In our article (1), we reported that smooth membranes connected with rough endoplasmic reticulum (ER) cisternae are incorporated within inclusion structures formed in reovirus-infected cells using both two-dimensional and three-dimensional electron microscopy (Fig. 1, 3, 5, and 6). Using rabbit polyclonal antisera raised against ER-Golgi intermediate compartment 53 (ERGIC-53) (H-245) and the KDEL receptor (KDEL-R) (FL-212), both of which were purchased from Santa Cruz Biotechnology, we observed staining attributable to ERGIC-53 (Fig. 4G to L) and KDEL-R (Fig. S2J to L) in reovirus inclusions in both HeLa cells and MDCK cells. We concluded from these observations that ERGIC, a membranous system that functionally links the ER and Golgi compartment, is a source of inclusion-associated membranes.

As part of our ongoing studies of the biogenesis of reovirus inclusions, we performed immunofluorescence assays using two monoclonal antibodies specific for ERGIC-53 (C-6 [Santa Cruz Biotechnology] and G1/93 [Enzo Life Sciences]) and a monoclonal antibody specific for KDEL-R (KR-10 [Thermo Scientific]). With these antibodies, we were unable to detect distribution of either ERGIC-53 or KDEL-R within viral inclusions. Immunoblotting experiments using either ERGIC-53 (H-245) or KDEL-R (FL-212) polyclonal antiserum revealed multiple protein bands in both uninfected and infected cells (Fig. 1). These new findings do not alter the main conclusion of our paper, which is that reovirus inclusions are embedded in membrane. The origin of the membranous elements that build reovirus inclusions is a focus of our current research.

Poor specificity of commercial antibodies has been reported previously (2, 3). Our findings using the H-245 and FL-212 antisera are most likely attributable to the nonspecific immunoreactivity of these reagents. We apologize for the erroneous conclusions made from the experiments using these antisera and alert readers to potential problems with the use of polyclonal antisera for immunohistochemical staining.

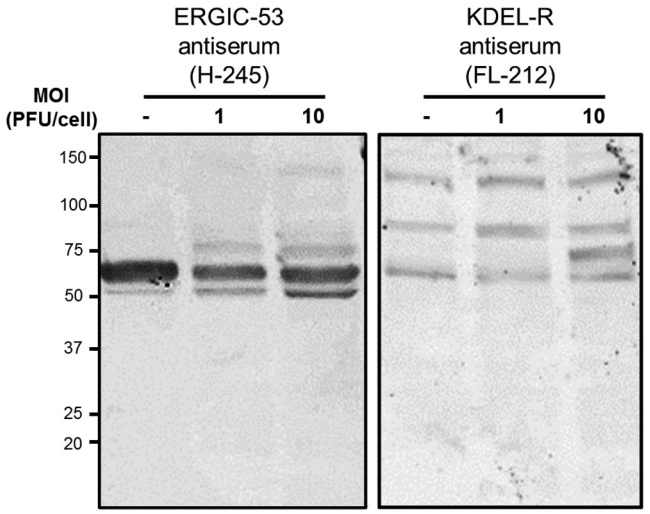

FIG 1 ERGIC-53 (H-245) and KDEL-R (FL-212) polyclonal antisera from Santa Cruz Biotechnology detect multiple protein bands. HeLa cells were infected with reovirus at a multiplicity of infection (MOI) of 1 or 10 PFU/cell. Cell lysates were prepared 24 h postinfection, resolved by SDS-PAGE, and transferred to nitrocellulose membranes. Membranes were blocked with 5% skim milk in TBS and immunoblotted using polyclonal antiserum H-245 (against ERGIC-53, left panel) or FL-212 (against KDEL-R, right panel). Anti-rabbit secondary antibody (IRDye 800CW goat anti-rabbit IgG [LI-COR]) was used for detection. Molecular mass markers (in kilodaltons) are indicated on the left.

REFERENCES

1. **Fernández de Castro I, Zamora PF, Ooms L, Fernández JJ, Lai CM-H, Mainou BA, Dermody TS, Risco C.** 2014. Reovirus forms neo-organelles for progeny particle assembly within reorganized cell membranes. mBio 5(1):e00931-13. http://dx.doi.org/10.1128/mBio.00931-13.
2. **Bordeaux J, Welsh A, Agarwal S, Killiam E, Baquero M, Hanna J, Anagnostou V, Rimm D.** 2010. Antibody validation. Biotechniques **48:** 197–209. http://dx.doi.org/10.2144/000113382.
3. **Benicky J, Hafko R, Sanchez-Lemus E, Aguilera G, Saavedra JM.** 2012. Six commercially available angiotensin II AT_1 receptor antibodies are non-specific. Cell Mol Neurobiol **32:**1353–1365. http://dx.doi.org/10.1007/s10571-012-9862-y.

Published 27 January 2015

Citation Fernández de Castro I, Zamora PF, Ooms LS, Fernandez JJ, Lai CM, Mainou BA, Dermody TS, Risco C. 2015. Correction for Fernández de Castro et al, Reovirus forms neo-organelles for progeny particle assembly within reorganized cell membranes. mBio 6(1): e02529-14. doi:10.1128/mBio.02529-14.

Address correspondence to Terence S. Dermody, jvi@vanderbilt.edu.

AMERICAN SOCIETY FOR MICROBIOLOGY | mBio®

RESEARCH ARTICLE

Antagonism of the Sodium-Potassium ATPase Impairs Chikungunya Virus Infection

Alison W. Ashbrook,[a,b] Anthony J. Lentscher,[b,c] Paula F. Zamora,[b,c] Laurie A. Silva,[a,b] Nicholas A. May,[d] Joshua A. Bauer,[e,f] Thomas E. Morrison,[d] Terence S. Dermody[a,b,c]

Department of Pediatrics, Vanderbilt University School of Medicine, Nashville, Tennessee, USA[a]; Elizabeth B. Lamb Center for Pediatric Research, Vanderbilt University School of Medicine, Nashville, Tennessee, USA[b]; Department of Pathology, Microbiology, and Immunology, Vanderbilt University School of Medicine, Nashville, Tennessee, USA[c]; Department of Immunology and Microbiology, University of Colorado School of Medicine, Aurora, Colorado, USA[d]; Department of Biochemistry, Vanderbilt University School of Medicine, Nashville, Tennessee, USA[e]; Vanderbilt Institute of Chemical Biology, High-Throughput Screening Facility, Vanderbilt University School of Medicine, Nashville, Tennessee, USA[f]

ABSTRACT **Chikungunya virus (CHIKV) is a reemerging alphavirus that has caused epidemics of fever, arthralgia, and rash worldwide. There are currently no licensed vaccines or antiviral therapies available for the prevention or treatment of CHIKV disease. We conducted a high-throughput, chemical compound screen that identified digoxin, a cardiac glycoside that blocks the sodium-potassium ATPase, as a potent inhibitor of CHIKV infection. Treatment of human cells with digoxin or a related cardiac glycoside, ouabain, resulted in a dose-dependent decrease in infection by CHIKV. Inhibition by digoxin was cell type-specific, as digoxin treatment of either murine or mosquito cells did not diminish CHIKV infection. Digoxin displayed antiviral activity against other alphaviruses, including Ross River virus and Sindbis virus, as well as mammalian reovirus and vesicular stomatitis virus. The digoxin-mediated block to CHIKV and reovirus infection occurred at one or more postentry steps, as digoxin inhibition was not bypassed by fusion of CHIKV at the plasma membrane or infection with cell surface-penetrating reovirus entry intermediates. Selection of digoxin-resistant CHIKV variants identified multiple mutations in the nonstructural proteins required for replication complex formation and synthesis of viral RNA. These data suggest a role for the sodium-potassium ATPase in promoting postentry steps of CHIKV replication and provide rationale for modulation of this pathway as a broad-spectrum antiviral strategy.**

IMPORTANCE **Mitigation of disease induced by globally spreading, mosquito-borne arthritogenic alphaviruses requires the development of new antiviral strategies. High-throughput screening of clinically tested compounds provides a rapid means to identify undiscovered, antiviral functions for well-characterized therapeutics and illuminate host pathways required for viral infection. Our study describes the potent inhibition of CHIKV and related alphaviruses by the cardiac glycoside digoxin and demonstrates a function for the sodium-potassium ATPase in CHIKV infection.**

Received 19 April 2016 **Accepted** 21 April 2016 **Published** 24 May 2016

Citation Ashbrook AW, Lentscher AJ, Zamora PF, Silva LA, May NA, Bauer JA, Morrison TE, Dermody TS. 2016. Antagonism of the sodium-potassium ATPase impairs chikungunya virus infection. mBio 7(3):e00693-16. doi:10.1128/mBio.00693-16.

Editor Anne Moscona, Columbia University Medical College

Address correspondence to Terence S. Dermody, terry.dermody@vanderbilt.edu.

Chikungunya virus (CHIKV) is an arthritogenic alphavirus responsible for explosive epidemics throughout the world. Since its reemergence in Kenya in 2004, millions of cases of CHIKV have been reported in sub-Saharan Africa and Asia in addition to regions in which CHIKV was not previously endemic, including Europe and the Americas (1–6). Autochthonous, mosquito transmission of CHIKV continues to occur in many countries of the Caribbean basin and South America, and the presence of CHIKV-competent mosquito vectors in these regions supports the potential for further spread of the virus to new populations.

The vast majority of CHIKV-infected individuals develop chikungunya fever, a disease characterized by debilitating polyarthralgia and arthritis, headache, and rash (7, 8). More severe disease and atypical symptoms also have been observed during recent epidemics (9–11), including neurological and cardiac manifestations, which have been reported in neonates, the elderly, and those with underlying comorbidities. Although most of the clinical signs and symptoms resolve 7 to 10 days after infection, the arthritis and polyarthralgia can recur for months to years after the initial diagnosis (2, 8, 12). To date, no licensed anti-CHIKV therapeutics or vaccines are available. The chronic, incapacitating disease, in addition to the high attack rates of the virus in naive populations, imposes a substantial burden on the quality of life of those infected and the economies of affected countries (13–15).

CHIKV displays broad tropism in humans, but many of the host factors required for infection are not fully understood. Following attachment to host cells via unidentified cell surface receptors, CHIKV particles are internalized by clathrin-mediated endocytosis (16–18). Acidification of endosomes triggers fusion of the viral envelope with the host endosomal membrane, which allows release of the nucleocapsid into the cytoplasm (19, 20). The CHIKV genome consists of a single-stranded, positive-sense RNA molecule approximately 12 kb in length that encodes four nonstructural proteins (nsP1 to 4) and three major structural proteins

(capsid, pE2, and E1) (21, 22). Together, the nonstructural proteins mediate interactions with cellular membranes and other host factors to form replication complexes that house synthesis of subgenomic RNA and additional copies of viral genomic RNA for encapsidation into progeny virions (23–28). Host factors and mechanisms involved in viral RNA synthesis of alphaviruses, particularly for CHIKV, are not well defined.

To identify host mediators of CHIKV replication, we screened a library of small molecules for the capacity to augment or diminish infection of human osteosarcoma (U-2 OS) cells by CHIKV replicon particles expressing an enhanced green fluorescent protein (eGFP) reporter. From this screen, we identified digoxin, a cardiac glycoside that antagonizes the sodium-potassium ATPase, as a potent inhibitor of CHIKV infection. Digoxin diminished infection by replication-competent CHIKV in both U-2 OS cells and primary human synovial fibroblasts. Ouabain, a related cardiac glycoside, also blocked CHIKV infection. Increasing extracellular concentrations of potassium alleviated CHIKV inhibition by digoxin, suggesting that antagonism of the sodium-potassium ATPase mediates the antiviral effect. Digoxin displayed antiviral activity against alphaviruses other than CHIKV, including Ross River virus (RRV) and Sindbis virus (SINV), and the unrelated mammalian orthoreovirus (called "reovirus" here) and vesicular stomatitis virus (VSV). Passage of CHIKV in digoxin-treated cells selected mutations in genes encoding nonstructural proteins, suggesting that digoxin impairs functions mediated by these replicase proteins. These data suggest a role for the sodium-potassium ATPase in CHIKV infection and highlight a new strategy for development of therapeutics to limit CHIKV replication and disease.

RESULTS

Identification of digoxin as an inhibitor of CHIKV infection. To identify host factors required for CHIKV infection, we screened 727 chemical compounds from the NIH Clinical Collection (NCC) for the capacity to impede or augment infection by CHIKV replicon particles (Fig. 1A). The NCC library consists almost entirely of compounds that have been used in phase I, II, and III clinical trials. U-2 OS cells were incubated with dimethyl sulfoxide (DMSO) as a vehicle control, 100 nM bafilomycin A1 as a positive control, or 1 μM NCC compound for 1 h. Treated cells were adsorbed with CHIKV strain SL15649 replicon particles expressing eGFP and incubated for 20 to 24 h. The percentage of infected cells was determined by GFP expression, and robust *Z* scores were calculated for each compound from three independent experiments. Seven compounds had average *Z* scores of ≤ -2.0 (inhibited infection), and 21 compounds had average *Z* scores of ≥ 2.0 (enhanced infection) (Fig. 1B). The largest class of compounds that influenced CHIKV infection, both positively and negatively, is that which affects steroid or hormone signaling and biosynthetic pathways (Fig. 1C). CHIKV infection was also positively and negatively affected by compounds that target ion transporters and neurotransmitter receptors, such as dopamine and serotonin. Homoharringtonine, a translation inhibitor and known antagonist of CHIKV infection (29), had the largest negative *Z* score, -41.94. Digoxin, a sodium-potassium ATPase inhibitor, had a negative *Z* score of -26.67, suggesting a function for the sodium-potassium ATPase in CHIKV infection.

Digoxin is a species-specific inhibitor of CHIKV infection. To determine whether inhibition of the sodium-potassium ATPase blocks infection by replication-competent CHIKV, we treated a variety of cell lines with DMSO, 5-nonyloxytryptamine (5-NT [a serotonin receptor agonist]) as a positive control (30), or increasing concentrations of digoxin for 1 h prior to adsorption with CHIKV. At 6 h postinfection, cells were scored for infection by indirect immunofluorescence (Fig. 2). Relative to DMSO-treated cells, treatment of U-2 OS cells with digoxin resulted in a dose-dependent decrease in CHIKV infection with a half-maximal effective concentration (EC_{50}) of 48.8 nM (Fig. 2A). Digoxin treatment similarly decreased CHIKV infection of primary human synovial fibroblasts (HSFs) and Vero African green monkey kidney cells with EC_{50}s of 43.9 nM and 67.3 nM, respectively (Fig. 2B and data not shown). Incubation of virus with digoxin prior to adsorption to cells had no effect on viral titers, suggesting that the antiviral effect is not attributable to an alteration in the virus (data not shown). Despite inhibition of CHIKV infection in multiple primate cell types, digoxin treatment of murine stromal ST2 and *Aedes albopictus* C6/36 cells at doses sufficient to block infection of primate cells did not decrease CHIKV infection (Fig. 2C and D). Together, these data indicate that digoxin is a potent inhibitor of CHIKV infection and that inhibition occurs in a host species-specific manner.

Species-specific inhibition by digoxin occurs via the sodium-potassium ATPase. Cardiac glycosides inhibit the sodium-potassium ATPase by binding to the catalytic α subunit but do so with less efficiency to specific murine isoforms relative to their human counterparts (31–33). To determine whether higher doses of digoxin are capable of inhibiting CHIKV infection of murine cells, ST2 cells and myoblast C2C12 cells were treated with DMSO, 5-NT, or increasing concentrations of digoxin for 1 h prior to adsorption with CHIKV. At 6 h postinfection, cells were scored for infection by indirect immunofluorescence (Fig. 3A and B). At higher concentrations, digoxin treatment significantly diminished CHIKV infection in these cell types, with EC_{50}s of 16.2 μM in ST2 cells and 23.2 μM in C2C12 cells, values 330 and 475 times the EC_{50} of digoxin in U-2 OS cells, without a decrease in cell viability (data not shown). These data indicate that digoxin can inhibit CHIKV infection of murine cells, but at significantly higher concentrations than in human cells.

We next assessed transcript levels of two α subunit isoforms (α1 and α3) in the human and murine cells tested. Whereas the human and murine α3 subunits are sensitive to cardiac glycosides, the murine α1 isoform is significantly less sensitive to cardiac glycoside treatment relative to the human isoform (31, 32). RNA was isolated from mock-infected and CHIKV-infected U-2 OS and ST2 cells and used as a template for reverse transcription-PCR (RT-PCR) amplification of ATP1A1 (α1), ATP1A3 (α3), and GAPDH (glyceraldehyde-3-phosphate dehydrogenase) (as a control) mRNAs (Fig. 3C). Expression of ATP1A1 was detected in both U-2 OS and ST2 cells and did not differ significantly following infection. In contrast, the ATP1A3 transcript was detected in U-2 OS cells but not in ST2 cells. Thus, decreased expression of ATP1A3 in murine cells correlates with reduced sensitivity to digoxin-mediated inhibition of CHIKV.

To determine whether blockade of the sodium-potassium ATPase is responsible for CHIKV inhibition, U-2 OS cells were treated with increasing concentrations of digoxin or ouabain, a related cardiac glycoside, for 1 h prior to adsorption with CHIKV. At 6 h postinfection, cells were scored for infection by indirect immunofluorescence (Fig. 4A). Again, treatment of cells with ouabain led to a dose-dependent decrease in CHIKV infection,

A

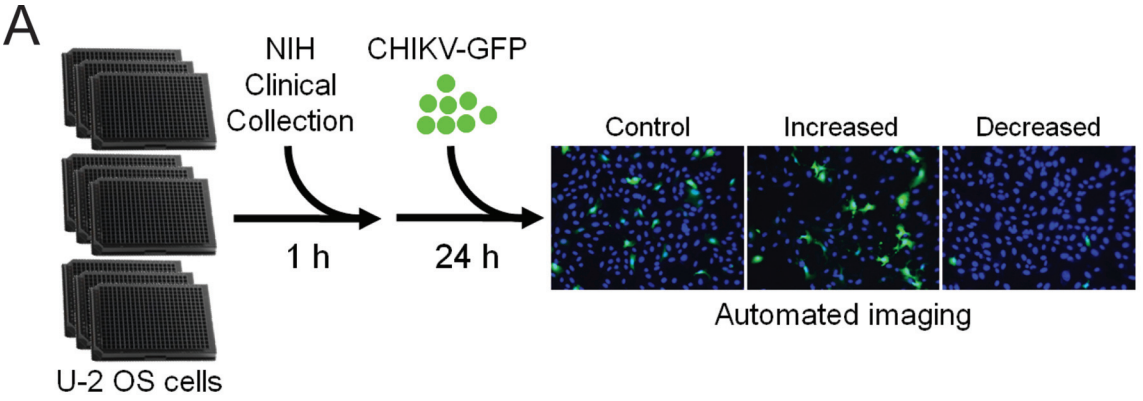

B

Compound Name	Target	*Z* Score
Homoharringtonine	Protein synthesis	-41.94
Digoxin	Sodium-potassium ATPase	-26.67
Goserelin acetate	LHRH agonist	-3.35
Metyrapone	Cortisol synthesis	-3.22
Vincristine sulfate	Microtubules	-2.48
Perphenazine	Dopamine antagonist	-2.47
SR 57,227A	Serotonin agonist	-2.31
Dehydrocholic acid	Steroid metabolism	2.00
Benzbromarone	Organic anion transporter	2.00
Anastrozole	Estrogen synthase	2.08
Balsalazide	Prostaglandin synthase and lipoxygenase	2.12
Cefaclor	Bacterial cell wall antibiotic	2.20
SDM25N	Opioid receptor antagonist	2.20
Resveratrol	Phosphodiesterase inhibitor	2.24
Lansoprazole	Proton-pump inhibitor	2.26
Palonosetron	Serotonin antagonist	2.39
Granisetron	Serotonin antagonist	2.71
Haloperidol	Dopamine and glutamate antagonist	2.78
Fluperlapine	Serotonin and α_2-adrenergic antagonist	2.85
Tibolone	Estrogen receptor	2.88
Desoximetasone	Glucocorticoid receptor	2.88
Ropivacaine	Sodium channel	2.89
Corticosterone	Corticoid receptors	2.96
Salmeterol	β_2-adrenergic receptor	3.09
Dehydroepiandrosterone	Steroid precursor	3.15
Cefixime trihydrate	Bacterial cell wall antibiotic	3.32
5-Methoxytryptamine	Serotonin agonist	3.41
Phenothiazine	Dopamine antagonist	3.86

C

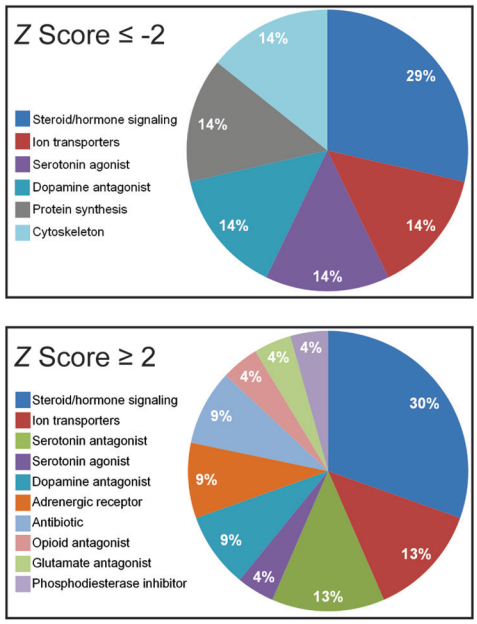

FIG 1 High-throughput screening to identify inhibitors of CHIKV infection. (A) U-2 OS cells were incubated with DMSO, 100 nM bafilomycin A1, or compounds from the NIH clinical collection at a concentration of 1 μM at 37°C for 1 h. Cells were adsorbed with SL15649 eGFP replicon particles at an MOI of ~5 IU/cell and incubated with compound at 37°C for 20 to 24 h. Cells were incubated with Hoechst dye to stain nuclei and imaged by automated, high-content fluorescence microscopy. (B) Robust *Z* scores were calculated for individual compounds. Shown are the average robust *Z* scores for compounds with robust *Z* scores of ≤ -2 or ≥ 2 median absolute deviations from the median of each plate identified in three independent screening experiments. (C) Distribution of candidate compounds by known biological targets.

indicating that treatment of cells with two independent cardiac glycosides results in decreased CHIKV infection. As the sodium-potassium ATPase is the only known target of cardiac glycosides, these data suggest that antagonism of this molecule is the mechanism by which digoxin restricts CHIKV. To further test whether inhibition of CHIKV by digoxin treatment occurs via changes in ion concentrations, cells were pretreated with DMSO or digoxin in the presence of increasing extracellular sodium or potassium for 1 h prior to adsorption with CHIKV. At 6 h postinfection, cells were scored for infection by indirect immunofluorescence (Fig. 4B). Addition of extracellular NaCl in the presence of digoxin enhanced inhibition of CHIKV by digoxin in a dose-dependent manner (Fig. 4B, left). Furthermore, addition of extracellular KCl in the presence of digoxin alleviated inhibition of CHIKV by digoxin (Fig. 4B, right). These data indicate that alterations of ion concentrations contribute to the antiviral activity of digoxin.

CHIKV inhibition by digoxin is not attributable to decreased cell viability. The sodium-potassium ATPase is essential for homeostasis in most multicellular organisms. As such, we sought to determine whether inhibition of CHIKV infection by digoxin occurs as a consequence of altered viability of treated cells. To assess possible digoxin cytotoxicity, cells were incubated with either propidium iodide (PI) or PrestoBlue to assess plasma membrane integrity and mitochondrial metabolic activity, respectively, posttreatment with DMSO, staurosporine (STS) (as an inducer of cell death), or increasing concentrations of digoxin (Fig. 5). Incubation of U-2 OS cells with digoxin did not alter cell viability by 6 h posttreatment (Fig. 5A and B). Moreover, cell viability was only

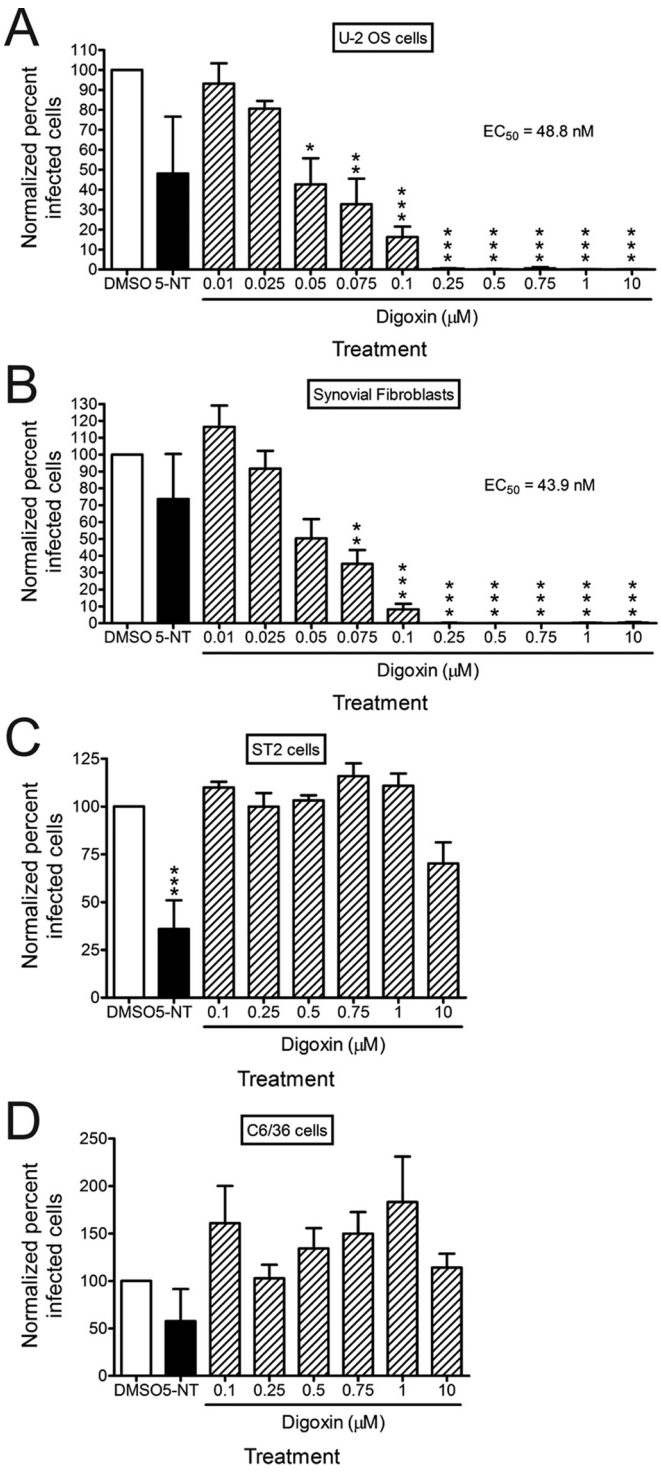

FIG 2 Digoxin potently inhibits CHIKV infection of human cells. (A) U-2 OS cells, (B) HSFs, (C) ST2 cells, or (D) C6/36 cells were incubated with DMSO, 10 μM 5-NT, or increasing concentrations of digoxin for 1 h prior to adsorption with CHIKV strain SL15649 at an MOI of 5 PFU/cell. After 1 h of incubation, virus was removed, and cells were incubated with medium containing DMSO or inhibitor for 5 h. Cells were stained with CHIKV-specific antiserum and DAPI to detect nuclei and imaged by fluorescence microscopy. Results are presented as percentages of infected cells normalized to DMSO-treated cells for triplicate experiments. Error bars indicate standard errors of the means. *, $P < 0.05$, **, $P < 0.01$, and ***, $P < 0.001$, in comparison to DMSO, as determined by ANOVA followed by Tukey's post hoc test.

modestly impaired at 24 h posttreatment with 1 μM digoxin, a dose 20 times the digoxin EC_{50} for CHIKV antiviral activity in these cells (Fig. 5B). Digoxin also did not significantly decrease viability of HSFs and Vero cells following treatment with doses of digoxin that inhibit CHIKV infection in these cells (data not shown). These data suggest that digoxin inhibition of CHIKV is not attributable to cytotoxic effects.

Digoxin treatment inhibits infection by diverse virus families. To determine whether digoxin blocks infection by other strains of CHIKV as well as related alphaviruses, we assessed the effect of digoxin treatment on infection by CHIKV strains SL15649 and 181/25, RRV strain T48, and SINV strain TRSB. U-2 OS cells were treated with DMSO, 5-NT, or digoxin for 1 h prior to adsorption with CHIKV, RRV, or SINV at a multiplicity of infection (MOI) of 1, 10, or 5 PFU/cell, respectively, to adjust for infectivity differences in these cells. At 6 h postadsorption, cells were scored for infection by indirect immunofluorescence (Fig. 6A). Digoxin treatment significantly diminished infection by all strains tested, with EC_{50}s of 108.9 nM for CHIKV strain SL15649, 100.9 nM for CHIKV strain 181/25, 126.5 nM for RRV, and 198.9 nM for SINV.

To determine whether digoxin displays inhibitory effects against diverse virus families, we assessed the capacity of the drug to inhibit mammalian reovirus, a nonenveloped, double-stranded RNA virus. Human brain microvascular endothelial cells (HBMECs) were treated with DMSO, 5-NT, or digoxin prior to adsorption with reovirus virions or infectious subvirion particles (ISVPs). ISVPs are reovirus disassembly intermediates formed following endocytosis and cleavage of the viral outer capsid by intracellular cathepsins or *in vitro* following protease treatment (34). ISVPs bind to cell surface receptors and internalize at the plasma membrane, bypassing the disassembly requirements of virions, including acidic pH and protease activity (34–37). At 20 h postadsorption with either reovirus virions or ISVPs, cells were scored for infection by indirect immunofluorescence (Fig. 6B). Treatment with digoxin impaired infection by both virions (Fig. 6B, left) and ISVPs (Fig. 6B, right), with EC_{50}s of 133.9 nM and 434.7 nM, respectively. Decreased infectivity of ISVPs following digoxin treatment suggests that digoxin inhibits reovirus infection at one or more replication steps following internalization and disassembly. We also tested the capacity of digoxin to inhibit VSV, an enveloped, negative-sense RNA virus (Fig. 6C). Digoxin treatment similarly inhibited infection by VSV, with an EC_{50} of 238.7 nM. These data indicate that digoxin inhibits infection by plus-strand, minus-strand, and double-stranded RNA viruses.

Digoxin impairs CHIKV infection at postentry steps. We next sought to define steps in CHIKV replication blocked by digoxin. To determine the temporal window during which digoxin acts to inhibit CHIKV infection, U-2 OS cells were treated with DMSO or 1 μM digoxin at 15-min intervals for 1 h prior to adsorption or at 15- or 60-min intervals for 4 h after adsorption. As a control for inhibition of CHIKV entry, 20 mM NH_4Cl was added at the same intervals to block acidification of endocytic compartments. Cells were fixed at 6 h postadsorption and scored for infection by indirect immunofluorescence (Fig. 7A). Maximal impairment of CHIKV infection by digoxin was achieved when digoxin was added 60 min prior to adsorption. The magnitude of inhibition gradually decreased when the drug was added at later times, with only negligible effects observed when added 120 min postadsorption. CHIKV bypassed digoxin inhibition with kinetics

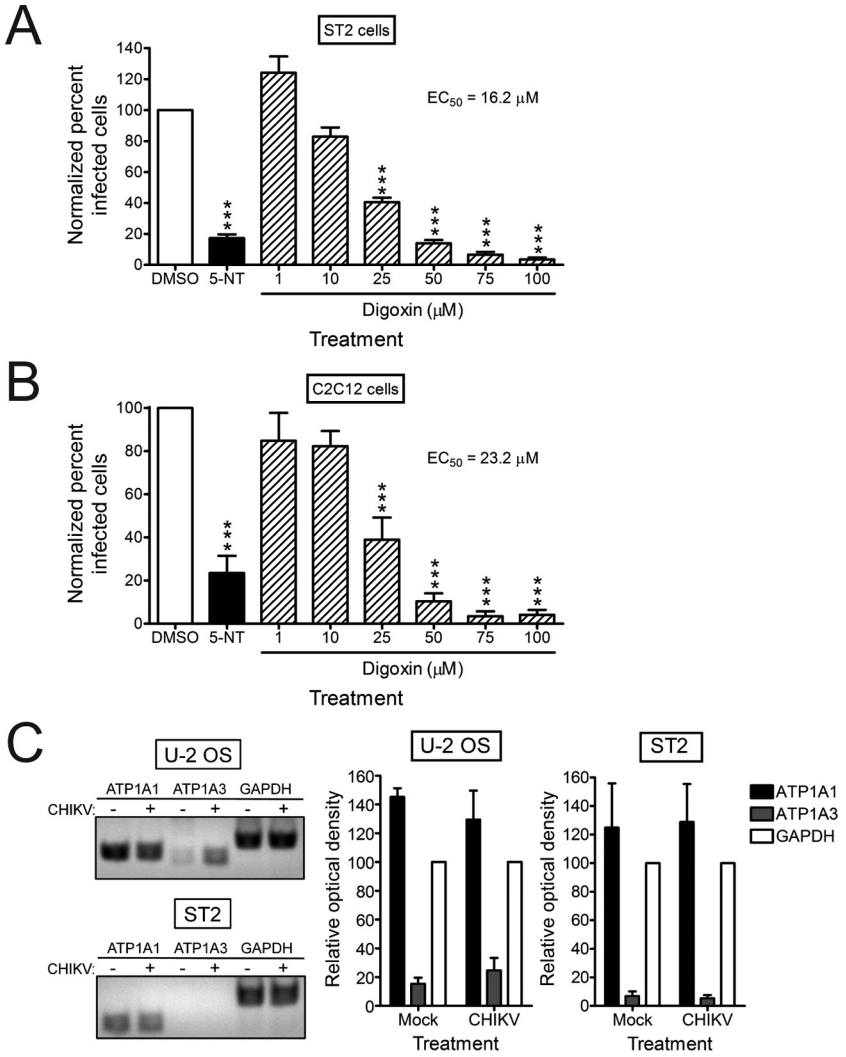

FIG 3 CHIKV resistance to digoxin in murine cells correlates with decreased expression of the α3 subunit of the sodium-potassium ATPase. (A) ST2 cells or (B) C2C12 cells were incubated with DMSO, 10 μM 5-NT, or increasing concentrations of digoxin for 1 h prior to adsorption with CHIKV strain SL15649 at an MOI of 5 PFU/cell. After 1 h, virus was removed, and cells were incubated with medium containing DMSO or inhibitor for 5 h. Cells were stained with CHIKV-specific antiserum and DAPI to detect nuclei and imaged by fluorescence microscopy. Results are presented as the percentages of infected cells normalized to DMSO-treated cells for triplicate experiments. Error bars indicate standard errors of the means. (C) U-2 OS and ST2 cells were mock infected or infected with CHIKV 181/25 at an MOI of 5 PFU/cell. RNA was isolated and used for RT-PCR amplification of ATP1A1 (α1), ATP1A3 (α3), and GAPDH transcripts with human- or murine-specific primer sets (see Table S1 in the supplemental material). Reaction products were resolved by electrophoresis in 1% agarose gels (left). Band intensity was quantified by optical densitometry for four independent experiments (right). ***, $P < 0.001$, in comparison to DMSO, as determined by ANOVA followed by Tukey's post hoc test.

similar to the bypass of NH_4Cl inhibition, suggesting that digoxin restricts CHIKV infection at early steps in the replication cycle. Alphavirus nonstructural proteins and double-stranded RNA (dsRNA) accumulate at the plasma membrane of infected cells to form replication complexes, as early as 45 min postadsorption, and RNA synthesis can be detected by 1 h postadsorption (28, 38). Thus, digoxin may inhibit these or earlier steps in CHIKV replication.

To determine whether digoxin blocks CHIKV infection by inhibiting viral entry (attachment, internalization, and membrane fusion), cells were treated with DMSO, 5-NT, or digoxin for 1 h prior to adsorption with CHIKV or SINV at 4°C to prevent internalization. At 1 h postadsorption, cells were exposed to acidic medium (pH 5.5) to trigger viral fusion at the plasma membrane or neutral medium (pH 7.4) as a control. Fused and unfused cells were incubated with drug and NH_4Cl at 37°C to block subsequent rounds of replication and scored for infection at 18 h postadsorption by indirect immunofluorescence (Fig. 7B). Triggering fusion at the plasma membrane partially bypassed inhibition of CHIKV and SINV by 5-NT treatment, which inhibits viral entry steps (30). However, fusion at the plasma membrane did not bypass digoxin-mediated inhibition of CHIKV or SINV, except at the lowest concentrations used. The failure of fusion at the plasma membrane to bypass digoxin-mediated inhibition was not due to decreased virus attachment, as the percentage of digoxin-treated cells bound by CHIKV was similar to that of DMSO-treated cells (see Fig. S1 in the supplemental material). Viral titers were similarly decreased following electroporation of digoxin-treated cells with CHIKV

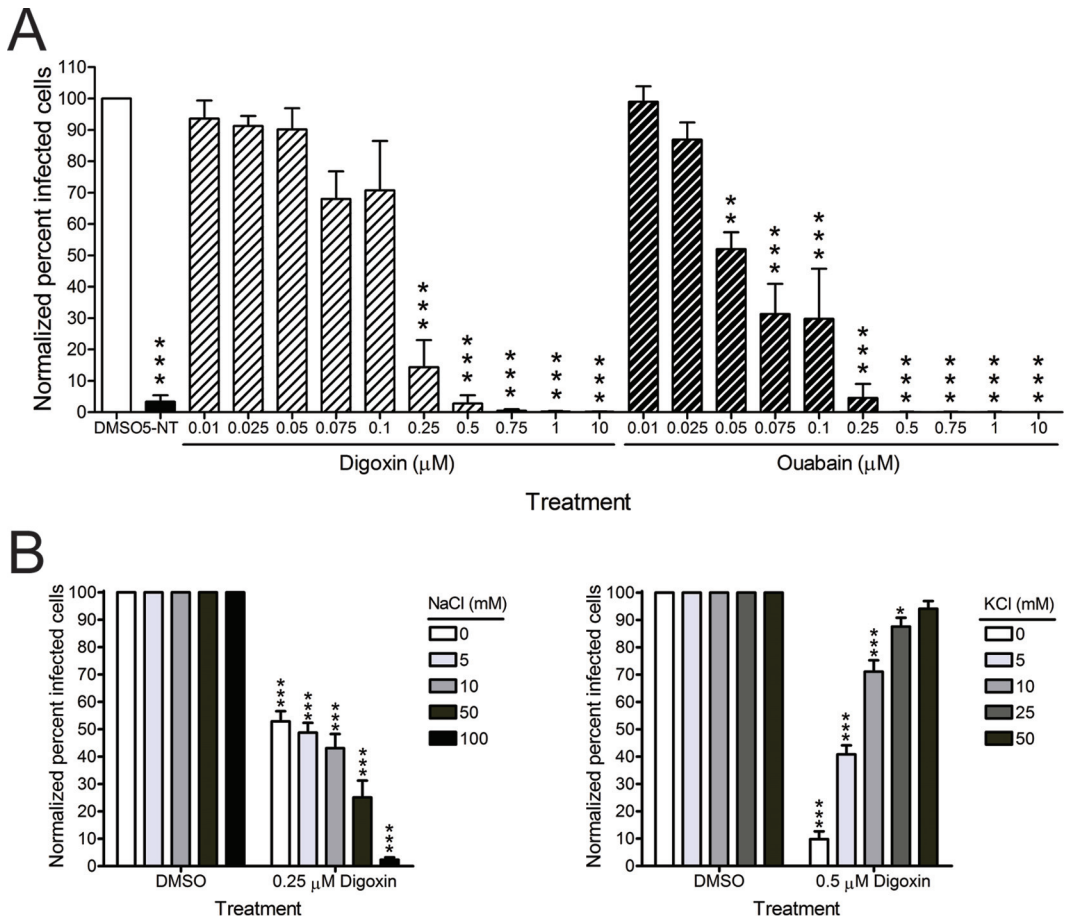

FIG 4 Inhibition by digoxin occurs via the sodium-potassium ATPase. (A) U-2 OS cells were incubated with DMSO, 10 μM 5-NT, or increasing concentrations of digoxin or the related cardiac glycoside, ouabain, for 1 h prior to adsorption with CHIKV SL15649 at an MOI of 5 PFU/cell. After 1 h, virus was removed, and cells were incubated with medium containing DMSO or inhibitor for 5 h. Cells were scored for infection by indirect immunofluorescence. Results are presented as percentage of infected cells normalized to DMSO-treated cells for triplicate experiments. Error bars indicate standard errors of the means. (B) U-2 OS cells were incubated with DMSO or digoxin in standard medium or medium supplemented with increasing concentrations of NaCl (left) or KCl (right) for 1 h prior to adsorption with CHIKV 181/25 at an MOI of 5 PFU/cell. After 1 h, virus was removed, and cells were incubated with medium containing DMSO or digoxin and the concentration of NaCl or KCl shown for 5 h. Cells were scored for infection by indirect immunofluorescence. Results are presented as percentages of infected cells normalized to DMSO-treated cells for triplicate experiments. Error bars indicate standard errors of the means. *, $P < 0.05$, **, $P < 0.01$, and ***, $P < 0.001$, in comparison to DMSO, as determined by ANOVA followed by Tukey's post hoc test.

RNA relative to those following electroporation of DMSO-treated cells (see Fig. S2 in the supplemental material). Together, these data suggest that CHIKV replication is impeded by digoxin at one or more postentry steps of the viral replication cycle.

Polymorphisms observed in digoxin-resistant CHIKV populations. To enhance an understanding of mechanisms underlying the digoxin-mediated restriction of CHIKV infection, we passaged CHIKV in cells treated with either DMSO or digoxin to select digoxin-resistant viruses. U-2 OS cells were adsorbed with CHIKV strain SL15649 for 1 h and incubated with medium containing either DMSO or 100 nM digoxin until comparable cytopathic effect (CPE) was observed. Supernatants from infected cells were used to inoculate fresh cells, and this process was repeated with increasing concentrations of digoxin until CPE was observed with doses 5 times the EC_{50} in U-2 OS cells. To test whether supernatants of digoxin-treated cells contained drug-resistant viruses, U-2 OS cells were pretreated with DMSO, 5-NT, or digoxin prior to adsorption with passage 14 supernatants from DMSO-treated ($SL15649_{DMSO}$) and digoxin-treated ($SL15649_{Digoxin}$) cells. Infected cells were scored for infection by indirect immunofluorescence at 6 h postinfection (Fig. 8A). Treatment of cells with 5-NT prevented infection by both $SL15649_{DMSO}$ and $SL15649_{Digoxin}$ supernatant stocks. In contrast, treatment of cells with 500 nM digoxin completely inhibited infection by $SL15649_{DMSO}$ (EC_{50} of 198.8 nM), but this dose resulted in only an ~50% inhibition of infectivity by $SL15469_{Digoxin}$ (EC_{50} of 521.4 nM). These data suggest that viral variants selected during serial passage in digoxin-treated cells are less susceptible to the inhibitory effects of digoxin.

To determine the genetic basis for digoxin resistance, we isolated virus clones from the $SL15649_{DMSO}$ and $SL15649_{Digoxin}$ supernatant stocks by plaque purification and assessed the sensitivity of these virus clones to digoxin treatment (Fig. 8B). In general, virus clones isolated from the $SL15649_{Digoxin}$ stock were more resistant to digoxin-mediated inhibition than those isolated from the $SL15649_{DMSO}$ stock, but one clone ($SL15649_{Digoxin}$ clone 2) was sensitive to digoxin treatment like that of the $SL15649_{DMSO}$ clones. To identify polymorphisms displayed by these virus

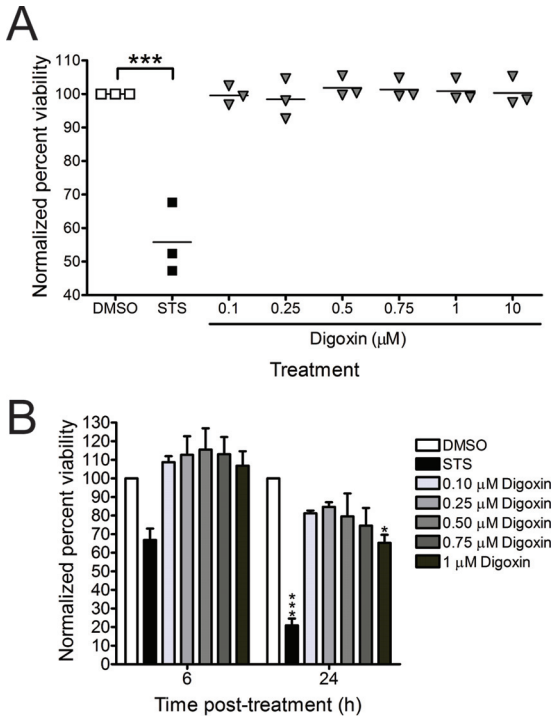

FIG 5 CHIKV inhibition by digoxin is not attributable to cytotoxicity. (A) U-2 OS cells were treated with DMSO, 10 μM STS, or increasing concentrations of digoxin for 6 h. Cell viability was quantified by PI staining. Results are expressed as percentages of viable cells normalized to DMSO-treated cells for individual experiments. Horizontal black lines indicate mean percentages of viability. (B) U-2 OS cells were treated with DMSO, 10 μM STS, or increasing concentrations of digoxin for 6 or 24 h. Cell viability was quantified by PrestoBlue fluorescence assay. Results are presented as percentages of viable cells normalized to DMSO-treated cells for triplicate experiments. Error bars indicate standard errors of the means. *, $P < 0.05$, and ***, $P < 0.001$, in comparison to DMSO, as determined by ANOVA followed by Tukey's post hoc test.

clones, we determined the full-length nucleotide sequences of each clone (Table 1). Sequence analysis identified three unique, nonsynonymous mutations in virus clones from DMSO-treated cells and six unique, nonsynonymous mutations in virus clones from digoxin-treated cells. The E2 S159R polymorphism was identified in virus clones from both DMSO- and digoxin-treated cells and likely was selected as a consequence of cell culture adaptation and increased glycosaminoglycan dependence (39). However, the unique mutations identified in virus clones from digoxin-treated cells were contained in the nonstructural open reading frame. Although the majority of the mutations were in nsP3, these mutations did not segregate completely with digoxin resistance, as digoxin-sensitive $SL15649_{Digoxin}$ clone 2 also encoded these changes. Instead, a mutation in the RNA-dependent RNA polymerase (RdRp), nsP4 V209I, was the only coding change that differed between $SL15649_{Digoxin}$ clone 2 (sensitive) and clones 3 and 4 (resistant). All 290 CHIKV strain sequences available in the NIAID ViPR database encode a valine at residue 209 in nsP4 (40), suggesting that this residue or region of nsP4 serves an important, conserved function in CHIKV replication. These findings indicate that multiple mutations are selected during passage of CHIKV in digoxin-treated cells. Furthermore, selection of mutations in the nonstructural proteins, particularly nsP4 V209I, suggests that digoxin inhibits CHIKV replication by disrupting RNA synthesis or replication complex formation.

DISCUSSION

CHIKV has reemerged to cause epidemics of fever, rash, and arthritis throughout Africa, South and Southeast Asia, and the Americas. The rapid, mosquito-borne transmission of CHIKV has resulted in millions of cases of CHIKV disease in the last decade alone. The high attack rate and global significance of CHIKV infection warrant development of CHIKV-specific therapeutics and vaccines. Thus far, none are available.

To enhance an understanding of the host factors required for CHIKV replication, we screened a library of chemical compounds for the capacity to diminish or enhance CHIKV infection in U-2 OS cells. We identified digoxin, a cardiac glycoside, as a host species-specific inhibitor of CHIKV replication. We discovered that digoxin impedes CHIKV infection at postentry steps of the replication cycle via antagonism of the sodium-potassium ATPase. Passage of CHIKV in digoxin-treated cells selected multiple mutations in the nonstructural proteins, and one particular mutation, nsP4 V209I, segregated with digoxin sensitivity. Taken together, these findings indicate that a functional sodium-potassium ATPase is required for CHIKV infection.

Our results demonstrate that CHIKV inhibition by digoxin occurs at an early but postentry step in the viral replication cycle. The temporal window in which digoxin inhibition occurs mirrors that of ammonium chloride, which supports an early block to CHIKV infection (Fig. 7A). However, fusion of CHIKV or SINV at the plasma membrane in an attempt to bypass the digoxin-mediated defect was not sufficient to restore viral replication to levels in untreated cells (Fig. 7B). In an analogous case, proteolytic cleavage of reovirus virions to form ISVPs *in vitro* overcame restriction by an entry inhibitor, 5-NT, but was insufficient to completely circumvent inhibition by digoxin. ISVPs are thought to enter cells at the plasma membrane and, therefore, are not susceptible to inhibition by compounds that inhibit reovirus internalization or disassembly (35, 36, 41). Selection of multiple mutations in CHIKV nonstructural proteins following passage of virus in digoxin-treated cells also points to inhibition of postentry viral replication steps as a mechanism of digoxin action. Although the majority of these mutations were selected in nsP3, a protein essential for formation of CHIKV replication complexes and modulation of host stress responses (42–46), these mutations also were observed in digoxin-sensitive variants ($SL15649_{Digoxin}$ clone 2). In otherwise isogenic viruses ($SL15649_{Digoxin}$ clones 2 to 4), the nsP4 V209I polymorphism was sufficient to confer resistance to digoxin treatment, but the digoxin-resistant phenotype may depend on the presence of the nsP3 Stop524C mutation to enhance levels of nsP4, suggesting that one or more functions of nsP4 are impaired by digoxin. However, additional combinations of mutations also may produce a digoxin-resistant virus ($SL15649_{Digoxin}$ clone 1). We conclude that individual or combinatorial substitutions within genes encoding nonstructural proteins can restore replication efficiency to bypass digoxin inhibition, with the substitution in nsP4 playing a pivotal role.

Inhibition of the sodium-potassium ATPase disrupts ion transport and alters many cellular biosynthetic, signaling, and vesicular sorting pathways (47). Although the precise alterations by which digoxin restricts CHIKV infection are not known, we envision two possible mechanisms. First, CHIKV may require a spe-

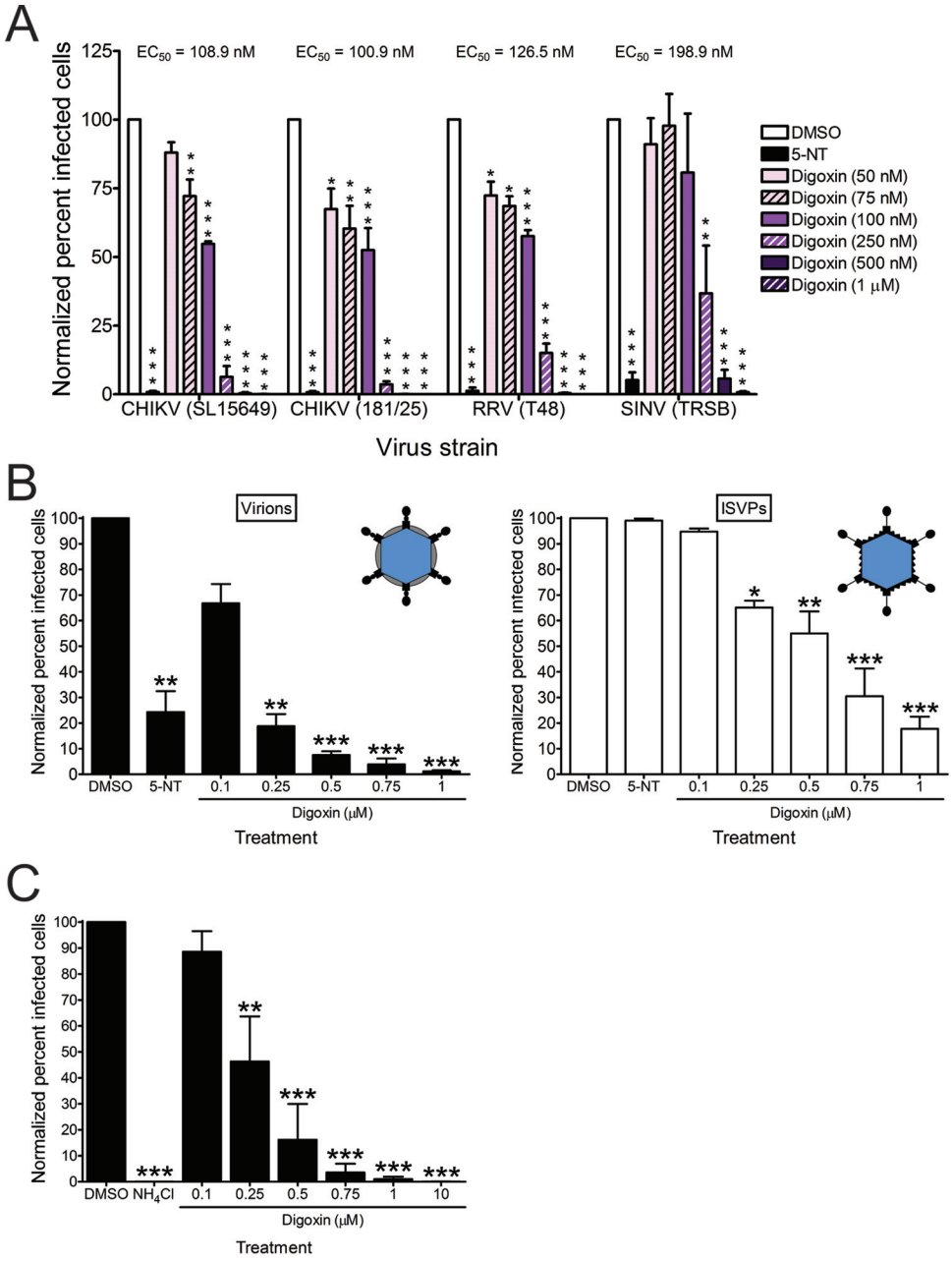

FIG 6 Digoxin inhibits multiple alphaviruses, mammalian reovirus, and VSV. (A) U-2 OS cells were incubated with DMSO, 10 μM 5-NT, or increasing concentrations of digoxin for 1 h prior to adsorption with CHIKV strains SL15649 and 181/25 at an MOI of 1 PFU/cell, RRV strain T48 at an MOI of 10 PFU/cell, or SINV strain TRSB at an MOI of 5 PFU/cell. After 1 h of incubation, virus was removed, and cells were incubated with medium containing DMSO or inhibitor for 5 h. Cells were stained with virus-specific antiserum and DAPI to detect nuclei and imaged by fluorescence microscopy. Results are presented as percentages of infected cells normalized to DMSO-treated cells for triplicate experiments. Error bars indicate standard errors of the mean. (B) HBMECs were incubated with DMSO, 10 μM 5-NT, or increasing concentrations of digoxin for 1 h prior to adsorption with reovirus virions (left) or ISVPs (right) at an MOI of 1,500 particles/cell (~15 PFU/cell). After 1 h of incubation, virus was removed, and cells were incubated with medium containing DMSO or inhibitor for 20 h. Cells were scored for infection by indirect immunofluorescence. Results are presented as percentages of infected cells normalized to DMSO-treated cells for duplicate experiments. Error bars indicate standard errors of the means. Insets show schematics of reovirus virions and ISVPs. (C) U-2 OS cells were incubated with DMSO, 20 mM NH_4Cl, or digoxin at the concentrations shown for 1 h prior to adsorption with VSV-eGFP at an MOI of 10 PFU/cell. After 1 h, virus was removed, and cells were incubated with medium containing DMSO or inhibitor for 5 h. Cells were incubated with Hoechst stain to detect nuclei and imaged by fluorescence microscopy. Results are presented as percentages of infected cells normalized to DMSO-treated cells for triplicate experiments. Error bars indicate the standard errors of the means. *, $P < 0.05$, **, $P < 0.01$, and ***, $P < 0.001$, in comparison to DMSO, as determined by ANOVA followed by Tukey's post hoc test.

cific ion composition to complete discrete steps in the viral replication cycle or coordinate the functions of specific viral proteins. Evidence for such an ion requirement is supported by the function of the alphavirus 6K protein in ion channel formation and the sensitivity of alphavirus particle maturation to the ionic strength of the culture medium (48, 49). The ion channels formed by 6K are selective for Na^+, K^+, and Ca^{2+} ions, which are specifically altered during cardiac glycoside treatment (48). In support of this

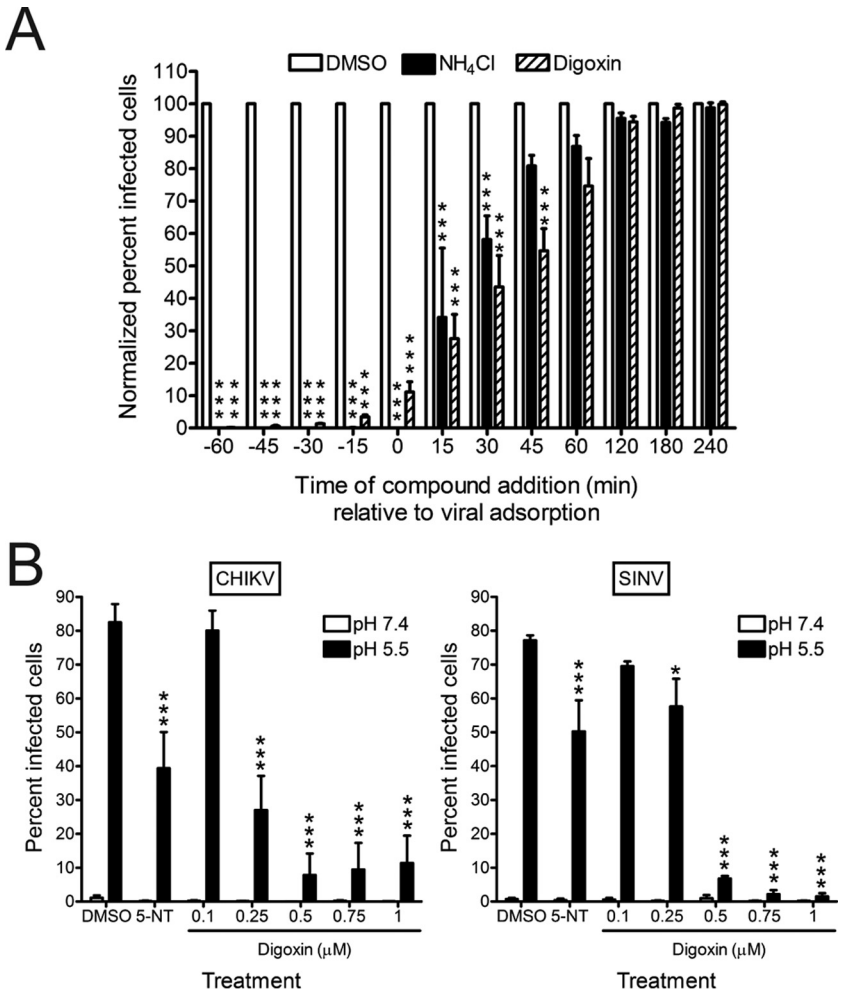

FIG 7 Digoxin inhibits CHIKV at postentry steps of the replication cycle. (A) U-2 OS cells were incubated with DMSO, 20 mM NH_4Cl, or 1 μM digoxin prior to (−60 to −15 min), during (0 to +45 min), or after (+60 to +240 min) adsorption with CHIKV 181/25 at an MOI of 5 PFU/cell for 1 h. Cells were incubated in the presence or absence of inhibitors for 5 h and scored for infection by indirect immunofluorescence. Results are presented as percentages of infected cells normalized to DMSO-treated cells for triplicate experiments. Error bars indicate standard errors of the means. (B) U-2 OS cells were incubated with DMSO, 10 μM 5-NT, or digoxin at the concentrations shown for 1 h prior to adsorption with CHIKV strain 181/25 (left) or SINV strain TRSB (right) at an MOI of 100 PFU/cell at 4°C for 1 h. Unbound virus was removed, and cells were treated at 37°C for 5 min with either acidic medium (pH 5.5 [black bars]) to trigger viral fusion at the plasma membrane or neutral medium (pH 7.4 [white bars]) as a control. Cells were incubated at 37°C for 18 h with medium containing DMSO or inhibitor and NH_4Cl to block subsequent rounds of infection. Cells were scored for infection by indirect immunofluorescence. Results are presented as percentages of infected cells for triplicate experiments. Error bars indicate standard errors of the means. *, $P < 0.05$, and ***, $P < 0.001$, in comparison to DMSO, as determined by ANOVA followed by Tukey's post hoc test.

possibility, we found that addition of extracellular potassium during digoxin treatment restored infectivity to levels observed for DMSO-treated cells (Fig. 4B). Second, digoxin may induce cellular stress responses to impede CHIKV replication. Cardiac glycoside treatment stimulates interactions between the sodium-potassium ATPase and the inositol 1,4,5-trisphosphate receptor (Ins[1,4,5]P_3R) to elicit calcium oscillations and activate calcium-dependent transcription factors, such as nuclear transcription factor κB (NF-κB) (50, 51). Activation of NF-κB enhances the expression of gene products involved in apoptosis and innate immune responses that promote an antiviral state that could ultimately restrict CHIKV infection (52). Although digoxin treatment induced modest activation of NF-κB (see Fig. S3 in the supplemental material), this increase was not statistically significant, suggesting that other calcium-dependent host molecules contribute to the restriction of CHIKV by digoxin. For example, it is possible that formation of CHIKV replication complexes and functions of specific viral proteins require precise spatial and temporal regulation of certain ion concentrations. Digoxin may directly perturb these viral activities to impede replication or trigger host stress responses that, in turn, accomplish the same effect. Digoxin-resistant viral variants may overcome this impairment by altering residues in the nonstructural proteins, including nsP4 V209I, to enhance ion-regulated functions of these proteins.

The complexity of cardiac glycoside-mediated effects on cells may contribute to multiple mechanisms of CHIKV inhibition, which would make it difficult to select digoxin-resistant mutants. Indeed, passage of CHIKV in digoxin-treated cells led to development of drug resistance only after approximately 14, 72-h passages. Digoxin is currently FDA approved for the treatment of

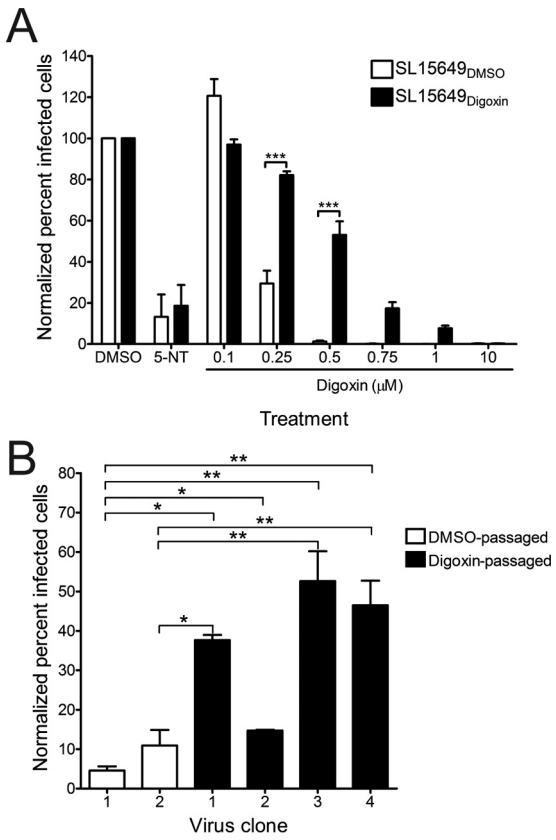

FIG 8 Passage of CHIKV in the presence of digoxin enriches for drug-resistant viruses. U-2 OS cells were incubated with DMSO, 10 μM 5-NT, or increasing concentrations of digoxin for 1 h prior to adsorption with CHIKV stocks that had been passaged 14 times in the presence of either DMSO ($SL15649_{DMSO}$) or digoxin ($SL15649_{Digoxin}$) at an MOI of 5 PFU/cell. After 1 h, virus was removed, and cells were incubated with medium containing DMSO or inhibitor for 5 h. Cells were stained with CHIKV-specific antiserum and DAPI to detect nuclei and imaged by fluorescence microscopy. Results are presented as percentages of infected cells normalized to DMSO-treated cells. Error bars indicate standard errors of the means. (B) U-2 OS cells were incubated with DMSO or 500 nM digoxin for 1 h prior to adsorption at an MOI of 5 PFU/cell with virus clones that were plaque purified from either the $SL15649_{DMSO}$ or $SL15649_{Digoxin}$ stock. After 1 h, virus was removed, and cells were incubated with medium containing DMSO or digoxin for 5 h. Cells were stained with CHIKV-specific antiserum and DAPI to detect nuclei and imaged by fluorescence microscopy. Results are presented as percentages of infected cells normalized to DMSO-treated cells for duplicate experiments. Error bars indicate standard errors of the means. *, $P < 0.05$, **, $P < 0.01$, and ***, $P < 0.001$, in comparison to DMSO-treated or DMSO-passaged virus-infected cells as determined by ANOVA followed by Tukey's post hoc test.

TABLE 1 Polymorphisms identified by serial passage of CHIKV in cells treated with either DMSO or digoxin

Virus clone[a]	Digoxin sensitivity	Viral gene product	Polymorphism(s)[b]
$SL15649_{DMSO}$			
Clone 1	Sensitive	E2	H170L
Clone 2	Sensitive	nsP1	P249L
		nsP3	S511R
		E2	S159R
$SL15649_{Digoxin}$			
Clone 1	Resistant	nsP2	T757A
		nsP3	D31N, P464L, Stop524_L525del
		E2	S159R
Clone 2	Sensitive	nsP3	D31N, Stop524C
		E2	S159R
Clone 3	Resistant	nsP3	D31N, Stop524C
		nsP4	V209I
		E2	S159R
Clone 4	Resistant	nsP3	D31N, Stop524C
		nsP4	V209I
		E2	S159R

[a] Virus titers in supernatants from infected DMSO- or digoxin-treated cells were determined by plaque assay, and viruses from individual plaques were amplified using U-2 OS cells.

[b] RNA isolated from supernatants of infected U-2 OS cells was used as a template for cDNA synthesis with random hexamers. Overlapping fragments covering the genome were amplified using CHIKV-specific primers and sequenced by Sanger sequencing.

congestive heart failure and cardiac arrhythmias, but clinically significant toxicity of digoxin precludes its widespread use (53–55). In patients treated with digoxin, acceptable serum concentrations range between 1 and 2.5 nM, concentrations appreciable lower than those required to inhibit CHIKV *in vitro*. Therefore, additional work is required to develop drugs that more selectively target steps within this pathway to limit toxicity. In this regard, less toxic derivatives of digoxin are effective in inhibition of T_H17 cell differentiation in the treatment of autoimmune diseases (56). The capacity of ouabain to inhibit CHIKV infection suggests that these analogous compounds also would diminish CHIKV infection in a similar manner.

Identification of CHIKV-specific therapeutics requires an improved understanding of CHIKV replication and pathogenesis. Findings presented in this report suggest that the sodium-potassium ATPase serves an essential function in CHIKV infection. Antagonism of this ion transporter with digoxin inhibits CHIKV infection of human cells. Digoxin inhibits one or more postentry steps of the CHIKV replication cycle as evidenced by time-of-addition and fusion-bypass experiments. Further studies to delineate mechanisms by which blockade of the sodium-potassium ATPase impedes CHIKV infection will illuminate host factors and pathways required for CHIKV replication. Such factors may serve as additional drug targets to ameliorate CHIKV disease.

MATERIALS AND METHODS

Cells, chemical inhibitors, antibodies, and plasmids. U-2 OS cells were maintained in McCoy's 5A medium (Gibco) supplemented to contain 10% fetal bovine serum (FBS [Gibco]). Primary HSFs were provided by James W. Thomas (Vanderbilt University) and cultivated as described previously (57). ST2 cells were provided by Julie A. Sterling (Vanderbilt University) and maintained in RPMI 1640 medium supplemented to contain 10% FBS. C2C12 cells were provided by David M. Bader (Vanderbilt University) and maintained in Dulbecco's modified Eagle's medium (DMEM) supplemented to contain 10% FBS. Baby hamster kidney (BHK-21), C6/36, and Vero cells were cultivated as described previously (58). HBMECs were provided by Kwang Sik Kim (Johns Hopkins University) and cultured in RPMI 1640 medium as described previously (59). L929 cells were maintained in Joklik's minimum essential medium supplemented to contain 5% FBS. All media for cell maintenance were supplemented to contain 2 mM L-glutamine (Gibco), 100 U/ml penicillin, 100 μg/ml streptomycin (Gibco), and 25 ng/ml amphotericin B (Sigma).

Bafilomycin A1 (Sigma), digoxin (Sigma), 5-NT oxalate (Tocris), ouabain octahydrate (Sigma), and STS (Cell Signaling Technology) were resuspended in DMSO. Polyclonal antisera obtained from ATCC were used for CHIKV (VR-1241AF), RRV (VR-1246AF), and SINV (VR-1248AF) infectivity assays. Reovirus-specific polyclonal antiserum (60) was used for reovirus infectivity assays.

Biosafety. Experiments involving the generation and testing of CHIKV SL15649 replicon particles and replication-competent CHIKV were conducted in a certified biological safety level 3 (BSL3) facility in biological safety cabinets with protocols approved by the Vanderbilt University Department of Environment, Health, and Safety and the Vanderbilt Institutional Safety Committee.

Generation of CHIKV replicon particles. The three-plasmid CHIKV SL15649 replicon system was used as described previously (61). Plasmids encoding CHIKV nonstructural proteins and eGFP, capsid protein, and the envelope glycoproteins (E3 to E1) were linearized and transcribed *in vitro* using mMessage mMachine SP6 transcription kits (Ambion). BHK-21 cells were electroporated with viral RNAs generated from the three plasmids and incubated at 37°C for 24 h. Supernatants containing replicon particles were collected from electroporated cells, clarified by centrifugation, and stored at −80°C. Replicon particles were tested for propagation-competent recombinant virus by serial passage of replicon stocks on monolayers of Vero cells. Stocks were removed from the BSL3 laboratory only if CPE was not detected 72 h after the second passage.

High-throughput screening of NCC. U-2 OS cells seeded in 384-well plates (Corning) were treated with DMSO, 100 nM bafilomycin A1, or compounds from the NCC at a concentration of 1 μM using a Bravo automated liquid handling platform (Velocity 11/Agilent) and incubated at 37°C for 1 h. CHIKV SL15649 eGFP-expressing replicon particles were inoculated into wells of treated cells at an MOI of 5 infectious units (IU)/cell and incubated at 37°C for 20 to 24 h. Medium was aspirated using an ELx405 microplate washer (Biotek), and cells were incubated with Hoechst dye to stain nuclei using a Multidrop Combi reagent dispenser (Thermo Scientific). Cells and nuclei were visualized using an ImageXpress Micro XL imaging system. Total cells and infected cells were quantified using MetaXpress software in two fields of view per well. The plate median and median absolute deviation (MAD) were calculated for each well and used to calculate robust Z scores with the following equation: Z score = $[\log_2(\%\ \text{infection}) - \log_2(\text{median})]/[\log_2(\text{MAD}) \times 1.486]$. Candidates were considered positive if the robust Z score was ≤ -2 or ≥ 2 in at least two of three independent replicates.

Generation of virus stocks. The CHIKV 181/25 and SL15649 infectious clone plasmids were generated as described previously (62). Plasmids containing the full-length cDNA sequences of RRV strain T48 (pRR64) and SINV strain AR339 (pTRSB) were generated as described previously (63, 64). CHIKV, RRV, and SINV infectious clone plasmids were linearized and transcribed *in vitro* using mMessage mMachine SP6 transcription kits. BHK-21 cells were electroporated with viral RNA and incubated at 37°C for 24 h. Supernatants containing progeny virus were collected from electroporated cells, clarified by centrifugation, and stored at −80°C. Viral titers were determined by plaque assay using Vero or BHK-21 cells. All experiments with CHIKV SL15649 virus were performed using BSL3 conditions.

Reovirus strain T1L M1 P208S (65) was generated using plasmid-based reverse genetics (66). Purified virions were prepared as described previously (67). The reovirus particle concentration was determined from the equivalence of 1 U of optical density at 260 nm to 2.1×10^{12} particles (68). Viral titers were determined by plaque assay using L929 cells (66). ISVPs were generated by treating virion particles with α-chymotrypsin (Sigma) as described previously (37).

VSV-eGFP was provided by Sean Whelan (Harvard University) and propagated on BHK-21 cells as described previously (69). Viral titers were determined by plaque assay using Vero cells.

CHIKV, RRV, and SINV infectivity assays. Vehicle- or compound-treated U-2 OS, HSF, ST2, C2C12, and C6/36 cells seeded in 96-well plates (Costar) were adsorbed with CHIKV, RRV, or SINV diluted in virus diluent buffer (VDB) (RPMI 1640 medium with 25 mM HEPES and 1% FBS) at various MOIs at 37°C (U-2 OS, HSF, ST2, and C2C12) or 28°C (C6/36) for 1 h. The inoculum was removed, complete medium containing DMSO or compound was added, and cells were incubated at 37°C or 28°C for an additional 5 h. Cells were fixed with ice-cold methanol, washed with PBS, and incubated with PBS containing 5% FBS and 0.1% Triton X-100 (TX) at room temperature for 1 h. Cells were incubated with CHIKV-, RRV-, or SINV-specific polyclonal antiserum (1:1,500) in PBS with FBS and TX at 4°C overnight. Cells were washed three times with PBS and incubated with Alexa Fluor 488-labeled anti-mouse IgG (1:1,000) in PBS with FBS and TX at room temperature for 2 h. Cells also were incubated with 4′,6-diamidino-2-phenylindole (DAPI; Invitrogen) to stain nuclei. Cells and nuclei were visualized using an ImageXpress Micro XL imaging system in four fields of view per well. Percentage of infectivity was determined by dividing the number of virus-infected cells by the total number of cells per field of view. CHIKV infectivity following digoxin treatment was determined in the presence of increasing concentrations of sodium and potassium by pretreating U-2 OS cells with vehicle or digoxin diluted in complete medium or in medium supplemented with NaCl or KCl at 37°C for 1 h. Pretreated cells were adsorbed with CHIKV strain 181/25 at an MOI of 5 PFU/cell at 37°C for 1 h. The inoculum was removed, complete medium or ion-supplemented medium containing DMSO or digoxin was added, and cells were incubated at 37°C for an additional 5 h. Cells were fixed, stained by indirect immunofluorescence to detect CHIKV antigen and nuclei, and visualized as described above.

Expression of gene transcripts by RT-PCR. RNA was isolated from U-2 OS and ST2 cells using a PureLink RNA minikit (Ambion). cDNA was prepared with the SuperScriptIII first strand kit (Invitrogen) with random hexamers to prime cDNA synthesis and used for PCR amplification by KOD polymerase with primers specific for the human or murine α1 and α3 isoforms of the sodium-potassium ATPase and GAPDH as a control (for primer sequences, see Table S1 in the supplemental material). Reaction products were resolved by electrophoresis in 1% agarose gels (Life Technologies).

Assessment of cell viability. U-2 OS cells seeded in 60-mm-diameter dishes were incubated with DMSO, 10 μM STS as an inducer of apoptosis, or increasing concentrations of digoxin at 37°C for 6 h. Cells were washed with fluorescence-activated cell sorter (FACS) buffer (PBS with 2% FBS) and stained with PI (Sigma). Cell staining was quantified using a BD LSRII flow cytometer and FlowJo software (Tree Star). Alternatively, U-2 OS cells seeded in 96-well plates were incubated with DMSO, STS, or increasing concentrations of digoxin at 37°C for 6 or 24 h. PrestoBlue reagent (Molecular Probes) was added to supernatants of compound-treated cells, and cells were incubated at 37°C for 30 min. Fluorescence as a surrogate for cell viability was quantified using a Synergy H1 plate reader (BioTek).

Reovirus infectivity assay. Vehicle- or compound-treated HBMECs seeded in 96-well plates (Costar) were adsorbed with reovirus virions or ISVPs at an MOI of 1,500 particles/cell at room temperature for 1 h. The inoculum was removed, and cells were washed with PBS and incubated with medium containing DMSO or compound at 37°C for 20 h. Cells were fixed with ice-cold methanol, washed with PBS, and incubated with PBS containing 5% bovine serum albumin at room temperature for 15 min. Cells were incubated with reovirus-specific polyclonal antiserum (1:1,000) in PBS with 0.5% TX at 37°C for 30 min. Cells were washed three times with PBS and incubated with Alexa Fluor 488-labeled anti-rabbit IgG (1:1,000) in PBS with 0.5% TX at 37°C for 30 min. Cells also were incubated with DAPI to stain nuclei. Cells and nuclei were visualized using an ImageXpress Micro XL imaging system in four fields of view per well. The percentage of infectivity was determined by dividing the number of virus-infected cells by the total number of cells per field of view.

VSV infectivity assay. Vehicle- or compound-treated U-2 OS cells seeded in 96-well plates (Costar) were adsorbed with VSV-eGFP at an MOI of 10 PFU/cell at 37°C for 1 h. The inoculum was removed, complete medium containing DMSO or compound was added, and cells were incubated at 37°C for an additional 5 h. Medium was removed, and cells were incubated with Hoechst dye to stain nuclei. Cells and nuclei were visualized using an ImageXpress Micro XL imaging system in four fields of view per well. The percentage of infectivity was determined by dividing

the number of GFP-positive cells by the total number of cells per field of view.

Fusion-bypass assay. U-2 OS cells seeded in 96-well plates (Costar) were incubated with DMSO, 5-NT, or increasing concentrations of digoxin at 37°C for 1 h. Compounds were removed, and cells were washed twice with ice-cold binding medium (RPMI 1640 medium with 25 mM HEPES [pH 7.4], 1% FBS, and 20 mM NH_4Cl) to prevent internalization by endosomal fusion. Cells were adsorbed with CHIKV or SINV diluted in binding medium at 4°C for 1 h, washed twice with binding medium to remove unbound virus, and incubated at 37°C for 5 min with either prewarmed fusion medium (RPMI 1640 medium with 25 mM HEPES, 1% FBS, and 30 mM succinic acid, pH 5.5) to trigger fusion at the plasma membrane or prewarmed binding medium as a control. Medium was removed, cells were incubated with complete medium containing vehicle or inhibitor and 20 mM NH_4Cl at 37°C, and infection was scored by indirect immunofluorescence at 18 h postadsorption.

Selection of digoxin-resistant mutants. U-2 OS cells were adsorbed with CHIKV SL15649 at an MOI of 0.01 PFU/cell in VDB at 37°C for 1 h. Virus was removed, and complete medium containing either DMSO or 100 nM digoxin was added to cells. Cells were incubated at 37°C for 48 to 72 h or until the CPEs were comparable in DMSO- and digoxin-treated cells. Cell culture supernatants were collected, and 0.5 ml was used to inoculate a fresh flask of U-2 OS cells. The remaining supernatant was stored at −80°C. Virus was passaged serially in this manner, gradually increasing the concentration of digoxin until it reached a dose that was 5 times the EC_{50} for the drug in U-2 OS cells.

Sequence analysis of digoxin-resistant and -sensitive mutants. Viruses from cell-culture supernatants of DMSO- or digoxin-treated cells were plaque purified using BHK-21 cells, and RNA was isolated using a PureLink RNA minikit. cDNA was prepared with the SuperscriptIII first strand kit with random hexamers to prime cDNA synthesis and subjected to PCR amplification using KOD polymerase with CHIKV-specific primer sets to enable amplification of fragments that collectively encompass the entire viral genome. Amplicons were sequenced using Sanger sequencing (GenHunter, Nashville, TN).

Statistical analysis. Mean values for at least duplicate experiments were compared using a one-way analysis of variance (ANOVA) followed by Tukey's post hoc test (GraphPad Prism). *P* values of <0.05 were considered to be statistically significant.

SUPPLEMENTAL MATERIAL

Supplemental material for this article may be found at http://mbio.asm.org/lookup/suppl/doi:10.1128/mBio.00693-16/-/DCSupplemental.

Text S1, DOCX file, 0.02 MB.
Figure S1, TIF file, 0.2 MB.
Figure S2, TIF file, 0.3 MB.
Figure S3, TIF file, 0.3 MB.
Table S1, DOCX file, 0.02 MB.

ACKNOWLEDGMENTS

We thank Bernardo Mainou, Kristen Ogden, and Clint Smith for critical review of the manuscript. We are grateful to members of the Dermody laboratory for useful discussions during these studies. The NIH Clinical Collection is provided through the National Institutes of Health Molecular Libraries Roadmap Initiative and was distributed by the Vanderbilt High-Throughput Screening Facility. High-content image acquisition was performed in the Vanderbilt High-Throughput Screening Facility in collaboration with the Vanderbilt Institute of Chemical Biology. Flow cytometry experiments were performed in the Vanderbilt Cytometry Shared Resource.

This work was supported by Public Health Service awards T32 HL07751 (A.W.A.), R01 AI108735 (T.E.M.), R01 AI123348 (T.S.D.), and U54 AI057157 (T.S.D.) and the Elizabeth B. Lamb Center for Pediatric Research. This work also was supported by Public Health Service awards P30 CA68485 for the Vanderbilt-Ingram Cancer Center and P60 DK20593 for the Vanderbilt Diabetes Research and Training Center.

FUNDING INFORMATION

This work, including the efforts of Thomas E. Morrison, was funded by HHS | NIH | National Institute of Allergy and Infectious Diseases (NIAID) (R01 AI108735). This work, including the efforts of Terence S. Dermody, was funded by HHS | NIH | National Institute of Allergy and Infectious Diseases (NIAID) (R01 AI123348 and U54 AI057157). This work, including the efforts of Alison Whitney Ashbrook, was funded by HHS | NIH | National Heart, Lung, and Blood Institute (NHLBI) (T32 HL07751).

REFERENCES

1. **Simon F, Parola P, Grandadam M, Fourcade S, Oliver M, Brouqui P, Hance P, Kraemer P, Ali Mohamed A, de Lamballerie X, Charrel R, Tolou H.** 2007. Chikungunya infection: an emerging rheumatism among travelers returned from Indian Ocean islands. Report of 47 cases. Medicine (Baltimore) **86:**123–137. http://dx.doi.org/10.1097/MD/0b013e31806010a5.
2. **Rezza G, Nicoletti L, Angelini R, Romi R, Finarelli AC, Panning M, Cordioli P, Fortuna C, Boros S, Magurano F, Silvi G, Angelini P, Dottori M, Ciufolini MG, Majori GC, Cassone A, CHIKV Study Group.** 2007. Infection with chikungunya virus in Italy: an outbreak in a temperate region. Lancet **370:**1840–1846. http://dx.doi.org/10.1016/S0140-6736(07)61779-6.
3. **Kee ACL, Yang S, Tambyah P.** 2010. Atypical chikungunya virus infections in immunocompromised patients. Emerg Infect Dis **16:**1038–1040. http://dx.doi.org/10.3201/eid1606.091115.
4. **Grandadam M, Caro V, Plumet S, Thiberge JM, Souarès Y, Failloux AB, Tolou HJ, Budelot M, Cosserat D, Leparc-Goffart I, Desprès P.** 2011. Chikungunya virus, southeastern France. Emerg Infect Dis **17:**910–913. http://dx.doi.org/10.3201/eid1705.101873.
5. **Leparc-Goffart I, Nougairede A, Cassadou S, Prat C, de Lamballerie X.** 2014. Chikungunya in the Americas. Lancet **383:**514. http://dx.doi.org/10.1016/S0140-6736(14)60185-9.
6. **Van Bortel W, Dorleans F, Rosine J, Blateau A, Rousseau D, Matheus S, Leparc-Goffart I, Flusin O, Prat C, Césaire R, Najioullah F, Ardillon V, Balleydier E, Carvalho L, Lemaître A, Noël H, Servas V, Six C, Zurbaran M, Léon L, Guinard A, van den Kerkhof J, Henry M, Fanoy E, Braks M, Reimerink J, Swaan C, Georges R, Brooks L, Freedman J, Sudre B, Zeller H.** 2014. Chikungunya outbreak in the Caribbean region, December 2013 to March 2014, and the significance for Europe. Euro Surveill **19:**20759. http://dx.doi.org/10.2807/1560-7917.ES2014.19.13.20759.
7. **Burt FJ, Rolph MS, Rulli NE, Mahalingam S, Heise MT.** 2012. Chikungunya: a re-emerging virus. Lancet **379:**662–671. http://dx.doi.org/10.1016/S0140-6736(11)60281-X.
8. **Suhrbier A, Jaffar-Bandjee MC, Gasque P.** 2012. Arthritogenic alphaviruses—an overview. Nat Rev Rheumatol **8:**420–429. http://dx.doi.org/10.1038/nrrheum.2012.64.
9. **Economopoulou A, Dominguez M, Helynck B, Sissoko D, Wichmann O, Quenel P, Germonneau P, Quatresous I.** 2009. Atypical chikungunya virus infections: clinical manifestations, mortality and risk factors for severe disease during the 2005–2006 outbreak on Reunion. Epidemiol Infect **137:**534–541. http://dx.doi.org/10.1017/S0950268808001167.
10. **Borgherini G, Poubeau P, Staikowsky F, Lory M, Le Moullec N, Becquart JP, Wengling C, Michault A, Paganin F.** 2007. Outbreak of chikungunya on Reunion Island: early clinical and laboratory features in 157 adult patients. Clin Infect Dis **44:**1401–1407. http://dx.doi.org/10.1086/517537.
11. **Tandale BV, Sathe PS, Arankalle VA, Wadia RS, Kulkarni R, Shah SV, Shah SK, Sheth JK, Sudeep AB, Tripathy AS, Mishra AC.** 2009. Systemic involvements and fatalities during chikungunya epidemic in India, 2006. J Clin Virol **46:**145–149. http://dx.doi.org/10.1016/j.jcv.2009.06.027.
12. **Borgherini G, Poubeau P, Jossaume A, Gouix A, Cotte L, Michault A, Arvin-Berod C, Paganin F.** 2008. Persistent arthralgia associated with chikungunya virus: a study of 88 adult patients on Reunion Island. Clin Infect Dis **47:**469–475. http://dx.doi.org/10.1086/590003.
13. **Krishnamoorthy K, Harichandrakumar KT, Krishna Kumari A, Das LK.** 2009. Burden of chikungunya in India: estimates of disability adjusted life years (DALY) lost in 2006 epidemic. J Vector Borne Dis **46:**26–35.
14. **Soumahoro MK, Gérardin P, Boëlle PY, Perrau J, Fianu A, Pouchot J, Malvy D, Flahault A, Favier F, Hanslik T.** 2009. Impact of chikungunya virus infection on health status and quality of life: a retrospective

cohort study. PLoS One 4:. http://dx.doi.org/10.1371/journal.pone.0007800.
15. **Soumahoro MK, Boelle PY, Gauzere BA, Atsou K, Pelat C, Lambert B, La Ruche G, Gastellu-Etchegorry M, Renault P, Sarazin M, Yazdanpanah Y, Flahault A, Malvy D, Hanslik T.** 2011. The chikungunya epidemic on la Reunion Island in 2005–2006: a cost-of-illness study. PLoS Negl Trop Dis **5:**e1197. http://dx.doi.org/10.1371/journal.pntd.0001197.
16. **Simizu B, Yamamoto K, Hashimoto K, Ogata T.** 1984. Structural proteins of chikungunya virus. J Virol **51:**254–258.
17. **Sourisseau M, Schilte C, Casartelli N, Trouillet C, Guivel-Benhassine F, Rudnicka D, Sol-Foulon N, Le Roux K, Prevost MC, Fsihi H, Frenkiel MP, Blanchet F, Afonso PV, Ceccaldi PE, Ozden S, Gessain A, Schuffenecker I, Verhasselt B, Zamborlini A, Saïb A, Rey FA, Arenzana-Seisdedos F, Despres P, Michault A, Albert ML, Schwartz O.** 2007. Characterization of reemerging chikungunya virus. PLoS Pathog **3:**e89. http://dx.doi.org/10.1371/journal.ppat.0030089.
18. **Bernard E, Solignat M, Gay B, Chazal N, Higgs S, Devaux C, Briant L.** 2010. Endocytosis of chikungunya virus into mammalian cells: role of clathrin and early endosomal compartments. PLoS One **5:**e11479. http://dx.doi.org/10.1371/journal.pone.0011479.
19. **Li L, Jose J, Xiang Y, Kuhn RJ, Rossmann MG.** 2010. Structural changes of envelope proteins during alphavirus fusion. Nature **468:**705–708. http://dx.doi.org/10.1038/nature09546.
20. **Kielian M, Chanel-Vos C, Liao M.** 2010. Alphavirus entry and membrane fusion. Viruses **2:**796–825. http://dx.doi.org/10.3390/v2040796.
21. **Khan AH, Morita K, Parquet MdC, Hasebe F, Mathenge EG, Igarashi A.** 2002. Complete nucleotide sequence of chikungunya virus and evidence for an internal polyadenylation site J Gen Virol **83:**3075–3084. http://dx.doi.org/10.1099/0022-1317-83-12-3075.
22. **Solignat M, Gay B, Higgs S, Briant L, Devaux C.** 2009. Replication cycle of chikungunya: a re-emerging arbovirus. Virology **393:**183–197. http://dx.doi.org/10.1016/j.virol.2009.07.024.
23. **Friedman RM, Levin JG, Grimley PM, Berezesky IK.** 1972. Membrane-associated replication complex in arbovirus infection. J Virol **10:**504–515.
24. **Froshauer S, Kartenbeck J, Helenius A.** 1988. Alphavirus RNA replicase is located on the cytoplasmic surface of endosomes and lysosomes. J Cell Biol **107:**2075–2086. http://dx.doi.org/10.1083/jcb.107.6.2075.
25. **Chen KC, Kam YW, Lin RT, Ng MM, Ng LF, Chu JJ.** 2013. Comparative analysis of the genome sequences and replication profiles of Chikungunya virus isolates within the East, Central and South African (ECSA) lineage. Virol J **10:**169. http://dx.doi.org/10.1186/1743-422X-10-169.
26. **Kujala P, Ikäheimonen A, Ehsani N, Vihinen H, Auvinen P, Kääriäinen L.** 2001. Biogenesis of the Semliki forest virus RNA replication complex. J Virol **75:**3873–3884. http://dx.doi.org/10.1128/JVI.75.8.3873-3884.2001.
27. **Frolova EI, Gorchakov R, Pereboeva L, Atasheva S, Frolov I.** 2010. Functional Sindbis virus replicative complexes are formed at the plasma membrane. J Virol **84:**11679–11695. http://dx.doi.org/10.1128/JVI.01441-10.
28. **Spuul P, Balistreri G, Kääriäinen L, Ahola T.** 2010. Phosphatidylinositol 3-kinase-, actin-, and microtubule-dependent transport of Semliki Forest virus replication complexes from the plasma membrane to modified lysosomes. J Virol **84:**7543–7557. http://dx.doi.org/10.1128/JVI.00477-10.
29. **Kaur P, Thiruchelvan M, Lee RC, Chen H, Chen KC, Ng ML, Chu JJ.** 2013. Inhibition of Chikungunya virus replication by harringtonine, a novel antiviral that suppresses viral protein expression. Antimicrob Agents Chemother **57:**155–167. http://dx.doi.org/10.1128/AAC.01467-12.
30. **Mainou BA, Ashbrook AW, Smith EC, Dorset DC, Denison MR, Dermody TS.** 2015. Serotonin receptor agonist 5-nonyloxytryptamine alters the kinetics of reovirus cell entry. J Virol **89:**8701–8712. http://dx.doi.org/10.1128/JVI.00739-15.
31. **Gupta RS, Chopra A, Stetsko DK.** 1986. Cellular basis for the species differences in sensitivity to cardiac glycosides (digitalis). J Cell Physiol **127:**197–206. http://dx.doi.org/10.1002/jcp.1041270202.
32. **Kent RB, Emanuel JR, Ben Neriah Y, Levenson R, Housman DE.** 1987. Ouabain resistance conferred by expression of the cDNA for a murine Na^+, K^+-ATPase alpha subunit. Science **237:**901–903. http://dx.doi.org/10.1126/science.3039660.
33. **Lin Y, Dubinsky WP, Ho DH, Felix E, Newman RA.** 2008. Determinants of human and mouse melanoma cell sensitivities to oleandrin. J Exp Ther Oncol **7:**195–205.
34. **Ebert DH, Deussing J, Peters C, Dermody TS.** 2002. Cathepsin L and cathepsin B mediate reovirus disassembly in murine fibroblast cells. J Biol Chem **277:**24609–24617. http://dx.doi.org/10.1074/jbc.M201107200.
35. **Borsa J, Morash BD, Sargent MD, Copps TP, Lievaart PA, Szekely JG.** 1979. Two modes of entry of reovirus particles into L cells. J Gen Virol **45:**161–170. http://dx.doi.org/10.1099/0022-1317-45-1-161.
36. **Sturzenbecker LJ, Nibert M, Furlong D, Fields BN.** 1987. Intracellular digestion of reovirus particles requires a low pH and is an essential step in the viral infectious cycle. J Virol **61:**2351–2361.
37. **Mainou BA, Dermody TS.** 2011. Src kinase mediates productive endocytic sorting of reovirus during cell entry. J Virol **85:**3203–3213. http://dx.doi.org/10.1128/JVI.02056-10.
38. **Kim KH, Rümenapf T, Strauss EG, Strauss JH.** 2004. Regulation of Semliki Forest virus RNA replication: a model for the control of alphavirus pathogenesis in invertebrate hosts. Virology **323:**153–163. http://dx.doi.org/10.1016/j.virol.2004.03.009.
39. **Gardner CL, Hritz J, Sun C, Vanlandingham DL, Song TY, Ghedin E, Higgs S, Klimstra WB, Ryman KD.** 2014. Deliberate attenuation of chikungunya virus by adaptation to heparan sulfate-dependent infectivity: a model for rational arboviral vaccine design. PLoS Negl Trop Dis **8:**e2719. http://dx.doi.org/10.1371/journal.pntd.0002719.
40. **Pickett BE, Sadat EL, Zhang Y, Noronha JM, Squires RB, Hunt V, Liu M, Kumar S, Zaremba S, Gu Z, Zhou L, Larson CN, Dietrich J, Klem EB, Scheuermann RH.** 2012. ViPR: an open bioinformatics database and analysis resource for virology research. Nucleic Acids Res **40:**D593–D598. http://dx.doi.org/10.1093/nar/gkr859.
41. **Barton ES, Forrest JC, Connolly JL, Chappell JD, Liu Y, Schnell FJ, Nusrat A, Parkos CA, Dermody TS.** 2001. Junction adhesion molecule is a receptor for reovirus. Cell **104:**441–451. http://dx.doi.org/10.1016/S0092-8674(01)00231-8.
42. **Neuvonen M, Kazlauskas A, Martikainen M, Hinkkanen A, Ahola T, Saksela K.** 2011. SH3 domain-mediated recruitment of host cell amphiphysins by alphavirus nsP3 promotes viral RNA replication. PLoS Pathog **7:**e1002383. http://dx.doi.org/10.1371/journal.ppat.1002383.
43. **Thaa B, Biasiotto R, Eng K, Neuvonen M, Götte B, Rheinemann L, Mutso M, Utt A, Varghese F, Balistreri G, Merits A, Ahola T, McInerney GM.** 2015. Differential PI3K-Akt-mTOR activation by Semliki Forest and chikungunya virus, dependent on nsP3 and connected to replication complex internalization. J Virol **89:**11420–11437. http://dx.doi.org/10.1128/JVI.01579-15.
44. **Rathore AP, Haystead T, Das PK, Merits A, Ng ML, Vasudevan SG.** 2014. Chikungunya virus nsP3 and nsP4 interacts with HSP-90 to promote virus replication: HSP-90 inhibitors reduce CHIKV infection and inflammation *in vivo*. Antiviral Res **103:**7–16. http://dx.doi.org/10.1016/j.antiviral.2013.12.010.
45. **Panas MD, Ahola T, McInerney GM.** 2014. The C-terminal repeat domains of nsP3 from the Old World alphaviruses bind directly to G3BP. J Virol **88:**5888–5893. http://dx.doi.org/10.1128/JVI.00439-14.
46. **Scholte FE, Tas A, Albulescu IC, Žusinaite E, Merits A, Snijder EJ, van Hemert MJ.** 2015. Stress granule components G3BP1 and G3BP2 play a proviral role early in chikungunya virus replication. J Virol **89:**4457–4469. http://dx.doi.org/10.1128/JVI.03612-14.
47. **Schoner W, Scheiner-Bobis G.** 2007. Endogenous and exogenous cardiac glycosides and their mechanisms of action. Am J Cardiovasc Drugs **7:**173–189. http://dx.doi.org/10.2165/00129784-200707030-00004.
48. **Melton JV, Ewart GD, Weir RC, Board PG, Lee E, Gage PW.** 2002. Alphavirus 6K proteins form ion channels. J Biol Chem **277:**46923–46931. http://dx.doi.org/10.1074/jbc.M207847200.
49. **Waite MR, Brown DT, Pfefferkorn ER.** 1972. Inhibition of Sindbis virus release by media of low ionic strength: an electron microscope study. J Virol **10:**537–544.
50. **Aizman O, Uhlén P, Lal M, Brismar H, Aperia A.** 2001. Ouabain, a steroid hormone that signals with slow calcium oscillations. Proc Natl Acad Sci U S A **98:**13420–13424. http://dx.doi.org/10.1073/pnas.221315298.
51. **Li J, Zelenin S, Aperia A, Aizman O.** 2006. Low doses of ouabain protect from serum deprivation-triggered apoptosis and stimulate kidney cell proliferation via activation of NF-kappaB. J Am Soc Nephrol **17:**1848–1857. http://dx.doi.org/10.1681/ASN.2005080894.
52. **Silverman N, Maniatis T.** 2001. NF-κB signaling pathways in mammalian and insect innate immunity. Genes Dev **15:**2321–2342. http://dx.doi.org/10.1101/gad.909001.
53. **Johansson S, Lindholm P, Gullbo J, Larsson R, Bohlin L, Claeson P.** 2001. Cytotoxicity of digitoxin and related cardiac glycosides in human

tumor cells. Anticancer Drugs **12:**475–483. http://dx.doi.org/10.1097/00001813-200106000-00009.

54. **Paula S, Tabet MR, Ball WJ, Jr.** 2005. Interactions between cardiac glycosides and sodium-potassium-ATPase: three-dimensional structure-activity relationship models for ligand binding to the E2-pi form of the enzyme versus activity inhibition. Biochemistry **44:**498–510. http://dx.doi.org/10.1021/bi048680w.
55. **Nesher M, Shpolansky U, Rosen H, Lichtstein D.** 2007. The digitalis-like steroid hormones: new mechanisms of action and biological significance. Life Sci **80:**2093–2107. http://dx.doi.org/10.1016/j.lfs.2007.03.013.
56. **Huh JR, Leung MW, Huang P, Ryan DA, Krout MR, Malapaka RR, Chow J, Manel N, Ciofani M, Kim SV, Cuesta A, Santori FR, Lafaille JJ, Xu HE, Gin DY, Rastinejad F, Littman DR.** 2011. Digoxin and its derivatives suppress TH17 cell differentiation by antagonizing RORgammat activity. Nature **472:**486–490. http://dx.doi.org/10.1038/nature09978.
57. **Thomas JW, Thieu TH, Byrd VM, Miller GG.** 2000. Acidic fibroblast growth factor in synovial cells. Arthritis Rheum **43:**2152–2159. http://dx.doi.org/10.1002/1529-0131(200010)43:10<2152::AID-ANR2>3.0.CO;2-R.
58. **Ashbrook AW, Burrack KS, Silva LA, Montgomery SA, Heise MT, Morrison TE, Dermody TS.** 2014. Residue 82 of the chikungunya virus E2 attachment protein modulates viral dissemination and arthritis in mice. J Virol **88:**12180–12192. http://dx.doi.org/10.1128/JVI.01672-14.
59. **Stins MF, Gilles F, Kim KS.** 1997. Selective expression of adhesion molecules on human brain microvascular endothelial cells. J Neuroimmunol **76:**81–90. http://dx.doi.org/10.1016/S0165-5728(97)00036-2.
60. **Barton ES, Connolly JL, Forrest JC, Chappell JD, Dermody TS.** 2001. Utilization of sialic acid as a coreceptor enhances reovirus attachment by multistep adhesion strengthening. J Biol Chem **276:**2200–2211. http://dx.doi.org/10.1074/jbc.M004680200.
61. **Smith SA, Silva LA, Fox JM, Flyak AI, Kose N, Sapparapu G, Khomandiak S, Ashbrook AW, Kahle KM, Fong RH, Swayne S, Doranz BJ, McGee CE, Heise MT, Pal P, Brien JD, Austin SK, Diamond MS, Dermody TS, Crowe JE, Jr.** 2015. Isolation and characterization of broad and ultrapotent human monoclonal antibodies with therapeutic activity against chikungunya virus. Cell Host Microbe **18:**86–95. http://dx.doi.org/10.1016/j.chom.2015.06.009.
62. **Mainou BA, Zamora PF, Ashbrook AW, Dorset DC, Kim KS, Dermody TS.** 2013. Reovirus cell entry requires functional microtubules. mBio **4:**e00405-13. http://dx.doi.org/10.1128/mBio.00405-13.
63. **Polo JM, Davis NL, Rice CM, Huang HV, Johnston RE.** 1988. Molecular analysis of Sindbis virus pathogenesis in neonatal mice by using virus recombinants constructed in vitro. J Virol **62:**2124–2133.
64. **Kuhn RJ, Niesters HG, Hong Z, Strauss JH.** 1991. Infectious RNA transcripts from Ross River virus cDNA clones and the construction and characterization of defined chimeras with Sindbis virus. Virology **182:**430–441. http://dx.doi.org/10.1016/0042-6822(91)90584-X.
65. **Kobayashi T, Ooms LS, Chappell JD, Dermody TS.** 2009. Identification of functional domains in reovirus replication proteins μNS and μ2. J Virol **83:**2892–2906. http://dx.doi.org/10.1128/JVI.01495-08.
66. **Virgin HW, IV, Bassel-Duby R, Fields BN, Tyler KL.** 1988. Antibody protects against lethal infection with the neurally spreading reovirus type 3 (Dearing). J Virol **62:**4594–4604.
67. **Furlong DB, Nibert ML, Fields BN.** 1988. Sigma 1 protein of mammalian reoviruses extends from the surfaces of viral particles. J Virol **62:**246–256.
68. **Smith RE, Zweerink HJ, Joklik WK.** 1969. Polypeptide components of virions, top component and cores of reovirus type 3. Virol **39:**791–810. http://dx.doi.org/10.1016/0042-6822(69)90017-8.
69. **Whelan SP, Barr JN, Wertz GW.** 2000. Identification of a minimal size requirement for termination of vesicular stomatitis virus mRNA: implications for the mechanism of transcription. J Virol **74:**8268–8276. http://dx.doi.org/10.1128/JVI.74.18.8268-8276.2000.

nature microbiology

ARTICLES

https://doi.org/10.1038/s41564-018-0122-x

The TRiC chaperonin controls reovirus replication through outer-capsid folding

Jonathan J. Knowlton[1,2], Isabel Fernández de Castro[3], Alison W. Ashbrook[1], Daniel R. Gestaut[4], Paula F. Zamora[1,2], Joshua A. Bauer[5], J. Craig Forrest[6], Judith Frydman[4], Cristina Risco[3] and Terence S. Dermody[2,7]*

Viruses are molecular machines sustained through a life cycle that requires replication within host cells. Throughout the infectious cycle, viral and cellular components interact to advance the multistep process required to produce progeny virions. Despite progress made in understanding the virus–host protein interactome, much remains to be discovered about the cellular factors that function during infection, especially those operating at terminal steps in replication. In an RNA interference screen, we identified the eukaryotic chaperonin T-complex protein-1 (TCP-1) ring complex (TRiC; also called CCT for chaperonin containing TCP-1) as a cellular factor required for late events in the replication of mammalian reovirus. We discovered that TRiC functions in reovirus replication through a mechanism that involves folding the viral σ3 major outer-capsid protein into a form capable of assembling onto virus particles. TRiC also complexes with homologous capsid proteins of closely related viruses. Our data define a critical function for TRiC in the viral assembly process and raise the possibility that this mechanism is conserved in related non-enveloped viruses. These results also provide insight into TRiC protein substrates and establish a rationale for the development of small-molecule inhibitors of TRiC as potential antiviral therapeutics.

Viruses require cellular machinery to complete each step in a replication cycle. This machinery includes cell surface receptors that mediate attachment, endosomal and cytoskeletal proteins involved in viral entry and uncoating, and the translational apparatus required for viral protein synthesis. Although progress has been made in understanding host proteins required for early events in viral infection, much less is known about the cellular machinery used by viruses to accomplish later replication steps.

Mammalian orthoreoviruses (reoviruses) infect most mammals and have been implicated in coeliac disease pathogenesis in humans[1]. Reoviruses are non-enveloped and encapsidate a segmented, double-stranded RNA genome within a particle formed by an inner core and an outer capsid[2]. Reovirus enters the cell following attachment to membrane-bound receptors[3,4] and clathrin-dependent endocytosis[5], whereafter the particle is uncoated by cysteine proteases[6], leading to delivery of the transcriptionally active core into the cytoplasm. In contrast to the well-characterized early infection steps, mechanisms governing genome assortment, assembly, transport and egress remain unclear. We conducted a two-step RNA interference (RNAi)-based screen to identify host proteins required for late steps in reovirus replication. Our screen uncovered three primary gene networks operating late in infection, including multiple components of the TRiC chaperonin.

TRiC is a ubiquitous, hetero-oligomeric complex formed by two eight-membered rings composed of paralogous subunits (CCT1–CCT8)[7]. These rings form a barrel-shaped structure with a central cavity that mediates ATP-dependent folding of newly translated proteins[8–10]. TRiC substrates often exhibit complex β-sheet topology, are aggregation prone and display slow folding kinetics[11]. Many TRiC substrates also are subunits that form higher-order structures, such as actin and tubulin[12–14]. A potential role for TRiC may exist in the replication of eukaryotic viruses. Certain viral proteins interact with TRiC[15–17], and gene-silencing studies suggest that TRiC is required for the replication of some viruses[18–20]. However, a mechanism for TRiC in viral protein folding or particle assembly has not been described.

Here, we show that TRiC is essential for reovirus replication. We discovered that TRiC forms a complex with the reovirus σ3 outer-capsid protein and folds σ3 into its native conformation. We also provide evidence that TRiC renders σ3 into a conformation that can coalesce onto mature particles, which is a critical step in viral assembly. These findings elucidate a dynamic pathway for the efficient folding of viral capsid components mediated by the TRiC chaperonin.

Results

RNA interference screen for cellular mediators of late steps in reovirus replication identifies the TRiC chaperonin. To identify host factors required for late steps in reovirus replication, we conducted a two-step RNAi-based screen to quantify reovirus replication after target gene knockdown (Fig. 1a). Human brain microvascular endothelial cells (HBMECs) were transfected with a small interfering (si)RNA library containing 7,518 siRNA pools, each targeting an individual human gene (step 1). After incubation for 48 h, cells were infected with reovirus and incubated for an additional 48 h to allow replication and release of progeny. Supernatants were transferred to new plates containing fresh HBMECs (step 2), which were incubated for 24 h. Step 1 and step 2

[1]Department of Pathology, Microbiology, and Immunology, Vanderbilt University School of Medicine, Nashville, TN, USA. [2]Department of Pediatrics, University of Pittsburgh School of Medicine, Pittsburgh, PA, USA. [3]National Center for Biotechnology, Spanish National Research Council, CNB-CSIC, Madrid, Spain. [4]Department of Biology, Stanford University, Palo Alto, CA, USA. [5]Department of Biochemistry, Institute of Chemical Biology, High-Throughput Screening Facility, Vanderbilt University School of Medicine, Nashville, TN, USA. [6]Department of Microbiology and Immunology, Center for Microbial Pathogenesis and Host Responses, University of Arkansas for Medical Sciences, Little Rock, AR, USA. [7]Department of Microbiology and Molecular Genetics, University of Pittsburgh School of Medicine, Pittsburgh, PA, USA. *e-mail: terence.dermody@chp.edu

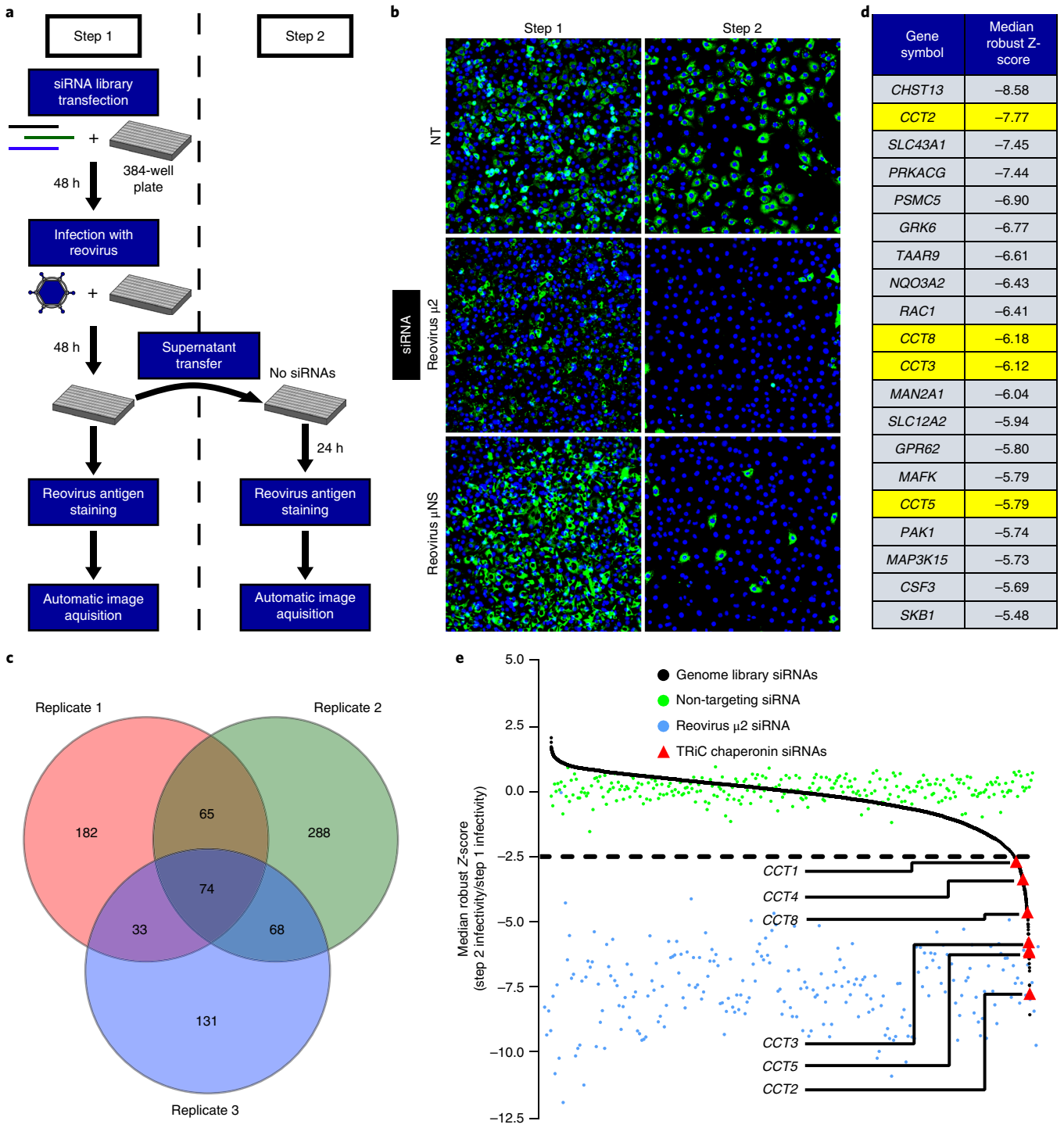

d

Gene symbol	Median robust Z-score
CHST13	–8.58
CCT2	–7.77
SLC43A1	–7.45
PRKACG	–7.44
PSMC5	–6.90
GRK6	–6.77
TAAR9	–6.61
NQO3A2	–6.43
RAC1	–6.41
CCT8	–6.18
CCT3	–6.12
MAN2A1	–6.04
SLC12A2	–5.94
GPR62	–5.80
MAFK	–5.79
CCT5	–5.79
PAK1	–5.74
MAP3K15	–5.73
CSF3	–5.69
SKB1	–5.48

Fig. 1 | RNAi screen for cellular mediators of late steps in reovirus replication identifies the TRiC chaperonin. a, High-throughput screening schematic. **b**, Representative immunofluorescence images from reovirus-infected step 1 and step 2 cells transfected with an NT scrambled siRNA or reovirus-specific siRNAs (μ2 or μNS) and stained with DAPI (blue) and reovirus σNS-specific antiserum (green). **c**, Venn diagram of the number of genes with robust *Z*-score <−2.5 in each independent screen replicate. Overlapping regions indicate the number of genes with a robust *Z*-score <−2.5 in multiple replicates. **d**, Top 20 candidate genes from the screen with *Z*-scores <−2.5 in all three replicates. TRiC chaperonin genes (CCT) are highlighted in yellow. **e**, Median robust *Z*-scores from three independent screen replicates for individual target genes (black, $n = 7{,}418$), NT siRNA (green, $n = 288$), reovirus μ2 siRNA (blue, $n = 240$) and CCT siRNAs (red).

cells were fixed, stained with a reovirus-specific antiserum and imaged to quantify infectivity.

As negative and positive controls for impaired virus release, HBMECs were transfected with a non-targeting (NT) scrambled siRNA or reovirus-specific siRNAs targeting the μ2 structural or μNS (non-structural) proteins. HBMEC transfection with an NT siRNA resulted in abundant infection of step 1 (81.7%) and step 2 (67.4%) cells, whereas μ2 or μNS targeting substantially reduced step 2 cell infectivity (13.6% and 13.1%, respectively) with little effect on infectivity of step 1 cells (70.5% and 85.3%, respectively)

(Fig. 1b). We hypothesized that any host factor required for a late step in viral infection would mirror the infectivity results observed with μ2 and μNS knockdown.

To identify candidate host genes, siRNA pools that compromised cell viability were excluded, and robust *Z*-scores for the siRNA library targets were calculated using step 1 and step 2 infectivity values. Negative robust *Z*-scores reflect diminished virus release. Seventy-four genes were at or below a predetermined robust *Z*-score threshold in each of the three independent screen replicates (Fig. 1c). STRING protein–protein interaction network analysis revealed an enrichment of Ras/MAPK, ubiquitin/proteasome and TRiC chaperonin gene networks (Supplementary Fig. 1). The top 20 candidates included chaperone components, kinases and phosphatases, molecule transporters and various enzymes (Fig. 1d). Remarkably, six of the eight subunits of the TRiC chaperonin (*CCT1*, *CCT2*, *CCT3*, *CCT4*, *CCT5* and *CCT8*) displayed median robust *Z*-scores less than −2.5, implicating this host chaperonin in viral replication (Fig. 1e).

The TRiC chaperonin is required for efficient reovirus replication, release and protein expression. To validate the RNAi screen findings, we repeated the screening procedure using HBMECs transfected with pools of four TRiC-specific siRNAs different from those used in the screen. Infectivity in step 1 cells transfected with TRiC-specific siRNAs was within 15% of infectivity in NT siRNA controls (Fig. 2a,b). However, TRiC disruption significantly reduced step 2 cell infectivity compared with NT controls (Fig. 2a,c). Thus, TRiC chaperonin knockdown decreases efficient release of infectious virus.

To determine the effect of TRiC disruption on reovirus replication, HBMECs were transfected with NT or TRiC-specific siRNAs and infected with reovirus. At 24 h post infection, reovirus titres were ~100-fold lower in cells transfected with CCT2-, CCT3- and CCT5-specific siRNAs compared with control cells (Fig. 2d). At 48 h post infection, reovirus titres were ~100 to 1,000-fold lower in cells transfected with each TRiC-specific siRNA compared with control cells. Similar results were observed in experiments using human adenocarcinoma cells and human embryonic kidney cells (Supplementary Fig. 2). Importantly, TRiC disruption did not alter cell viability (Supplementary Fig. 3). Disruption of TRiC also did not affect the replication of chikungunya virus, an unrelated enveloped RNA virus that replicates in the cytoplasm[21]. Combined, these data indicate that TRiC function is required for efficient reovirus replication and that the requirement is not universal for all viruses.

To assess whether TRiC disruption alters reovirus protein expression, HBMECs were transfected with NT or TRiC-specific siRNAs and infected with reovirus. At 24 h post infection, cell lysates were prepared, resolved by SDS–PAGE and immunoblotted for reovirus proteins (Fig. 2f) or TRiC subunits and GAPDH (Fig. 2g). RNAi knockdown of each TRiC subunit substantially reduced the levels of intracellular reovirus proteins, providing evidence that TRiC is required for the production or stabilization of viral polypeptides.

TRiC redistributes to viral inclusions and is required for inclusion morphogenesis. Reovirus forms inclusions in infected cells that serve as sites of progeny particle production[22]. To determine whether reovirus infection induces changes in the intracellular distribution of TRiC, we visualized TRiC in infected and uninfected cells by confocal and electron microscopy. The CCT1 and CCT3 TRiC subunits displayed a diffuse staining pattern in uninfected HBMECs (Supplemental Fig. 4). By contrast, their distribution was substantially altered in reovirus-infected cells, localizing primarily to viral inclusions (Fig. 3a). Electron microscopy of immunogold-labelled TRiC revealed sparse, diffuse staining in uninfected cells and concentrated, inclusion-associated staining in infected cells (Fig. 3b). These observations demonstrate that TRiC redistributes to sites of viral replication.

To determine the effect of TRiC disruption on viral inclusion morphogenesis, HBMECs were transfected with NT or TRiC-specific siRNAs, infected with reovirus and imaged by confocal and electron microscopy. In contrast to cells transfected with an NT siRNA, cells transfected with siRNAs targeting TRiC subunits exhibited distorted inclusion morphology (Fig. 3c). Instead of forming large globular structures, inclusions appeared as puncta or diffuse throughout the cytoplasm. Electron microscopy of reovirus-infected cells treated with an NT siRNA revealed electron-dense viral inclusions with numerous mature particles (Supplementary Fig. 4). In cells transfected with TRiC-specific siRNAs, viral inclusions appeared abnormal, and virions were occasionally distorted. Thus, the TRiC chaperonin is required for formation of viral inclusions and production of virions with normal morphology.

The TRiC chaperonin forms a complex with the reovirus σ3 outer-capsid protein. The TRiC chaperonin folds newly translated polypeptides through an ATP-dependent mechanism[8–10]. To determine whether TRiC folds 1 or more of the 11 viral proteins during infection, TRiC was immunoprecipitated from reovirus-infected HBMECs after metabolically labelling newly translated proteins with ^{35}S-methionine/cysteine. SDS–PAGE of the input protein identified reovirus-specific large (λ), medium (μ) and small (σ) polypeptides in infected cells (Fig. 4a, left). SDS–PAGE of immunoprecipitated TRiC revealed known TRiC binding partners (actin and tubulin[23]) and an additional virus-specific band migrating at ~40 kDa (Fig. 4a, right). To confirm this interaction, TRiC was immunoprecipitated from reovirus-infected HBMECs, and co-immunoprecipitating proteins were resolved by SDS–PAGE and immunoblotted for reovirus proteins. The same viral protein at ~40 kDa co-immunoprecipitated with the TRiC chaperonin (Supplementary Fig. 5). Using protein-specific monoclonal antibodies, the 40 kDa band was identified as σ3 (Fig. 4b, lane 4). Reovirus σ3 is an essential structural component that complexes with the viral μ1 protein to form $\mu1_3\sigma3_3$ heterohexamers. These heterohexamers coalesce onto assembling virions to form the outer capsid[24,25]. The identification of an intracellular TRiC–σ3 complex led us to hypothesize that TRiC functions in reovirus replication by folding σ3 into its native state or contributing to its assembly into higher order structures.

To determine whether reovirus σ3 is a TRiC substrate, σ3 was translated in rabbit reticulocyte lysates (RRLs) in the presence of ^{35}S-methionine (met), resolved by native PAGE and visualized by phosphorimaging. RRLs are rich in chaperones, including TRiC, and have been used to identify putative TRiC substrates[26,27]. In addition to σ3, human β-actin (a TRiC substrate[13,28]) and green-fluorescent protein (GFP) (folds independently of TRiC[27]) were translated as controls. GFP migrated as a low molecular weight monomer over the intervals of translation (Fig. 4c, lanes 1–3). β-Actin migrated in two primary forms: a low molecular weight monomer and a high molecular weight ~800 kDa species corresponding to a TRiC-actin complex (Fig. 4c, lanes 4–6). In vitro translated σ3 from two prototype reovirus strains (T1L and T3D) migrated almost exclusively as a high molecular weight species (Fig. 4c, lanes 7–12). A free σ 3 monomer did not accumulate over time, suggesting that in vitro translated σ3 remains bound to TRiC in a stable complex. To determine whether structurally-related viral outer-capsid proteins form a complex with TRiC, American grass carp aquareovirus (GCRV) VP7 and Colorado tick fever virus (CTFV, a coltivirus) VP11 were translated in RRLs. GCRV VP7 and CTFV VP11 migrated primarily as high molecular weight complexes by native PAGE, as was observed with σ3 (Fig. 4d). Therefore, homologous capsid proteins of *Reoviridae* members form a complex with the TRiC chaperonin.

For certain substrates, TRiC functions as a holdase, retaining the polypeptide in a quasi-native state until an interaction with a binding partner or co-chaperone mediates a final folding or release event[29,30]. To assess the stability of the complex formed between σ3

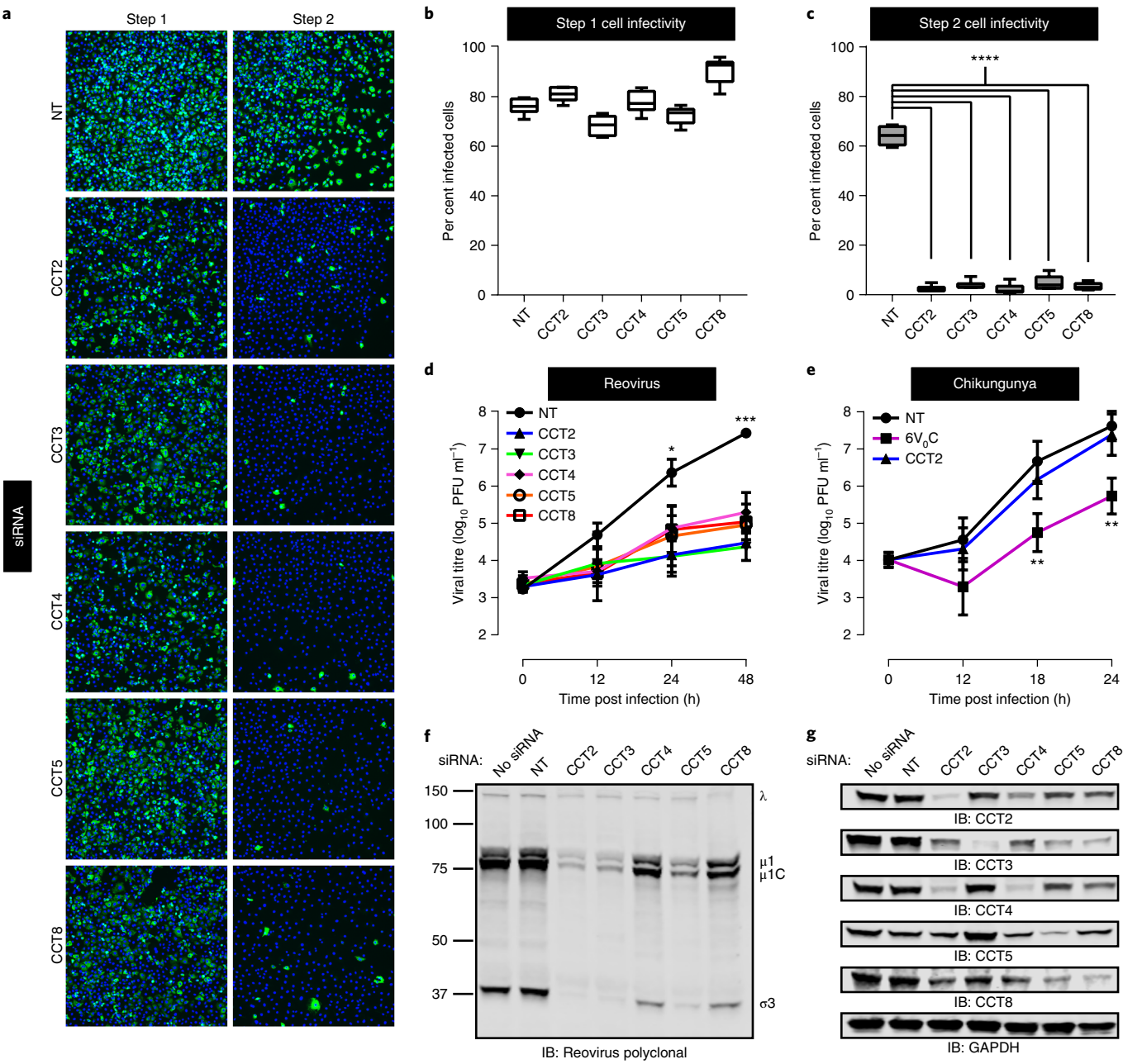

Fig. 2 | The TRiC chaperonin is required for efficient reovirus replication, release and protein expression. a, Representative immunofluorescence images of step 1 and step 2 T1L reovirus-infected HBMECs transfected with an NT luciferase-specific siRNA or TRiC subunit-specific (CCT) siRNAs and stained with DAPI (blue) and reovirus σNS-specific antiserum (green). **b**,**c**, Quantification of step 1 (**b**) and step 2 (**c**) per cent infected cells from **a**. Data are presented as box-and-whisker plots of six technical replicates and are representative of three independent experiments (****$P < 0.0001$; one-way ANOVA). **d**,**e**, Viral titres from T1L reovirus-infected HBMECs (multiplicity of infection (MOI) of one plaque forming unit (PFU) per cell) (**d**) or chikungunya virus-infected U-2 OS cells (MOI of 0.01 PFU per cell) (**e**) transfected with NT or TRiC subunit-specific siRNAs. An siRNA targeting the $6V_0C$ subunit of the vacuolar ATPase was used as a positive control to impair chikungunya virus replication[61]. Data are presented as mean ± s.e.m. of three independent experiments (*$P < 0.05$; **$P < 0.01$; ***$P < 0.001$; one-way ANOVA). **f**,**g**, Sodium dodecyl sulfate–polyacrylamide gel electrophoresis (SDS–PAGE) of HBMECs transfected with the indicated siRNAs, infected with T1L reovirus (MOI of 100 PFU per cell, 24 h post infection), and immunoblotted for reovirus proteins (**f**) or TRiC subunits and GAPDH (**g**). Immunoblots are representative of three independent experiments conducted with similar results.

and TRiC, σ3 was translated in the presence of ^{35}S-met for 5 minutes, incubated with cold met for 4 h, and resolved by native (Fig. 4e) and SDS–PAGE (Supplementary Fig. 5). Newly translated β-actin migrated in both TRiC-bound and TRiC-free forms (Fig. 4e, lane 3). After a 4 h chase, the high molecular weight TRiC–actin complex decreased in abundance with a corresponding increase in free, monomeric β-actin (Fig. 4e, lane 4). By contrast, in vitro translated σ3 remained TRiC-bound throughout the duration of the cold met chase (Fig. 4e, lanes 5–8). These data indicate that the complex formed between TRiC and σ3 is stable long after translation has completed, suggesting that TRiC functions as a holdase for σ3.

To confirm that the high molecular weight species in the in vitro translation reactions corresponds to TRiC-bound substrate, σ3 was translated in TRiC-immunodepleted RRLs and resolved by native

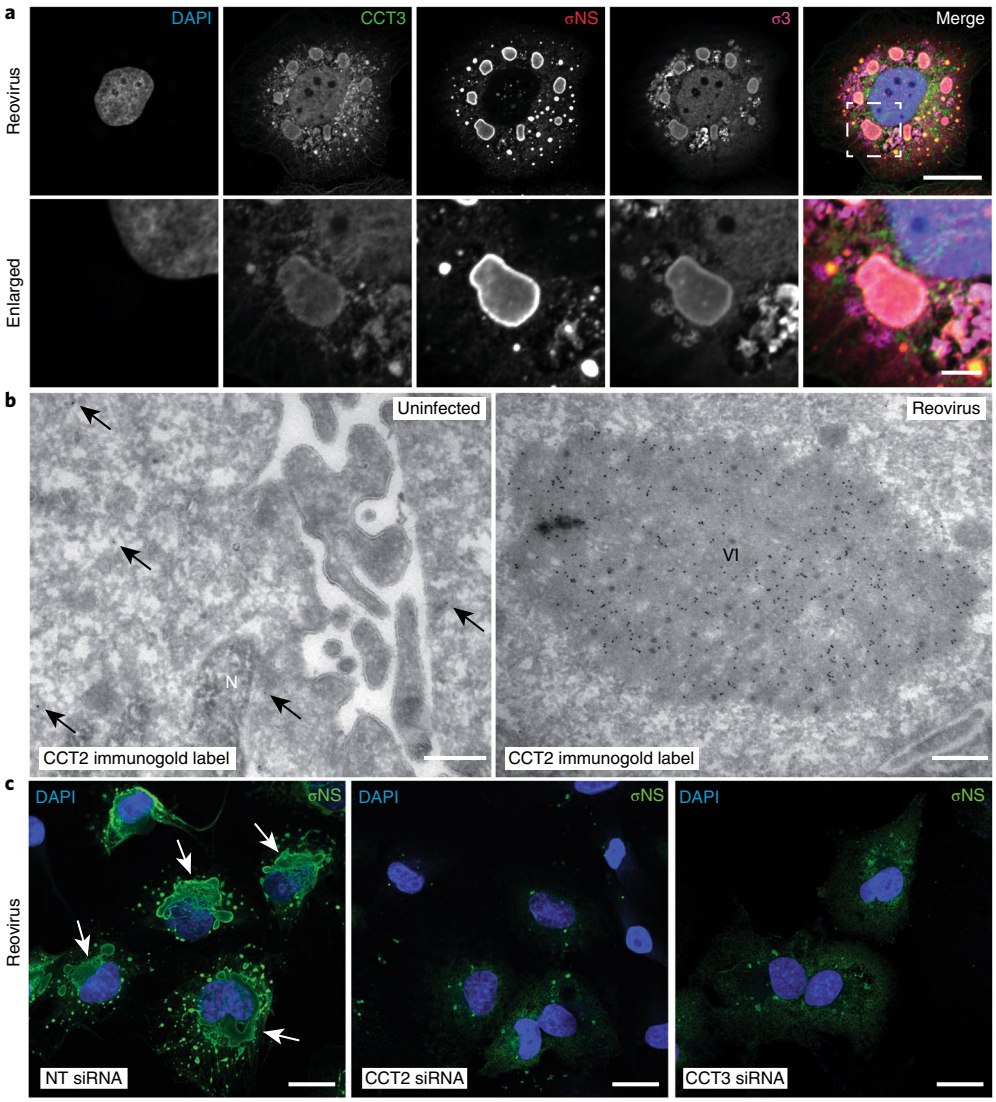

Fig. 3 | TRiC redistributes to viral inclusions and is required for inclusion morphogenesis. a, Confocal immunofluorescence images of T3D reovirus-infected HBMECs (MOI of 100 PFU per cell, 24 h post infection) stained with DAPI (blue) and antibodies specific for CCT3 (green), σNS (red) and σ3 (magenta). Viral inclusions are identifiable by σNS staining. Enlarged images correspond to the region indicated by the white dashed box in the merged image. Scale bars, 20 μm and 4 μm in full-size and enlarged images, respectively. **b**, Tokuyasu cryosections of uninfected or T1L reovirus-infected (MOI of 1 PFU per cell, 20 h post infection) HBMECs immunogold labelled for CCT2. Scale bars, 500 nm. Arrows indicate gold particles observed in uninfected cells. VI, viral inclusion; N, nucleus. **c**, confocal immunofluorescence images of HBMECs transfected with NT or TRiC subunit-specific siRNAs, infected with T1L reovirus (MOI of 100 PFU per cell, 24 h post infection) and stained with DAPI (blue) and a σNS-specific antiserum (green). Scale bars, 20 μm. Large, globular inclusions are marked by white arrows. Images are representative of three independent experiments conducted with similar results.

PAGE (Fig. 4f). TRiC was reproducibly immunodepleted to levels 80–85% less than that of mock-depleted RRLs (Supplementary Fig. 5). The ~800 kDa form of σ3 was substantially reduced in TRiC-depleted RRLs (Fig. 4f, lane 4). In addition, σ3 translated in TRiC-depleted RRLs accumulated in a high molecular weight form that did not enter the native gel, indicative of protein aggregation (Fig. 4f, lane 4, asterisk). Reconstitution of immunodepleted RRLs with purified human TRiC (hTRiC) restored the intensity of the ~800 kDa band (Fig. 4f, lane 5), providing evidence that the high molecular weight species constitutes a stable TRiC-σ3 complex.

Since TRiC forms a complex with σ3, we hypothesized that the defects in viral protein production (Fig. 2f) and viral inclusion formation (Fig. 3c) with TRiC disruption are attributable to a failure in σ3 biogenesis. We tested whether siRNA disruption of σ3 mirrored the effect of TRiC disruption on viral inclusion formation. RNAi knockdown of σ3 in reovirus-infected cells resulted in decreased viral protein expression and distorted viral inclusions that failed to mature into large globular structures (Supplementary Fig. 6), mimicking results observed with TRiC knockdown. We conclude that the observed effects of TRiC disruption on viral protein synthesis and inclusion morphology are a result of defects in σ3 production.

The intracellular biogenesis of native σ3 conformers requires the TRiC chaperonin. To determine whether TRiC is required to fold σ3 within infected cells, HBMECs expressing CCT2 or CCT5 short hairpin (sh)RNAs were infected with reovirus, and intracellular σ3 was visualized by confocal microscopy. Folded σ3 was detected using a conformation-sensitive monoclonal antibody specific for the native form of the protein[31]. TRiC disruption substantially reduced the forms of σ3 recognized by the conformation-specific antibody, whereas infected cells with intact TRiC produced abundant folded σ3 (Fig. 5a). To assess total levels of σ3, cells were

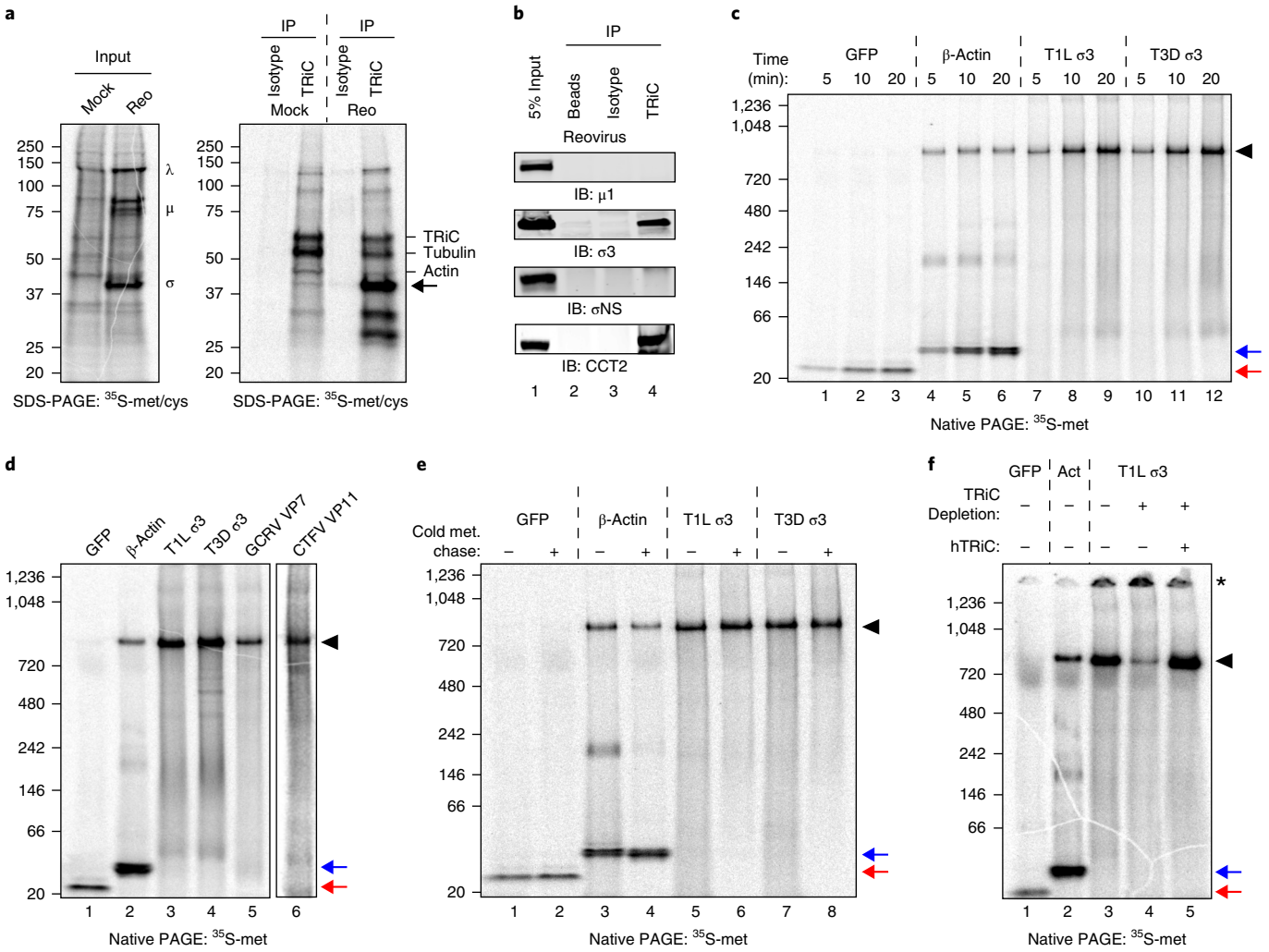

Fig. 4 | The TRiC chaperonin forms a complex with the reovirus σ3 outer-capsid protein. a, SDS–PAGE of mock or T1L reovirus-infected HBMECs (MOI of 100 PFU per cell, 20 h post infection) pulse-labelled for 5 min with ^{35}S-methionine/cysteine. Left, 2% input protein. Large (λ), medium (μ) and small (σ) viral proteins are labelled. Right, immunoprecipitation with isotype control or TRiC-specific antibody. A virus-specific band at ~40 kDa is denoted by an arrow. **b**, SDS–PAGE of TRiC immunoprecipitated from T3D reovirus-infected HBMECs (MOI of 100 PFU per cell, 48 h post infection) immunoblotted for μ1, σ3, σNS, and CCT2. **c**, Native PAGE of ^{35}S-methionine (met)-labelled green fluorescent protein (GFP), β-actin, and T1L and T3D reovirus σ3 translated for the intervals shown in rabbit reticulocyte lysates (RRLs). **d**, Native PAGE of ^{35}S-met-labelled GFP, β-actin, T1L and T3D σ3, GCRV VP7 and CTFV VP11 translated for 1 h in RRLs. CTFV VP11 is shown separately because of the low methionine content, requiring an independent exposure. **e**, Native PAGE of ^{35}S-met-labelled GFP, β-actin, and T1L and T3D σ3 translated in RRLs with (+) or without (−) a 4 h cold methionine chase. **f**, Native PAGE of ^{35}S-met-labelled GFP, β-actin (Act) and T1L σ3 translated in mock-depleted (−) or TRiC-depleted (+) RRLs with or without addition of purified human TRiC (hTRiC; +, 0.25 μM). The asterisk denotes protein unable to enter the native gel. In all native gels, the black arrowhead indicates the TRiC-bound substrate, and the red and blue arrows indicate free GFP and β-actin monomers, respectively. In **a**–**f**, three independent experiments were conducted with similar results.

stained with a σ3-specific polyclonal antiserum capable of recognizing folded and unfolded epitopes. Total σ3 immunofluorescence (folded and unfolded) was substantially greater than folded σ3 in TRiC-deficient cells (Fig. 5b). The average σ3 staining area (Fig. 5c) and intensity (Fig. 5d) were significantly higher for total σ3 relative to folded σ3. Despite the increased levels of total σ3 observed by confocal microscopy, the total amount of full-length, soluble σ3 detectable by immunoblotting was substantially reduced in TRiC-deficient cells (Fig. 5e, lanes 7–12). Therefore, TRiC disruption results in accumulation of σ3 conformers that are partially translated, proteolytically cleaved or aggregated and insoluble.

To determine the effect of TRiC disruption on the production of native intracellular σ3, HEK-293T cells were transfected with an NT or TRiC-specific siRNA and transfected with expression plasmids or infected with reovirus (Fig. 5f). Cell lysates were resolved by native PAGE and immunoblotted for σ3 (Fig. 5g) or TRiC (Supplementary Fig. 7). Expression of all proteins was confirmed by SDS–PAGE (Fig. 5h). When expressed alone, σ3 migrated in two predominant forms: a low molecular weight complex at ~140 kDa, corresponding to a σ3 homo-oligomer[32,33], and a high molecular weight complex at ~800 kDa, corresponding to the TRiC-bound form of σ3 (Fig. 5g, lane 2). When co-expressed with its outer-capsid binding partner, μ1, σ3 migrated primarily at a molecular weight of ~400 kDa (Fig. 5g, lane 3), corresponding to the assembled $\mu1_3\sigma3_3$ heterohexamer[34]. In reovirus-infected cells, the forms of intracellular σ3 included the TRiC-bound species, $\mu1_3\sigma3_3$ heterohexamer, and σ3 homo-oligomer, as well as an unknown band migrating at ~250 kDa (Fig. 5g, lane 4). RNAi disruption of TRiC resulted in a striking perturbation of the intracellular forms of σ3. When expressed alone in TRiC-disrupted cells, σ3 migrated as a single, low-intensity, high molecular weight band corresponding to a complex with residual intracellular TRiC (Fig. 5g, lane 6). When co-expressed with μ1

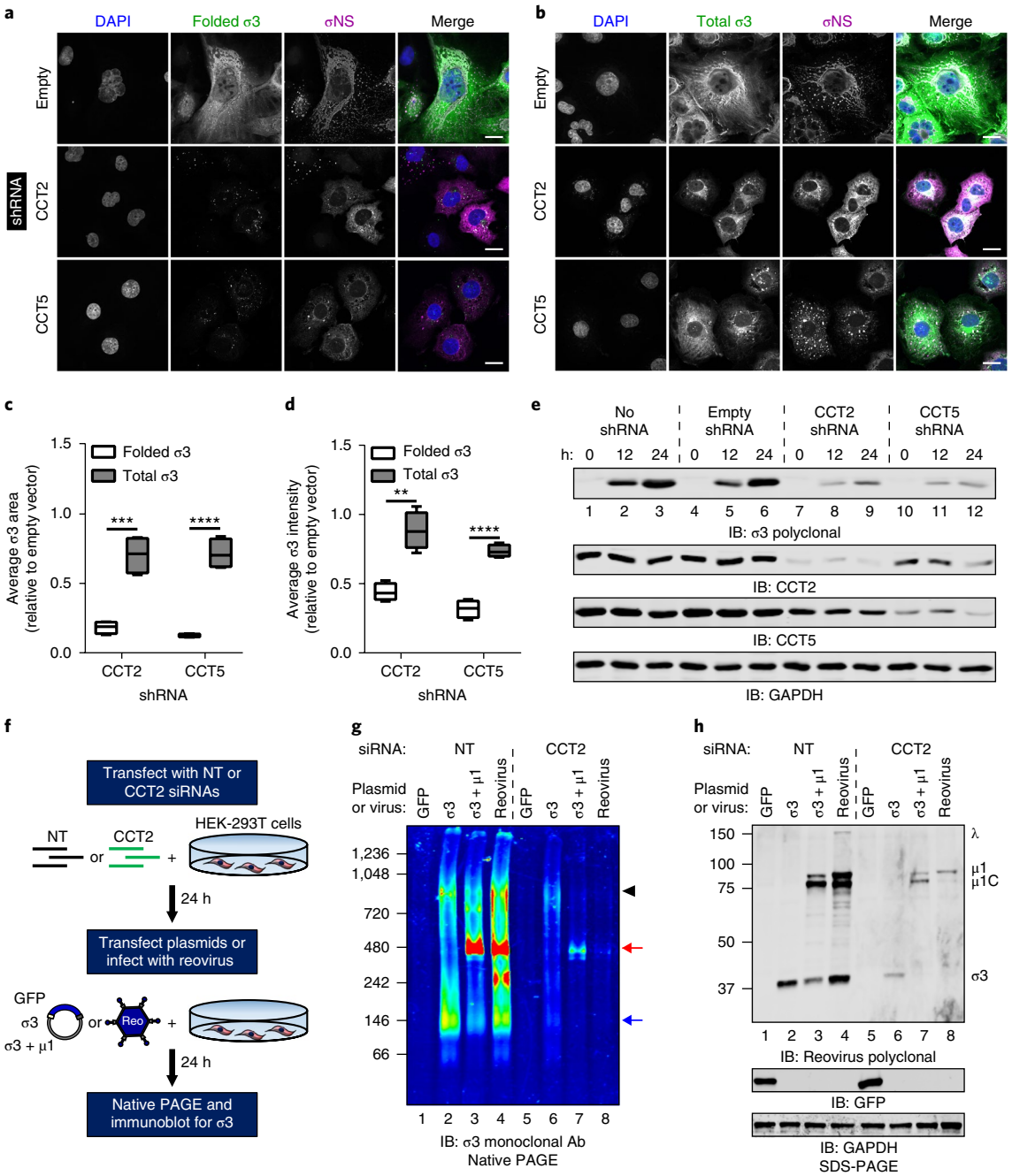

Fig. 5 | The intracellular biogenesis of native σ3 requires the TRiC chaperonin. a,**b**, Immunofluorescence images of HBMECs stably transduced with TRiC subunit-specific shRNAs (or empty vector), infected with T1L reovirus (MOI of 100 PFU per cell, 24 h post infection), and stained with DAPI (blue) and antibodies specific for σNS (magenta) and folded (**a**, 10C1 monoclonal antibody) or total (**b**, VU219 polyclonal antiserum) σ3 (green). Scale bars, 20 μm. **c**,**d**, Quantification of folded or total σ3 staining area (**c**) or fluorescence intensity (**d**) per infected cell in CCT–shRNA transduced cells relative to empty vector control cells (>200 cells quantified per experiment) from images acquired in **a** and **b**. Data are presented as box-and-whisker plots of four independent experiments (**$P < 0.01$; ***$P < 0.001$; ****$P < 0.0001$; unpaired, two-tailed *t*-test). **e**, SDS–PAGE of shRNA-transduced HBMECs infected with T1L reovirus (MOI of 100 PFU per cell), harvested at the intervals shown and immunoblotted for reovirus σ3, CCT2, CCT5 or GAPDH. **f**, Schematic of RNAi knockdown and plasmid transfection or reovirus infection of HEK-293T cells. **g**, Native PAGE of HEK-293T cells transfected with an NT or TRiC subunit-specific siRNA and transfected with the indicated expression plasmids or infected with T3D reovirus (MOI of 100 PFU per cell, 24 h post infection) and immunoblotted for σ3. Black arrowhead, TRiC-σ3 position; red arrow, $\mu1_3\sigma3_3$ heterohexamer position; blue arrow, σ3 homo-oligomer position. **h**, SDS–PAGE of cell lysates from **g** immunoblotted for reovirus proteins, GFP and GAPDH. Individual reovirus proteins are labelled. Immunoblots are representative of three independent experiments conducted with similar results.

in TRiC-disrupted cells, σ3 exclusively migrated as a faint band at ~400 kDa (Fig. 5g, lane 7). Finally, native intracellular σ3 was virtually undetectable in reovirus-infected, TRiC-disrupted cells (Fig. 5g, lane 8). Importantly, overall levels of de novo translation were not affected by TRiC disruption, as GFP expression was equivalent in cells treated with NT or TRiC-specific siRNAs (Fig. 5h, lane 1,5). These data indicate that TRiC is required for the intracellular production of the multiple native forms σ3.

The TRiC chaperonin folds σ3 into a native, assembly-competent conformation. To determine whether TRiC directly folds σ3 into its native conformation, σ3 was translated in mock- or TRiC-depleted RRLs (Fig. 6a). Translated σ3 was immunoprecipitated using a conformation-specific antibody and resolved by SDS–PAGE (Fig. 6a, i). Reovirus σ3 was efficiently immunoprecipitated from mock-depleted RRLs (Fig. 6b, lane 3). By contrast, there was a 67% reduction in the amount of σ3 immunoprecipitated from TRiC-depleted reactions (Fig. 6b, lane 6). Immunoprecipation of σ3 translated in TRiC-depleted RRLs reconstituted with hTRiC yielded levels similar to mock-depleted RRLs (Fig. 6b, lane 9, quantified in Supplementary Fig. 8). To identify the σ3 species recognized by the conformation-specific antibody, we resolved the immunoprecipitation flow-through containing unbound protein by native PAGE (Supplementary Fig. 8). The σ3-specific antibody depleted the ~800 kDa form of σ3 from translation reactions, revealing that the antibody recognizes an exposed region of σ3 bound to TRiC. These results provide evidence that TRiC directly folds and retains σ3 in an exposed conformation capable of interacting with binding partners.

To further test whether TRiC directly folds σ3, we quantified the protease sensitivity of σ3 translated in mock- or TRiC-depleted RRLs (Fig. 6a, ii). Unfolded proteins often exhibit increased protease sensitivity because of the exposure of additional cleavage sites[35,36]. Reovirus σ3 was translated in mock- or TRiC-depleted RRLs, digested with proteinase K for various intervals and resolved by SDS–PAGE. Compared with mock-depleted RRLs, σ3 translated in TRiC-depleted RRLs displayed enhanced proteinase K sensitivity (Fig. 6c, Supplementary Fig. 8). Reconstitution of depleted RRLs with purified hTRiC decreased the sensitivity of translated σ3 to protease digestion, providing further evidence that TRiC folds σ3 into its native conformation.

To determine whether TRiC renders σ3 into a conformation capable of assembly, we tested whether reovirus infectious subvirion particles (ISVPs) could be recoated with σ3 translated in RRLs. (Fig. 6a, iii). ISVPs are naturally occurring reovirus disassembly intermediates formed during cell entry. These particles lack σ3 and contain a cleaved form of the σ3-binding partner, μ1 (μ1δ) (Fig. 6d). ISVPs can be recoated with purified σ3 to produce the mature outer capsid[37]. We translated σ3 in mock or TRiC-depleted RRLs (Fig. 6e), incubated reactions with ISVPs and immunoprecipitated recoated particles with a μ1δ-specific antibody. We confirmed that this antibody recognizes μ1δ and not σ3 (Supplementary Fig. 8). TRiC depletion resulted in a 92% reduction in the efficiency of ISVP recoating (Fig. 6e, lane 6, quantified in Supplementary Fig. 8). Concordantly, reconstitution of RRLs with purified hTRiC restored recoating activity (Fig. 6e, lanes 9 and 12). Thus, TRiC folds σ3 into a conformation capable of recoating ISVPs, providing evidence that TRiC functions in viral particle assembly by folding the σ3 outer-capsid protein.

Discussion

In this study, we used an RNAi-based screen to identify cellular factors required for late steps in reovirus infection and discovered that the TRiC chaperonin mediates reovirus capsid protein folding. Found within all eukaryotic cells, TRiC interacts with 5–10% of cytoplasmic proteins and exhibits substrate specificity, although no consensus TRiC-binding determinants have been identified[11]. Our data support a model in which TRiC binds and folds reovirus σ3 into its native conformation, after which the folded protein is retained within TRiC, released as a stable homo-oligomer or incorporated into the $\mu1_3\sigma3_3$ heterohexamer for assembly onto progeny virions (Fig. 6f). These observations enhance an understanding of the cell biology of reovirus infection and yield a new function for the TRiC chaperonin.

Presently no rules or patterns have been defined for viral substrates of the TRiC chaperonin. In certain cases, such as with reovirus σ3, retroviral Gag[15,38] and the hepatitis B virus core protein[16], TRiC appears to fold capsid components, potentially directing their assembly into mature particles. For other viruses, TRiC interacts with less abundant non-structural proteins, such as Epstein–Barr virus EBNA-3[17] and hepatitis C virus NS5B[18]. In the case of capsid components, the requirement for TRiC-mediated folding might be due to the propensity of these proteins to rapidly misfold and form insoluble aggregates. As for viral non-structural proteins, the presence of multiple domains with independent folding requirements may dictate the need for TRiC. Why certain viruses require TRiC and others do not, and whether viral substrates of TRiC can be predicted, remain key unanswered questions.

Although we provide evidence that TRiC folds σ3, we do not understand the biochemical features that render σ3 an obligate TRiC substrate. A complex between TRiC and σ3 may form during translation to prevent nascent chain misfolding. Alternatively, σ3 may be refractory to spontaneous folding after release from ribosomes, requiring the exploration of various intermediates before achieving a native conformation. The structure of σ3 contains β-sheets that form via long-range intramolecular interactions[32], and these secondary structures may not form spontaneously, requiring the iterative cycling of TRiC to complete the folding process. The σ3 protein also harbours a hydrophobic amino-terminal domain that forms the binding interface between homo-oligomers and molecules of μ1 in the $\mu1_3\sigma3_3$ heterohexamer. This domain is likely to be insoluble and aggregation prone in the aqueous cytoplasm, and TRiC, like other chaperonins[39], may function to provide a thermodynamically favourable environment to allow the domain to fold. The combined effect of TRiC co-translational binding and iterative folding may be necessary for the efficient folding and assembly of σ3 onto new virus particles.

After folding, TRiC substrates are usually released from the interior chamber and exit into the cytosol. However, for certain substrates, such as the Von Hippel–Lindau (VHL) protein, release is more complex. After an initial folding event, TRiC functions as a holdase for VHL, retaining the protein in a quasi-native conformation competent for assembly into higher-order structures[29]. The complete folding and release of VHL occurs only after interaction with elongin-BC, the VHL binding-partner[29]. Our observation that σ3 translated in RRLs forms a stable complex with TRiC (Fig. 4d) suggests that TRiC functions as a σ3 holdase, stabilizing σ3 in a form primed for assembly. Through its holdase activity, TRiC could sequester aggregation-prone domains of σ3, such as the hydrophobic amino terminus, and maintain the protein in a conformation competent for assembly into homo-oligomers or heterohexamers. Owing to similarities in the replication cycles of Reoviridae viruses, we predict that this TRiC-mediated folding mechanism operates broadly to stabilize and assemble aggregation-prone viral capsid components.

Despite its observed holdase function, TRiC must liberate native σ3 for virus assembly. An interaction between TRiC-bound σ3 and nascent μ1 could trigger σ3 release. Alternatively, an unknown host co-chaperone could facilitate the productive release of native σ3 from TRiC. There is precedent for such a mechanism, as certain substrate-specific co-chaperones function following the action of TRiC to aid in the folding and assembly of oligomers. The α/β tubulin co-chaperones function following TRiC to assemble microtubules[40], and phosducins participate in the assembly of the G-protein βγ dimer after TRiC-mediated β-subunit folding[41]. In the case of reovirus σ3, assembly into a complex with a host or viral protein is likely required for the release of the native protein following TRiC-mediated folding.

The different subunits in hetero-oligomeric TRiC have distinct binding specificities[38] and, thus, substrate selection results from the combinatorial recognition of unique binding determinants in a substrate[42,43]. These binding determinants may associate with TRiC

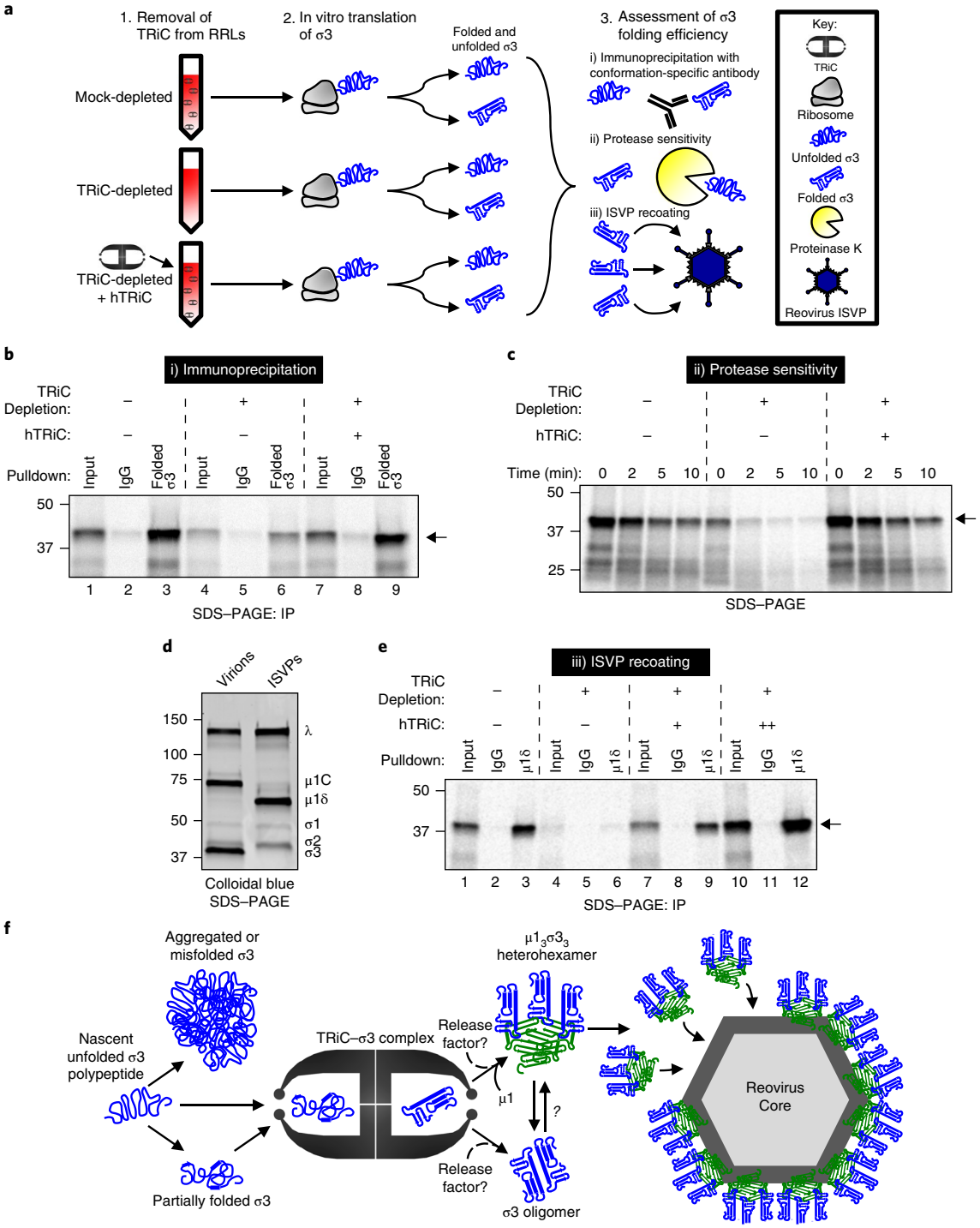

Fig. 6 | The TRiC chaperonin folds σ3 into a native, assembly-competent conformation. a, Schematic of σ3 folding and assembly experiments. **b**, SDS-PAGE of ^{35}S-met-labelled σ3 immunoprecipitated from RRLs using a conformation-specific antibody (10C1 monoclonal antibody) or isotype control. Where indicated, RRLs were TRiC-depleted and reconstituted with purified hTRiC (+, 0.25 μM) (10% input loaded into lanes 1, 4, 7). **c**, SDS–PAGE of ^{35}S-met-labelled σ3 translated in RRLs mock-depleted, TRiC-depleted or TRiC-depleted and reconstituted with purified hTRiC (+, 0.25 μM) and incubated with proteinase K (2.5 μg ml^{-1} final concentration) for the times shown. **d**, SDS–PAGE and colloidal blue stain of T1L reovirus virions and ISVPs. **e**, SDS–PAGE of ISVPs recoated with ^{35}S-met-labelled σ3 translated in RRLs and immunoprecipitated using a μ1δ-specific antibody, which is specific to the μ1 species on ISVPs. Where indicated, RRLs were TRiC-depleted and reconstituted with purified hTRiC (+, 0.125 μM; ++, 0.50 μM) (20% input loaded into lanes 1, 4, 7, 10). The arrows in SDS–PAGE gels indicate full-length σ3. In **b**–**e**, three independent experiments were conducted with similar results. **f**, Model of the TRiC–σ3 folding and assembly pathway.

as helical structures, such as in a 54 amino acid stretch in the p6 domain of HIV Gag[15,38], or in an extended state, as in a 6–9 amino acid sequence in Box 1 of VHL[7,44]. Our finding that outer-capsid proteins of mammalian orthoreovirus (σ3), aquareovirus (VP7), and coltivirus (VP11) bind to TRiC suggests that certain shared biochemical features facilitate chaperonin binding. These viral

capsid proteins exhibit less than 20% amino acid identity but show similar hydrophobicity profiles in certain sequence regions[45]. These conserved hydrophobic regions may dictate TRiC binding and constitute a shared substrate motif, which supports a potential new determinant of TRiC binding.

Our results establish a function for the TRiC chaperonin in the folding of a non-enveloped virus capsid component. The broad conservation of TRiC in eukaryotes and the common principles of assembly of non-enveloped viruses raise the possibility that TRiC folds capsid components of other viruses. Findings reported here establish a foundation to better understand the rules governing TRiC substrate selection and set the stage for development of TRiC inhibitors as potentially broad-spectrum antiviral therapeutics.

Methods

Cells and viruses. HBMECs were provided by Kwang Sik Kim[46] (Johns Hopkins University) and cultured in RPMI 1640 medium as described. U-2 osteosarcoma (OS) (ATCC HTB-96) cells were maintained in McCoy's 5A medium supplemented to contain 10% fetal bovine serum (FBS). HEK-293T (ATCC CRL-3216) cells were maintained in DMEM supplemented to contain 10% FBS and 1% sodium pyruvate. Caco-2 cells (ATCC HTB-37) were maintained in DMEM supplemented to contain 10% FBS, 1% non-essential amino acids and 1% sodium pyruvate. Spinner-adapted murine L929 fibroblast cells were grown in either suspension or monolayer cultures as described[47]. Viral titres were determined by plaque assay using L929 cells as described[48]. Cell viability was quantified by PrestoBlue assay (Thermo Fisher, A13261) according the manufacturer's instructions. HBMECs were tested for mycoplasma contamination using the Venor GeM mycoplasma detection kit (Sigma, MP0025). No authentication was performed on the cell lines used in this study.

Reovirus strains T1L and T3D were recovered using plasmid-based reverse genetics[49] and purified as described[50]. Reovirus T1L M1 P208S, which harbours a point mutation in the M1 gene allowing it to form globular, T3D-like inclusions[51], was used in the RNAi screen to facilitate visualization of reovirus-infected cells by high-throughput automated microscopy. The chikungunya virus 181/25 infectious clone plasmid was generated as described[52].

siRNA and DNA transfections, plasmid cloning and shRNA lentiviral transductions. Cells were reverse-transfected with siRNAs (Supplementary table 1) at a final concentration of 2.5 nM (HBMECs and U2-OS cells) or 5 nM (HEK-293T and Caco-2 cells) using Lipofectamine RNAiMax (Thermo Fisher, 13778075). Cells were used in viability, infection, imaging and immunoblotting assays 48 h post transfection. For transient DNA transfections of HEK-293T cells, 7.2 µg of pcDNA3.1+ expression vectors were combined with FuGene 6 (Promega, E2691) in Opti-MEM and incubated at room temperature for 15 min. DNA/FuGene mixtures were added dropwise onto 5×10^5 cells and incubated at 37 °C for 24 h.

To engineer plasmids for transient transfection and in vitro translation studies, open reading frames were amplified by PCR using primers containing 5′ *Kpn*I and 3′ *Not*I restriction sites (Supplementary table 2). PCR fragments were purified, digested and ligated into the corresponding *Kpn*I/*Not*I restrictions sites in the pcDNA3.1+ vector. The following templates were used for PCR amplification: human β-actin (DNASU, HsCD00042977), American grass carp reovirus VP7 (GeneScript, Gene ID: 6218809), Colorado tick fever virus VP11 (GeneScript, Gene ID: 993319), peGFP-N1 (Addgene, 6085-1), pT7-T1L S4 (σ3) (Addgene, 33295), pT7-T3D S4 (σ3) (Addgene, 33285), pT7-T1L M2 (µ1) (Addgene, 33290).

To propagate shRNA-encoding lentiviruses, 1×10^7 HEK-293T cells were cotransfected with 0.6 µg pVSVG, 3 µg pCMV Lenti 8.92 Gag/Pol and 6 µg of an empty shRNA control (Sigma, SHC201), CCT2-specific shRNA (Sigma, SHCLNG-NM_006431) or CCT5-specific shRNA (Sigma, SHCLNG-NM_012073) using the FuGene 6 transfection reagent. The culture medium was replaced 24 h post transfection with complete RPMI medium, and cells were incubated at 37 °C for 48 h. The medium containing packaged lentiviral particles was clarified by centrifugation at 4,000*g* at 4 °C for 10 min and stored at −80 °C. For lentiviral transduction, 3 ml of lentivirus-containing cell culture medium was combined with 3 µl of polybrene (Millipore, TR-1003-G), vortexed briefly, incubated at room temperature for 5 min and added to HBMECs. After incubation overnight, the culture medium was supplemented to contain 1 µg ml^{-1} puromycin. Target knockdown was confirmed by immunoblotting.

In vitro transcription, translation and ^{35}S-metabolic labelling. Coupled in vitro transcription and translation reactions were conducted using the TNT coupled rabbit reticulocyte lysate system (Promega, L4610) according to the manufacturer's instructions. Using pcDNA3.1+ templates for in vitro transcription and translation, reactions were incubated at 30 °C for variable intervals depending on the experimental conditions. Reactions were supplemented with [^{35}S]-methionine (Perkin Elmer, NEG709A500UC) for radiolabelling and RNasin Plus RNase Inhibitor (N2611). Where indicated, reactions were chased with cold methionine added to a final concentration of 2 mM. Translation reactions were terminated by fourfold dilution in stop buffer (20 mM HEPES-KOH pH 7.4, 100 mM potassium acetate, 5 mM magnesium acetate, 5 mM EDTA, 2 mM methionine) supplemented with a final concentration of 1 mM dithiothreitol (DTT) and 2 mM puromycin. Samples were used for immunoprecipitation, ISVP recoating, proteinase K (Sigma, P4850) digestion (final concentration of 2.5 µg ml^{-1}), or resolved by native and SDS–PAGE.

For metabolic labelling of de novo protein synthesis in cells, 4×10^6 HBMECs were infected with reovirus for 20 h. Cells were incubated in methionine/cysteine-free medium for 20 min, labelled with medium supplemented with ^{35}S-methionine and cysteine (0.4 mCi ml^{-1}) (Perkin Elmer, NEG772007MC) for 5 min and chased with medium supplemented with 50 mM cold methionine and cysteine for 1 min. Radiolabelled TRiC-bound proteins were isolated by immunoprecipitation and visualized by SDS–PAGE.

Native cell lysis, immunoprecipitations and immunodepletions. Native HEK-293T cell lysates were prepared by suspending cells in ice-cold ATP depletion buffer (1 mM sodium azide, 2 mM 2-deoxyglucose, 5 mM EDTA and 5 mM cycloheximide in phosphate-buffered saline without calcium and magnesium (PBS−/−)), followed by centrifugation at 300*g* at 4 °C for 5 min. Cells were resuspended in lysis buffer A (50 mM HEPES pH 7.4, 100 mM KCl, 1.5 mM $MgCl_2$, 0.5% NP-40) supplemented to contain 2 mM phenylmethylsulfonyl fluoride (PMSF, Sigma, P7626), protease inhibitor cocktail (Sigma, P8340) and benzoase (Sigma, E1014) and incubated on ice for 10 min. Lysates were clarified by centrifugation at 20,000*g* at 4 °C for 10 min, and the protein concentration was quantified using a DC protein assay (BioRad, 5000112). DTT was added to each sample to a final concentration of 1 mM, and equal amounts of protein sample were diluted in 4× Native PAGE Sample Buffer and Native PAGE G-250 Sample Additive (0.125% final concentration, Thermo Fisher, BN2004).

To immunoprecipitate TRiC from reovirus-infected cells, HBMECs were harvested in ice-cold ATP-depletion buffer and collected by centrifugation at 300*g* at 4 °C for 5 min. Cells were resuspended in lysis buffer B (50 mM HEPES-KOH pH 7.5, 100 mM KCl, 5 mM EDTA, 10% glycerol) supplemented with protease inhibitor cocktail and lysed by dounce homogenization (70 strokes). Lysates were clarified by centrifugation at 20,000*g* at 4 °C for 10 min. Clarified cell lysates were combined with 2 µg of a rabbit CCT2-specific monoclonal antibody (Abcam, ab92746) or an immunoglobulin (Ig)G isotype control antibody (Abcam, ab172730) and incubated at 4 °C for 30 min with rotation. Cell lysates were combined with Protein G Dynabeads (Thermo Fisher, 10004D) and incubated at 4 °C for 30 min with rotation. Bead-bound antibody–antigen complexes were washed four times with ice-cold TRiC wash buffer (50 mM HEPES-KOH pH 7.5, 100 mM KCl, 5 mM EDTA, 10% glycerol, 0.05% NP-40), eluted with SDS sample buffer and resolved by SDS–PAGE.

To immunoprecipitate proteins translated in vitro in RRLs, 5 µg of mouse 10C1 σ3 monoclonal antibody (for σ3 immunoprecipitations), mouse 8H6 µ1/µ1δ monoclonal antibody (for recoated ISVP immunoprecipitations) or IgG isotype control antibody (mouse 2F5 σNS monoclonal antibody[53]) were incubated with reactions at 4 °C for 1 h with rotation. Samples were added to Protein G Dynabeads and incubated at 4 °C for 1 h with rotation. The flow-through containing unbound protein was resolved by native PAGE. Dynabeads were washed four times with Tris-buffered saline (20 mM Tris-HCl pH 7.5, 150 mM NaCl) containing 0.1% Tween-20, eluted with SDS sample buffer and resolved by SDS–PAGE.

TRiC was immunodepleted from RRLs by incubating 75 µl of RRLs with 8 µg of a rabbit CCT2-specific polyclonal antiserum[27] or an equivalent volume of resin wash buffer (10 mM Tris-HCl pH 7.5, 25 mM KCl, 0.5 mM magnesium acetate) and incubated at 4 °C for 2 h with rotation. Protein A-agarose fast flow resin (Sigma, P3476) was pre-washed four times with 1 ml of resin wash buffer. RRLs were incubated with protein A beads at 4 °C for 2 h, and bead-bound antibody/TRiC complexes were collected by centrifugation at 2,000*g* at 4 °C for 5 min. This process was repeated twice with the supernatant to further deplete TRiC. Where indicated, RRLs were reconstituted with recombinant human TRiC (provided by the Frydman laboratory, Stanford University).

Native and SDS–PAGE, immunoblotting, phosphorimaging. *Native PAGE.* Samples for native PAGE were diluted in 4× Native PAGE Sample Buffer (Thermo Fisher, BN2003) and loaded into wells of 4–16% Native PAGE Bis-Tris acrylamide gels (Thermo Fisher). Samples were electrophoresed using the blue native PAGE Novex Bis-Tris gel system (Thermo Fisher) at 150 V at 4 °C for 60 min, followed by 250 V at 4 °C for 40 min. Light blue anode buffer was supplemented with 0.1% L-cysteine and 1 mM ATP. Following electrophoresis, gels were incubated in 40% methanol, 10% acetic acid at RT for 1 h, washed three times with ddH_2O, and dried on filter paper at 80 °C for 2 h using a BioRad model 583 gel dyer. Dried gels were exposed on a phosphorimaging screen for 12–36 h and imaged using a Perkin Elmer Cyclone Phosphor System Scanner (B431200). Protein bands labelled with ^{35}S-met were analysed using ImageJ software[54]. To immunoblot native cell lysates, samples were resolved by blue native PAGE with the following modification: DTT was added to the light blue cathode buffer to a final concentration of 1 mM. Following electrophoresis, proteins were transferred to a polyvinylidene difluoride (PVDF) membrane (BioRad, 162-0177) at 25 V at 4 °C for 2 h. Following

transfer, the membrane was soaked in 8% acetic acid for 15 min, rinsed with ddH_2O, and dried. The membrane was incubated with 100% methanol for 1 min, rinsed with ddH_2O, blocked with 5% bovine serum albumin (BSA) diluted in PBS−/−, and incubated with antibodies for immunoblotting. All native gels were electrophoresed with the NativeMark Protein Standard (ThermoFisher, LC0725) for molecular weight estimation.

SDS–PAGE. Samples for denaturing PAGE were diluted in 5× SDS–PAGE sample buffer and incubated at 95 °C for 10 min. Samples were loaded into wells of 10% acrylamide gels (BioRad, 4561036) and electrophoresed at 100 V for 90 min. Follow electrophoresis, gels were either stained with colloidal blue (ThermoFisher, LC6025) or transferred to nitrocellulose for immunoblotting. Immunoblots were scanned using an Odyssey CLx imaging system (Li-Cor) and analyzed as described[55].

The following antibodies were used for immunoblotting: guinea pig σNS polyclonal antiserum[56], rabbit reovirus-specific polyclonal antiserum[57], mouse 4F2 σ3 monoclonal antibody[31], rabbit VU219 σ3 polyclonal antiserum (this study), mouse 8H6 μ1/μ1δ monoclonal antibody[31], rat CCT1 monoclonal antibody (Enzo Life Sciences, ADI-CTA-123), rabbit CCT2 monoclonal antibody (Abcam, ab92746), rabbit CCT3 polyclonal antiserum (ABclonal, A6547), mouse CCT4 monoclonal antibody (Santa Cruz, sc-137092), rabbit CCT5 monoclonal antibody (Abcam, ab129016), mouse CCT8 polyclonal antibody (Novus Biologicals, H00010694-B02P), mouse GAPDH monoclonal antibody (Sigma, G8795) and rabbit GFP polyclonal antiserum (Santa-Cruz, sc-8334).

Immunofluorescence microscopy, image analysis and quantification. Confocal microscopy was performed as described[47] with the following modifications: cells were fixed in 4% paraformaldehyde (PFA, Electron Microscopy Sciences, 15712-s) diluted in PBS−/− at RT for 20 min and counterstained with 4′,6-diamidino-2-phenylindole (DAPI, Invitrogen, D3571) to label nuclei. Confocal images were captured using a Zeiss LSM 710 laser scanning confocal microscope equipped with a 63× oil objective. Images were processed using Zen 2012 and ImageJ software with the Fiji plugin[54]. Immunofluorescence images to quantify folded and unfolded reovirus σ3 were captured using a Lionheart FX automated microscope (BioTek) equipped with a 20× air objective. Images were processed and signals quantified using Gen5+ software (BioTek). The following antibodies were used: guinea pig σ NS polyclonal antiserum[56], mouse 10C1 σ3 monoclonal antibody (conformation-specific antibody, used to label native σ3 (ref. [31]), rabbit VU219 σ3 polyclonal antiserum (used to label total σ3), rabbit anti-CCT1 polyclonal antiserum (NeoScientific, A1950), rabbit CCT3 polyclonal antiserum (ABclonal, A6547).

ISVP purification and recoating. To generate ISVPs, 2×10^{12} purified T1L reovirus particles were incubated with chymotrypsin (Sigma, C3142) diluted to 200 μg ml^{-1} at 37 °C for 60 min. Digestion was terminated by the addition of PMSF to a final concentration of 2 mM. ISVPs were purified by caesium chloride gradient (1.25 g ml^{-1} to 1.45 g ml^{-1}) centrifugation with a Beckman Coulter Optima L-90K ultracentrifuge and SW-41 rotor at 25,000 rpm at 5 °C overnight. Purified ISVPs were dialysed in four 1 l volumes of virion storage buffer (10 mM Tris-HCl pH 7.5, 150 mM KCl, 15 mM $MgCl_2$) and stored at 4 °C. Virion-to-ISVP conversion was confirmed by SDS–PAGE and colloidal blue staining to assess the loss of σ3 and cleavage of μ1C to μ1δ. For recoating experiments, ISVPs (5×10^{10}) or an equal volume of virion storage buffer were added to in vitro translated σ3 and incubated at 37 °C for 2 h.

Electron microscopy. Cells were incubated with a mixture of 4% PFA and 1% glutaraldehyde in 0.4 M HEPES buffer, pH 7.4 at room temperature for 1 h. Cells were incubated with 1% osmium tetroxide and 0.8% potassium ferricyanide in water at 4 °C for 1 h and dehydrated in 5 minute steps with increasing concentrations of acetone (50%, 70%, 90% and twice in 100%) at 4 °C. Samples were incubated at room temperature overnight with a 1:1 mixture of acetone-resin, infiltrated for 8 h in pure epoxy resin EML-812 (TAAB Laboratories)[22] and polymerized at 60 °C for 48 h. Ultrathin (~60 nm) oriented serial sections were prepared using a UC6 ultramicrotome (Leica Microsystems), collected on uncoated 300-mesh copper grids (TAAB Laboratories), stained with saturated uranyl acetate and lead citrate, and imaged by transmission electron microscopy (TEM). Images were acquired using a JEOL JEM 1011 electron microscope operating at 100 kv. Reovirus inclusion and particle morphology were assessed by imaging more than 100 HBMECs reverse-transfected with non-targeting (luciferase siRNA) or TRiC subunit-specific siRNAs by TEM.

For immunogold labelling on thawed cryosections (Tokuyasu method[58,59]),cells were incubated with 4% PFA in PHEM buffer, pH 7.2 (60 mM piperazine-N,N′-bis (2-ethanesulfonic acid), 25 mM HEPES, 10 mM EGTA, 2 mM $MgCl_2$) at RT for 2 h, followed by 50 mM NH_4Cl to quench free aldehydes groups. Cells were collected by centrifugation, embedded in 12% gelatin (TAAB Laboratories) in PBS, and incubated on ice for 15 min. Pellets were divided into 1 mm^3 cubes and incubated at 4 °C overnight with 2.1 M sucrose in PBS. Blocks were mounted on metal pins and frozen in liquid nitrogen. Ultrathin cryosections (50–100 nm) were prepared using a diamond knife and a UC6 cryoultramicrotome (Leica Microsystems) operating at −120 °C. Sections were collected using a mixture of 2% methylcellulose in H_2O and 2.1 M sucrose in PBS (1:1) and transferred to 200-mesh grids with a carbon-coated Formvar film. Grids were incubated with PBS at 37 °C for 25 min in a humid chamber. Free aldehydes were quenched with 50 mM NH_4Cl (five times at 2 min each) before incubation with 1% BSA for 5 min. Cryosections were incubated with a rabbit CCT2-specific monoclonal antibody (Abcam, ab92746) diluted 1:20 in 1% BSA for 1 h. After washes with 0.1% BSA (5 times at 2 min each) and 1% BSA (5 min), grids were incubated for 30 min with a secondary antibody conjugated with 10 nm colloidal gold particles (BB International) diluted 1:50 in 1% BSA. Cryosections were washed with 0.1% BSA (twice at 2 min each) and PBS (3 times at 2 min each) before incubation with 1% glutaraldehyde in PBS for 5 min. After washing with water (nine times at 2 min each), grids were incubated with uranyl acetate and methylcellulose (9:1) on ice for 5 min. Grids were collected, dried, and imaged using a JEOL JEM 1011 electron microscope operating at 100 kv. Images from immunogold-labelled Tokuyasu cryosections were selected from more than 50 mock-infected and reovirus-infected cells.

High-throughput RNA interference screen. *Day 1: reverse transfection of siRNA library (step 1).* The Dharmacon human ON-TARGETplus druggable genome siRNA library (7,518 genes total with pools of four unique siRNAs targeting each gene) was aliquoted in triplicate into black, clear-bottom, 384-well plates (Greiner, 781091) for a final diluted siRNA concentration of 25 nM. Control siRNAs targeting JAM-A (receptor for reovirus), reovirus μ2, reovirus μNS and a non-targeting control were seeded into empty wells. As a control for transfection efficiency, wells also were seeded with the AllStars Cell Death control siRNA (Qiagen). Lipofectamine RNAiMax transfection reagent was diluted in Opti-MEM reduced-serum medium, and aliquoted into each well (0.07 μl RNAiMax per well). Following a 15 min incubation at room temperature, the siRNA/lipid solution was combined with 5×10^2 HBMECs per well in complete RPMI medium. Cells were incubated at 37 °C for 48 h to allow efficient target knockdown.

Day 3: reovirus infection. Previously transfected HBMECs were adsorbed with reovirus T1L M1 P208S at a MOI of 1,000 PFU per cell at 37 °C for 3 h. Cells were washed twice with PBS−/−, supplemented with complete RPMI medium, and incubated at 37 °C for 48 h.

Day 5: supernatant transfer and fixation of step 1 cells. The cell culture medium (30 μl) covering step 1 infected cells was transferred to V-bottom 384-well plates using an Agilent Bravo automated liquid handling platform. The remaining medium covering step 1 cells was removed, and cells were incubated with ice-cold 100% methanol and stored at −20 °C. Supernatants in V-bottom plates were centrifuged at 1,000 r.p.m. at RT for 10 min to collect cellular debris. The supernatant was transferred to new (step 2) 384-well plates. HBMECs (2×10^3 cells per well) were seeded on top of the transferred supernatants and cultured at 37 °C for 24 h.

Day 6: fixation of step 2 cells. The culture medium covering step 2 cells was aspirated, and cells were incubated with ice-cold 100% methanol and stored at −20 °C.

Day 7: immunofluorescence staining. Step 1 and step 2 cells were brought to RT, the methanol fixative was aspirated, and cells were washed twice with PBS−/−. PBS−/− containing 5% BSA was added to each well and incubated at 37 °C for 15 min. The BSA blocking solution was aspirated, and cells were incubated with a reovirus σNS-specific guinea pig polyclonal antiserum diluted 1:2000 in PBS−/− containing 0.5% Triton-X 100 (PBS-T) at 37 °C for 1 h. Cells were washed twice with PBS−/− and incubated with DAPI and a guinea pig-specific Alexa 488 secondary antibody (diluted 1:1000) in PBS-T at 37 °C for 1 h. Cells were wash twice with PBS−/− and covered with H_2O for imaging.

Day 8: high-content imaging. Fluorescent images were captured using an ImageXpress Micro XL (Molecular Devices) automated microscope equipped with a 20× air objective. Four independent fields of view were acquired for each well.

Day 9: quantitative image analysis. Reovirus-infected HBMECs in step 1 and step 2 plates were enumerated using MetaXpress image analysis software (Molecular Devices). Fluorescence intensity thresholds were defined to identify objects containing DAPI (total cell count) and objects containing DAPI and Alexa 488 (infected cell count). The percentage of infected cells was calculated by dividing the infected cell count by the total cell count and multiplying by 100.

Data analysis. The efficiency of reovirus release from step 1 cells and subsequent infection of step 2 cells was determined by dividing the percentage of infected cells in step 2 plates by the percentage of infected cells in step 1 plates. We termed this calculation the egress ratio. The egress ratio for each siRNA pool was transformed to a $\log_2$ scale. Candidate genes were identified by calculating robust Z-scores using the log-transformed egress ratios. The log-transformed egress ratio values of the aggregate samples in each 384-well plate were used to calculate median and median absolute deviation values. The robust Z-scores for individual genes were then calculated using the formula below:

$$\text{*Robust Z score} = \frac{\text{Gene egress ratio} - \text{Plate egress ratio median}}{1.486 \times \text{Plate egress ratio median absolution deviation}}$$

All values are $\log_2$ transformed in the equation above.

As a viability filter, all siRNAs that reduced the step 1 cell count 2.5 standard deviations below the mean step 1 cell count for the aggregated wells in the entire screen, were removed from the analysis (102/7, 518 = 1.35% of genes). A median robust *Z*-score cutoff of −2.5 was applied across the three replicates of the remaining 7,416 genes to identify candidate mediators of late steps in reovirus replication. All screening experiments were conducted in the Vanderbilt High Throughput Screening Core.

STRING protein–protein interaction prediction. STRING functional protein association network analysis[60] was conducted using the 242 candidate genes with median robust Z-scores less than or equal to −2.5. Of the candidate genes, 241 were recognized in the analysis and assembled into an interactome map. The K_{means} clustering algorithm was used to group the genes into four clusters.

Statistical analysis. All experiments were performed with a minimum of three independent replicates. Data are presented as the mean ± s.e.m. unless otherwise indicated. Two-tailed unpaired Student's *t*-tests were used with an $\alpha = 0.05$. Where indicated, ordinary one-way ANOVA analyses were performed with Tukey's multiple comparisons test ($\alpha = 0.05$). For all box-and-whisker plots, whiskers denote the minimum and maximal values, boxes denote the 25th and 75th percentiles and the centre denotes the median value. Exact *P*-values and confidence intervals are tabulated in Supplementary Table 3. All statistical analyses were conducted using GraphPad Prism 7.00 data analysis software.

Life Sciences Reporting Summary. Further information on experimental design is available in the Life Sciences Reporting Summary.

Data availability. The authors declare that the main data supporting the findings of this study are available within the article and its Supplementary Information files. Purified recombinant human TRiC is a limited resource that was provided by the Frydman Lab (Stanford University). Please contact Judith Frydman directly (jfrydman@stanford.edu) for inquiries related to purified human TRiC.

Received: 18 August 2017; Accepted: 2 February 2018;
Published online: 12 March 2018

References

1. Bouziat, R. et al. Reovirus infection triggers inflammatory responses to dietary antigens and development of celiac disease. *Science* **356**, 44–50 (2017).
2. Dermody, T. S., Parker, J. S. & Sherry, B. in *Fields Virology,* Vol. 2 (eds. D. M. Knipe & P. M. Howley) pp. 1304–1346 (Lippincott Williams & Wilkins, Philadelphia, 2013).
3. Barton, E. S. et al. Junction adhesion molecule is a receptor for reovirus. *Cell* **104**, 441–451 (2001).
4. Konopka-Anstadt, J. L. et al. The Nogo receptor NgR1 mediates infection by mammalian reovirus. *Cell Host Microbe* **15**, 681–691 (2014).
5. Maginnis, M. S. et al. NPXY motifs in the β1 integrin cytoplasmic tail are required for functional reovirus entry. *J. Virol.* **82**, 3181–3191 (2008).
6. Ebert, D. H., Deussing, J., Peters, C. & Dermody, T. S. Cathepsin L and cathepsin B mediate reovirus disassembly in murine fibroblast cells. *J. Biol. Chem.* **277**, 24609–24617 (2002).
7. Leitner, A. et al. The molecular architecture of the eukaryotic chaperonin TRiC/CCT. *Structure* **20**, 814–825 (2012).
8. Bigotti, M. G. & Clarke, A. R. Chaperonins: the hunt for the group II mechanism. *Arch. Biochem. Biophys.* **474**, 331–339 (2008).
9. Hartl, F. U., Bracher, A. & Hayer-Hartl, M. Molecular chaperones in protein folding and proteostasis. *Nature* **475**, 324–332 (2011).
10. Spiess, C., Meyer, A. S., Reissmann, S. & Frydman, J. Mechanism of the eukaryotic chaperonin: protein folding in the chamber of secrets. *Trends Cell Biol.* **14**, 598–604 (2004).
11. Yam, A. Y. et al. Defining the TRiC/CCT interactome links chaperonin function to stabilization of newly made proteins with complex topologies. *Nat. Struct. Mol. Biol.* **15**, 1255–1262 (2008).
12. Frydman, J. et al. Function in protein folding of TRiC, a cytosolic ring complex containing TCP-1 and structurally related subunits. *EMBO J.* **11**, 4767–4778 (1992).
13. Gao, Y., Thomas, J. O., Chow, R. L., Lee, G. H. & Cowan, N. J. A cytoplasmic chaperonin that catalyzes beta-actin folding. *Cell* **69**, 1043–1050 (1992).
14. Gao, Y., Vainberg, I. E., Chow, R. L. & Cowan, N. J. Two cofactors and cytoplasmic chaperonin are required for the folding of alpha- and beta-tubulin. *Mol. Cell Biol.* **13**, 2478–2485 (1993).
15. Hong, S. et al. Type D retrovirus Gag polyprotein interacts with the cytosolic chaperonin TRiC. *J. Virol.* **75**, 2526–2534 (2001).
16. Lingappa, J. R. et al. A eukaryotic cytosolic chaperonin is associated with a high molecular weight intermediate in the assembly of hepatitis B virus capsid, a multimeric particle. *J. Cell Biol.* **125**, 99–111 (1994).
17. Kashuba, E., Pokrovskaja, K., Klein, G. & Szekely, L. Epstein-Barr virus-encoded nuclear protein EBNA-3 interacts with the epsilon-subunit of the T-complex protein 1 chaperonin complex. *J. Hum. Virol.* **2**, 33–37 (1999).
18. Inoue, Y. et al. Chaperonin TRiC/CCT participates in replication of hepatitis C virus genome via interaction with the viral NS5B protein. *Virology* **410**, 38–47 (2011).
19. Zhang, J. et al. Cellular chaperonin CCTγ contributes to rabies virus replication during infection. *J. Virol.* **87**, 7608–7621 (2013).
20. Fislova, T., Thomas, B., Graef, K. M. & Fodor, E. Association of the influenza virus RNA polymerase subunit PB2 with the host chaperonin CCT. *J. Virol.* **84**, 8691–8699 (2010).
21. Solignat, M., Gay, B., Higgs, S., Briant, L. & Devaux, C. Replication cycle of chikungunya: a re-emerging arbovirus. *Virology* **393**, 183–197 (2009).
22. Fernandez de Castro, I. et al. Reovirus forms neo-organelles for progeny particle assembly within reorganized cell membranes. *mBio* **5**, e00931-13 (2014).
23. Thulasiraman, V., Yang, C. F. & Frydman, J. In vivo newly translated polypeptides are sequestered in a protected folding environment. *EMBO J.* **18**, 85–95 (1999).
24. Shing, M. & Coombs, K. M. Assembly of the reovirus outer capsid requires μ1/σ3 interactions which are prevented by misfolded σ3 protein in temperature-sensitive mutant tsG453. *Virus Res.* **46**, 19–29 (1996).
25. Chandran, K. et al. In vitro recoating of reovirus cores with baculovirus-expressed outer-capsid proteins μ1 and σ3. *J. Virol.* **73**, 3941–3950 (1999).
26. Kasembeli, M. et al. Modulation of STAT3 folding and function by TRiC/CCT chaperonin. *PLoS Biol.* **12**, e1001844 (2014).
27. Freund, A. et al. Proteostatic control of telomerase function through TRiC-mediated folding of TCAB1. *Cell* **159**, 1389–1403 (2014).
28. Tian, G., Vainberg, I. E., Tap, W. D., Lewis, S. A. & Cowan, N. J. Specificity in chaperonin-mediated protein folding. *Nature* **375**, 250–253 (1995).
29. Feldman, D. E., Thulasiraman, V., Ferreyra, R. G. & Frydman, J. Formation of the VHL-elongin BC tumor suppressor complex is mediated by the chaperonin TRiC. *Mol. Cell* **4**, 1051–1061 (1999).
30. Miyata, Y., Shibata, T., Aoshima, M., Tsubata, T. & Nishida, E. The molecular chaperone TRiC/CCT binds to the Trp-Asp 40 (WD40) repeat protein WDR68 and promotes its folding, protein kinase DYRK1A binding, and nuclear accumulation. *J. Biol. Chem.* **289**, 33320–33332 (2014).
31. Virgin, H. W. IV, Mann, M. A., Fields, B. N. & Tyler, K. L. Monoclonal antibodies to reovirus reveal structure/function relationships between capsid proteins and genetics of susceptibility to antibody action. *J. Virol.* **65**, 6772–6781 (1991).
32. Olland, A. M., Jané-Valbuena, J., Schiff, L. A., Nibert, M. L. & Harrison, S. C. Structure of the reovirus outer capsid and dsRNA-binding protein σ3 at 1.8 Å resolution. *EMBO J.* **20**, 979–989 (2001).
33. Miller, J. E. & Samuel, C. E. Proteolytic cleavage of the reovirus σ3 protein results in enhanced double-stranded RNA-binding activity: identification of a repeated basic amino acid motif within the C-terminal binding region. *J. Virol.* **66**, 5347–5356 (1992).
34. Liemann, S., Chandran, K., Baker, T. S., Nibert, M. L. & Harrison, S. C. Structure of the reovirus membrane-penetration protein, μ1, in a complex with its protector protein, σ3. *Cell* **108**, 283–295 (2002).
35. Martin, J. et al. Chaperonin-mediated protein folding at the surface of groEL through a 'molten globule'-like intermediate. *Nature* **352**, 36–42 (1991).
36. Frydman, J., Nimmesgern, E., Ohtsuka, K. & Hartl, F. U. Folding of nascent polypeptide chains in a high molecular mass assembly with molecular chaperones. *Nature* **370**, 111–117 (1994).
37. Jané-Valbuena, J. et al. Reovirus virion-like particles obtained by recoating infectious subvirion particles with baculovirus-expressed σ3 protein: an approach for analyzing σ3 functions during virus entry. *J. Virol.* **73**, 2963–2973 (1999).
38. Joachimiak, L. A., Walzthoeni, T., Liu, C. W., Aebersold, R. & Frydman, J. The structural basis of substrate recognition by the eukaryotic chaperonin TRiC/CCT. *Cell* **159**, 1042–1055 (2014).
39. Georgescauld, F. et al. GroEL/ES chaperonin modulates the mechanism and accelerates the rate of TIM-barrel domain folding. *Cell* **157**, 922–934 (2014).
40. Tian, G. & Cowan, N. J. Tubulin-specific chaperones: components of a molecular machine that assembles the α/β heterodimer. *Methods Cell Biol.* **115**, 155–171 (2013).
41. Plimpton, R. L. et al. Structures of the Gβ-CCT and PhLP1-Gβ-CCT complexes reveal a mechanism for G-protein β-subunit folding and Gβγ dimer assembly. *Proc. Natl Acad. Sci. USA* **112**, 2413–2418 (2015).
42. Spiess, C., Miller, E. J., McClellan, A. J. & Frydman, J. Identification of the TRiC/CCT substrate binding sites uncovers the function of subunit diversity in eukaryotic chaperonins. *Mol. Cell* **24**, 25–37 (2006).
43. Leroux, M. R. & Hartl, F. U. Protein folding: versatility of the cytosolic chaperonin TRiC/CCT. *Curr. Biol.* **10**, R260–R264 (2000).

44. Feldman, D. E., Spiess, C., Howard, D. E. & Frydman, J. Tumorigenic mutations in VHL disrupt folding in vivo by interfering with chaperonin binding. *Mol. Cell* **12**, 1213–1224 (2003).
45. Attoui, H. et al. Common evolutionary origin of aquareoviruses and orthoreoviruses revealed by genome characterization of Golden shiner reovirus, Grass carp reovirus, Striped bass reovirus and golden ide reovirus (genus Aquareovirus, family Reoviridae). *J. Gen. Virol.* **83**, 1941–1951 (2002).
46. Stins, M. F., Gilles, F. & Kim, K. S. Selective expression of adhesion molecules on human brain microvascular endothelial cells. *J. Neuroimmunol.* **76**, 81–90 (1997).
47. Mainou, B. A. & Dermody, T. S. Transport to late endosomes is required for efficient reovirus infection. *J. Virol.* **86**, 8346–8358 (2012).
48. Virgin, H. Wt, Bassel-Duby, R., Fields, B. N. & Tyler, K. L. Antibody protects against lethal infection with the neurally spreading reovirus type 3 (Dearing). *J. Virol.* **62**, 4594–4604 (1988).
49. Kobayashi, T. et al. A plasmid-based reverse genetics system for animal double-stranded RNA viruses. *Cell Host Microbe* **1**, 147–157 (2007).
50. Furlong, D. B., Nibert, M. L. & Fields, B. N. Sigma 1 protein of mammalian reoviruses extends from the surfaces of viral particles. *J. Virol.* **62**, 246–256 (1988).
51. Parker, J. S., Broering, T. J., Kim, J., Higgins, D. E. & Nibert, M. L. Reovirus core protein μ2 determines the filamentous morphology of viral inclusion bodies by interacting with and stabilizing microtubules. *J. Virol.* **76**, 4483–4496 (2002).
52. Mainou, B. A. et al. Reovirus cell entry requires functional microtubules. *mBio* **4**, e00405-13 (2013).
53. Becker, M. M. et al. Reovirus σNS protein is required for nucleation of viral assembly complexes and formation of viral inclusions. *J. Virol.* **75**, 1459–1475 (2001).
54. Schindelin, J. et al. Fiji: an open-source platform for biological-image analysis. *Nat. Methods* **9**, 676–682 (2012).
55. Mainou, B. A. & Dermody, T. S. Src kinase mediates productive endocytic sorting of reovirus during cell entry. *J. Virol.* **85**, 3203–3213 (2011).
56. Becker, M. M., Peters, T. R. & Dermody, T. S. Reovirus σNS and μNS proteins form cytoplasmic inclusion structures in the absence of viral infection. *J. Virol.* **77**, 5948–5963 (2003).
57. Barton, E. S., Connolly, J. L., Forrest, J. C., Chappell, J. D. & Dermody, T. S. Utilization of sialic acid as a coreceptor enhances reovirus attachment by multistep adhesion strengthening. *J. Biol. Chem.* **276**, 2200–2211 (2001).
58. Fontana, J., Lopez-Montero, N., Elliott, R. M., Fernandez, J. J. & Risco, C. The unique architecture of Bunyamwera virus factories around the Golgi complex. *Cell Microbiol.* **10**, 2012–2028 (2008).
59. Hurbain, I. & Sachse, M. The future is cold: cryo-preparation methods for transmission electron microscopy of cells. *Biol. Cell* **103**, 405–420 (2011).
60. Szklarczyk, D. et al. STRINGv10: protein–protein interaction networks, integrated over the tree of life. *Nucleic Acids Res.* **43**, D447–D452 (2015).
61. Sourisseau, M. et al. Characterization of reemerging chikungunya virus. *PLoS Pathog.* **3**, e89 (2007).

Acknowledgements

This work was supported in part by Public Health Service awards AI032539, AI122563, GM007347, UL1TR000445, and the Vanderbilt Lamb Center for Pediatric Research. The RNAi screen was performed in the Vanderbilt high-throughput screening facility, which is an institutionally supported core. Confocal images were captured in the cell imaging core at the Rangos Research Center at Children's Hospital of Pittsburgh of UPMC. The authors thank P. Aravamudhan, J. Brown, B. Mainou, L. Silva, D. Sutherland and G. Taylor of the Dermody lab for essential discussions and critically editing the manuscript.

Author contributions

J.J.K. conceived, designed experiments and performed experiments, analysed data, contributed materials/analysis tools and wrote the paper. T.S.D. conceived and designed experiments, analysed the data and wrote the paper. I.F.C., A.W.A. and P.F.Z. conceived, designed experiments and performed experiments, and analysed data. J.A.B. conceived and designed experiments and performed experiments. D.R.G, J.F. and C.R. conceived and designed experiments, analysed data, and contributed materials/analysis tools. J.C.F. analysed data. All authors reviewed, critiqued and provided comments on the manuscript.

Competing interests

The authors declare no competing interests.

Additional information

Supplementary information accompanies this paper at https://doi.org/10.1038/s41564-018-0122-x.

Reprints and permissions information is available at www.nature.com/reprints.

Correspondence and requests for materials should be addressed to T.S.D.

Publisher's note: Springer Nature remains neutral with regard to jurisdictional claims in published maps and institutional affiliations.

nature research

Jonathan Knowlton, Isabel Fernandez De Castro, Alison Ashbrook, Daniel Gestaut, Paula Zamora, J Craig Forrest, Joshua Bauer, Judith Frydman, Cristina Risco,
Corresponding author(s): Terence Dermody

☐ Initial submission ☐ Revised version ☒ Final submission

Life Sciences Reporting Summary

Nature Research wishes to improve the reproducibility of the work that we publish. This form is intended for publication with all accepted life science papers and provides structure for consistency and transparency in reporting. Every life science submission will use this form; some list items might not apply to an individual manuscript, but all fields must be completed for clarity.

For further information on the points included in this form, see Reporting Life Sciences Research. For further information on Nature Research policies, including our data availability policy, see Authors & Referees and the Editorial Policy Checklist.

Experimental design

1. Sample size

   Describe how sample size was determined.

   All experiments were performed with a minimum of three independent replicates and included a minimum of three technical replicates within each independent experiment. A sample size of three was chosen to limit experimental bias or random error. This is convention for the field of virology.

2. Data exclusions

   Describe any data exclusions.

   In our RNAi screen for cellular mediators of late events in reovirus replication we applied a filter for viable cells and excluded non-viable cells from our data analysis. Non-viable cells were defined as step 1 cells with a mean cell count 2.5 standard deviations below the mean step 1 cell count for the aggregated wells in the entire screen. This was an arbitrary cut-off established before the screen was conducted.

3. Replication

   Describe whether the experimental findings were reliably reproduced.

   All attempts at replication were successful.

4. Randomization

   Describe how samples/organisms/participants were allocated into experimental groups.

   No randomization was used in this study. For tissue culture and in vitro work, experiments were conducted with a minimum of three technical replicates with the appropriate positive and negative controls.

5. Blinding

   Describe whether the investigators were blinded to group allocation during data collection and/or analysis.

   No blinding was used in this study. When possible, automated machine-based methods were used for quantification to avoid observer bias. This included machine-based analysis of RNAi screen data, cell infectivity, 35S-labeled gels, and immunofluorescence images.

Note: all studies involving animals and/or human research participants must disclose whether blinding and randomization were used.

6. Statistical parameters

For all figures and tables that use statistical methods, confirm that the following items are present in relevant figure legends (or in the Methods section if additional space is needed).

n/a	Confirmed
☐	☒ The exact sample size (*n*) for each experimental group/condition, given as a discrete number and unit of measurement (animals, litters, cultures, etc.)
☐	☒ A description of how samples were collected, noting whether measurements were taken from distinct samples or whether the same sample was measured repeatedly
☐	☒ A statement indicating how many times each experiment was replicated
☐	☒ The statistical test(s) used and whether they are one- or two-sided (note: only common tests should be described solely by name; more complex techniques should be described in the Methods section)
☐	☒ A description of any assumptions or corrections, such as an adjustment for multiple comparisons
☐	☒ The test results (e.g. *P* values) given as exact values whenever possible and with confidence intervals noted
☐	☒ A clear description of statistics including central tendency (e.g. median, mean) and variation (e.g. standard deviation, interquartile range)
☐	☒ Clearly defined error bars

See the web collection on statistics for biologists for further resources and guidance.

▸ Software

Policy information about availability of computer code

7. Software

Describe the software used to analyze the data in this study.

1. MetaExpress software (Molecular Devices, version 5.3.0.5) was used to analyze images from a high-throughput RNAi screen.

2. ImageJ software (Schindelin et al., 2015, version 1.51t) was used to process immunofluorescence images and phosphorimaging files.

3. Gen5+ software (BioTek, version 3.03) was used for automated image analysis of folded and unfolded protein by immunofluorescence microscopy.

4. Image Studio software (Licor, version 5.2) was used to capture and process immunoblotted membranes and colloidal blue-stained gels.

5. ZEN 2012 software (Zeiss, blue edition, version 1.1.2.0) was used to process confocal immunofluorescence images.

6. STRING functional protein association network analysis software (Szklarczyk et al., 2015, version 10.5) was used to generate an interaction network for candidates identified in RNAi screen.

7. Prism software (GraphPad, version 7.00) was used to analyze numerical data and generate charts and graphs.

8. Microsoft excel (2016 edition) was used to process raw numerical data for entry into Prism software.

For manuscripts utilizing custom algorithms or software that are central to the paper but not yet described in the published literature, software must be made available to editors and reviewers upon request. We strongly encourage code deposition in a community repository (e.g. GitHub). *Nature Methods* guidance for providing algorithms and software for publication provides further information on this topic.

Materials and reagents

Policy information about availability of materials

8. Materials availability

Indicate whether there are restrictions on availability of unique materials or if these materials are only available for distribution by a for-profit company.

Purified recombinant human TRiC is a limited resource that was provided by the Frydman Lab (Stanford University). Please contact Judith Frydman directly (jfrydman@stanford.edu) for inquiries directly related to purified human TRiC.

9. Antibodies

Describe the antibodies used and how they were validated for use in the system under study (i.e. assay and species).

1. Guinea pig σNS-specific polyclonal serum. Used for immunofluorescence microscopy and immunoblotting (1:2000 dilution). Produced and characterized by Becker et al. in 2001. Citation: Becker, M. M. et al. Citation: Becker, M.M., Peters, T.R. & Dermody, T.S. Reovirus sigma NS and mu NS proteins form cytoplasmic inclusion structures in the absence of viral infection. J Virol 77, 5948-63 (2003).
2. Rabbit reovirus-specific polyclonal serum. Used for immunoblotting (1:1000 dilution). Produced and characterized by Barton et al. in 2001. Citation: Barton, E.S., Connolly, J.L., Forrest, J.C., Chappell, J.D. & Dermody, T.S. Utilization of sialic acid as a coreceptor enhances reovirus attachment by multistep adhesion strengthening. J Biol Chem 276, 2200-11 (2001).
3. Mouse reovirus σ3-specific monoclonal antibody (clone 4F2). Used for immunoblotting (1:1000 dilution). Produced and characterized by Virgin et al. in 1991. Citation: Virgin, H.W.t., Mann, M.A., Fields, B.N. & Tyler, K.L. Monoclonal antibodies to reovirus reveal structure/function relationships between capsid proteins and genetics of susceptibility to antibody action. J Virol 65, 6772-81 (1991).
4. Mouse reovirus σ3-specific monoclonal antibody (clone 10C1). Used for immunofluorescence (1:1000 dilution) and immunoprecipitation (5 µg per immunoprecipitation reaction). Produced and characterized by Virgin et al. in 1991. Citation: Virgin, H.W., Mann, M.A., Fields, B.N. & Tyler, K.L. Monoclonal antibodies to reovirus reveal structure/function relationships between capsid proteins and genetics of susceptibility to antibody action. J Virol 65, 6772-81 (1991).
5. Mouse reovirus µ1-specific monoclonal antibody (clone 8H6). Used for immunoprecipitation (5 µg of antibody per immunoprecipitation reaction). Produced and characterized by Virgin et al. in 1991. Citation: Virgin, H.W., Mann, M.A., Fields, B.N. & Tyler, K.L. Monoclonal antibodies to reovirus reveal structure/function relationships between capsid proteins and genetics of susceptibility to antibody action. J Virol 65, 6772-81 (1991).
6. Mouse reovirus σNS-specific monoclonal antibody (clone 2F5). Used as an isotype control for immunoprecipitation (5 µg of antibody per immunoprecipitation reaction). Citation: Becker, M. M. et al. Citation: Becker, M.M. et al. Reovirus sigma-NS protein is required for nucleation of viral assembly complexes and formation of viral inclusions. J Virol 75, 1459-75 (2001).
7. Rabbit σ3-specific polyclonal antiserum (VU219). Produced by Cocalico Biologicals, Inc. First used in this study for immunofluorescence and immunoblotting (1:1000 dilution). Confirmed as σ3-specific by immunoblot and immunofluorescence (Supplementary figure 10).
8. Rabbit CCT1-specific polyclonal antibody. Used in this study for immunofluorescence (1:100 dilution). (NeoScientific. Catalog number: A1950). Validated by manufacturer for immunoblotting, immunohistochemistry, and immunofluorescence.
9. Rabbit CCT2-specific monoclonal antibody (clone EPR4048). Used in this study for immunoblotting (1:1000 dilution), immunoprecipitation (2 µg), and immunogold labeling (1:20 dilution). (Abcam. Catalog number: ab92746). Validated by manufacturer for immunoblotting, immunoprecipitation, immunohistochemistry, flow cytometry, and immunofluorescence. Cited in 4 publications.
10. Rabbit CCT2-specific polyclonal antibody. Used for immunodepletion of TRiC from rabbit reticulocyte lysates (8 µg per round of immunodepletion). Produced and characterized by the Frydman lab (Stanford University). Validated for immunodepletion by the following study4: Freund, A. et al. Proteostatic control of telomerase function through TRiC-mediated folding of TCAB1. Cell 159, 1389-403 (2014).
11. Rabbit CCT3-specific polyclonal antibody. Used in this study for immunoblotting (1:100 dilution) and immunofluorescence (1:100 dilution). (ABclonal. Catalog number: A6547) Validated by manufacturer for immunoblotting, immunohistochemistry, and immunofluorescence.
12. Mouse CCT4-specific monoclonal antibody (clone H1). Used in this study for immunoblotting (1:200 dilution). (Santa Cruz. Catalog number: sc-137092). Validated by manufacturer for immunoblotting, immunoprecipitation,

10. Eukaryotic cell lines

a. State the source of each eukaryotic cell line used.

Human brain microvascular endothelial cells (HBMECs) were provided by Kwang Sik Kim (Johns Hopkins University).
U-2 OS human osteosarcoma cells were purchased from ATCC (ATCC HTB-96).
HEK-293T cells were purchased from ATCC (ATCC CRL-3216).
Caco-2 cells were purchased from ATCC (ATC HTB-37)

b. Describe the method of cell line authentication used.

No cell lines have been authenticated.

c. Report whether the cell lines were tested for mycoplasma contamination.

HBMECs were tested for mycoplasma contamination using a commercially available kit (Sigma, MP0025). U-2 OS cells, HEK-293T, and Caco-2 cells were not tested for mycoplasma contamination.

d. If any of the cell lines used are listed in the database of commonly misidentified cell lines maintained by ICLAC, provide a scientific rationale for their use.

No commonly misidentified cell lines were used in this study.

Animals and human research participants

Policy information about studies involving animals; when reporting animal research, follow the ARRIVE guidelines

11. Description of research animals

Provide details on animals and/or animal-derived materials used in the study.

No animals were used in this study.

Policy information about studies involving human research participants

12. Description of human research participants

Describe the covariate-relevant population characteristics of the human research participants.

This study did not involve human research participants.